Transactions of the ASME

Journal of Engineering for Gas Turbines and Power

Published Quarterly by The American Society of Mechanical Engineers
VOLUME 108 • NUMBER 4 • OCTOBER 1986

Technical Editor
ARTHUR J. WENNERSTROM
Senior Associate Editor
G. K. SEROVY
Associate Editors
Advanced Energy Systems
S. I. FREEDMAN
Environmental Control
H. E. HESKETH
Fuels and Combustion Technologies
R. E. BARRETT
Gas Turbine
S. KUO
Internal Combustion Engine
K. J. SPRINGER
Nuclear Engineering
S. M. CHO
Power
R. W. PORTER

BOARD ON COMMUNICATIONS
Chairman and Vice-President
K. N. REID, JR.

Members-at-Large
W. BEGELL
J. T. COKONIS
W. G. GOTTENBERG
M. KUTZ
J. R. LLOYD
T. C. MIN
R. E. NICKELL
C. F. PHILLIPS
R. E. REDER
F. W. SCHMIDT

President, **N. D. FITZROY**
Executive Director,
PAUL ALLMENDINGER
Treasurer, **ROBERT A. BENNETT**

PUBLISHING STAFF
Mng. Dir., Publ., **J. J. FREY**
Dep. Mng. Dir., Pub.,
JOS. SANSONE
Managing Editor,
CORNELIA MONAHAN
Sr. Production Editor,
VALERIE WINTERS
Editorial Prod. Asst.
MARISOL ANDINO

The Transactions of the ASME, Journal of Engineering for Gas Turbines and Power (ISSN 0022-0825) is published quarterly (Jan., Apr., July, Oct.) for $85 per year by The American Society of Mechanical Engineers, 345 East 47th Street, New York, NY 10017. Second class postage paid at New York, NY and additional mailing offices. POSTMASTER: Send address change to The Journal of Engineering for Gas Turbines and Power, c/o The AMERICAN SOCIETY OF MECHANICAL ENGINEERS, 22 Law Drive, Box 2300, Fairfield, NJ 07007-2300."

CHANGES OF ADDRESS must be received at Society headquarters seven weeks before they are to be effective. Please send old label and new address.

PRICES: To members, $24.00, annually; to nonmembers, $85.00.

Add $6.00 for postage to countries outside the United States and Canada.

STATEMENT from By-Laws. The Society shall not be responsible for statements or opinions advanced in papers or ... printed in its publications (B 7.1, para. 3).

COPYRIGHT © **1986** by the American Society of Mechanical Engineers. Reprints from this publication may be made on condition that full credit be given the TRANSACTIONS OF THE ASME – JOURNAL OF ENGINEERING FOR GAS TURBINES AND POWER, and the author, and date of publication be stated.

INDEXED by Engineering Information

TECHNICAL PAPERS

ANNOUNCEMENTS

Downloaded 03 Jun 2010 to 171.66.16.159. Redistribution subject to ASME license or copyright; see http://www.asme.org/terms/Terms_Use.cfm

Analytical and Experimental Investigation of the Coupled Bladed Disk/Shaft Whirl of a Cantilevered Turbofan

E. F. Crawley
Associate Professor,
Department of Aeronautics and Astronautics.

E. H. Ducharme
Research Assistant.

D. R. Mokadam[1]
Research Assistant.

Gas Turbine and
Plasma Dynamics Laboratory,
Massachusetts Institute of Technology,
Cambridge, MA 02139

The structural dynamics of a rotating flexible blade-rigid disk-flexible cantilevered shaft system is analytically and experimentally investigated. A simple analytical model yields the equations of motion expressed in the rotating frame, which show that the blade one nodal diameter modes dynamically couple to the rigid body whirling motion of the shaft-disk system. The blade modes higher than one nodal diameter are uncoupled from the shaft-disk dynamics. Nondimensionalization of the coupled equations of motion yield the criteria for the propensity and magnitude of the interaction between the bladed disk and shaft-disk modes. The analytical model was then correlated with the results of a structural dynamic experiment performed on the MIT Aeroelastic Rotor, a fan similar in design to a modern high bypass ratio shroudless turbofan. A special whirl excitation apparatus was used to excite both forward and backward asynchronous whirl, in order to determine the natural frequencies of the system. The agreement between the predicted and experimental natural frequencies is good and indicates the possibility of significant interaction of the one nodal diameter blade modes with the shaft-disk modes.

Introduction

The traditional approach to the structural dynamic modeling of gas turbines has been to perform an analysis of the bladed disk vibration problem [1] separately from the shaft-disk system critical speed or rotor dynamic problem [2]. The possibility of dynamic interaction between the bladed disk and the shaft-disk system is generally not analyzed. However these interactions have been observed in other rotating machinery, such as the ground resonance phenomenon in helicopters [3], whirl flutter in flexibly mounted propellers [4, 5], and horizontal axis wind turbines [6]. This paper will investigate the possibilities of such interactions occurring in gas turbine fans.

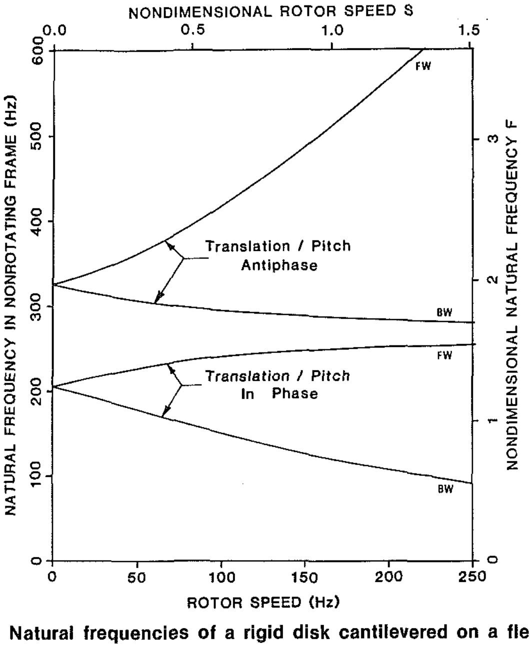

Fig. 1 Natural frequencies of a rigid disk cantilevered on a flexible shaft, expressed in the nonrotating frame of reference. Case of: $D = 0.474$, $E = 0.520$.

Current trends in the design of turbofan engines have resulted in lighter, more structurally efficient fans operating at higher speeds. As fan bypass ratios increase and shrouds are removed, the flexibility of the fan blading increases, thereby depressing the blade natural frequencies toward those of the shaft-disk system. The possibility of interaction between the structural dynamics of the bladed disk and the whirling behavior of the shaft-disk system is increased. At a minimum, neglecting this interaction may result in the inaccurate prediction of the natural frequencies of the bladed disk system and the rotor critical speeds. Even if the bladed disk frequency predictions were only a few percent in error, forced response amplitude may increase since engine order crossings on a Campbell diagram are typically designed with a margin of

---

[1] Presently Engineer, Martin Marietta Corp., Denver, CO.

Contributed by the Gas Turbine Division of The American Society of Mechanical Engineers and presented at the 31st International Gas Turbine Conference and Exhibit, Düsseldorf, Federal Republic of Germany, June 8-12, 1986. Manuscript received at ASME Headquarters January 20, 1986. Paper No. 86-GT-98.

only a few percent in frequency. The extreme result of neglecting these interactions could be the unexpected onset of whirl flutter or rotor dynamic instabilities.

Several investigators have previously studied the stability and dynamics of rotating coupled blade-disk-shaft systems. In an effort to analyze the influence of blade flexibility on rotor dynamics, Palladino and Rossettos [7] presented a model with a finite element representation of the shaft which included an analytical representation of the bladed disk. In contrast, Loewy and Khader [8] utilized a modal synthesis method to determine the degree to which the flexibility of the shaft might affect the one nodal diameter bladed disk frequencies. Gallardo and Stallone [9] also employed a modal synthesis method to analyze the dynamics of a flexible bladed disk on a flexible shaft in a two rotor system. They numerically simulated the resonant response of such systems when the difference in spool speeds coincides with a system natural frequency. Crawley [10] and Crawley and Mokadam [11] studied the dynamics of nonrotating blade-disk-shaft systems both experimentally and analytically. The nature and extent of the inertial coupling of blade vibration to the rigid body motion of the supporting disk on a flexible shaft were investigated. Nondimensionalization of the equations of motion yielded the relevant dimensionless parameters which determine the degree to which the dynamics of the blades and the dynamics of the shaft-disk are coupled for a nonrotating system.

The present study builds upon the work of [11] by developing a simple analytical model of a rotating flexible blade, rigid disk, flexible shaft system expressed in the rotor frame of reference. The results of this model compare favorably with those of the more detailed numerical model of Loewy and Khader [8]. Nondimensionalization of the simplified analytic equations of motion provides parameters which determine the propensity for, and the degree to which the bladed disk modes and the shaft-disk modes interact at speed. The analytical model was then correlated with the results of a structural dynamic experiment performed in vacuum at high rotational speed on a rotor which is typical of modern high bypass ratio fans. A swept sine experimental technique was developed to test for the natural frequencies of the rotor system. A special whirl excitation apparatus was also developed to excite both the forward and backward asynchronous whirl of the rotor. The system natural frequencies measured experimentally using this technique are then compared to those predicted by the analytical model.

Analytical Model

The analytical model of a shroudless fan with flexible blades affixed to a rigid disk which is cantilevered on a flexible shaft will include the physical features of two traditional turbomachine problems: the structural dynamics of flexible shroudless blading on a rigid disk; and the rotor dynamics of a whirling rigid disk cantilevered on a flexible shaft. After a brief review of the salient points of each individual analysis, a coupled analysis can be derived which shows the criteria for and nature of the interaction between blade vibration and shaft-disk dynamics.

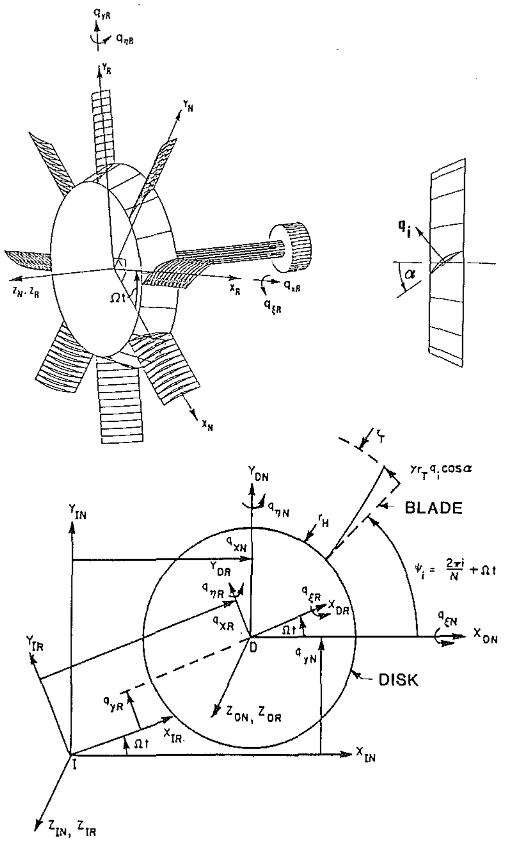

Fig. 2 Coordinate system for the whirl equations of motion for an *N*-bladed shroudless fan cantilevered on a flexible disk

Uncoupled Analyses. The simplest analytical model which captures the physics of the asynchronous whirl modes and the critical speeds of a cantilevered massless flexible shaft supporting a rigid disk is the classic model presented by Den Hartog [2]. The degrees of freedom included in the analysis are the translational displacement of the disk and the pitch angle of the disk about a diametral line. The system is free to vibrate at an angular frequency ω, not necessarily equal to the rotor

Nomenclature

a_n, b_n = nth sine and cosine multiblade coordinate
d = radius of gyration for rotor pitching
I_d = moment of inertia for rotor pitching
k_B = blade modal stiffness
K = shaft stiffness
m_0 = blade modal mass
m_1 = blade consistent mass coupling to disk pitching
m_2 = blade consistent mass coupling to disk translation
m_Ω = blade consistent mass due to extensional bending of the blade
M = total mass of rotor
N = number of blades
q_i = Ritz displacement amplitude coefficient of ith blade
q_x, q_y = disk rigid body translation degrees of freedom
q_ξ, q_η = disk rigid body pitch degrees of freedom
S = axial rotor CG offset from coordinate system origin
α = effective stagger angle of the blades
β = interblade phase angle
γ = blade mode shape function
κ = shaft translation/pitch stiffness coupling
μ = inertial coupling parameter
ϕ = relative phase angle between applied shaker forces
θ_i = angular position of ith blade in rotor frame
ψ_i = angular position of ith blade in nonrotating frame

Subscripts

B = relating to the blade
F = forcing frequency
i = of the ith blade
n = of the nth multiblade mode
N = in the nonrotating frame
P = relating to disk pitch
R = in the rotating frame
T = relating to disk translation

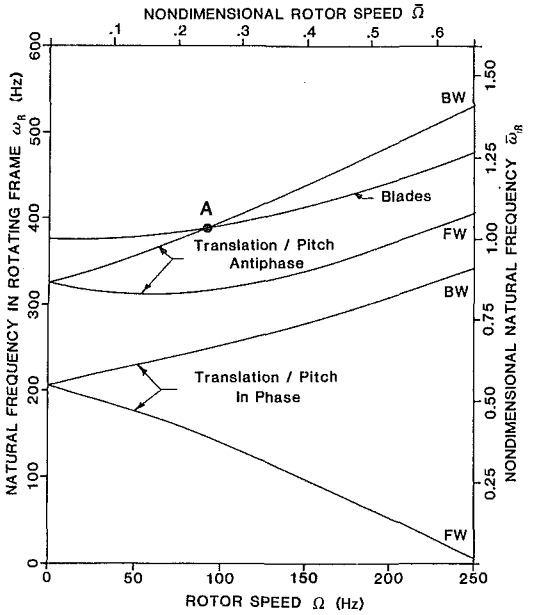

Fig. 3 Overplot of the uncoupled bladed disk frequencies with the frequencies of the uncoupled shaft-disk system, all expressed in the rotating frame of reference

speed Ω. The equations of motion, which are formulated with respect to the inertial or nonrotating frame, yield the characteristic equation for the natural frequencies [2]

$$F^4 - 2SF^3 + \frac{D+1}{D(E-1)} F^2 - \frac{2S}{E-1} F - \frac{1}{D(E-1)} = 0 \qquad (1)$$

where $F = \omega_N M/(1-\kappa^2)K_x$, the nondimensional natural frequency; $D = I_d K_x/M K_\eta$, the disk centrifugal stiffening effect; $E = \kappa^2 = K_{x\eta}^2/K_x K_\eta$, the disk translation to pitch elastic coupling; and $S = \Omega M/(1-\kappa^2)K_x$, the nondimensional rotor speed. Solution of equation (1) yields four natural frequencies ω_N, as would be observed in the nonrotating frame, for each speed Ω (Fig. 1). The two lower modes correspond to a whirling motion of the disk where the translational motion is in phase with the disk pitching motion. These are sometimes called the "bounce" modes of the rotor. One branch corresponds to whirl in the direction of rotation (forward whirl) while the other corresponds to whirl against the direction of rotation (backward whirl). The upper two branches correspond to whirling motions with the pitch component being antiphase to the translational component, one for forward whirl and the other for backward whirl. These modes are sometimes called the "pitch" modes. It is important to note that the displacements in Den Hartog's model are defined with reference to the nonrotating reference frame, and the natural frequencies calculated are those that would be observed by a nonrotating observer.

In contrast to the shaft-disk problem, the dynamics of flexible blades attached to a rotating disk is traditionally analyzed in the rotating frame of reference [1]. The simplest possible model assumes N tuned blades attached to a rigid disk, each deflecting with a single mode shape γ and amplitude q_i normal to the effective stagger angle α, as shown in Fig. 2 [10]. The equations of motion can be expressed in terms of nodal diameter patterns of displacement by applying the multiblade coordinate transformation which expresses the displacement of each blade as the sum of nodal diametral modes

$$q_i = \sum_{n=0}^{\frac{N-1}{2}} [-a_n \sin n\theta_i + b_n \cos n\theta_i] \qquad (2)$$

where $\theta_i = 2\pi i/N$, angular position of the ith blade on the rotor, and n is the nodal diameter number for the mode. If the rotor is shroudless and the disk is rigid, then the blades are elastically uncoupled and the homogeneous equations of motion for an odd number of blades are

$$m_0\ddot{a}_n + [k_B + (m_\Omega - m_0 \cos^2\alpha)\Omega^2]a_n = 0$$
$$m_0\ddot{b}_n + [k_B + (m_\Omega - m_0 \cos^2\alpha)\Omega^2]b_n = 0$$
$$n = 1, \frac{N-1}{2} \qquad (3)$$

where m_0 is the modal mass of the blade, m_Ω is the blade mass foreshortening term, and k_B is the blade modal stiffness. The centrifugal stiffening behavior of this system can be seen in Fig. 3 on the curve labeled "blades." The natural frequency ω_R (as observed in the rotor frame) for each nodal diameter blade mode increases with rotor speed Ω. This dependence of the blade natural frequency on the rotor speed is normally conveyed on a Campbell diagram.

The possibility for interaction between the rotor dynamic whirl problem and the bladed disk structural dynamic problem can be seen by the overplot of Fig. 1 onto Fig. 3. Note, however, that in the rotor analysis of equation (1) and Fig. 1, the natural frequencies ω_N are those which would be observed by the nonnrotating observer. In order to compare them with the blade natural frequencies of equation (3) and Fig. 3, it is necessary to transform the frequencies of the rotor to those that would be observed in the rotating frame. The transformation depends on the nature of the whirl, with the frequencies ω_R observed in the rotating frame being given by:

$$\omega_R = \omega_N - \Omega \text{ (for forward whirl)}$$
$$\omega_R = \omega_N + \Omega \text{ (for backward whirl)} \qquad (4)$$

The approximate criterion for the existence of a dynamic interaction between the bladed disk and the shaft-disk systems is the presence of a close approach or intersection of the blade frequencies and rotor frequencies as plotted in Fig. 3. Such an intersection of the disk antiphase backward whirl mode with the blade mode is seen at point A. If this intersection point were to occur within the operating range of the turbomachine, then a coupled analysis would be warranted for accurate blade natural frequency and rotor critical speed prediction.

Analytical Blade-Disk-Shaft Model. In order to investigate this interaction, an analytical model is developed which includes a shroudless fan with N flexible blades affixed to a rigid disk which is supported by a flexible shaft (Fig. 2). The blades are assumed to be tuned (i.e., identical) and elastically uncoupled. Each blade deflects with a single Ritz bending mode shape γ of amplitude q_i. In terms of the blade modal coordinate q_i, the displacements in the rotor frame of a point on the blade are (Fig. 2)

$$u = -\frac{1}{2} r_T^2 q_i^2 \int_{r_T}^{r} \left[\frac{\partial\gamma}{\partial r}\right]^2 dr$$
$$v = \gamma r_T q_i \cos\alpha \qquad (5)$$
$$w = \gamma r_T q_i \sin\alpha$$

where u is the foreshortening of the blade due to bending and v and w are the components of deflection of the blade in and out of the plane of the disk, respectively [10, 11]. The disk to which the blades are attached is supported by a flexible shaft which allows for two orthogonal translations of the disk centroid in the plane of rotation (q_{x_N} and q_{y_N}), and for pitching motions of the disk about two orthogonal disk diameters (q_{ξ_N} and q_{η_N}) as shown in Fig. 2. The inertial position of a point on the ith blade (r, $2\pi i/N$) can be expressed in terms of the disk motion and blade deflection as

$$\begin{Bmatrix} x_{I_N} \\ y_{I_N} \\ Z_{I_N} \end{Bmatrix} = \begin{Bmatrix} q_{x_N} \\ q_{y_N} \\ 0 \end{Bmatrix} + \begin{bmatrix} cq_{\eta_N} & 0 & sq_{\eta_N} \\ sq_{\eta_N}sq_{\xi_N} & cq_{\xi_N} & -cq_{\eta_N}sq_{\xi_N} \\ -sq_{\eta_N}cq_{\xi_N} & sq_{\xi_N} & cq_{\eta_N}cq_{\xi_N} \end{bmatrix} \begin{Bmatrix} (r-u)c\psi_i - vs\psi_i \\ (r-u)s\psi_i + vc\psi_i \\ w \end{Bmatrix} \tag{6}$$

where $\psi_i = 2\pi i/N + \Omega t$, and $cq_{\eta_N} = \cos(q_{\eta_N})$, $sq_{\eta_N} = \sin(q_{\eta_N})$, etc. The first term in equation (6) represents the translation of the centroid of the disk from the origin. The matrix multiplication in the second term represents the large angle pitching motion of the disk, first about its q_{ξ_N} axis, then about its q_{η_N} axis [8]. Note that in equation (6) the blade degrees of freedom are expressed in the rotating frame (through equation (5)), but the disk degrees of freedom are still expressed in the nonrotating frame. In order to transform the disk degrees of freedom into the rotating frame the following are used

$$\begin{bmatrix} q_{x_N} \\ q_{y_N} \end{bmatrix} = [T] \begin{bmatrix} q_{x_R} \\ q_{y_R} \end{bmatrix}, \quad \begin{bmatrix} q_{\xi_N} \\ q_{\eta_N} \end{bmatrix} = [T] \begin{bmatrix} q_{\xi_R} \\ q_{\eta_R} \end{bmatrix} \tag{7}$$

where

$$[T] = \begin{bmatrix} c\Omega t & -s\Omega t \\ s\Omega t & c\Omega t \end{bmatrix}$$

Substitution of equations (5) and (7) into equation (6), the assumption of small pitching angles, and the application of Lagrange's equations yield a coupled set of $N+4$ equations of motion. The equations can be partially decoupled by expressing the blade bending coefficients q_i in terms of multiblade coordinates (equation (2)). Then only the one nodal diameter ($n=1$ or 1ND) sine and cosine modes couple with the translation and pitching of the disk on the shaft. This occurs because the overall motion of the blades in the 1ND mode is not reactionless, i.e., the overall motion exerts a net pitching moment and shearing force which must be reacted by the shaft [8, 11]. By comparison the zero nodal diameter or umbrella mode of the blades does not couple with the disk motion in this simple model because no disk axial translational degree of freedom is permitted and the rotor speed Ω is assumed to be steady. The higher blade modes, those having more than one nodal diameter ($n>1$), also decouple from the shaft-disk motion. These are called reactionless modes because they exert no net translational or pitching inertial reaction on the disk due to their motion [11]. The $n = 0$ and $n > 1$ modes are still governed by the simple uncoupled equation (3).

The homogeneous equations of motion that express the coupling of the blade 1ND sine and cosine modes with the shaft-disk whirling modes is given in matrix form in equation (8). Definitions of the terms in equation (8) and their values for the MIT AE Rotor are given in the Appendix. The upper left 4×4 submatrix of equation (8) describes the whirling motion of the simple shaft-disk system. This model is slightly more complex than the Den Hartog model of equation (1). It includes both elastic coupling between the disk pitch and translation and inertial coupling between disk translation and pitching due to the static imbalance term S, which represents the axial offset of the rotor center of mass from the disk geometric centroid (the coordinate system origin). The 4×4 submatrix shows the gyroscopic coupling of the two disk translation modes to each other and to the disk pitch modes. The diagonal entries of the 4×4 stiffness submatrix show the centrifugal destiffening of the translation degrees of freedom and centrifugal stiffening of the pitch degrees of freedom. The lower right 2×2 submatrices of equation (8) describe the bladed disk one nodal diameter dynamics similar to those described in equation (3).

The objective of this coupled blade-disk-shaft analysis is to determine the nature and extent of the coupling between these two problems. The blade 1ND modes couple to the shaft-disk degrees of freedom through the upper right and lower left 2×4 submatrices to produce a coupled six degree of freedom system. In particular, the blade 1ND modes couple to disk translation inertially through the $N/2\ m_2 \cos\alpha$ terms, gyroscopically through the $N\Omega m_2 \cos\alpha$ terms, and centrifugally through the $-\Omega^2 N/2\ m_2 \cos\alpha$ terms. The blade 1ND modes couple to disk pitching motion inertially through the $-N/2\ m_1 \sin\alpha$ terms and centrifugally through the $-\Omega^2 N/2\ m_1 \sin\alpha$ terms. The effect of a nonzero static imbalance S on the 2×4 coupling submatrices is of second order for small C.G. offsets and is not included.

$$\begin{bmatrix} M & 0 & 0 & S & \frac{N}{2} m_2 \cos\alpha & 0 \\ & M & -S & 0 & 0 & \frac{N}{2} m_2 \cos\alpha \\ & & I_P & 0 & -\frac{N}{2} m_1 \sin\alpha & 0 \\ & & & I_P & 0 & -\frac{N}{2} m_1 \sin\alpha \\ & & & & \frac{N}{2} m_0 & 0 \\ \text{SYMMETRIC} & & & & & \frac{N}{2} m_0 \end{bmatrix} \begin{Bmatrix} \ddot{q}_{xR} \\ \ddot{q}_{yR} \\ \ddot{q}_{\xi R} \\ \ddot{q}_{\eta R} \\ \ddot{a}_1 \\ \ddot{b}_1 \end{Bmatrix} +$$

$$2\Omega \begin{bmatrix} 0 & -M & S & 0 & 0 & -\frac{N}{2} m_2 \cos\alpha \\ & 0 & 0 & S & \frac{N}{2} m_2 \cos\alpha & 0 \\ & & 0 & 0 & 0 & 0 \\ & & & 0 & 0 & 0 \\ & & & & 0 & 0 \\ \text{SKEW-SYMMETRIC} & & & & & 0 \end{bmatrix} \begin{Bmatrix} \dot{q}_{xR} \\ \dot{q}_{yR} \\ \dot{q}_{\xi R} \\ \dot{q}_{\eta R} \\ \dot{a}_1 \\ \dot{b}_1 \end{Bmatrix} +$$

$$\begin{bmatrix} K_{xR}-\Omega^2 M & 0 & 0 & K_{x\eta R}-\Omega^2 S & -\Omega^2 \frac{N}{2} m_2 \cos\alpha & 0 \\ & K_{yR}-\Omega^2 M & K_{y\xi R}+\Omega^2 S & 0 & 0 & -\Omega^2 \frac{N}{2} m_2 \cos\alpha \\ & & K_{\xi R}+\Omega^2 I_P & 0 & -\Omega^2 \frac{N}{2} m_1 \sin\alpha & 0 \\ & & & K_{\eta R}+\Omega^2 I_P & 0 & -\Omega^2 \frac{N}{2} m_1 \sin\alpha \\ & & & & \frac{N}{2}(K_B+\Omega^2 [m_\Omega - m_0 \cos^2\alpha]) & 0 \\ \text{SYMMETRIC} & & & & & \frac{N}{2}(K_B+\Omega^2 [m_\Omega - m_0 \cos^2\alpha]) \end{bmatrix} \begin{Bmatrix} q_{xR} \\ q_{yR} \\ q_{\xi R} \\ q_{\eta R} \\ a_1 \\ b_1 \end{Bmatrix} = 0 \tag{8}$$

The dynamic behavior of the coupled 6×6 system can be seen in the system natural frequency plot of Fig. 4. Note that in the uncoupled analysis of Fig. 3 the natural frequencies of the a_n and b_n sine and cosine modes were identical. In the coupled analysis of Fig. 4 the two modes split into backward and forward whirl branches. Note also that while the blade modes in the uncoupled analysis of Fig. 3 intersected the antiphase backward whirl disk pitch mode, the coupled analysis yields higher blade mode frequencies and a lower frequency antiphase backward mode. This effect eliminates the intersection of frequencies labeled as point A on Fig. 3.

Thus when the blade frequency is above but close to the rotor antiphase mode frequency the following effects of coupling are observed:

(*a*) The blade modes are elevated in frequency and split into a forward and backward pair, found at different frequencies.

(*b*) The disk modes are depressed in frequency, and are split less than the uncoupled analysis would indicate.

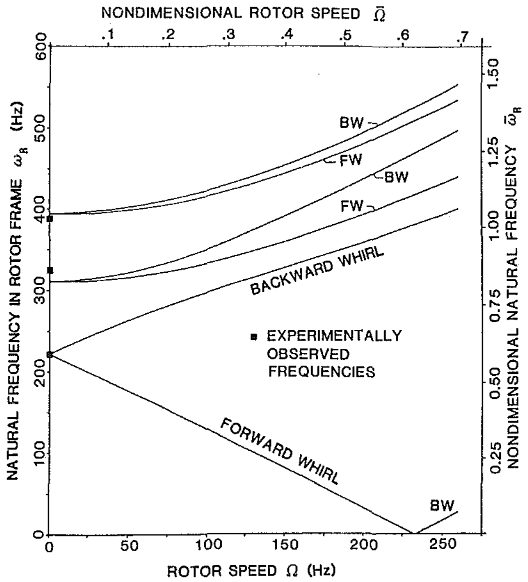

Fig. 4 Natural frequencies of the coupled system as observed in the rotor frame

Nondimensionalization of the Coupled Model. In order to more readily identify the parameters which govern the nature and extent of the bladed disk-shaft/disk coupling it is useful to nondimensionalize equation (8). For a symmetric rotor there are 15 dimensional quantities in equation (8): six disk-shaft properties M, S, I_d, K_x, $K_{x\eta}$, K_η; three blade properties k_B, m_0, m_Ω; two coupling parameters m_1 and m_2; the rotor speed Ω; the two translational deflections q_x and q_y; and the implicit eigenvalue ω. Choosing the uncoupled blade frequency $\omega_B^2 = k_B/m_0$ as the time scale and the disk radius of gyration $d^2 = I_d/M$ as the length scale, the rational set of 12 nondimensional parameters is:

Rotor parameters

$\hat{\omega}_P^2 = \dfrac{\omega_P^2}{\omega_T^2} = \dfrac{K_\eta}{I_d}\dfrac{M}{K_x} = \dfrac{1}{D}$	disk pitch to translation frequency ratio
$\kappa^2 = \dfrac{K_{x\eta}^2}{K_x K_\eta} = E$	shaft elastic coupling
$\mu_{TP}^2 = \dfrac{S^2}{M I_d}$	shaft inertial coupling

Blade parameters

$l = \dfrac{m_\Omega}{m_0} + \cos^2\alpha$	blade centrifugal stiffening (Southwell coefficient)

Coupling parameters

$\mu_{TB}^2 = \dfrac{\frac{N}{2} m_2^2 \cos^2\alpha}{m_0 M}$	blade bending to disk translation inertial coupling
$\mu_{PB}^2 = \dfrac{\frac{N}{2} m_1^2 \sin^2\alpha}{m_0 I_d}$	blade bending to disk pitch inertial coupling
$\rho^2 = \dfrac{N}{2}\dfrac{m_0}{I_d}$	blade mass to rotor inertia ratio

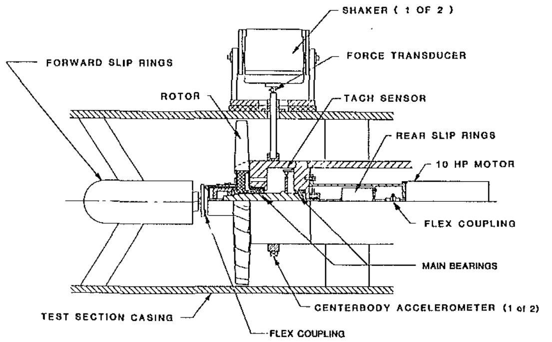

Fig. 5 Cutaway view of test section modified for whirl testing

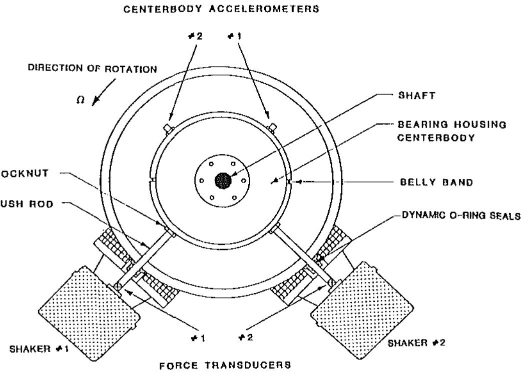

Fig. 6 View looking downstream of the whirl excitation system with the rotor and the forward slip rings removed

$\bar{\omega}_T^2 = \omega_x^2/\omega_B^2 = \dfrac{K_x}{M}\dfrac{m_0}{k_B}$	disk translation to blade bending natural frequency

General parameters

$\bar{\omega}^2 = \omega^2/\omega_B^2 = F^2(1-E^2)\bar{\omega}_T^2$	nondimensional natural frequency
$\bar{\Omega}^2 = \Omega^2/\omega_B^2 = S^2(1-E^2)\bar{\omega}_T^2$	nondimensional rotational speed
$\bar{q}_{x_R} = \dfrac{q_{x_R}}{d}, \bar{q}_{y_R} = \dfrac{q_{y_R}}{d}$	nondimensional translational deflections

Where appropriate, this set of nondimensional parameters has been compared with the four of the Den Hartog model (D, E, F, S) of equation (1). With these parameters, the governing coupled differential equation can be written in nondimensional form as shown in equation (9).

The nondimensional analysis can be used to estimate the nature of the coupling between the bladed disk and shaft-disk dynamics. The procedure is to calculate the eigenvalues of the upper left 4×4 submatrix of equation (9). If any of the eigenvalues of this matrix are greater than one, this implies that the frequency of the rotor approaches or crosses that of the blades. It can be said that the nondimensional eigenvalue of the 4×4 submatrix indicates the propensity of the shaft-disk to couple to the blades. Maximum coupling occurs as any eigenvalue of the 4×4 submatrix approaches unity [11]. The extent of the coupling between the blade modes and the antiphase or pitching shaft-disk mode is measured by μ_{PB}^2, the blade bending to disk pitching mass coupling parameter, as defined above. The parameter μ_{PB}^2 can take on values from zero to one, the latter indicating a high degree of coupling. Although μ_{PB}^2 can be calculated directly, simple formulae for its estimation can be found in [11].

$$\begin{bmatrix} 1 & 0 & 0 & \mu_{TP} & \rho\mu_{TB} & 0 \\ & 1 & -\mu_{TP} & 0 & 0 & \rho\mu_{TB} \\ & & 1 & 0 & -\rho\mu_{PB} & 0 \\ & & & 1 & 0 & -\rho\mu_{PB} \\ & & & & \rho^2 & 0 \\ & \text{SYMMETRIC} & & & & \rho^2 \end{bmatrix} \begin{Bmatrix} \bar{q}_x \\ \bar{q}_y \\ q_\xi \\ q_\eta \\ q_1 \\ b_1 \end{Bmatrix}''$$

$$+2\bar{\Omega} \begin{bmatrix} 0 & -1 & \mu_{TP} & 0 & 0 & -\rho\mu_{TB} \\ & 0 & 0 & \mu_{TP} & -\rho\mu_{TB} & 0 \\ & & 0 & 0 & 0 & 0 \\ & & & 0 & 0 & 0 \\ & & & & 0 & 0 \\ & \text{SKEW - SYMMETRIC} & & & & 0 \end{bmatrix} \begin{Bmatrix} \bar{q}_x \\ \bar{q}_y \\ q_\xi \\ q_\eta \\ q_1 \\ b_1 \end{Bmatrix}'$$

$$+ \begin{bmatrix} (\bar{\omega}_T^2-\Omega^2) & 0 & 0 & (\kappa\hat{\omega}_P\bar{\omega}_T^2-\bar{\Omega}^2\mu_{TP}) & -\bar{\Omega}^2\rho\mu_{TB} & 0 \\ & (\bar{\omega}_T^2-\bar{\Omega}^2) & (\kappa\hat{\omega}_P\omega_T^2-\bar{\Omega}^2\mu_{TP}) & 0 & 0 & -\bar{\Omega}^2\rho\mu_{TB} \\ & & (\hat{\omega}_P^2\omega_T^2+\bar{\Omega}^2) & 0 & -\bar{\Omega}^2\rho\mu_{PB} & 0 \\ & & & (\hat{\omega}_P^2\omega_T^2+\bar{\Omega}^2) & 0 & -\bar{\Omega}^2\rho\mu_{PB} \\ & & & & \rho^2(1+\Omega^2\ell) & 0 \\ & \text{SYMMETRIC} & & & & \rho^2(1+\Omega^2\ell) \end{bmatrix} \begin{Bmatrix} \bar{q}_x \\ \bar{q}_y \\ q_\xi \\ q_\eta \\ a_1 \\ b_1 \end{Bmatrix} = 0 \quad (9)$$

Experimental Determination of Coupled Fan/Rotor Modes

An extensive program of experimental testing of a cantilevered turbofan was undertaken in order to determine the structural dynamics of a coupled bladed disk-shaft system and in doing so to verify the analytic model developed. The experiments were caried out on the MIT Aeroelastic (AE) Rotor installed in the Blowdown Compressor Facility [12] of the MIT Gas Turbine Laboratory. The use of this facility for transient testing of compressor stages for their performance and aeroelastic response has been well documented [13]. In the current investigation, the facility was used as a high-speed spin rig and all tests were performed in the vacuum of the test section. The MIT AE Rotor is aerodynamically typical of modern high bypass ratio fans with a blade hub to tip ratio of 0.5, a blade aspect ratio of 2, a design pressure ratio of 1.6, and axial and tip Mach numbers of 0.5 and 1.2, respectively. The rotor was cantilevered at the front of a shaft supported by two forward angular contact thrust bearings and a single spring loaded rear angular contact bearing, as shown in Fig. 5. Flexible couplings forward and aft of the rotor-shaft system dynamically isolate the system from the forward slip rings and rear drive motor. The rotor was balanced before installation in order to minimize any cyclic bearing loads due to imbalance. The rotor is extensively instrumented, with piezoelectric blade displacement transducers on each of the 23 blades. A more detailed description of the experiment is presented in [14].

Determination of System Parameters. In order to employ the analytical model for the prediction of the natural frequencies of whirl of the MIT AE rotor, its mass and stiffness parameters were determined. The mass parameters were determined by direct measurement. A holographic measurement of the blade first bending mode shape was made and the results were used to calculate the blade model mass (m_0), consistent mass coupling terms (m_1 and m_2), and blade mass foreshortening term (m_Ω).

The stiffness parameters of the system were difficult to determine by direct static measurement due to effects such as the nonlinear stiffness behavior of the angular contact thrust bearings. Therefore the stiffnesses were calculated using the equations of motion with the rotation speed set to zero ($\Omega = 0$), the natural frequencies and mode shapes experimentally determined at zero rotational speed, and the known inertia parameters. The blade stiffness k_B was calculated in a similar manner by using the experimental first bending frequency for an isolated cantilevered blade ω_B and the calculated blade modal mass m_0. With this knowledge of the mass and stiffness parameters of the system, the natural frequencies of whirl can be calculated and are shown in Fig. 4. These predictions served as a guideline for choosing the frequency ranges for the whirl excitation of the MIT AE rotor.

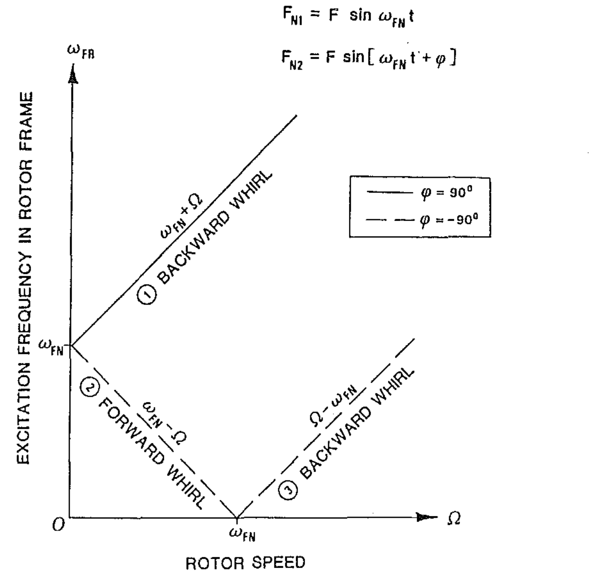

Fig. 7 Summary plot of the whirl excitation transformation from the inertial to the rotating frame of reference

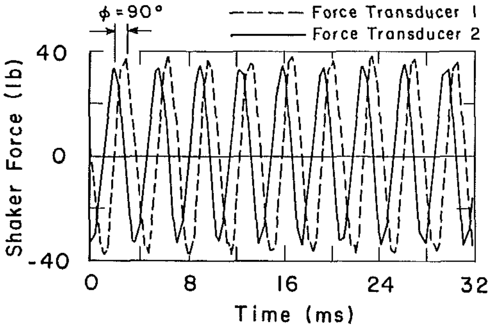

Fig. 8 Shaker force transducer signals for the case of: $\phi = -90$ deg, $\Omega = 60$ Hz, $\omega_{FN} = 290$ Hz, $\omega_{FR} = 350$ Hz

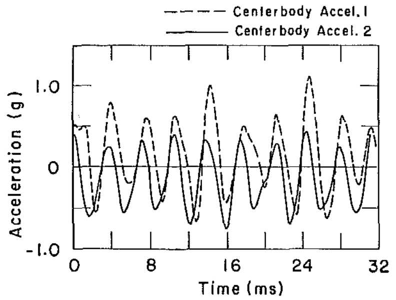

Fig. 9 Bearing housing accelerometer signals for the case of: $\phi = -90$ deg, $\Omega = 60$ Hz, $\omega_{FN} = 290$ Hz, $\omega_{FR} = 350$ Hz

Whirl Excitation System. The test section of the Blowdown Compressor Facility was modified in order install the whirl excitation system which included two Ling Model 420 100 lb_f

electromagnetic shakers mounted circumferentially 90 deg apart, as shown in Fig. 6. The whirl excitation forces were applied to the shaft bearing housing centerbody through push rods connected to the two shakers. By controlling the frequency, relative phase, and amplitude of the shaker forces, arbitrary forward or backward whirl excitation could be applied to the rotating system. A slowly swept sine technique was chosen as the preferred system identification protocol over sine dwell or random excitation, based on consideration of bearing life and ease of data interpretation. Since the sweep rate was on the order of 1 Hz/s, and typical data samples taken were less than 50 ms in duration, the data reduction procedure will be described assuming a quasi-stationary frequency of excitation.

The two shakers shown in Fig. 6 were driven by amplified command signals which were of the same frequency and amplitude but with a relative phase shift. Therefore the forces applied to the nonrotating bearing support structure by shaker 1 (F_{N1}) and by shaker 2 (F_{N2}) can be represented as

$$\begin{aligned} F_{N1} &= F \sin \omega_{FN} t \\ F_{N2} &= F \sin (\omega_{FN} t + \phi) \end{aligned} \tag{10}$$

If F_{N2} leads F_{N1} by 90 deg ($\phi = 90$ deg), then the vector sum of the two applied shaker forces is a force of amplitude F rotating in a clockwise direction with angular speed ω_{FN}, as viewed from the inertial frame. Since the rotor turns in the counterclockwise direction, the resultant force vector rotates in a direction opposite or backwards with respect to the rotor. For a shaker forcing frequency ω_{FN}, the rotor senses this backward whirl excitation at a shifted frequency $\omega_{FR} = \omega_{FN} + \Omega$. This condition corresponds to curve 1 of Fig. 7, which illustrates the shift in forcing frequency as observed in the rotating frame as a function of rotor speed.

If F_{N2} lags F_{N1} by 90 deg ($\phi = -90$ deg), then a counterclockwise rotating resultant force vector is produced. Depending on the relative magnitude of ω_{FN} and Ω, two forcing conditions are possible. If $\omega_{FN} > \Omega$, then the counterclockwise rotating force vector produced rotates at a rate faster than that of the rotor and the rotor senses an excitation in the same direction as its rotation, or a forward whirl excitation at the frequency $\omega_{FR} = \omega_{FN} - \Omega$. This forcing condition corresponds to curve 2 in Fig. 7. The other case is when $\omega_{FN} < \Omega$. Then the counterclockwise rotating force vector produced rotates at a rate slower than that of the rotor and the rotor senses a backward whirl excitation at the frequency $\omega_{FR} = \Omega - \omega_{FN}$. This forcing condition corresponds to curve 3 in Fig. 7. Thus, by controlling the shaker excitation frequency ω_{FN} and the relative phase angle ϕ, a forward or backward whirl excitation of known frequency ω_{FR} can be created in the rotor frame of reference. By slowly sweeping the shaker force frequency ω_{FN} between present limits, a swept sine excitation of any whirl mode can be achieved.

Whirl Test Results. The response of the rotor system to the whirl forcing excitation was measured for a range of subcritical rotor speeds up to 9000 rpm ($\Omega = 150$ Hz). The data obtained at these speeds were sufficient to illustrate the trends in frequency of the coupled shaft/bladed disk system of the MIT AE Rotor and to allow for comparison of the experimental results with the analytical model derived above.

In order to verify that the desired mode of whirl excitation was indeed being produced by the shaker system, a particular instant in one forcing sweep will be examined. The case illustrated here will be for a rotor speed of 3600 rpm ($\Omega = 60$ Hz), backward whirl phasing $\phi = 90$ deg, and a shaker forcing frequency $\omega_{FN} = 290$ Hz. The force input to the system was measured by the two force transducers (Fig. 6). The signals from force transducers 1 and 2 are shown in Fig. 8, and indicate that the forces applied by the two shakers were of nearly equal amplitude and that the force applied by shaker 2 leads that of shaker 1 by 90 deg, as is required for backward whirl excitation. The response of the nonrotating bearing housing centerbody to this excitation was measured by the centerbody accelerometers (Fig. 6). The signals from accelerometers 1 and 2 (Fig. 9) show that the bearing housing does indeed respond to the excitation pattern, with accelerometer 2 leading accelerometer 1 by approximately 90 deg and with approximately equal amplitude.

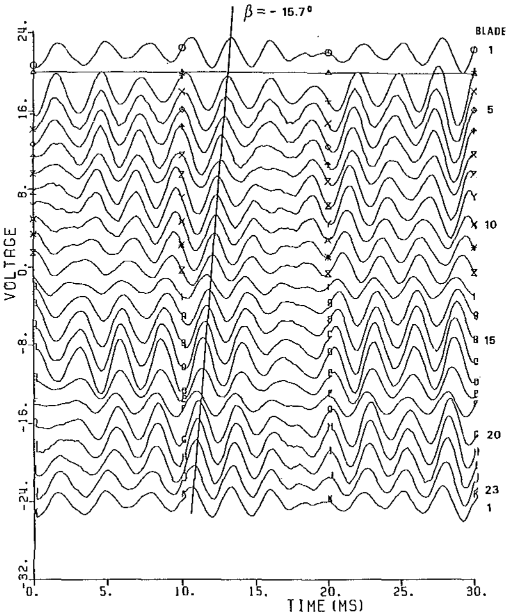

Fig. 10 *Simultaneous displacement time histories of all blades showing a 1ND backward whirl traveling wave pattern; case of: $\phi = -90$ deg, $\Omega = 60$ Hz, $\omega_{FN} = 290$ Hz, $\omega_{FR} = 350$ Hz*

Having established that the nonrotating bearing housing centerbody responds to the whirl excitation at ω_{FN}, it remains to be determined how the excitation is sensed in the rotating system and how the blades respond. The transformation of forces from the nonrotating to the rotating frame is summarized in Fig. 7, with the present case corresponding to a point on curve 1 of the plot. By the transformation rule, the rotating system should sense a backward whirl excitation at $\omega_{FR} = \omega_{FN} + \Omega = 290 + 60 = 350$ Hz. In Fig. 10 the simultaneous responses of the blade displacement transducers are shown for the present whirl excitation condition. The plot is arranged with the signal of each blade positioned next to the signals of neighboring blades in order to more clearly illustrate the interblade phase angle β of the response. The interblade phase angle apparent in the data, $\beta = -15.7$ deg, corresponds to a 1ND backward-traveling pattern. This is consistent with the result of the analytical model, which indicated that the blade 1ND mode is the only blade mode which couples to the shaft/disk motion and can be excited by the whirl excitation. By performing an FFT on the data of Fig. 10, the largest frequency component of the blade response is seen at the target backward whirl frequency $\omega_{FR} = \omega_{FN} + \Omega = 350$ Hz (all blade frequencies are by definition observed in the rotating frame). Thus the excitation scheme was successful in producing the desired forced response, in this case the backward whirl mode, with a relatively "monochromatic" spectral content.

The natural frequencies of whirl were determined at six rotor speeds through the production and interpretation of cascade plots. These plots consist of a sequence of blade response FFT traces, each trace for a single quasi-steady excitation frequency ω_{FR}. All the traces on a given cascade plot

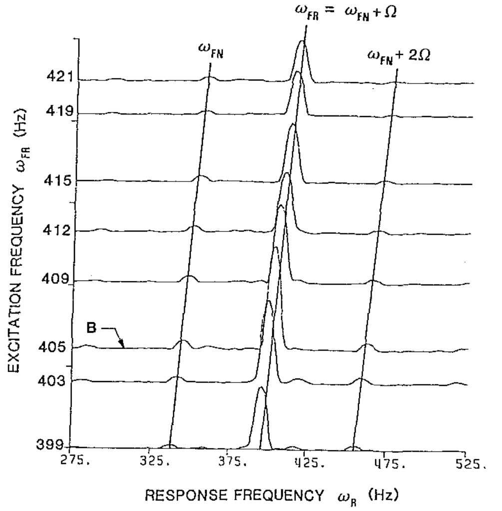

Fig. 11 Blade displacement spectral carpet plot for rotation speed Ω = 60 Hz; backward whirl excitation of the blade 1ND mode and excitation frequency range ω_{FR} = 399–421 Hz

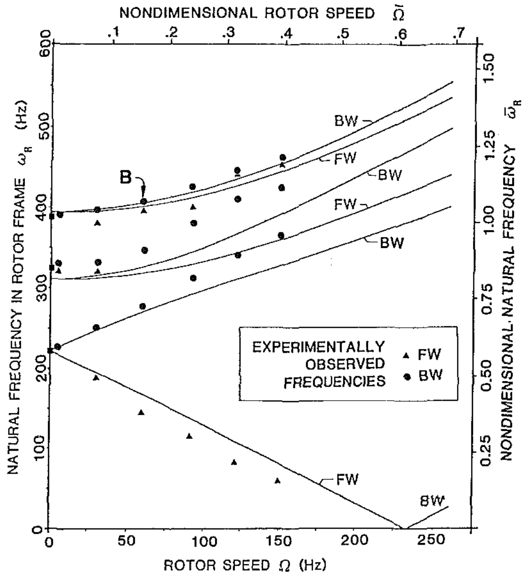

Fig. 12 Summary plot of experimentally determined natural frequencies overplotted on the predicted system natural frequency plot

are for the same blade, same rotational speed and same whirl phasing. Such a plot is shown in Fig. 11, where the blade response FFT's are presented for several forcing frequencies during the sweep from which the data in Figs. 8-10 were obtained. The cascade plot shows that the forced response of the blade in the target backward whirl mode peaks at an excitation frequency ω_{FR} = 405 Hz. This data point, which corresponds to a resonance at ω_R = 405 Hz at a rotor speed of 60 Hz, is plotted as point B on the experimental summary plot of Fig. 12, where the natural frequencies referred to the rotor frame are plotted as a function of Ω and compared with the prediction of the analytical model.

The response cascade plots (Fig. 11) also show the presence of frequency components other than the target frequency ω_{FR}. Difficulty in producing a pure whirl excitation and asymmetries in the stiffness of the rotating and nonrotating structure lead to response components at $\omega_{FN} \pm p\Omega$, where p is a positive integer. Because of cyclic bearing noise, additional frequency components at integer multiplies of the rotor speed Ω (engine order excitation) were also observed. The signal-to-noise ratio was found to be on the order of at least ten for the backward whirl sweeps but only on the order unity for the forward whirl sweeps. This poor signal-to-noise ratio for forward whirl sweeps precluded the determination of the forward whirl antiphase disk translation/pitch mode frequency at rotor speeds over 3600 rpm ($\Omega > 60$ Hz).

The resulting correlation between the system natural frequencies predicted by the simple 6 DOF coupled model and the experiment show that the agreement is quite reasonable. The lowest two curves of Fig. 12 are essentially the in-phase translation/pitch mode of the disk (the bounce mode) and the middle two modes are the antiphase pitch/translation mode of the disk (the pitch mode). The upper two curves are the blade 1ND modes. The simplified model of the shaft and the uncertainty in the values of the shaft stiffness parameters is reflected in the errors in predicting the $\Omega = 0$ natural frequencies, especially for the antiphase pitch/translation mode which was experimentally observed at 325 Hz. As the speed of the rotor increases, the experimentally determined 1ND blade frequencies agree well with the predicted frequencies, especially for the blade 1ND backward whirl mode. However the split between the blade 1ND backward and forward whirl modes is seen to be greater than predicted at low rotor speeds and less than predicted at higher speeds. The oversimplified shaft model leads to qualitative agreement between the experimental and analytically predicted shaft-disk modes. The interaction of the backward whirl antiphase pitch mode with the blade 1ND modes was underestimated. The poor detectability of the antiphase forward whirl pitch mode leads to uncertainty in the evaluation of the correlation for that mode. Note also that the critical speed, i.e., the intersection of the forward whirl in-phase translation mode leg with the horizontal ($\omega = 0$) axis at Ω = 230 Hz, is overpredicted by the model by about 15 percent. This effect arises because the in-phase translation rotor speed more than was predicted. However the trends predicted by the simple model are clearly observed in the experimental results.

Conclusions

A simplified model has been developed for the coupled dynamics of flexible blades affixed to a rigid disk which is supported by a flexible cantilevered shaft. The model shows that the 1ND blade modes couple to the rigid body translation and pitching motion of the disk on the end of the shaft, while the other nodal diameter blade modes are uncoupled from the disk motion. The approximate criterion for the propensity of interaction between the bladed disk and shaft-disk dynamics is that the eigenvalues associated with the 4×4 shaft-disk portion of the problem approach or cross the eigenvalues associated with the uncoupled 2×2 blade one nodal diameter portion of the problem. The degree to which the interaction occurs is associated with the value of the coupling parameter μ_{PB}^2. The nature of the interaction is a split of the blade one nodal diameter modes into forward and backward whirl legs and the depression of the antiphase shaft-disk modes, especially the backward whirl leg.

In order to validate the model, an experiment was performed to determine the natural frequencies of the MIT Aeroelastic Rotor, typical of a cantilevered turbofan. The forward and backward whirl modes of the rotor were successfully excited using a swept sine forcing technique. The observed response of the system indicates that only the 1ND blade modes couple to the rigid body motion of the disk. The splitting of the 1ND blade modes into forward and backward modes is observed, as is the interaction of the disk antiphase modes with the 1ND blade modes. The correlation between the experiment and the analytical model is good, however rigid the body motion of the disk. The splitting of the 1ND blade modes into forward and backward modes is observed, as is the interaction of the disk antiphase modes with the 1ND blade modes. The correlation between the experiment and the analytical model is good; however some inaccuracy is noted due to the oversimplified model of the shaft flexibility and difficulties in determining the stiffness parameters of the system.

Acknowledgments

This research was sponsored by the NASA Lewis Research Center, under Grant NAG3-200, with Dr. Robert Kielb serving as technical monitor. A concurrent grant activity at Rensselaer Polytechnic Institute focused on a detailed numerical modeling of the same system. The authors are grateful to Drs. Robert Loewy and Naim Khader of RPI and Dr. Robert Kielb of NASA LeRC for their technical advice and support.

References

1 Ewins, D. J., "Vibration Characteristics of Bladed Disk Assemblies," *Journal of Mechanical Engineering Science*, Vol. 15, No. 3, 1973, pp. 165–186.

2 Den Hartog, J. P., *Mechanical Vibrations*, 4th ed., McGraw-Hill, New York, 1956.

3 Coleman, R. P., and Feingold, A. M., "Theory of Self-Excited Mechanical Oscillations of Helicopter Rotors With Hinged Blades," NACA TR 1351, 1958.

4 Reed, W. H., III, "Review of Propeller Rotor Whirl Flutter," NASA TR R-264, July 1967.

5 Crandall, S. H., and Dugundji, J., "Resonant Whirling of Aircraft Propeller-Engine Systems," ASME *J. Appl. Mech.*, Vol. 48, Dec. 1981, pp. 929–935.

6 Janetzke, D. C., and Kaza, K. R. V., "Whirl Flutter of a Horizontal-Axis Wind Turbine With a Two-Bladed Teetering Rotor," *Solar Energy*, Vol. 31, No. 2, 1983, pp. 173–182; also in NASA CP-2185, Feb. 1981.

7 Palladino, J. A., and Rossettos, J. N., "Finite Element Analysis of the Dynamics of Flexible Disk Rotor Systems," ASME Paper No. 82-GT-240.

8 Loewy, R., and Khader, N., "Structural Dynamics of Rotating Bladed-Disk Assemblies Coupled With Flexible Shaft Motions," *AIAA J.*, Vol. 22, No. 9, Sept. 1984, pp. 1319–1327.

9 Gallardo, V. C., and Stallone, M. J., "The Dynamics of a Flexible Bladed Disc on a Flexible Rotor in a Two Rotor System," presented at the Third International Conference on Vibrations of Rotating Machinery, Heslington, Yorkshire, U.K., Sept. 13–15, 1984.

10 Crawley, E. F., "In-Plane Inertial Coupling in Tuned and Severely Mistuned Bladed Disks," ASME JOURNAL OF ENGINEERING FOR POWER, Vol. 105, July 1983, pp. 585–590.

11 Crawley, E. F., and Mokadam, D. R., "Stagger Angle Dependence of Inertial and Elastic Coupling in Bladed Disks," ASME *J. Vibration, Acoustics, Stress, and Reliability in Design*, Vol. 106, Apr. 1984, pp. 181–188.

12 Kerrebrock, J. L., et al., "The MIT Blowdown Compressor Facility," ASME JOURNAL OF ENGINEERING FOR POWER, Vol. 96, No. 4, Oct. 1974, pp. 394–405.

13 Crawley, E. F., "Aerodynamic Damping Measurements in a Transonic Compressor," ASME JOURNAL OF ENGINEERING FOR POWER, Vol. 105, July 1983, pp. 575–584.

14 Ducharme, E. H., Crawley, E. F., and Mokadam, D. R., "Forced Rotating Whirl Tests on a Cantilevered Turbofan Stage," MIT Gas Turbine and Plasma Dynamics Laboratory Report No. 182, Mar. 1985.

APPENDIX

Structural Properties of the MIT AE Rotor

Dimensional Parameters

$$M = \text{total mass of rotor assembly} = \int_v dm = 25.4 \text{ kg}$$

$$S = \text{axial mass imbalance} = \int_v z\, dm = -0.741 \text{ kg}\bullet\text{m}$$

$$I_d = \text{rotor pitch moment of inertia} = \int_v (x^2+z^2)dm$$

$$= 0.297 \text{ kg}\bullet\text{m}^2$$

$$m_0 = \text{blade modal mass} = r_T^2 \int_{r_H}^{r_T} \gamma^2 dr = 1.43\times 10^{-3}\text{kg/m}^2$$

$$m_1 = \text{blade consistent mass coupling to disk pitch}$$

$$= r_T \int_{r_H}^{r_T} r\gamma dr = 2.41\times 10^{-3}\text{kg}\bullet\text{m}^2$$

$$m_2 = \text{blade consistent mass coupling to disk translation}$$

$$= r_T \int_{r_H}^{r_T} \gamma dr = 1.01\times 10^{-3}\text{kg}\bullet\text{m}^2$$

$$m_\Omega = \text{blade mass foreshortening} = \int_{r_H}^{r_T} r \int_{r_H}^{r} \left[\frac{\partial\gamma}{\partial r}\right]^2 dr\, dm$$

$$= 3.70\times 10^{-3}\text{kg}\bullet\text{m}^2$$

$K_x = K_y$ = shaft translational stiffness = 5.68×10^7 N/m
$K_\eta = K_\xi$ = shaft pitch stiffness = 1.40×10^6N•m/rad
$K_{x\eta} = -K_{y\xi}$ = shaft coupling stiffness = 6.43×10^6 N/rad
k_B = blade modal stiffness = $\omega_B^2\, m_0$ = 6.43×10^3 N•m
α = effective stagger angle = 36 deg

Nondimensional Parameters

μ_{TP}^2 = shaft inertial coupling = 0.073
μ_{TB}^2 = blade bending/disk translation inertial coupling = 0.021
μ_{PB}^2 = blade bending/disk pitch inertial coupling = 0.054
ρ^2 = blade mass/rotor inertia ratio = 0.055
l = Southwell coefficient = 1.93
$\bar{\omega}_T^2$ = disk translation/blade bending frequency ratio = 0.497
$\hat{\omega}_P^2$ = disk pitch/translation frequency ratio = 2.11
κ^2 = shaft elastic coupling = 0.520

analytical model is good; however some inaccuracy is noted due to the oversimplified model of the shaft flexibility and difficulties in determining the stiffness parameters of the system.

Acknowledgments

This research was sponsored by the NASA Lewis Research Center, under Grant NAG3-200, with Dr. Robert Kielb serving as technical monitor. A concurrent grant activity at Rensselaer Polytechnic Institute focused on a detailed numerical modeling of the same system. The authors are grateful to Drs. Robert Loewy and Naim Khader of RPI and Dr. Robert Kielb of NASA LeRC for their technical advice and support.

References

1 Ewins, D. J., "Vibration Characteristics of Bladed Disk Assemblies," *Journal of Mechanical Engineering Science*, Vol. 15, No. 3, 1973, pp. 165–186.

2 Den Hartog, J. P., *Mechanical Vibrations*, 4th ed., McGraw-Hill, New York, 1956.

3 Coleman, R. P., and Feingold, A. M., "Theory of Self-Excited Mechanical Oscillations of Helicopter Rotors With Hinged Blades," NACA TR 1351, 1958.

4 Reed, W. H., III, "Review of Propeller Rotor Whirl Flutter," NASA TR R-264, July 1967.

5 Crandall, S. H., and Dugundji, J., "Resonant Whirling of Aircraft Propeller-Engine Systems," ASME *J. Appl. Mech.*, Vol. 48, Dec. 1981, pp. 929–935.

6 Janetzke, D. C., and Kaza, K. R. V., "Whirl Flutter of a Horizontal-Axis Wind Turbine With a Two-Bladed Teetering Rotor," *Solar Energy*, Vol. 31, No. 2, 1983, pp. 173–182; also in NASA CP-2185, Feb. 1981.

7 Palladino, J. A., and Rossettos, J. N., "Finite Element Analysis of the Dynamics of Flexible Disk Rotor Systems," ASME Paper No. 82-GT-240.

8 Loewy, R., and Khader, N., "Structural Dynamics of Rotating Bladed-Disk Assemblies Coupled With Flexible Shaft Motions," *AIAA J.*, Vol. 22, No. 9, Sept. 1984, pp. 1319–1327.

9 Gallardo, V. C., and Stallone, M. J., "The Dynamics of a Flexible Bladed Disc on a Flexible Rotor in a Two Rotor System," presented at the Third International Conference on Vibrations of Rotating Machinery, Heslington, Yorkshire, U.K., Sept. 13–15, 1984.

10 Crawley, E. F., "In-Plane Inertial Coupling in Tuned and Severely Mistuned Bladed Disks," ASME JOURNAL OF ENGINEERING FOR POWER, Vol. 105, July 1983, pp. 585–590.

11 Crawley, E. F., and Mokadam, D. R., "Stagger Angle Dependence of Inertial and Elastic Coupling in Bladed Disks," ASME *J. Vibration, Acoustics, Stress, and Reliability in Design*, Vol. 106, Apr. 1984, pp. 181–188.

12 Kerrebrock, J. L., et al., "The MIT Blowdown Compressor Facility," ASME JOURNAL OF ENGINEERING FOR POWER, Vol. 96, No. 4, Oct. 1974, pp. 394–405.

13 Crawley, E. F., "Aerodynamic Damping Measurements in a Transonic Compressor," ASME JOURNAL OF ENGINEERING FOR POWER, Vol. 105, July 1983, pp. 575–584.

14 Ducharme, E. H., Crawley, E. F., and Mokadam, D. R., "Forced Rotating Whirl Tests on a Cantilevered Turbofan Stage," MIT Gas Turbine and Plasma Dynamics Laboratory Report No. 182, Mar. 1985.

APPENDIX

Structural Properties of the MIT AE Rotor

Dimensional Parameters

$$M = \text{total mass of rotor assembly} = \int_v dm = 25.4\ \text{kg}$$

$$S = \text{axial mass imbalance} = \int_v z\, dm = -0.741\ \text{kg}\bullet\text{m}$$

$$I_d = \text{rotor pitch moment of inertia} = \int_v (x^2+z^2)dm$$

$$= 0.297\ \text{kg}\bullet\text{m}^2$$

$$m_0 = \text{blade modal mass} = r_T^2 \int_{r_H}^{r_T} \gamma^2 dr = 1.43\times 10^{-3}\text{kg/m}^2$$

m_1 = blade consistent mass coupling to disk pitch

$$= r_T \int_{r_H}^{r_T} r\gamma dr = 2.41\times 10^{-3}\text{kg}\bullet\text{m}^2$$

m_2 = blade consistent mass coupling to disk translation

$$= r_T \int_{r_H}^{r_T} \gamma dr = 1.01\times 10^{-3}\text{kg}\bullet\text{m}^2$$

$$m_\Omega = \text{blade mass foreshortening} = \int_{r_H}^{r_T} r \int_{r_H}^{r} \left[\frac{\partial\gamma}{\partial r}\right]^2 dr\, dm$$

$$= 3.70\times 10^{-3}\text{kg}\bullet\text{m}^2$$

$K_x = K_y$ = shaft translational stiffness = 5.68×10^7 N/m
$K_\eta = K_\xi$ = shaft pitch stiffness = 1.40×10^6N•m/rad
$K_{x\eta} = -K_{y\xi}$ = shaft coupling stiffness = 6.43×10^6 N/rad
k_B = blade modal stiffness = $\omega_B^2\, m_0$ = 6.43×10^3 N•m
α = effective stagger angle = 36 deg

Nondimensional Parameters

μ_{TP}^2 = shaft inertial coupling = 0.073
μ_{TB}^2 = blade bending/disk translation inertial coupling = 0.021
μ_{PB}^2 = blade bending/disk pitch inertial coupling = 0.054
ρ^2 = blade mass/rotor inertia ratio = 0.055
l = Southwell coefficient = 1.93
$\bar{\omega}_T^2$ = disk translation/blade bending frequency ratio = 0.497
$\hat{\omega}_P^2$ = disk pitch/translation frequency ratio = 2.11
κ^2 = shaft elastic coupling = 0.520

DISCUSSION

N. Klompas[1]

By their excellent investigation into a dynamic interaction that has been ignored too long and their clear and thorough presentation, the authors have made a significant contribution to potential advancement of engine design. While they have demonstrated that two important mechanisms traditionally treated separately may interact and should be combined, an actual engine presents a much more complicated structure and more interacting mechanisms which also are currently ignored. Progress toward integration of valuable research, such as represented by this paper, into the analysis of a whole engine requires physcial interpretation of results into the context of engine needs. My published work [15-20] toward evolving a physical basis for analyzing a whole engine with accounting for exceptional mechanisms should be helpful in providing necessary interpretation.

While the present study incorporates the bladed disk and shaft into a single analysis of the system, the previous papers [15, 16] had accounted for bladed disk flexing by assuming independent characterization of effective gyroscopic moment which would be expressed as the product of the gyroscopic moment assuming rigidity and a magnification factor which depends on the speed of precession with respect to the disk (ω_R) and the speed of spin (Ω). For a bladed disk where the deflected forms due to the body forces producing the gyroscopic moment and due to the inertial forces of flexing are similar, the magnification factor would be the same as for the classic spring/mass. When the relative speed of precession passes through the natural circular frequency of the bladed disk spinning while rigidly supported at the juncture to the shaft, the magnification factor goes through magnitude peak and sign reversal.

---

[1] 29246 Lake Park Drive, Farmington Hills, MI 48018; Mem. ASME.

The possibility of this peak coinciding with a critical speed of the whole engine has been intriguing and the present paper suggests proximity to such a coincidence (point A) as a criterion for the existence of dynamic interaction which should signal caution in accepting critical speeds calculated by assuming bladed disk rigidity. Although the experimental data do not show significant error in the calculated natural frequency of the backward whirl mode responsible for the coincidence, strong interaction may be inferred from other observations.

The experimentally determined natural frequencies show coalescence of forward and backward frequencies at approximately 400 Hz with spin speed of approximately 120 Hz, a point close to point A. The blade natural frequency at the same speed is shown also as approximately 400 Hz. The previous paper [15] has shown analytically that forced whirl passing through the resonance of a bladed disk with system natural frequency close to coinciding does not produce sharp change in whirl amplitude and the present experimental results show that the system becomes indifferent to changes in direction of the strong effective gyroscopic reaction. Therefore, it is now concluded that the dynamic stiffness at the shaft becomes overwhelming and the natural frequency represents the bladed disk alone. The thesis that the coalescence of forward and backward whirl natural frequencies occurs at the natural frequency of the bladed disk alone is now asserted.

Significant errors in calculated resonant whirl speeds are seen at points more remote from point A. The forward speed relative to the stationary frame of reference at the point of coalescence is approximately 445 Hz, or 16 percent higher than that calculated assuming rigidity. For the lower, or "bounce" mode the critical speed for synchronous backward whirl—the whirl speed relative to the disk would be twice spin speed—is approximately 22 percent higher than that calculated for the rigid disk. Such errors with respect to the usual assumption of disk rigidity are to be expected where the higher natural frequency of the bladed disk raises the coupled natural frequency. However, the opposite effect is also possible and is represented by the splitting of the higher mode.

The current practice in analysis of the complete engine, as typified by Hibner [21], is to assume rigid bladed disks and circular orbits. Therefore, backward whirl is not accounted for unless counterrotating spools are incorporated. However, it occurs often because asymmetry of engine support structure causes interaction between forward and backward whirl so as to produce coupled whirl of elliptical modeform; experimental evidence of ellipticity has been shown previously [17, 18].

The current practice has led to previous studies on the effect of bladed disk flexibility on synchronous forward critical speeds, such as represented by Palladino and Rossettos [7], with the consistent finding of inconsequence. The present data confirm this finding.

Previous papers [18–20] derive physical interpretation, and possible integration into the analysis of the whole engine, of exceptional mechanisms that might arise. The method of modifying a basic linear response analysis of a complete engine to account for a mechanism involving secondary interaction or nonlinearity would be useful in extending the assumed mechanism of disk flexing to shroudless bladed disks. While the effective gyroscopic moment accounts for blade flexing which produces a moment only in the plane of precession, shroudless fans would involve also effects due to translational displacement of the centroid in the plane and would produce cross coupling between the plane of precession and the orthogonal whirl plane. Whereas this cross coupling would exist only at locations of flexing shroudless bladed disks, the previous accounting for steady torque [19] has demonstrated analysis with similar cross coupling distributed along the length of a shaft.

A significant exceptional mechanism might be the excitation of harmonics by asymmetry of the effective gyroscopic moment due to blade mistuning. This possibility has been discussed previously [18] and is implied by the present paper. The method of accounting for exceptional mechanisms [19, 20] should provide effective means of determining whether an engine would be sensitive to such asymmetry.

The present paper performs a great service by revealing potential shortcomings in current design practice. Future work should include developing and validating analytical models of complete engines.

References

15 Klompas, N., "Significance of Disk Flexing in Viscous-Damped Jet Engine Dynamics," ASME JOURNAL OF ENGINEERING FOR POWER, Vol. 100, Oct. 1978, pp. 647–654.

16 Klompas, N., "Unbalance Response Analysis of a Complete Turbomachine," ASME JOURNAL OF ENGINEERING FOR POWER, Vol. 105, Jan. 1983, pp. 184–191.

17 Klompas, N., "Blade Excitation by Elliptical Whirling in Viscous-Damped Jet Engines," ASME JOURNAL OF ENGINEERING FOR POWER, Vol. 103, Apr. 1981, pp. 326–330.

18 Klompas, N., "A Frictionally Induced Bladed Disk/Shaft Instability: Physical Explanation of an Experimental Fan Failure," ASME Paper No. 86-GT-131.

19 Klompas, N., "Accounting for Axial Torque in Analysis of Turbomachine Dynamics," submitted to ASME Gas Turbine Division.

20 Klompas, N., "Effects of Anomalous Rotor Joints on Turbomachine Dynamics," ASME JOURNAL OF ENGINEERING FOR POWER, Vol. 105, Oct. 1983, pp. 927–934.

21 Hibner, D. H., "Dynamic Response of Viscous-Damped Multi-shaft Jet Engines," *Journal of Aircraft*, Vol. 12, Apr. 1975, pp. 305–312.

Mass Balancing of Hollow Fan Blades

R. E. Kielb
NASA Lewis Research Center,
Cleveland, OH 44135

This paper uses a typical section model to investigate analytically the effect of mass balancing as applied to hollow, supersonic fan blades. A procedure to determine the best configuration of an internal balancing mass to provide flutter alleviation is developed. This procedure is applied to a typical supersonic shroudless fan blade which is unstable both in the solid configuration and when it is hollow with no balancing mass. The addition of an optimized balancing mass is shown to stabilize the blade at the design condition.

Introduction

One research objective at NASA Lewis is to develop the technology to allow improved fan blade designs. Aeroelastic considerations currently prevent the operation of efficient, lightweight, unshrouded fan blades. To alleviate flutter problems of such blades, recent research has investigated concepts such as mistuning and passive damping. However, relatively little attention has been given to the classical aeroelastic concept of mass balancing.

Mass balancing refers to the systematic distribution of mass for the purpose of alleviating aeroelastic instabilities. This concept has been recognized and utilized since the earliest days of aeroelastic research. Perhaps the first treatment of this subject was by von Baumhauer and Koning [1]. In this work the effect of adding appropriately positioned weights to a wing was shown to alleviate a flutter problem. A comprehensive study of the effect of center of mass location is given in a classical paper by Theodorsen and Garrick [2]. For incompressible flow they show that the parameter controlling the instability is dependent on the value of the bending-to-torsion frequency ratio (ω_h/ω_α). For low values of ω_h/ω_a (≈ 0) the instability is controlled by the center of mass offset from the aerodynamic center. For higher values of ω_h/ω_α the instability is controlled by the center of mass offset from the elastic axis. These trends are also shown to hold for supersonic flow in the work of Ashley and Zartarian [3]. Approximate rules for frequency coalescence flutter are given by Pines [4]. These rules state that flutter is not possible for the case where the center of mass is forward of the elastic axis. When the center of mass is behind the elastic axis the possibility of flutter is dependent on the system parameters.

The concepts described above have been extensively used in the designs of fixed wings (e.g., the placement of wing-mounted engines), helicopter blades, rockets, and satellites. In the past fan blades have been of solid construction due to the inability to manufacture practical hollow blades. Thus, little design freedom has been available in distributing the blade mass and is one explanation for the lack of research in mass balancing as applied to fan blades. However, recent manufacturing technology breakthroughs have led to the development of hollow fan blades such as the configuration shown in Fig. 1. With the introduction of internal voids in the airfoil, the designer has much greater latitude in distributing mass.

Although the author knows of no publications that explicitly treat the effect of mass balancing on a cascade of blades, at least two recent papers give results which implicitly address the subject. Reference [5] shows the stability characteristics of a cascade in incompressible flow with the center of gravity at midchord and the elastic axis at 25, 50, and 75 percent chord for a variety of bending-to-torsion frequency ratios. For bending-to-torsion frequency ratios less than one the 75 percent chord location is shown to have the highest flutter speed. For ratios greater than one the 25 percent chord location is the best. A comprehensive study of the effect of elastic axis and

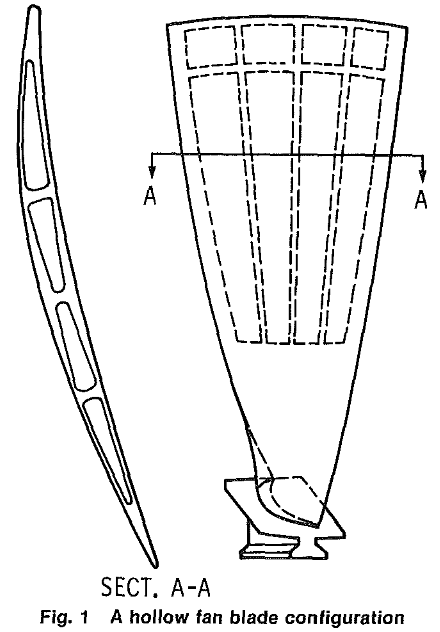

Fig. 1 A hollow fan blade configuration

Contributed by the Gas Turbine Division of The American Society of Mechanical Engineers and presented at the 31st International Gas Turbine Conference and Exhibit, Düsseldorf, Federal Republic of Germany, June 8–12, 1986. Manuscript received at ASME Headquarters February 11, 1986. Paper No. 86-GT-195.

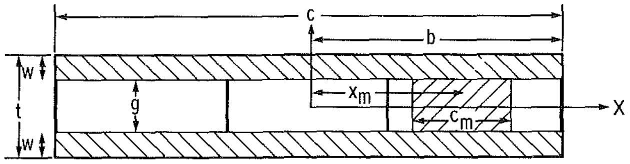

Fig. 2 Idealized fan blade section

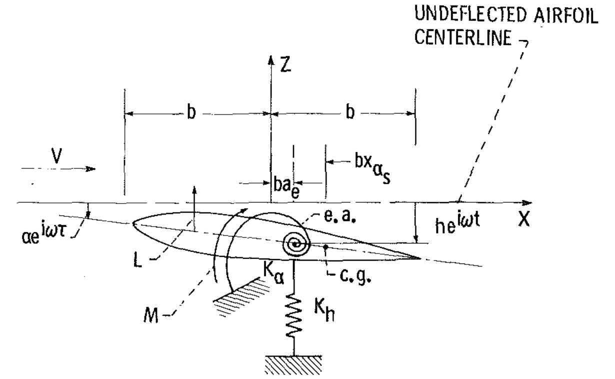

Fig. 3 Airfoil restrained from bending and torsional motion (sinusoidal wakes not shown)

center of mass location on supersonic fan blade stability is given in [6]. The elastic axis was fixed at midchord and the center of gravity was located at a variety of positions aft of midchord. In general, it was found that positions ahead of the center of gravity were beneficial for bending-to-torsion frequency ratios less than one (which is normally the case when considering the first bending and torsion modes) and detrimental for ratios greater than one. In simulating a typical supersonic fan blade with the center of mass at midchord, the best elastic axis position was found to be near 75 percent chord, which is in agreement with [5]. Neither of the studies [5] or [6] determined the optimum mass balanced configuration. Some additional experimental and analytical studies which consider the effect of elastic axis and center of mass location on flutter are given in [7, 8].

The objective of this paper is to investigate the effect of mass balancing on hollow, supersonic fan blades and to provide the designer with a method to distribute optimally the blade mass for maximum flutter alleviation. A supersonic hollow fan blade with an internal balancing mass is studied by using a typical section model. Procedures to determine the best balancing mass configuration are given. Only high-speed, supersonic, unstalled flutter is considered.

Theory

The actual cross section of a hollow blade may appear as shown in Fig. 1. For the purposes of this study the cross section is idealized as shown in Fig. 2, in which the blade is assumed to consist of two thin walls separated by "massless stiffeners" which form a hollow region. In this gap region is a balancing mass which has the same thickness as the gap and has a variable chordwise dimension and location. The variables are limited to cases where the balancing mass does not protrude from the thin walls. The balancing mass is assumed to be nonstructural and can have a different density from the blade wall material. This idealization simplifies the model yet maintains the basic physics of the mass balancing phenomenon. The following nondimensional ratios are used to define a mass balancing configuration

$$\begin{aligned} t_r &= t/c \\ w_r &= w/t \\ g_r &= g/t \\ c_{mr} &= c_m/b \\ x_{mr} &= x_m/b \\ \rho_{mr} &= \rho_m/\rho \end{aligned} \tag{1}$$

As in [5, 6, 9] the blade is modeled as a two degree of freedom oscillator in which the plunging and pitching motions are inertially coupled (see Fig. 3). In the following only a brief summary of the governing equations is given. For a more detailed description see one or more of the above references. The blade motion is assumed to be simple harmonic with a

Nomenclature

a = sonic velocity
a_e = elastic axis position
b = semichord
c = chord
c_m = chordwise dimension of balancing mass
c_{mr} = c_m/b
g = thickness of gap region
g_r = g/t
$[I]$ = identity matrix
I = polar mass moment of inertia about elastic axis
I_{xx} = area moment of inertia about x axis
J = torsion stiffness coefficient
K = torsion stiffness
K_h = bending stiffness
k = reduced frequency = $\omega b/V$
k_f = flutter reduced frequency
L = aerodynamic lift
l_{hh}, $l_{h\alpha}$ = nondimensional lift due to plunging and pitching motions, respectively
$l_{\alpha h}$, $l_{\alpha\alpha}$ = nondimensional moment due to plunging and pitching motions, respectively
M = Mach number of free stream relative to blade
M_e = aerodynamic moment
m = mass per unit span of blade
m_r = $m/(m$ of solid blade)
r_α = nondimensional radius of gyration
S_α = mass moment about elastic axis
s = circumferential gap between adjacent blades
t = blade thickness
t_r = thickness ratio = t/c
V = freestream air velocity relative to blade
w = thickness of blade wall
w_r = w/t
x_α = dimensionless static unbalance
x_m = chordwise location of balancing mass
x_p = nondimensional pitching axis location
x_{pd} = pitching axis location selected for design
x_{mr} = x_m/b
γ_α = nondimensional uncoupled torsion frequency
γ_h = nondimensional uncoupled bending frequency
ζ = critical damping ratio
λ = nondimensional eigenvalue
μ = mass ratio = $m/\pi\rho b^2$
ξ = stagger angle
ρ = density of blade material
ρ_a = air density
ρ_m = density of balancing mass material
ρ_{mr} = ρ_m/ρ
τ = time
ω = frequency
ω^* = nondimensional frequency = $\omega b/a$
ω_d^* = nondimensional design frequency
ω_f^* = nondimensional flutter frequency
ω_h = bending frequency
ω_α = torsion frequency

constant phase angle between adjacent blades. With this assumption the equation of motion for single blade (neglecting structural damping) is

$$\begin{bmatrix} m & S_\alpha \\ & \\ S_\alpha & I_\alpha \end{bmatrix} \begin{Bmatrix} \dfrac{d^2}{dt^2}(he^{i\omega\tau}) \\ \\ \dfrac{d^2}{dt^2}(\alpha e^{i\omega\tau}) \end{Bmatrix} + \begin{bmatrix} K_h & 0 \\ & \\ 0 & K_\alpha \end{bmatrix} \begin{Bmatrix} he^{i\omega\tau} \\ \\ \alpha e^{i\omega\tau} \end{Bmatrix} = \begin{Bmatrix} -L \\ \\ M_e \end{Bmatrix} \qquad (2)$$

The unsteady aerodynamic loads are defined in terms of the linear lift and moment coefficients as

$$L = -\pi\rho_a b^3\omega^2\left(l_{hh}\frac{h}{b} + l_{h\alpha}\alpha\right)e^{i\omega\tau}$$
$$\mathrm{M} = \pi\rho_a b^4\omega^2\left(l_{\alpha h}\frac{h}{b} + l_{\alpha\alpha}\alpha\right)e^{i\omega\tau} \qquad (3)$$

After being nondimensionalized and put in standard eigenvalue form the equation becomes

$$\begin{bmatrix} \dfrac{1}{\gamma_h^2}\left(1+\dfrac{l_{hh}}{\mu}\right) & \dfrac{1}{\gamma_h^2}\left(x_\alpha+\dfrac{l_{h\alpha}}{\mu}\right) \\ \\ \dfrac{1}{r_\alpha^2\gamma_\alpha^2}\left(x_\alpha+\dfrac{l_{\alpha h}}{\mu}\right) & \dfrac{1}{\gamma_\alpha^2}\left(1+\dfrac{l_{\alpha\alpha}}{\mu r_\alpha^2}\right) \end{bmatrix} - \lambda[I] = 0 \qquad (4)$$

The variables γ_h and γ_α are nondimensionalized with respect to the natural frequencies of the solid blade

$$\gamma_h^2 = \frac{\left(\dfrac{K_h}{m}\right)_{\text{hollow}}}{\left(\dfrac{K_h}{m}\right)_{\text{solid}}} \text{ and } \gamma_\alpha^2 = \frac{\left(\dfrac{K_\alpha}{I_\alpha}\right)_{\text{hollow}}}{\left(\dfrac{K_\alpha}{I_\alpha}\right)_{\text{solid}}} \qquad (5)$$

Additional variables are defined in the nomenclature.

The stability characteristics of the system can be determined by iteratively solving the complex eigenvalue problem of equation (4). For a given system the stability characteristics can be found by choosing a Mach number and interblade phase angle and iterating on reduced frequency until the calculated frequencies are consistent with the assumed reduced frequency and Mach number. The aerodynamic damping for that Mach number and interblade phase angle can then be calculated. This procedure should be repeated for various Mach numbers and interblade phase angles until the neutral stability point is determined.

To determine the effects of the balancing mass this procedure could be followed for various balancing mass configurations. The predicted flutter Mach numbers for each configuration could then be compared to determine the best. However, to find the best configuration using this procedure would require an unnecessarily large number of configurations to be analyzed. Following is a description of a more efficient method.

It is helpful to pay attention to the pitching axis location associated with any mode of interest. The location of the pitching axis for a typical section is the point along the chordline which experiences no plunging motion when the blade oscillates in some mode, and is not the same as the elastic axis (locus of shear centers) used in the two degree of freedom analysis. As shown in [6], the predicted stability characteristics can be drastically different from one and two degree of freedom flutter analyses if the pitching axis for the one degree of freedom analysis is assumed to be the blade elastic axis. However, for a given elastic axis (and other defined blade properties), a pitching axis can be found for every mode shape, and the one degree of freedom analysis can be used to estimate the stability of the mode based on that pitching axis. This estimate will be very accurate as long as the frequencies of the modes are separated by at least 10 percent (see [5, 6]). In the following it is assumed that the single degree of freedom flutter analysis can be used to find the best pitching axis location. Note that in the present work the balancing mass is assumed to add no stiffness; therefore, the position of the elastic axis is the same for all mass balancing configurations.

For a single degree of freedom flutter analysis the neutral stability condition, with respect to the system variables, can be simply determined by finding the point where the imaginary part of the moment coefficient vanishes (or the lift coefficient for pure plunging motion). For a fixed stagger angle and gap-to-chord ratio, the reduced frequency (k_f) at which the imaginary part vanishes should be calculated for the Mach number range of interest for various pitching axis locations (normally a range from the leading edge to four semichords downstream is sufficient). These calculations will show the pitching axis location x_{pd} that results in the best stability characteristics over the chosen range of Mach numbers. They will also yield the aerodynamically required minimum value of the modal frequency for the mass balanced blade. (Note the best overall pitching axis location may not be the best at any single Mach number, such as that of the design point.) It is useful to define the following nondimensional frequencies [10]

$$\omega^* = k\mathrm{M} \text{ and } \omega_f^* = k_f\mathrm{M} \qquad (6)$$

The nondimensional frequency, required by aerodynamics, for the mass balanced blade is denoted as ω_d^*. This is the minimum frequency which results in a stable blade for the chosen pitching axis location over the entire Mach number range of interest.

The next step is to find the best mass balancing configuration which results in a pitching axis at x_{pd} and a frequency of ω_d^* or greater. Because the aerodynamic forces normally cause very little change in blade frequencies (for supersonic fans), we can neglect them. In the absence of these forces equation (2) simplifies to a real eigenvalue analysis from which the uncoupled modal frequencies and mode shapes of the inertially coupled system can be determined

$$\begin{bmatrix} \dfrac{1}{\gamma_h^2} & \dfrac{x_\alpha}{\gamma_h^2} \\ \\ \dfrac{x_\alpha}{r_\alpha^2\gamma_\alpha^2} & \dfrac{1}{\gamma_\alpha^2} \end{bmatrix} - \lambda[I] = 0 \qquad (7)$$

Using simple cantilever beam expressions these variables can be defined in terms of the geometric and material properties

$$\gamma_h^2 = \frac{\left(\dfrac{I_{xx}}{m}\right)_{\text{hollow}}}{\left(\dfrac{I_{xx}}{m}\right)_{\text{solid}}} \text{ and } \gamma_\alpha^2 = \frac{\left(\dfrac{J}{I_\alpha}\right)_{\text{hollow}}}{\left(\dfrac{J}{I_\alpha}\right)_{\text{solid}}} \qquad (8)$$

Next these quantities can be expressed in terms of the nondimensional parameters defining the mass balancing configuration

$$\gamma_h^2 = (1-g_r^3)\Big/\left(2\omega_r + \frac{\rho_{mr}c_{mr}g_r}{2}\right) \qquad (9)$$

$$\gamma_\alpha^2 = 3\left(\frac{\omega_\alpha}{\omega_h}\right)_{\text{solid}} w_r(1-w_r)^2(1+t_r^2)$$

$$\bullet\left[w_r\left(1+w_r^2t_r^2+3t_r^2(1-w_r)^2\right)\right.$$

$$\left.+\frac{\rho_{mr}c_{mr}g_r}{4}\left(\frac{c_{mr}^2}{4}+t_r^2g_r^2+3x_{mr}^2\right)\right] \tag{10}$$

The radius of gyration, static unbalance, and mass ratio can also be expressed in terms of these nondimensional parameters

$$r_\alpha^2 = 2\left\{w_r\left[1+w_r^2t_r^2+3t_r^2(1-w_r)^2\right]\right.$$

$$\left.+\frac{\rho_{mr}c_{mr}g_r}{4}\left(\frac{c_{mr}^2}{4}+t_r^2g_r^2+3x_{mr}^2\right)\right\}\Big/3\left(2w_r+\frac{\rho_{mr}c_{mr}g_r}{2}\right) \tag{11}$$

$$x_\alpha = (x_{mr}\rho_{mr}c_{mr}g_r)/(4w_r+\rho_{mr}g_rc_{mr}) \tag{12}$$

$$\mu = \mu_{\text{solid}}\left(2w_r+\frac{\rho_{mr}c_{mr}g_r}{2}\right) \tag{13}$$

When solving equation (7) the following trends are found. As the centroid of the balancing mass moves away from the elastic axis position, the frequencies of both normal modes decrease. By itself this decrease would tend to reduce the stability of the system because it lowers the reduced frequency. However, the coupling between the plunging and pitching motions increases. If this coupling moves the pitching axis for one of the modes near to the "best" location (determined from the single degree of freedom flutter analysis described above), an overall beneficial effect on the stability may be found. Therefore, the balancing mass has competing detrimental and beneficial effects. Which of these effects dominates depends on the parameters of the blade being studied. For some blades the effect of the reduction of frequency is so strong that the blade cannot be practically stabilized with mass balancing. These competing effects will be shown graphically in the example of the following section.

There can be many mass balancing configurations which result in the same required pitching axis location and frequency as determined from the single degree of freedom flutter analysis. To find efficiently the best mass balancing configuration, the following sequence of solutions of equation (7) should be followed.

To obtain a mass balanced blade with modal frequencies as high as possible, the density ratio should be chosen as large as possible. The reason is that, for a fixed balancing mass (quantity and location), the area and polar mass moment of inertia decrease as the density of the balancing mass increases, and the frequency increases as the polar mass moment of inertia decreases. A common material having a high density is tungsten. The density ratio ρ_{mr} for a tungsten balancing weight is approximately 4 for a titanium blade and 7 for an aluminum blade.

Next we select a chordwise dimension for the balancing mass c_{mr} (usually less than 0.5) and determine the location of the balancing mass x_{mr}, which results in a pitching axis at x_{pd}. This can be done by iteratively solving equation (7). Repeat this process for other values of c_{mr} until a value is found which results in an acceptable frequency ($\omega^* > \omega_d^*$) and the lowest mass per unit span m_r.

In the above discussion emphasis has been placed on only one mode of the system. For high-speed fan flutter this is normally the torsional mode, which is represented in this model as pitching about some point near midchord. However, it may be found that as this predominantly torsion mode is stabilized the predominantly bending mode is destabilized. Therefore, when a stable configuration for the one mode is found, the other mode must be checked for stability.

Once the above procedure is followed to find the best mass balancing configuration, a two (or multiple) degree of freedom flutter analysis should be used to define accurately the stability characteristics of the mass balanced design.

Table 1 Solid blade properties; 75 percent span, design point

Thickness ratio, R_t	0.037
Stagger angle, deg	64.86
Gap-to-chord ratio, s/c	0.8
Mass ratio	206
Radius of gyration, r_α	0.5774
Center of mass, x_α	0
Elastic axis position, a_e	0
Relative design Mach number	1.27
Reduced frequency for bending mode	0.194
Reduced frequency for torsion mode	0.412
ω_α/ω_h	2.124

In summary, the steps to define the best mass balancing configuration for fixed values of t_r and w_r are:

1 For fixed values of the stagger angle and gap-to-chord ratio (usually taken near 75 percent span) construct a plot of aerodynamically required frequency ω_f^* versus pitching axis location by finding where the imaginary part of the moment coefficient vanishes. Determine the "best" location x_{pd} and the frequency ω_d^* that exceeds ω_f^* over the Mach number range of interest.

2 Select a balancing mass material with as high a density as possible and determine the density ratio ρ_{mr}.

3 Iteratively solve equation (7) for selected values of c_{mr} to determine the balancing mass location x_{mr}, which results in a pitching axis at x_{pd}. For this configuration determine the blade modal frequency ω^* and mass per unit span m_r.

4 From the results of step 3 determine the value of c_{mr} which results in a modal frequency ω^* greater than or equal to ω_d^* and has the lowest total blade mass. If the frequencies are all less than ω_d^*, this blade is not a good candidate for mass balancing using the selected density ratio.

5 Using the configuration from step 4 perform a complete multiple degree of freedom flutter analysis for all modes to check that you have a stable design.

In the above steps it is important to consider all possible interblade phase angles when calculating k_f and system stability. The example in the following section further clarifies the above discussion.

Results and Discussion

An advanced unshrouded fan stage representative of a next-generation fan was chosen for analysis. A similar blade was analyzed in [12] to investigate mistuning effects. The properties of this blade (in the solid configuration) at the design condition are given in Table 1. The aspect ratio of the blade is 3.1 and the stage contains 28 blades. At the design point (tip relative Mach number is 1.45) the blade encounters high-speed unstalled torsional flutter in both the solid and hollow (with no balancing mass) configuration. This section gives an example of an efficient method to find the best mass balancing configuration to stabilize the blade.

For this example the unsteady aerodynamic coefficients in equation (3) are calculated by using Adamczyk and Goldstein's theory [11] for a cascade in supersonic flow with a subsonic leading edge. In this theory the effect of airfoil thickness, camber, and steady-state angle of attack are neglected, and the flow is assumed to be isentropic and irrotational. For more information see [11].

The dependence of aerodynamically required frequency ω_f^* on Mach number for selected pitching axis locations is shown in Fig. 4. As can be seen, the hollow blade with no balancing mass ($\omega^* = 0.725$ and $x_p = 0.0$) would encounter a strong instability just below the design point. As the pitching axis

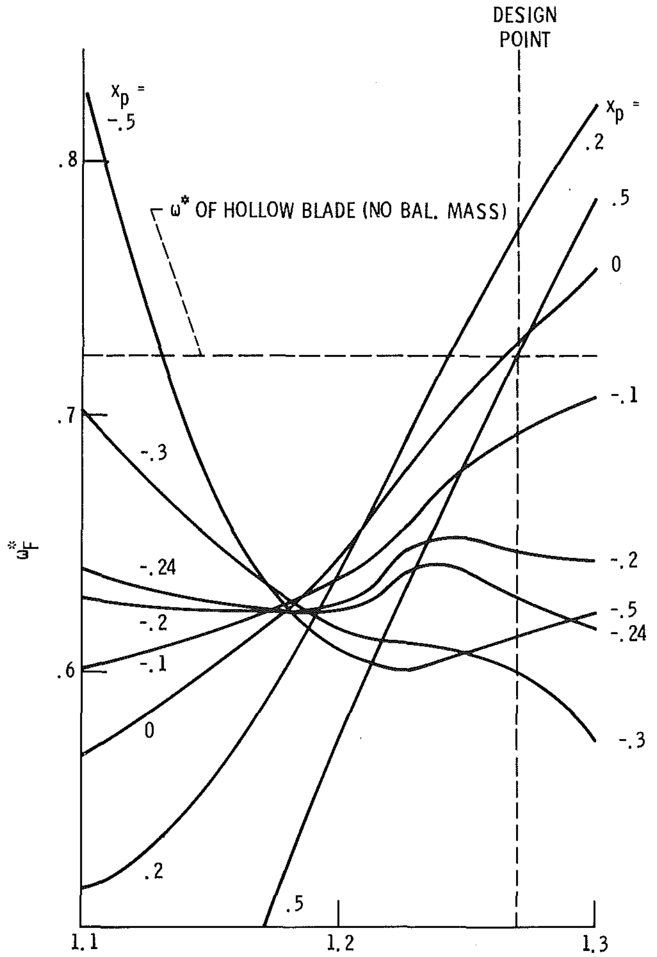

Fig. 4 Effect of pitching axis location on flutter frequency (ξ = 64.68 deg, s/c = 0.8)

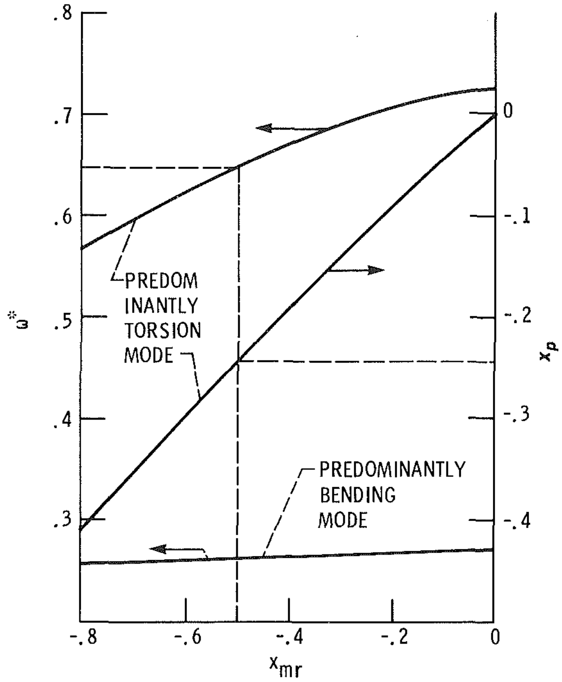

Fig. 5 Effect of mass balancing location on blade frequencies and pitching axis location (c_{mr} = 0.22, ρ_{mr} = 4)

moves toward the leading edge, the required frequency is significantly reduced for the design Mach number. Athough not shown, the minimum required frequency (for M = 1.27) is achieved with the pitching axis at $x_p = -0.37$. However, for pitching axis locations forward of midchord, the required frequency is significantly increased at lower Mach numbers. Note that the unsteady aerodynamics theory used herein gives unreliable results as the Mach number approaches one. For pitching axis locations aft of midchord the effect is reversed, i.e., the required frequency is increased for the higher Mach numbers and decreased for the lower. The best pitching axis location is one which reduces the required frequency for the design condition, but does not affect the lower Mach number conditions to a serious extent. As seen in Fig. 4, the pitching location of −0.24 (38 percent chord) results in a relatively constant required frequency over the Mach number range of interest. As a result, this value was chosen as the best.

It may appear from Fig. 4 that a pitching axis location near the trailing edge ($x_p > 0.5$) would be desirable, however the frequency of the modes with these pitching axis locations drops to such an extent that it is substantially less than the frequency required at the design point.

The aerodynamic theory used herein predicts that there can be no pure bending flutter (pitching axis at infinity). Therefore the curves in Fig. 4 approach zero for all Mach numbers as x_p approaches positive and negative infinity. For values of x_p greater than 4 the value of ω_f^* at the design Mach number is less than 0.18. The predominantly bending mode ($\omega^* \approx 0.25$) for this blade was found to be stable when x_p is greater than 3.5; however, this mode could be easily destabilized by positioning a large balancing mass near the leading edge.

As mentioned previously all possible interblade phase angles must be considered when constructing Fig. 4. Although the critical interblade phase angle varies with pitching axis location, it was found that the interblade phase angles in the range of 38.6 to 64.3 deg (3 to 5 nodal diameter forward traveling waves) were critical for most of the cases.

A tungsten balancing mass was selected. Since the blade being considered is titanium, a density ratio of 4 was used. The real eigenvalue problem of equation (7) was solved for various values of c_{mr} and x_{mr}. An example of the effect of balancing mass position on both frequency and mode shape is shown in Fig. 5 for $c_{mr} = 0.22$ (as will be shown below this is the best value). The location of the mass has a much stronger effect on the torsion mode than on bending mode. To obtain the required pitching axis location, −0.24, the balancing mass must be located at −0.5 (25 percent chord). Although the frequency ω^* of the mode has decreased significantly it is still above the aerodynamically required value ω_d^*. Note that the frequency curves of Fig. 5 are symmetric about $x_{mr} = 0.0$ (the pitching axis curve is antisymmetric).

The curves shown in Fig. 5 were generated for other values of c_{mr} and the values of ω^* and m_r for which $x_p = -0.24$ were determined. The resulting blade frequencies are shown in Fig. 6 as a function of the blade mass. In addition to a curve for the selected frequency ratio of 4, Fig. 6 includes curves for ratios of one and infinity (a point mass). As can be seen a higher density ratio will result in a lower blade mass to achieve a given frequency. For the chosen density ratio ($\rho_{mr} = 4$) the curve peaks at a maximum obtainable frequency of slightly over 0.65. Fortunately, this is slightly above the aerodynamically required value of 0.646. If the required value is greater than 0.651, this blade could not be stabilized with this density ratio. The value of m_r corresponding to the desired frequency is 0.664. This represents the fraction of blade mass as compared to the solid blade and is 1.66 times the mass of the hollow blade without a balancing mass ($m_r = 0.4$). Thus, a significant weight penalty has been paid in stabilizing the hollow blade. As a result, the best mass balancing configuration for

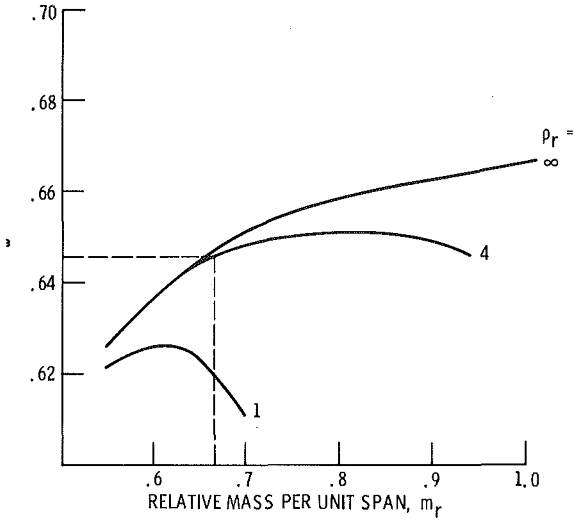

Fig. 6 Dependence of frequency on blade mass (x_p = −0.24)

flutter suppression may not be the best when considering the whole engine and all design requirements. If the increase in engine weight is not tolerable, other passive flutter suppression schemes such as damping and/or mistuning may be more desirable.

A summary of the aerodynamic damping for the solid, hollow (with no balancing mass), and best mass balanced configurations is shown in Fig. 7. The solid blade is seen to be unstable for all Mach numbers shown. A significant improvement in blade stability can be achieved by making the blade hollow. This is simply due to the increase in frequency of the torsional mode. However, the blade still encounters a strong instability below the design point. The best mass balancing configuration is shown to eliminate the instability completely.

As was seen in Fig. 4, the aerodynamically required blade frequencies are very sensitive to the pitching axis location. For example, the best mass balanced configuration has x_p = −0.24, yet if the pitching axis is moved slightly to −0.30, the blade (which has $\omega^* = 0.65$) would experience an instability at lower Mach numbers. The range of x_p over which the blade is stable for $1.1 < M < 1.3$ is relatively narrow. Furthermore, as previously noted, the bending mode can be destabilized when adding a balancing mass. These sensitivities imply that the designer must be extremely careful in choosing the configuration of the balancing mass.

Summary and Conclusions

An efficient procedure for assessing mass balancing as a passive means to alleviate flutter for fan blades is presented. The procedure is applied to a fan blade which encounters high-speed, unstalled supersonic flutter. A mass balancing configuration is defined which stabilizes the blade over the desired operating range. The major conclusions from this investigation are the following:

1 For the particular blade studied the best location for the pitching axis of the predominantly torsional mode is at 38 percent chord.

2 The best mass balanced configuration was one with a mass centered at 25 percent chord, a chordwise length of 11 percent of the blade chord, and a density four times that of the blade wall.

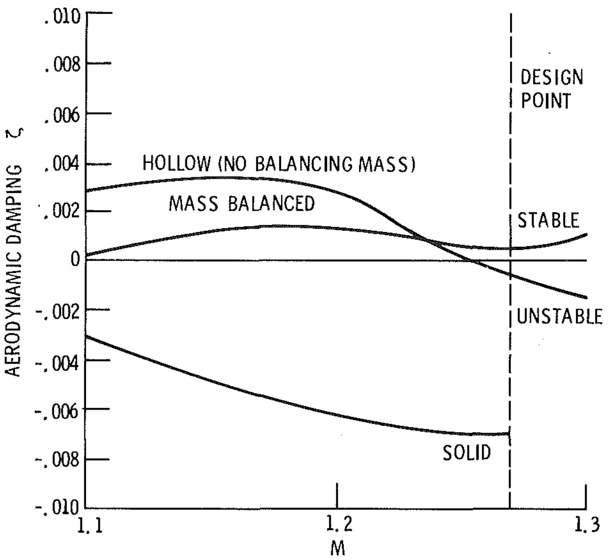

Fig. 7 Aerodynamic damping for solid and hollow blades

3 Because of the sensitivity of blade stability to pitching axis location and the possibility that the predominantly bending mode may be destabilized, a careful procedure to define the balancing mass configuration, such as that given herein, is required.

4 A major improvement in blade stability can be realized by using a hollow blade with no balancing mass.

5 The mass penalty which must be paid to stabilize the blade may be so large that other blade and engine design requirements may be affected.

References

1 von Baumhauer, A. G., and Koning, C., "On the Stability of Oscillations of an Airplane Wing," NACA TM-223, 1923.

2 Theodorsen, T., and Garrick, I. E., "Mechanism of Flutter—A Theoretical and Experimental Investigation of the Flutter Problem," NACA Report 685, 1940.

3 Ashley, H., and Zartarian, G., "Supersonic Flutter Trends as Revealed by Piston Theory Calculations," USAF Wright Air Development Center Technical Report 58-74, May 1958.

4 Pines, S., "An Elementary Explanation of the Flutter Mechanism," *Dynamics and Aeroelasticity*, Proc. Natl. Specialists Meeting on Dynamics and Aeroelasticity, Fort Worth, TX, Nov. 1958, pp. 52–58.

5 Kaza, K. R. V., and Kielb, R. E., "Flutter and Response of a Cascade Mistuned in Incompressible Flow," *AIAA Journal*, Vol. 20, 1982, pp. 1120–1127.

6 Bendiksen, O., and Friedmann, P., "Coupled Bending-Torsion Flutter in Cascades," *AIAA Journal*, Vol. 18, 1980, pp. 194–201.

7 Troha, W., and Swain, K., "Composite Inlays Increase Flutter Resistance of Turbine Engine Fan Blades," ASME Paper No. 76-GT-29, Mar. 1976.

8 Carta, F. O., "Coupled Blade-Disk-Shroud Flutter Instabilities in Turbojet Engine Rotors," ASME JOURNAL OF ENGINEERING FOR POWER, Vol. 89, 1967, pp. 419–426.

9 Kielb, R. E., and Kaza, K. R. V., "Aeroelastic Characteristics of a Cascade of Mistuned Blades in Subsonic and Supersonic Flows," *Journal of Vibration, Acoustics, Stress, and Reliability in Design*, Vol. 105, 1983, pp. 425–433.

10 Brown, G. V., NASA Lewis Research Center, private communication on nondimensional frequency.

11 Adamczyk, J. J., and Goldstein, M. E., "Unsteady Flow in a Supersonic Cascade With Subsonic Leading-Edge Locus," *AIAA Journal*, Vol. 16, 1978, pp. 1248–1254.

12 Kaza, K. R. V., and Kielb, R. E., "Flutter of Turbofan Rotors With Mistuned Blades," *AIAA Journal*, Vol. 22, 1984, pp. 1618–1625.

More Comprehensive Vibration Limits for Rotating Machinery

A. Lifshits
Senior Research Engineer.

H. R. Simmons
Senior Research Engineer.

A. J. Smalley
Institute Engineer.

Southwest Research Institute,
San Antonio, TX

Vibrations are often found to be the cause of rotating machinery failures. To minimize these outages a large number of vibration criteria have been introduced by technical societies, equipment manufacturers, and experienced individuals. While useful, these vibration criteria have often been found to be contradictory and restricted to particular transducer types, machine design, or failure mechanisms. Based on this work and adding the experience accumulated by SwRI with various types of rotating equipment, more comprehensive combined vibration severity limits are established. These limits are divided into several severity regions, and cover filtered and unfiltered vibration. The appropriate correction factors are also introduced to equitably accommodate different machine designs, installations, and vibration problems. Vibration severity limits are provided for relative shaft displacement, for shaft displacement with respect to bearing clearance, and for vibration measurements taken on machine casing or bearing housing. The use of these limits is clarified by reviewing the results obtained from five field studies of actual operating equipment. Advantages, disadvantages, and use of various transducer types (proximity probes, velocity pickups, accelerometers, dual probes), as well as sources of machinery vibration (subsynchronous instabilities, resonance, imbalance, misalignment, etc.) are analyzed to assure proper application of the vibration limits.

Introduction

This paper contains topics which have been of increasing concern to many rotating machinery users and manufacturers over the past few years. The significance of vibration levels in the operation of rotating machinery is well understood [1-4]. These levels are often a direct indicator of a machine's operating condition. High vibration amplitudes or changing vibration amplitude patterns can be an indication of an impending equipment failure, or can provide important clues to the cause of declining machinery health. Vibration measuring instrumentation is now commonly employed on rotating machinery to identify characteristic levels and trends. In order to successfully fulfill its purpose, however, the vibration instrumentation must measure amplitudes and frequencies which are meaningful and truly indicative of the machinery's condition. These amplitudes and frequencies must, in turn, be compared against "standard" reference values which establish the condition on status of the machinery and determine which machine requires additional attention.

The problem faced by maintenance personnel is to quickly and reliably sort out vibration trends that might indicate trouble ahead. Thus, it is quite popular for an inspection program to be set up whereby overall vibration levels are monitored on a regular basis. This approach has had some success in avoiding unexpected outages or unnecessary overhauling of healthy equipment; however, all vibration problems are not reliably indicated by this method. Those individuals who try to cover too much area with a simple criterion may find that they are missing some problems that will result in costly shutdowns if their limits are too liberal for the application or if their monitoring system is inadequate. Obviously, unnecessary maintenance shutdowns of operating components due to overly conservative vibration standards are equally costly.

The main thrust of this paper is to provide a user with comprehensive vibration limits which are applicable to vibration taken on machine housing or relative to the shaft and account for different machine design and probable failure mechanisms. The use of these limits is clarified by reviewing the vibration data obtained from several field studies of malfunctioning rotating equipment. To bring out the importance of applying an appropriate monitoring system to avoid potential problems, an overview of various transducer types and sources of machinery vibration is also presented.

Transducer Selection

The installation of vibration measuring devices has become common practice on critical and costly industrial machines. The underlying objective is to detect an increase in vibration level before mechanical problems occur. To achieve this, it is necessary to select a transducer type that will measure the vibration (machine housing or shaft) most likely to reveal the expected failure characteristics [5, 6]. Shaft measurements are recommended for rotor-related malfunctions which include: imbalance, misalignment, shaft bow, and fluid film bearing instability problems. Velocity pickups or accelerometers, installed on machine casings or bearing housings, are recommended to detect housing and high-frequency rotor-related

---

Contributed by the Gas Turbine Division of The American Society of Mechanical Engineers and presented at the 31st International Gas Turbine Conference and Exhibit, Düsseldorf, Federal Republic of Germany, June 8-12, 1986. Manuscript received at ASME Headquarters January 30, 1986. Paper No. 86-GT-148.

Table 1 Vibration transducer applications

1) **Machine Housing Measurement** - Accelerometers and Velocity Pickups:
Typical gas turbines, fans, axial compressors, small and medium-duty pumps. Detects housing-related or high frequency malfunctions: bearing support, casing or foundation resonances, loose parts, blade vibration, rolling element bearing defects, and gear noise.

2) **Relative Shaft Displacement Measurements** - Proximity Probes:
Equipment with fluid film bearings, centrifugal compressors, gears, large electric motors and pumps, sometimes turbines and fans. Detects excessive bearing loading, and instabilities.

3) **Absolute Shaft Displacement Measurements** - Shaft Riders and Dual Probes:
Shaft riders are common on older turbogenerators; new installations usually use proximity probes while dual probes may be required if machine also has significant casing motion.

Accelerometers

Advantages	Disadvantages
(1) Simple to install, (2) good high frequency response, (3) small size, (4) high temperature environments.	(1) Sensitive to high frequency noise, (2) requires external power source, (3) requires electric integration for displacement.

Velocity Pickups

Advantages	Disadvantages
(1) Simple to install, (2) strong mid-frequency ranges, (3) high temperature environments, (4) no external power source.	(1) Transducer resonance noise and phase shift, (2) cross-axis signal noise, (3) requires electronic integration for displacement, (4) can be affected by magnetic fields, (5) large and heavy.

Proximity Probes

Advantages	Disadvantages
(1) Measures static and dynamic shaft motion, (2) accurate low frequency data, (3) no wear, (4) small size, low cost.	(1) Mechanical or electrical runout noise, (2) limited high frequency sensitivity, (3) uncalibrated for unusual materials, (4) requires external power source, (5) difficult to install.

Shaft Riders

Advantages	Disadvantages
(1) Not affected by electrical runout, (2) no external power source.	(1) Probe resonance noise, (2) noise due to mechanical runout and irregularities, (3) wear, (4) difficult to install.

Dual Probes

Advantages	Disadvantages
(1) Combined advantages of proximity probes, and velocity pickups or accelerometers, (2) measures shaft and housing vibration separately.	(1) Combined disadvantages of proximity probes, and velocity pickups or accelerometers.

malfunctions which include: ball bearing failure, support looseness, casing or foundation resonances, loose parts, and gear or blade problems.

Since every transducer type has its merits as well as shortcomings and limitations, no single transducer type can be relied upon to meet all application requirements. Therefore, many critical installations may require more than one type of transducer for complete protection. Typical applications of the various transducers are presented in Table 1.

Machinery monitoring represents a cost that is not directly reflected in increased production; therefore, a compromise must be reached to what extent each machine should be monitored. The factors that usually affect the amount of monitoring equipment installed are:

- Untried equipment design
- Frequency maintenance requirements
- Newly installed or recently rebuilt equipment
- Severe environment (corrosion, erosion, etc.)
- Low cycle fatigue possibilities (stress risers)
- Consequences of failure
- Previous failure experience

To provide reliable data for trend evaluation, comparison with vibration criteria, and problem identification, all significant noise sources must be eliminated. The most common source of noise found in proximity probes on a variety of rotating equipment is shaft electrical or mechanical runout. The greatest runout errors are created when a journal is flame sprayed or plated to rebuild worn surfaces. To prevent the probe signals from becoming useless after such an operation, the shaft surface sensed by the probe should be properly masked. Surface grinding and rolling or shot peening are treatments that can be used to improve uncoated shafts. Alternately, special analysis equipment can be used to subtract the runout signal; however, such runout subtraction is either expensive if applied permanently to each channel, or time consuming if manual subtraction is used.

Any approach to determine machine condition should provide a criterion based on the type of problem or equipment involved for comparison with vibration measurements. The vibration amplitudes throughout a machine and their relationships to transmitted forces and stresses are often described by modal theories which superimpose vibration at various resonant frequencies. Although these vibration relationships are

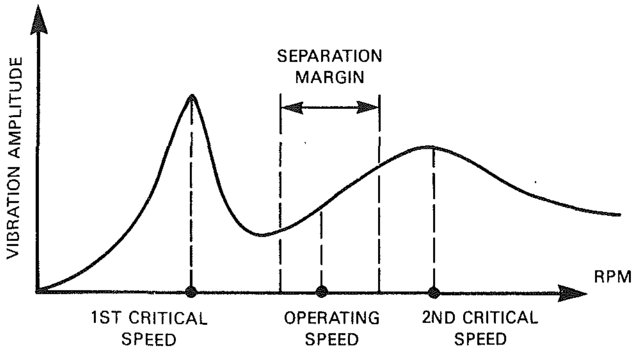

Fig. 1 Vibration rotor response

not explicitly defined in many cases, we know that rough proportionality exists between the vibration we can measure and the components where failure will occur. Thus, vibration relating to most failures can be detected if the measurement can be made with the least influence from unrelated sources (low noise). Achieving low noise signals is a matter of choosing appropriate measurement locations and transducers.

To use the vibration criteria for machinery, the type of problems anticipated should be determined based on a comparison of the expected dynamic characteristics with observed frequency spectra. Appropriate factors are then applied to the measured data that account for the perceived severity of different types of excitation, expected transmissibility, and other design conditions. The appropriate charts are entered to determine the degree of risk that might be expected for a large population of machines.

Vibration Sources

Establishing the proper source of excessive vibration is probably the most difficult task of machinery analysis. After the source of vibration is determined, it is generally possible to assess the severity of the existing problem by comparing the vibration level against a specified vibration standard. As the sources of the various excitation forces often occur at different frequencies, it is very useful to characterize measured vibration signals with respect to frequency. Thus, spectral analysis is a recommended procedure for solving vibration problems and evaluating the reliability of equipment.

Vibration amplitudes obtained from spectral analysis should be investigated in relation to machine design, installation, and vibration source. Judicious placement of vibration transducers so that a vibration source can be separately identified is necessary to gain maximum use of the vibration criteria [6–9]. Separation of gear mesh excitation from turbine blade vibrations, for example, might be determined by analyzing signals from a few trial locations and applying judgment based on knowledge of the machine's design and exact frequencies of each source.

An overview of several most common vibration sources is outlined below.

Resonance is probably the most common cause of high vibration and most vibration-related failures. Very often user vibration specifications ignore resonances completely and depend upon the manufacturer for such criteria. If resonant margins are not specified and verified by testing, the component could be very precisely balanced or adjusted to meet the acceptance vibration limits at the time of purchase. However, long-term use of such a machine may result in high maintenance requirements as slight imbalances or other distortions accumulate causing vibrations to increase to unacceptable levels. General guidelines on critical speed margins for lateral shaft vibration are provided by API standards for several different types of rotating equipment. For example, compressors and pumps are required to have lateral critical speed margins of 20 percent above maximum operating speed or 15 percent below minimum operating speed, and amplification factors should not exceed 8 while going through criticals (Fig. 1). If the measured critical speed falls within the excluded range, then the manufacturer must demonstrate that the vibrations at the critical speed are within acceptable vibration limits with considerably more imbalance than would normally be expected.

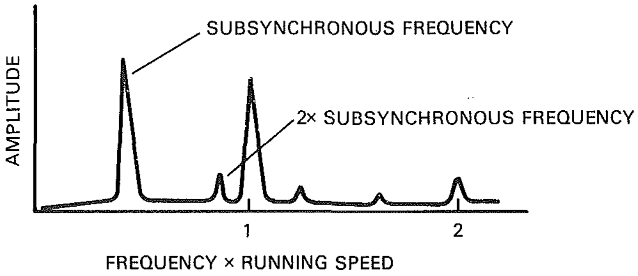

Fig. 2 Spectral characteristics of subsynchronous instabilities

Special attention should be given to blade-related problems. Very little can be done to minimize blade vibrations after they have occurred as a problem in the field. The blade design should be investigated thoroughly prior to actual manufacturing of the unit. The fundamental principle in dealing with blade vibrations is to avoid resonance. The blade natural frequency should not be within 10 percent of any identifiable excitation frequencies at any point in the normal operating range, including multiples of blade passage frequency and multiples of running speed. The aerodynamic phenomena are too complex to be predictable at the present time and vary greatly from machine to machine. As a result, any attempt to live with an excitation of the lower four or five blade modes is likely to cause blade loss failure regardless of excitation force predictions. If the frequency of the driving forces cannot be changed, the blade design should be changed to detune it from resonance. The calculations of the natural frequencies of a blade are quite involved and should include the effect of centrifugal forces combined with a knowledge of the root fixity factor. Simplified calculations, however, can give sufficient accuracy for the lower modes to determine whether a blade vibration can be a problem.

Subsynchronous instabilities are another possible source of vibration in plant operating equipment. "Instabilities" is the term given to those vibration sources that are self-excited by some mechanism where fluid, aerodynamic, or frictional forces interact with the rotor. Instabilities usually exhibit vibration frequencies at about 1/2 running speed (Fig. 2) and have a tendency to increase suddenly in amplitude with disastrous results. Rotating stall of draft fan air foils at low flow is another source of subsynchronous rotor vibration, but generally is not as dangerous because the excitations are not unstable, but are simply the result of unbalanced flow forces. The following items increase the susceptibility of a rotor to subsynchronous instabilities:

- Rotors operating above the first critical speed
- Compressors with high outlet pressure and high-molecular-weight gas
- Lightly loaded bearings
- Presence of high-pressure pulsations and acoustic resonances
- Stiff radial bearings relative to the shaft flexural stiffness
- Inadequate seal design
- Sudden shock loads
- Presence of rotor frictional sources such as light shrink fits over a long section

The most common types of instabilities include:

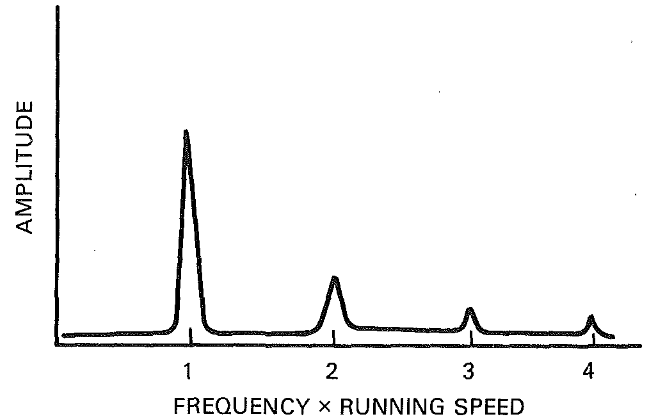

Fig. 3 Spectral characteristics of imbalance

- *Fluid Film Bearing Instability.* Self-excited rotor vibration due to fluid film bearing instability, known as oil whirl and oil whip, has been an area of concern for a long time. This type of instability can often be eliminated by a change in bearing configuration to more stable design. Bearing designs which have the highest order of stability are tilting pad and squeeze film bearings.

- *Floating Ring Seal Instability.* Floating ring seals can act in a manner similar to journal bearings and thus potentially contribute to self-excited vibration. The analogy to a circular short bearing is quite obvious and the corresponding theories allow their stiffness and damping properties in the locked-up condition to be estimated. In lock-up, floating ring seals are held radially by friction forces which do not allow them to follow the shaft motion. Their destabilizing effect may be reduced by balancing the floating ring seal axial force in such a way that the friction forces are as small as possible. Another possibility is to optimize the clearance geometry in order to obtain favorable dynamic stiffness properties.

- *Labyrinth Seal Instability.* One of the dominant self-excitation mechanisms in high-pressure compressors has been found to have its origin in the labyrinth seals. Labyrinth seal instability problems depend heavily on the labyrinth seal geometry and machine operating conditions; more specifically: labyrinth radius, strip height, rotational speed, internal pressures, Mach number, and inlet swirl velocity. Generally, the best way to reduce labyrinth seal instability is by suppressing the inlet swirl velocity of the leakage flow entering the seal.

- *Aerodynamic Whirl Instability.* Aerodynamic whirl instability is related to lateral aerodynamic forces acting on the compressor or turbine blades. These forces are generated by varying tip clearances when the rotor is displaced from the center position. It has been determined that susceptibility of the rotor to this type of instability increases with an increase in gas density and rotational speed of the machine.

- *Hysteretic Instability.* Hysteretic (frictional) instability usually occurs if rotors operate above the first critical speed and internal forces that lag the bending displacements are allowed to occur. The source of excitation is normally the frictionally suppressed movement in the shrink fits of wide discs or impellers shrunk to the shaft. To reduce this type of instability, the axial contact length of the shrink fit should be as short and as tight as possible without exceeding the yield strength of the material.

Imbalance is a common source of machinery vibrations. Imbalance is always characterized by radial vibration of the shaft or casing which is in exact synchronization with rotor speed (Fig. 3). Unavoidable geometry imperfections due to fabrication or material variation will result in rotor imbalance such that virtually all new high-speed machines will require balancing at the factory. Some very sensitive machines will also require rebalancing after installation. Vibration should be expected to gradually change with time as the effects of erosion, wear, and particle adhesion act to change the imbalance. Thus, rebalancing will eventually be necessary on most machinery. Rotor parts such as thrust collars, cooling fans, and coupling hubs may be significant sources of imbalance but are often overlooked because of their small size.

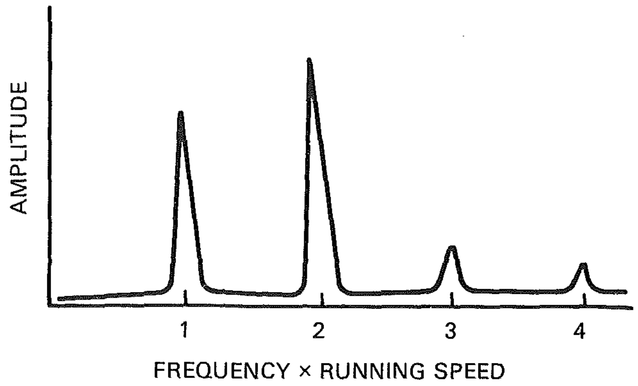

Fig. 4 Spectral characteristics of misalignment

Shaft bow is a type of imbalance caused by gravity sag or shaft thermal gradients. This bow will "roll out" or change with time after the rotor is started. The application of turning gear and roll-out procedures to minimize shaft bow is well known in the industry.

Shaft bow due to thermal distortion, which has been observed on ID fans, is a more difficult problem to identify and solve than normal shaft bow. The root cause of the thermal distortion is an apparent variation of thermal coefficient of expansion or Young's Modulus throughout the shaft or impeller. A bimetallic strip effect occurs as the rotor is heated, causing the shaft's center of mass to be moved away from the center of rotation. Careful correlation of vibration with shaft thermal growth is necessary to identify this source of variable imbalance.

Magnetic imbalance in motors is an excitation source that is often mistaken for mass imbalance. Forces due to magnetic asymmetry usually rotate at electrical synchronous speed and will beat with mass imbalance on induction machines. A test to distinguish magnetic imbalance from mass imbalance is to observe the real time vibration spectra as power to the machine is cut off. If a significant vibration reduction appears to occur instantaneously, then that portion was due to magnetic imbalance and the remainder due to mass imbalance.

Excessive misalignment of rotating elements driven through flexible couplings is usually indicated by a large second-order vibration component (Fig. 4). Occasionally, large first-order vibrations are also observed. High axial vibration is another indication that misalignment is likely. Shaft operating misalignment is affected by relative thermal growth, static forces applied by piping or condenser attachments, deterioration of support grouting, etc. Vibration due to first-order misalignment can be differentiated from imbalance by recording vibration in relation to speed. Imbalance vibration will increase with speed squared, while misalignment vibration will not change if resonances are not involved. For machines which cannot be conveniently shut down, it is recommended that a record be made of the vibration spectrum when the machine is first started up and in good alignment. This can be used for later comparison to determine if the alignment of the machine is still satisfactory.

Rubs between a rotor and close clearance stationary components can cause damage to seals and blade tips. Rubbing is

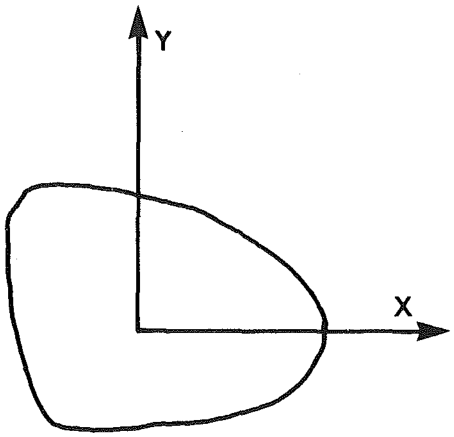

Fig. 5 Shaft orbit for rub-induced synchronous vibration

usually undesirable and sometimes catastrophic. The reported characteristics of rub-induced vibration include fixed rotor subharmonics, subsynchronous vibration at a natural frequency, supersynchronous vibration at a natural frequency, time-varying synchronous vibrations, and vibration at multiples of running speed. Thus it is difficult to make general statements about rubs, and the symptoms of rubbing are influenced by the materials in contact, the impedance to motion of the seal when contacted, location of natural frequencies, etc. Rubs of stainless steel rotors appear particularly damaging and are known to cause rapid permanent rotor deformation. High performance steam turbines, on the other hand, are designed with very tight labyrinth clearances and are almost expected to rub mildly during the early stages of commissioning. These temporary rubs can cause localized heating and a temporary bow in the rotor, with associated high imbalance, particularly when the rotor is running below its first critical speed. The symptoms of this particular rub-induced vibration are a slow time variation of synchronous amplitude and phase, and often a square like orbit (Fig. 5).

There are, of course, other sources of vibration which can cause machine failure; to mention a few: defective rolling element bearings, noise which is produced by faulty gears, mechanical looseness of shaft parts, loose mounting bolts, excessive clearance in rolling element bearings, coupling shifts, loose or weak sole plates, etc.

More Comprehensive Vibration Limits and Test Cases

Due to the large variation in machine designs, vibration limits are based on statistical or consensus evaluations of vibration and failure data from many operating units. As such, there are no absolute limits that will assure successful long-term operation nor firm upper limit that will cause failure for any specific machine. The best we can hope for is to increase our probability of successful long-term operation and minimize unscheduled outages due to equipment failure. Using statistical criteria, there will always be unexpected failures and amazing vibration endurance of some machines. In general, high vibrations are bad, low vibrations are good, and the line separating the two is somewhat uncertain. We know of several plants where a vibration reduction program resulted in considerable savings due to reduced machine outages. Thus, lowering the vibration to reasonably obtainable levels should be encouraged.

Vibration in rotating machinery may be the result of several different phenomena and affect various machine parts. Therefore, reliable vibration measurements and their assessment should be based on each particular machine type, its installation, vibration sources, and failures that are likely to occur.

Most vibration failures can be classified according to the consequences listed below:

- Structural fracture due to fatigue or dynamic overload
- Wear, fretting, or surface fatigue of bearings, gears, couplings, etc.
- Performance loss due to internal machine clearance rubs (seals, blades, impellers)

An important factor to recognize in applying vibration limits is growth of vibration amplitudes with time. All machines, regardless of their health, exhibit some form of vibration; however, on machines where a mechanical defect has deteriorated to an unacceptable level, rapid growth in vibration and consequent failure can be expected. In addition to vibration severity criteria, machine resonance characteristics should be controlled. The margin between the rotor-bearing resonance (critical speed) of a machine and its operating speed range has a very strong influence on the resultant vibration sensitivity to imbalance. Only a slight change in this margin can have a dramatic effect on vibration level. This is also true for such sources as blade resonance problems on fans and turbines.

During the past several years, there have been many vibration severity guidelines proposed by standards organizations [10, 11], technical societies [12–15], and equipment manufacturers [16–18], as well as experienced individuals [19]. Using these standards as a base and adding the experience accumulated by Southwest Research Institute with various types of rotating equipment, vibration limits have been established for machine housing vibration (Fig. 6), for shaft vibration relative to bearing housing (Fig. 7), and for shaft vibration in relation to bearing clearance (Fig. 8). These vibration limits cover a wide range of rotating equipment (reciprocating machines are excluded), installation types, and machine malfunction characteristics.

Of course, any vibration criteria utilized should be compared with the manufacturer's recommendations and user's experience with the particular type of machinery. Obviously, the manufacturer's vibration limits should be used if they are more stringent and have a clear basis.

The housing vibration chart (Fig. 6) corresponds to vibration which is measured on the machine casing or bearing housing utilizing velocity pickups or accelerometers. For more convenient analysis of vibration problems, this chart is divided into regions where velocity or acceleration measurements are most appropriate.

It is important to realize that some subjective judgment is required in conjunction with these charts. To equitably accommodate different machine designs, installations, and vibration problems, the Fig. 6 and Fig. 7 charts should be used with a table of appropriate correction factors (Table 2).

Relative shaft vibration is measured by proximity probes. Two vibration severity charts are provided for relative shaft vibration. The first chart (Fig. 7) utilizes only actual relative shaft displacement and requires usage of appropriate correction factors. The second chart (Fig. 8) establishes journal severity limits with respect to bearing clearance. It should be noted that this chart does not require the application of any correction factors.

Five quality grades (similar to Blake's classification [19]) for measured vibration are defined for these charts:

(*A*) No faults (typical new equipment)
(*B*) Acceptable (correction is not necessary)
(*C*) Marginal (correction is recommended to save on future maintenance)
(*D*) Failure probable (watch closely for changes and prepare to shut down or change operating conditions to reduce vibration)
(*F*) Danger of immediate failure

Table 2 Vibration correction factors

Correction Factors	Application
K_1 = 1.0	Normal factor for unbalance, misalignment and other filtered vibration near running speed.
K_2 = 0.85	Unfiltered vibration for near running speed sources.
K_3 = 3.3	Self excited subsynchronous vibration sources on pumps, compressors, turbines, or vertical rotors.
K_4 = 1.4	Equipment rated less than 300 hp.
K_5 = 0.7	Machines with rigid rotors; *i.e.*, operate well below the first shaft critical speed.
K_6 = 0.6	Soft foundation or machines having isolators/compliant soils.
K_7 = 3.5-10	Machines with high casing-to-rotor weight ratios.
K_8 = 3.5	High frequency blade vibration sources using housing measurements.
K_9 = 0.35	High frequency gear or roller bearing sources.

NOTES
- All correction factors apply to housing vibration (Figure 6).
- Shaft vibration (Figure 7) should only use K_1, K_2, K_3, and K_4.
- Shaft vibration-to-clearance ratio (Figure 8) should not use any correction factors.
- High frequency vibration, use only K_8 or K_9.
- Housing measurements (Figure 6) should be avoided on high casing-to-rotor weight ratios machines.

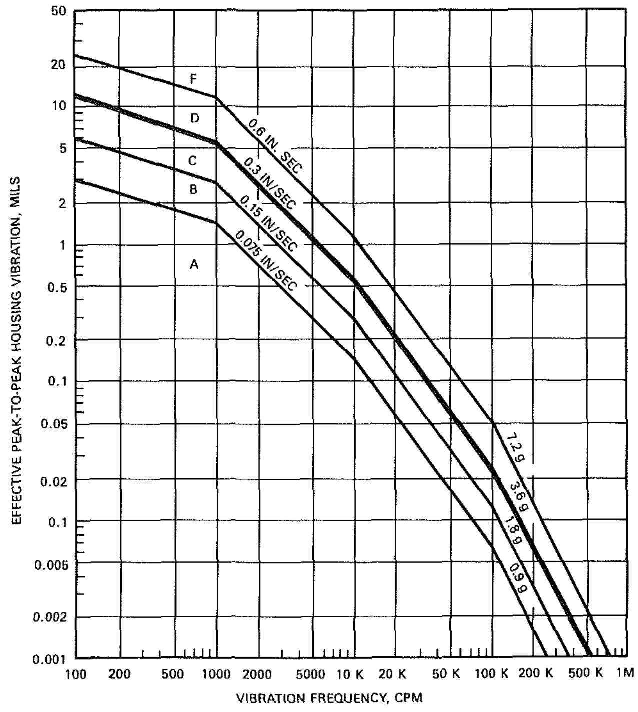

Fig. 6 Housing vibration limits

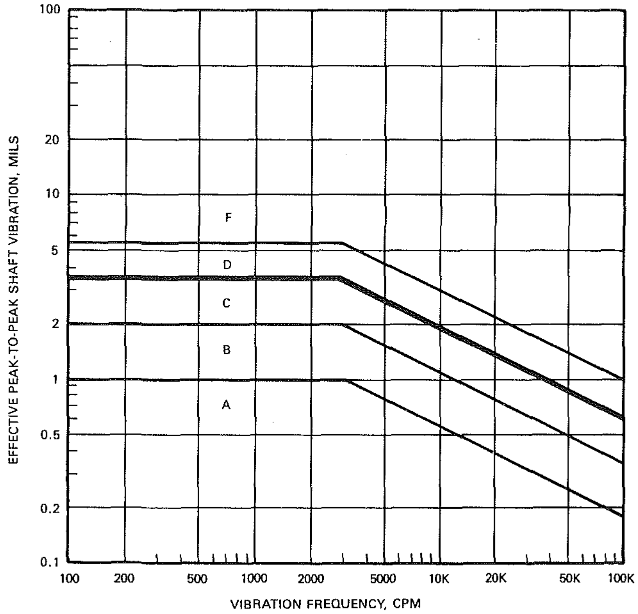

Fig. 7 Relative shaft displacement vibration limits, proximity probes

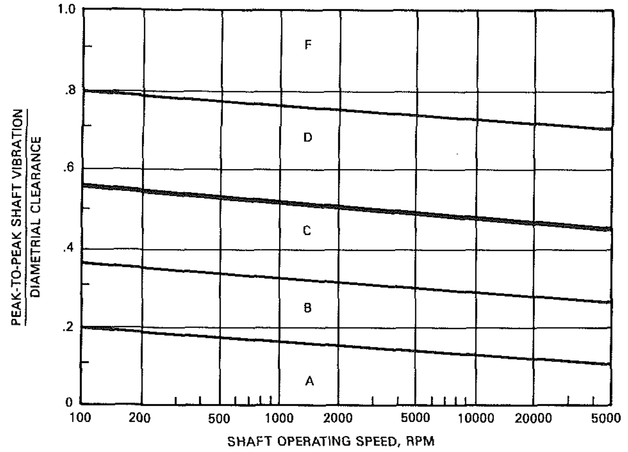

Fig. 8 Shaft vibration-to-clearance ratio vibration limits

Some important points should be emphasized to assure that these vibration charts are properly applied when machine vibration measurements are evaluated:

- Vibration limits for machine housing vibration should be considered separately from relative shaft motion.
- An effective vibration value must be obtained by multiplying the measured vibration value by one or more applicable correction factors listed in Table 2. Correction factors that apply to housing vibration include: rotor rigidity, foundation type, power rating, casing-to-rotor weight ratio, high-frequency vibration, instabilities, and unfiltered vibration. Shaft vibration correction factors differentiate running speed vibration from rotor instabilities, power rating, and unfiltered data.
- If vibration frequencies below running speed are apparent, then one must determine if the source is an instability or forced excitation. As an example, the judgment can be made based on the bearing loading parameters. If it is an instability, then the factor of 3.3 must be applied to the measured data and entered in the chart at the *running speed frequency*.
- The severity criteria based on *unfiltered vibration* readings is only applicable for excitations at running speed frequency (imbalance, etc.). In this case, an additional correction factor of 0.85 is applied and the resultant effective values entered on the charts at shaft rotational speed.
- To convert filtered vibration displacement in mils to velocity in in./s, and acceleration in *g*, the following formulas should be used:

$$V_{\text{peak}} = 5.23 \times 10^{-5} D_{p-p} \times N$$
$$A_{\text{peak}} = 1.41 \times 10^{-8} D_{p-p} \times N^2$$

where

D_{p-p} = peak-to-peak displacement measurement, mils
V_{peak} = 0 to peak, velocity measurement, in./s
A_{peak} = 0 to peak, acceleration measurement, *g*
N = frequency, cpm

The applications of these vibration severity criteria are clarified by reviewing the results obtained from field studies of actual plant equipment.

1 The first example involved a troubleshooting investigation and balancing of two boiler feed pump turbines operating at 4000-5800 rpm that had experienced bearing failure. Turbine rotor resonances were found at 2200 and 5800 cpm. For one turbine, the apparent *filtered shaft relative vibration* was about 3.5 mils near top speed, but further investigation revealed that 1.4 mils of the signal was due to shaft runout. For the remaining 2.1 mils of actual shaft vibration, a correction factor (K_1) of 1 would apply. Comparison of this effective vibration with Fig. 7 indicates the level was marginal.

On the adjacent turbine, a *filtered bearing housing vibration* of 3.0 mils was measured at maximum running speed. The structure was considered soft mounted since a turbine pedestal resonance of 3400 cpm was present below running speed. Applying a correction factor (K_6) of 0.6 yields an effective vibration of 1.8 mils. Comparison of this effective vibration with Fig. 6 indicates that failure is probable, which was consistent with experience on the turbines.

Balancing reduced vibrations to less than 1 mil on housing and shaft. Thus, after applying the appropriate correction factors, final vibrations were acceptable for both turbines.

2 Draft fan blade failures are especially dangerous, as the housing cannot restrain the massive parts that might be released from the impeller. In the second example, an investigation of the original design blade vibrations on a 900 rpm fan revealed a blade resonance of only about 6 percent above three times running speed when the fan was cold. Changes in operational temperatures every time the unit was started would cause this resonance to match with the excitation frequency at three times running speed for brief periods.

A *filtered bearing housing vibration* of 1.3 mils was measured during the resonance period. Multiplying this vibration by the appropriate correction factor (1.3×3.5) yields 4.55 mils, which is in the *F* or immediate failure region of Fig. 6 for 2700 cpm. After several days of operation and several startups, the vibrations increased suddenly and the fan was tripped off. Subsequent inspection revealed blade cracks near the welds, which indicated that blade modifications were necessary to avoid excitation of transient resonances.

3 In the third example, *bearing housing measurement* indicated 14.5 mils filtered vibration on a 900 rpm induced draft fan. As the rotor critical speed and foundation resonance were found by testing to be 1100 cpm and 720 cpm, respectively, then correction factors for rigid rotors (K_5) and soft foundations (K_6) can be applied. The effective vibration is calculated by multiplying these factors by the measured vibration ($14.6 \times 0.7 \times 0.6$) which yields 6.1 mils. Entering this effective vibration on the housing severity chart (Fig. 6) indicates the severity level is between marginal and probable failure, which is undesirable for long-term operation. Correction of the thermal bow problem and rebalancing reduced the vibration to 2 mils, or an effective vibration of 0.8 mils, which is in the no-faults region.

4 A lube oil pump motor for an auxiliary turbine had experienced repeated bearing failures prior to commissioning. An investigation of the system dynamics found that 13 mils *filtered casing vibration* occurred at the running speed frequency of 3600 cpm and the applicable correction factors, K_4 and K_5, essentially cancel each other and the effective vibration is well into the immediate danger region so the pump was shut down. Further investigation yielded that the motor shaft had excessive misalignment and the motor casing resonance existed only 1.5 percent below running speed. Once the alignment problem was fixed and the motor support was stiffened to move the case resonance, vibrations were reduced to acceptable level and no further problems were reported.

5 An investigation of a 3000 hp steam turbine was conducted to determine whether it was safe to operate the unit. Maximum vibration readings of 1.5 in./s *bearing housing motion* and 2.0 mils *shaft relative motion* were found at running speed frequency of 11,400 cpm. In evaluating the vibration severity, a correction factor of 1.0 was applied as no other factors were appropriate. It was decided to shut the turbine down immediately as the bearing housing was in the *F*, or danger, region and shaft vibrations were in the *D*, or probable failure, region. Inspection revealed some seal rub damage and excessive imbalance, which was 40 times the specified value. Further investigation indicated that high imbalance was due to the previous shaft repair which involved sleeving one of the journals causing shift of the rotor mass center. Rebalancing at high speed (flexible shaft) using multiplane balancing techniques and adding weights on both sides of the sleeve journal brought the vibration down to the no-fault region, *A*; housing vibration was reduced to 0.025 in./s and shaft vibration was reduced to less than 0.5 mils. Subsequently no problems have been reported for this turbine.

Summary

The summary of major points for applying vibration severity criteria to assess machinery condition is given below:

- First-hand experience with a variety of equipment has shown that the simplified vibration criteria used in the past are less than adequate for many actual rotating components.
- To equitably accommodate different machine designs, installations, and vibration problems, an effective vibration value must be obtained by multiplying the measured vibration value by one or more applicable correction factors listed in Table 2.
- Due to the large variation in machine designs, vibration limits are based on statistical or consensus evaluations of vibration and failure data from many operating units. As such, there are no absolute limits that will assure successful long-term operation, nor firm upper limit that will cause failure for any specific machine. As a result, some subjective judgment is always required in application of any vibration limits.
- Any vibration criteria utilized should be compared with the manufacturer's recommendations and user's experience with the particular type of machinery. Obviously, the manufacturer's vibration limits should be used if they are more stringent and have a clear basis.
- An important factor to recognize in applying vibration limits is growth of vibration amplitudes with time. All machines, regardless of their health, exhibit some form of vibration; however, on machines where a mechanical defect has deteriorated to an unacceptable level, rapid growth in vibration and consequent failure can be expected.
- In addition to vibration severity criteria, machine resonance characteristics should be controlled. If resonance margins are not specified and verified by testing, the component could be very precisely balanced or adjusted to meet the acceptance vibration limits at the time of purchase. Long-term use of such a machine, however, may result in high maintenance requirements as slight imbalances or other distortions accumulate causing vibrations to increase to unacceptable levels.
- To properly assess the severity of existent problems, it is necessary to establish the source of machine vibration. To achieve this, a transducer type should be selected to measure the vibration (machine housing or shaft) most likely to reveal the expected failure mechanism.

Acknowledgments

Some aspects of this work were sponsored by the Southern Gas Association Pipeline and Compressor Research Council, SwRI Project No. 04-7820-500. The authors wish to thank the Council for permission to publish this paper.

References

1 Baxter, R. L., and Bernhard, D. L., "Vibration Tolerances for Industry," ASME Paper No. 67-PEM-14.

2 Eshleman, R. L., "Vibration Standards," *Shock and Vibration Handbook*, C. M. Harris, and C. E. Crede, eds., 2nd ed., McGraw-Hill, Sec. 19.

3 Fox, R. L., "A Practical Guide to In-Place Balancing," *Proceedings of the Tenth Turbomachinery Symposium*, Texas A&M University, 1981, pp. 113-126.

4 Nimitz, W., and Wachel, J. C., "Vibrations in Centrifugal Compressors and Turbines," ASME Paper No. 70-Pet-25.

5 Gilstrap, M., "Shaft Versus Housing Measurements," *Orbit*, June 1983, pp. 14-16.

6 Mitchell, J. S., *Machinery Analysis and Monitoring*, PennWell Books, Tulsa, OK.

7 Fieldhouse, K. N., "Techniques for Identifying Sources of Noise and Vibration," *Sound and Vibration*, Dec. 1970, pp. 14-18.

8 Maxwell, A. S., "Vibration Monitoring, The Search for Optimum Protection," *Proceedings of the Fourth Turbomechanic Seminar*, National Research Council of Canada, Ottawa, Sept. 1976.

9 Simmons, H. R., and Lifshits, A., "Vibration Measurements for Determining Plant Component Reliability," *Proceedings of American Power Conference*, Apr. 23-25, 1985.

10 "Mechanical Vibration of Machines With Operating Speeds From 10 to 200 rev/s – Basis for Specifying Evaluation Standards," *International Standard ISO 2372*, 1st ed., 1974-11-01, Ref. No. ISO 2372-1974(E).

11 "Mechanical Vibration of Large Rotating Machines With Speed Range From 10 to 200 rev/s – Measurement and Evaluation of Vibration Severity In Situ," *International Standard ISO 3945*, 1st ed., 1977-03-15, Ref. No. ISO 3945-1977(E).

12 "Specification for Measurement of Lateral Vibration on High Speed Helical and Herringbone Gear Units," *AGMA Standard*, American Gear Manufacturers Association No. 426.01, Apr. 1974.

13 "Centrifugal Pumps for General Refinery Services," 6th ed., American Petroleum Institute, *API-610*, Jan. 1982.

14 "Centrifugal Compressors for General Refinery Service," *API-617*, 4th ed., Nov. 1979.

15 "Special Purpose Centrifugal Fans for General Refinery Services," *API-673*, 1st ed., Jan. 1982.

16 *General Guidelines for Vibration*, Dresser-Clark, Incorporated, Olean, NY, 1968.

17 *Audio-Visual Customer Training Instruction Manual*, IRD Mechanalysis.

18 Ludwig, G. A., and Erdman, O. D., "Gas Turbine Vibration Limits – A Fundamental View," ASME Paper No. 73-GTR-48.

19 Blake, M. P., "New Vibration Standards for Maintenance," *Hydrocarbon Processing and Petroleum Refinery*, Vol. 43, Jan. 1964, pp. 111-114.

Analysis and Solution of a Nonsynchronous Vibration Problem in the Last Row Turbine Blade of a Large Industrial Combustion Turbine

A. J. Scalzo
Manager, Engine Design & Development.

J. M. Allen
Advisory Engineer, Stress & Dynamics.

R. J. Antos
Manager, Engineering Field Support.

Westinghouse Electric Corporation,
Combustion Turbine Engineering Department,
Concordville, PA 19331

This paper presents the analysis and corrective action taken to solve a flow-induced nonsynchronous vibration failure problem encountered in the last-stage rotating blade in a large industrial combustion turbine. A description of the fatigue failures and of temporary operation restrictions that precluded further failure is given. The results from a strain gage telemetry test are presented which show that failure was due to high vibratory stress excursions from fundamental mode vibration, which resulted from broad band buffeting excitations and very low aerodynamic damping at high levels of power and mass flow. From these data, design criteria were developed for designing a retrofittable blade that removed the operating restrictions. Telemetry test results (from the same turbine), which verified the new design, are also briefly presented and discussed. This investigation shows that the design of future high-performance exhaust end combustion turbine blading must take into account nonsynchronous excitation (buffeting) and the aeroelastic interaction between blade structure and flow, in addition to the synchronous excitations traditionally allowed for in the design process.

Introduction

Combustion turbine blade failures due to high cycle fatigue (HCF) have generally been attributable to vibratory resonance driven by external forces fluctuating at engine order (EO) frequencies (multiples of running speed). Thus, for constant-speed power generation turbines, a standard design approach has evolved requiring that blade fundamental mode resonant frequencies should be tuned away from all EO frequencies below about eight times running speed and that all resonant frequencies should be tuned away from identifiable sources of EO excitation, such as the number of stationary vanes, number of vane segments, number of combustor baskets, etc. To allow for EO vibrations not limited by the tuning criteria, an allowable magnification factor (ratio of fatigue endurance strength to steady gas bending stress) is required, the magnitude of which depends on experience.

Modern electric power generation combustion turbines, such as the Westinghouse model W501D5 – a 3600 rpm production unit in commercial service with a base load rating of 104 MW at ISO (International Standards Organization) conditions [1, 2] – have been designed to maximize specific power and to minimize heat rate. A key element in achieving optimum performance is the design of the last-stage rotating blade. In this regard, the most desirable configuration is a wrought, free-standing blade, inasmuch as annulus area per unit of steady stress (from the centrifugal forces on the blade) is maximized, and hence leaving velocities and losses are minimized, while a forging is preferrable to a casting owing to its superior fatigue strength. With regard to vibratory response and strength, however, the conventional design practice proved to be unsatisfactory for the W501D5 free standing last stage (fourth stage) turbine blade. Fatigue failures occurred from a flow-induced nonsynchronous (non-EO) resonant vibration, which prompted a temporary limit on power output and mass flow followed by the retrofitting of a redesigned blade capable of operating at maximum power conditions.

In this paper, the failure experience with this blade is reviewed, and the corrective action program that was instituted to understand and solve the problem is described.

Failure Analysis

In 1981, the first two W501D5 units began operation at the Comision Federal de Electricidad combined cycle plant in Tula, Mexico. These units have operated since that time with the original last-stage turbine blade design, and no fatigue cracking has occurred. However, subsequent units that began operation in the U.S. in 1982 suffered fatigue cracking, during 1983, in the last-stage blades on six occasions. The Mexico

---

Contributed by the Gas Turbine Division of The American Society of Mechanical Engineers and presented at the 31st International Gas Turbine Conference and Exhibit, Düsseldorf, Federal Republic of Germany, June 8–12, 1986. Manuscript received at ASME Headquarters February 14, 1986. Paper No. 86-GT-230.

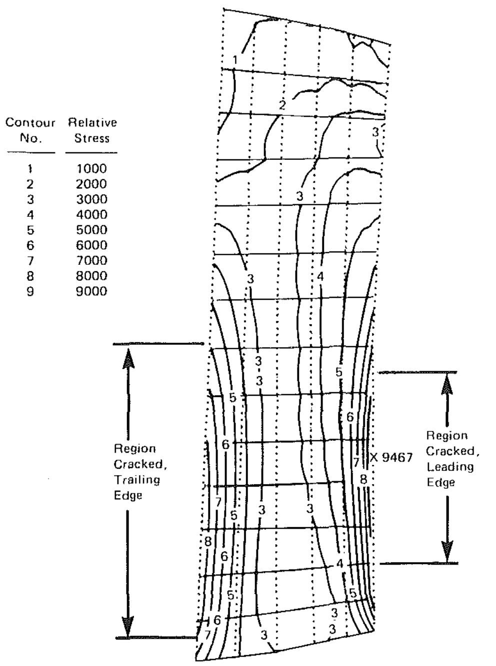

Fig. 1 Regions of fatigue cracking and fundamental mode effective stress pattern on pressure surface of blade

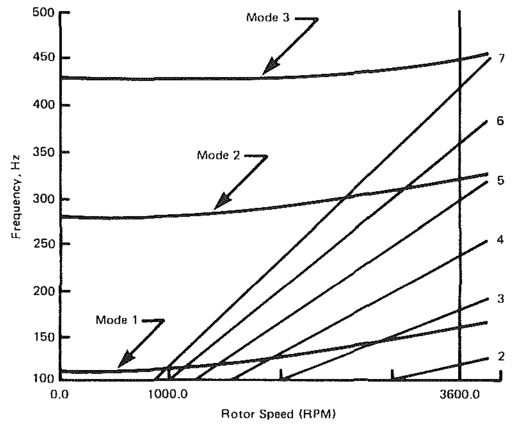

Fig. 2 Campbell diagram for the original blade

units are located at an elevation of 6922 ft (2110 m), where air density is 22 percent lower than at sea level, and where ambient temperatures rarely fall below 50°F (10°C). The domestic units that experienced blade failures were all located at essentially sea level elevation. In addition, the failures occurred while operating at ambient temperatures well below 50°F (10°C), which has the effect of further increasing inlet air density and hence mass flow, power level, and blade loading compared to the Mexico experience.

The failures were characterized by multiple fatigue cracking on the leading and trailing edges as indicated in Fig. 1. Cracking was observed in 20–40 percent of the blade row. The fact that so many blades were found with fatigue cracks indicated that many blades were vibrating at a similar stress level, and the fact that so many blades were found cracked without one blade separating, on three of the six occasions, suggested that the vibration was transitory, as opposed to a constant amplitude of vibratory stress that would be expected from an EO type of forced vibration.

The vibratory stress pattern, obtained by finite element analysis, for the blade resonating in its fundamental mode is shown in Fig. 1. Note that the regions of maximum vibratory stress are on the leading and trailing edges, that they are approximately equal on both edges, and that the regions of fatigue cracking correspond to the regions of maximum stress. The finite element analysis also showed that vibratory stress patterns for higher modes did not resemble the cracking pattern. Thus the close similarity between the fatigue crack pattern and the fundamental mode stress pattern clearly established that this was the mode of failure.

Figure 2 shows the Campbell diagram for the blade developed from finite element analysis and rotating rig tests. It can be seen that the first three modes are well tuned and that the fundamental mode lies midway between the second and third EO at design speed, 3600 rpm. Thus, it was concluded that the resonant vibration was nonsynchronous.

Telemetry Test

In order to gain more insight into the nature of the nonsynchronous vibration phenomenon that caused these failures, a telemetry test was conducted on a newly installed unit at the Texas Division of the Dow Chemical Co. USA in Freeport, Texas. The decision to employ the telemetry approach for transmitting the vibratory strain gage signals to the recording equipment was prompted by the need to instrument blades without having to disassemble the rotor and by many years of experience within the corporation utilizing telemetry in field testing steam turbine blading.

Instrumentation. The difficulty in using telemetry in combustion turbines is that the transmitters, which must be mounted on the rotor (in this case, on the downstream side of the last-stage turbine disk), cannot withstand temperatures above about 300°F (150°C). Therefore, special provisions had to be made to cool the transmitter, as well as the antennae. To

Nomenclature

C = blade chord length
F = function of unsteady aerodynamic loading coefficients and vibration mode shape
$\bar{K}$ = generalized stiffness of blade when vibrating at a resonant frequency
N = number of increments
$\bar{q}$ = Cartesian displacement component, at a reference nodal point in blade model, used to normalize the free vibration modal displacements of the blade
V = exit flow velocity relative to the blade
$\bar{W}$ = work input per cycle of vibration from buffeting forces when the reference vibratory amplitude is $\bar{q}$
δ_a = aerodynamic damping logarithmic decrement
δ_m = mechanical damping logarithmic decrement
Δh = increment of blade height
λ = reduced frequency parameter
π = 3.14159
σ = actual stress amplitude in resonating blade
$\bar{\sigma}$ = relative stress amplitude in resonating blade from a free vibration modal analysis in which the reference displacement is $\bar{q}$
φ = mass density of the gas
ω = natural circular frequency of the blade

Subscripts

a = aerodynamic
i = ith nodal point in the blade model
m = mechanical
n = nth increment in blade height

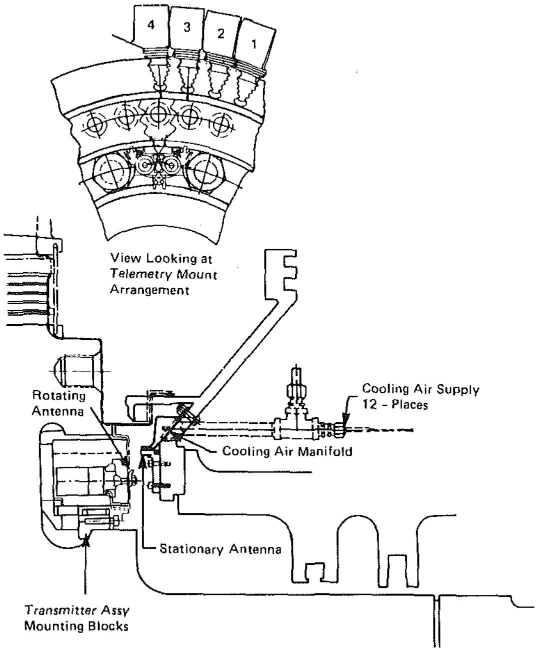

Fig. 3 General telemetering instrumentation hardware assembly

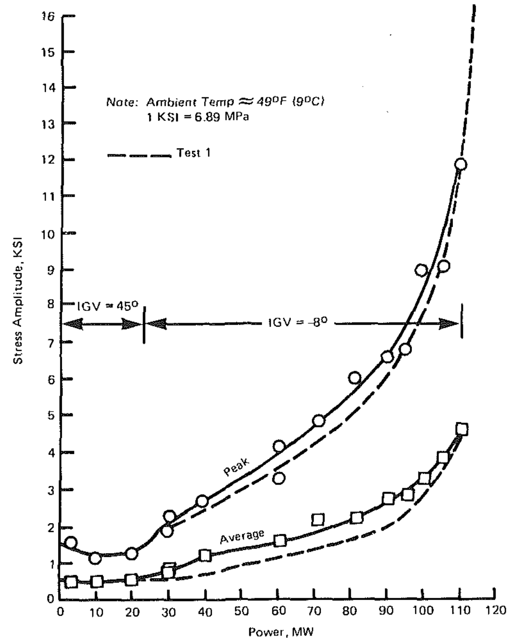

Fig. 5 Fundamental mode stress response versus power for blade 29 during test 2

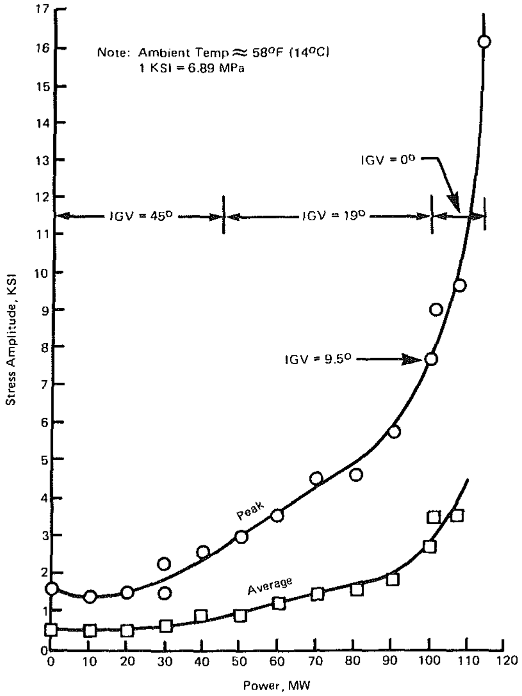

Fig. 4 Fundamental mode stress response versus power for blade 29 during test 1

accomplish this, a transmitter mounting block with integral cooling fins was designed, together with a cooling air manifold to provide externally supplied compressed air to maintain transmitters and antennae below 300°F (150°C), as shown in Fig. 3. This system was designed, manufactured, and installed in approximately three months. Details on the system are described in [3].

Four blades were instrumented in two pairs located at 180 deg apart on the rotor. Strain gages were located 3 in. (76 mm) above the base of the blade on the pressure surface approximately 0.25 in. (6 mm) from the trailing edge, so that near-maximum vibratory stresses could be monitored when the blades were vibrating in the fundamental mode.

Test Results. Two tests, designated as test 1 and test 2 herein, were conducted on successive days on the Dow Freeport machine in which strain gage data were recorded and analyzed from zero to peak power operating conditions. The results are summarized in Figs. 4–11. Turbine operating conditions during the testing are indicated in Fig. 4 (test 1) and Fig. 5 (test 2).

Figures 4 and 5 summarize the on-line spectral response at the fundamental mode frequency for blade number 29 from zero to maximum generator load. Two curves are shown: The upper curve is the peak amplitude response that occurred during a sampling period (on the order of one minute) while the lower curve is the average amplitude response over a similar period of time. The peak amplitude was about 2.5 times the average, when the compressor inlet guide vanes (IGV's) were open to the maximum flow position (zero to −8 deg), and about three times the average when the IGV's were closed to 19 deg. The response of the adjacent blade (number 28) was essentially the same as for blade 29. However, the response of the other pair, blade numbers 3 and 4, was generally less than half as much, regardless of power output.

In the 30 to 90 MW power output range, blade response was slightly greater in test 2, as shown in Fig. 5. This is attributed to the higher blade loadings associated with the significantly higher flow in test 2 in this power range. The higher flows in test 2 were a result of the different IGV setting used in this power range as compared to test 1. Above 100 MW, blade response was similar in both tests, as was blade loading. Maximum blade response was measured in test 1 at 114 MW where a maximum spectral stress of approximately 17 ksi (117 MPa) was recorded (Fig. 4).

Although not systematically studied during this or subsequent telemetry tests, it was noticed that maximum stress always seemed to occur immediately after a load change and that it diminished to a significantly lower value after several minutes at constant operating conditions. It was also observed that the magnitude of the stress peak increased with the rate of load change. The maximum stress measured at 114 MW, in test 1, occurred after a faster rate of load change than otherwise employed during the testing. Thus the nonsynchronous vibratory phenomenon observed appears to reach a transitory peak immediately after a change in load occurs, and the

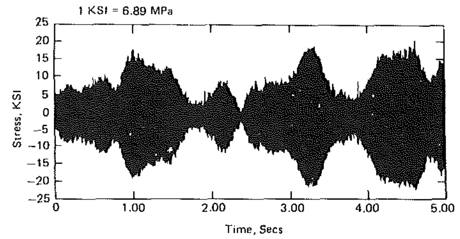

Fig. 6 Envelope of stress peaks for blade 29 over a 5 s period at 114 MW, test 1

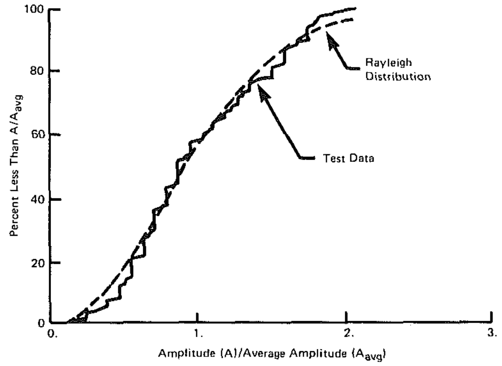

Fig. 7 Cumulative distribution of peaks (Fig. 6)

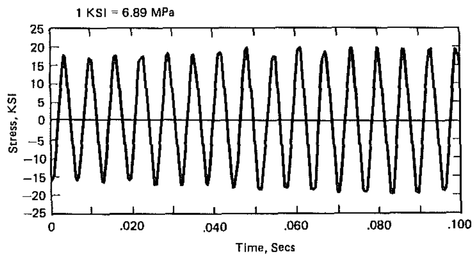

Fig. 8 Stress waveform over a 0.1 s period for blade 29 at maximum envelope height (Fig. 6), test 1

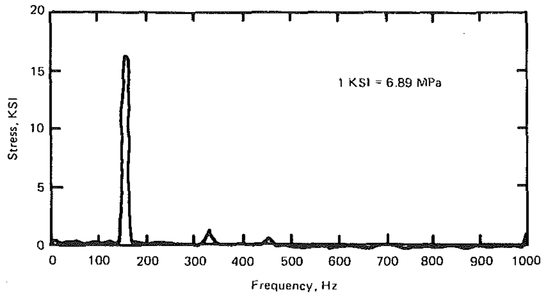

Fig. 9 Frequency spectrum (2.5 Hz resolution) for blade 29 at 114 MW, test 1

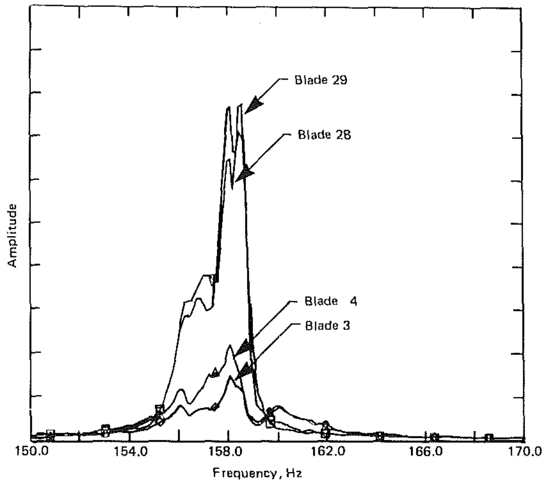

Fig. 10 Zoom spectrum analysis (0.125 Hz resolution) for the four instrumented blades at 114 MW, test 1

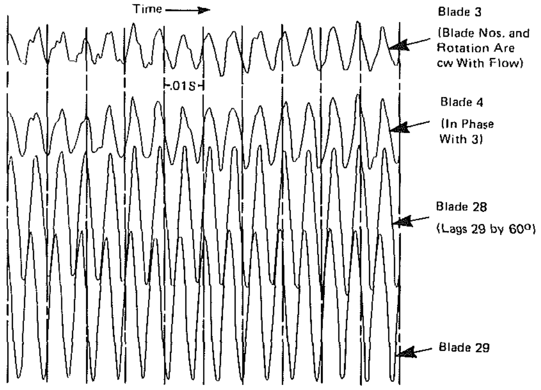

Fig. 11 Wave forms and phasing between the four instrumented blades during maximum response at 114 MW in test 1

magnitude of the peak appears to increase with the rate of load change.

The envelope of stress peaks, obtained during the period of maximum response at 114 MW, in test 1, is shown in Fig. 6 over a 5.0 s period. It can be seen that the amplitude of vibration is not constant but fluctuates in a manner similar to the response of a lightly damped single degree of freedom oscillator to a broad band random excitation. A statistical analysis of the envelope indicates that its cumulative distribution is essentially a Rayleigh distribution (Fig. 7), which is characteristic of this type of random vibration [4].

Figure 8 is a plot of the stress wave form over a 0.1 s period at maximum envelope height. It can easily be deduced from Fig. 8 that the blade is vibrating at 158 Hz, its fundamental natural frequency, and that the maximum stress is about 20 ksi (138 MPa). This is over 80 percent of the endurance strength of the blade material and about 20 percent higher than the peak amplitude obtained from the on-line spectral analysis (Figs. 4 and 9). Figure 9 is a frequency spectrum from 0 to 1000 Hz and also shows that the blade was only vibrating at frequencies at or very near its fundamental natural frequency over this range of frequencies.

Figure 10 shows the results of a zoom analysis in which the spectral analysis was performed in 0.125 Hz increments, compared to the 2.5 Hz increments used in the on-line spectral analysis (Fig. 9). Because a 0.125 Hz frequency resolution requires an 8 s time sample, greater than the irregular time sample shown in Fig. 6, such an analysis is of little value as far as amplitude resolution is concerned. What it does show, however, is that the blades respond over a band of frequencies around the natural frequency. In this case, the band is about 3.0 Hz wide, which accounts for the modulation in vibratory amplitude exhibited in Fig. 6.

It is interesting to note in Fig. 10 that maximum response of all blades occurs at about the same frequency, 158 Hz. This suggests that the blades were not only responding to a broad band random excitation but also that aerodynamic coupling between blades was significant. It is well known that when a row of blades becomes unstable (self-excited) all blades vibrate at the same frequency at a definite interblade phase angle between blades [5]. Even if the row is not unstable, aerodynamic coupling is still pronounced as instability conditions are approached, and hence a strong correlation between high response at nonsynchronous frequencies and interblade phase angle would also be expected in such circumstances.

The interblade phase relationship between the four blades during a 0.1 s period of maximum response is shown in Fig. 11. Note that there was a very definite phase shift between blades 28 and 29, the high-response pair of blades. Blade 28 lags blade 29 by approximately 60 deg, which indicates that the vibration wave was backward traveling relative to the direction of rotation. Blades 3 and 4 were much less responsive and show little or no phase shift. The striking difference in behavior in the two zones on the rotor is believed to be due to the effects of mistuning [6]. An order tracking frequency analysis of the four blades during startup revealed that blades 3 and 4 had natural frequencies about 1.8 Hz apart, while the natural frequency difference between blades 28 and 29 was only about 0.1 Hz. In summary, Figs. 10 and 11 suggest that the phenomenon observed is dependent on the aeroelastic interaction between the blades and the flow, as well as on the random excitation (buffeting) associated with the turbine through flow.

Interpretation of Data

The vibratory behavior described in the previous section can be more fully explained by reference to the well-known approximate relationship [7] between amplitude of stress, excitation, and damping for lightly damped systems at resonance, i.e.,

$$\sigma_i = \bar{W}\bar{\sigma}_i / \bar{K}\bar{q}^2 (\delta_a + \delta_m) \tag{1}$$

In equation (1), σ_i is the actual vibratory stress amplitude at nodal point i in the blade model, $\bar{\sigma}_i$ is the relative vibratory stress amplitude at the same nodal point from a free vibration modal analysis of the blade [when the reference (normalizing) displacement is equal to $\bar{q}$], $\bar{W}$ is the maximum work input per cycle of vibration from the buffeting forces when the reference vibratory amplitude is $\bar{q}$, $\bar{K}$ is the generalized stiffness (twice the maximum kinetic energy in a cycle of blade vibration divided by $\bar{q}$ squared), δ_a is the aerodynamic damping logarithmic decrement, and δ_m is the mechanical damping logarithmic decrement.

The aerodynamic damping δ_a is defined as the ratio of work done per cycle of vibration by aerodynamic forces induced on the blade from its motion divided by twice the strain energy [8]. The resulting equation is of the form

$$\delta_a = (-2\pi^2/\bar{K}) \sum_{n=1}^{N} \left(\frac{\varphi V^2}{2}\right)_n (\Delta h)_n F_n \tag{2}$$

where $(\varphi V^2/2)$ is the dynamic head, V is the exit flow velocity relative to the blade, Δh is an increment of blade height, N is the number of increments, and F is a function of the unsteady aerodynamic loading coefficients and vibration mode shape of the blade. F is the key variable in equation (2); if it is negative the blade is aeroelastically stable, but if it is positive and the resulting negative damping equals or exceeds the mechanical damping δ_m the blade can flutter, i.e., vibrate at unbounded stress levels without external stimuli. For a given row of free standing blades vibrating in the fundamental mode, which is predominantly a flapwise bending motion, the key variables affecting F are the interblade phase angle between vibrating blades, the aeroelastic parameter reduced frequency, the steady lift on the blades, and the natural frequency distribution of the blades, i.e., the degree of mistuning [5, 6, 9].

Returning to equation (1), it can be seen that if the aerodynamic damping becomes negative and begins to approach the mechanical damping in absolute magnitude, stresses can become extremely high – well before the blade becomes self-excited – because very little external energy input $\bar{W}$ is required to sustain the vibration. The test data show that there is more than enough buffeting excitation in the through flow of a gas turbine to satisfy this requirement, especially immediately after load changes take place at a relatively fast rate.

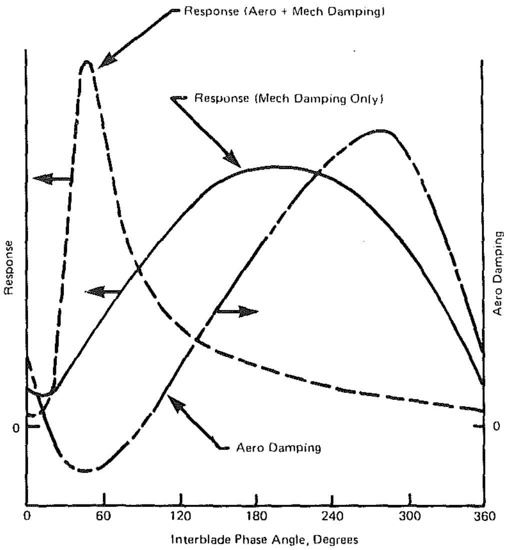

Fig. 12 Effect of interblade phase angle on aerodynamic damping and on response of an idealized blade model

The effect that interblade phase angle can have on aerodynamic damping, and in turn response, is illustrated in Fig. 12. Figure 12 was obtained using a flat plate representation of a blade row vibrating in a coupled bending-torsion mode. Unsteady aerodynamic load coefficients due to a 0.1 percent gust excitation (unsteady flow velocity divided by steady flow velocity) and from the torsional and bending motions of the blades were computed using the method developed in [10] for interblade phase angles varying from 0 to 360 deg. Mechanical damping assumed was 1.5 percent (log decrement). Although such a simplified aeroelastic model cannot predict actual blade behavior, it does demonstrate the physics of the problem. Figure 12 shows how a blade might respond as a function of interblade phase angle when aerodynamic damping is considered, and when it is not. Note that if the aerodynamic damping is neglected, so that total damping is constant and equal to the mechanical damping, maximum response occurs at interblade phase angles in the vicinity of 180 deg, due to the fact that the unsteady excitation that results from a 0.1 percent gust is maximum at these interblade phase angles. However, when aerodynamic damping is considered the picture changes dramatically. Because the variation in aerodynamic damping with interblade phase angle is roughly sinusoidal (Fig. 12), becoming minimum (as well as negative) around 50 deg and maximum (and decidedly positive) at approximately 270 deg, maximum response occurs around 50 deg. Moreover, the response is narrow banded with respect to interblade phase angle, compared to the response for constant damping. The behavior demonstrated by this model suggests why such a definite relationship between interblade phase angle and maximum response was observed on the highly responding pair of blades, numbers 28 and 29 (Fig. 11).

In this paper, the reduced frequency parameter

$$\lambda = \omega C / V \tag{3}$$

is defined as in [5] for turbine airfoils, i.e., ω is the natural circular frequency of the blade, C is the full chord length, and V is the exit flow velocity relative to the blade. The response of blade 29 shown in Figs. 4 and 5 is replotted in Fig. 13 against the reduced frequency of the tip streamline section of the blade divided by the apparent critical value. While the effect of reduced frequency on response per se is not represented by

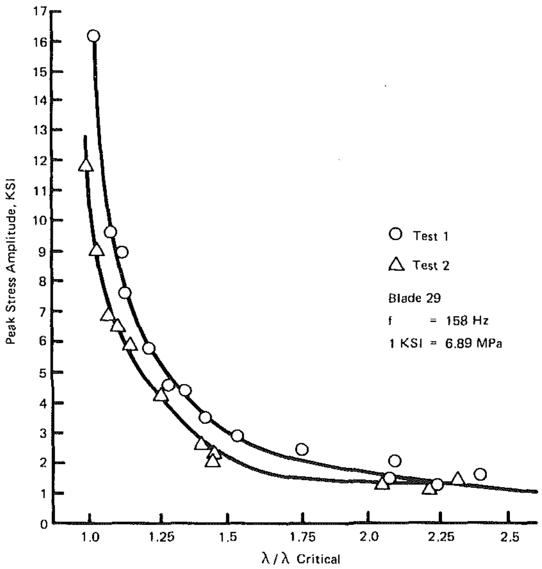

Fig. 13 Response versus reduced frequency ratio

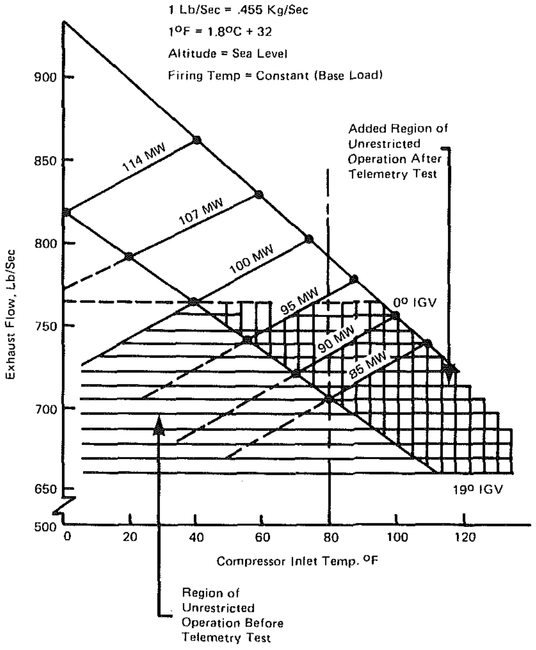

Fig. 14 Relationship between ambient temperature, exhaust flow, and power for various inlet guide vane (IGV) settings, and restricted regions of turbine operation for the original blade

the curves shown in Fig. 13, since the change in reduced frequency was accomplished by varying power output and hence the steady and buffeting loads on the blade changed as well, it is apparent that a critical value, below which the blade becomes unstable, was approached in the telemetry test. This was also demonstrated in a dynamic cascade facility described in [11], in which aerodynamic damping was measured as a function of reduced frequency and interblade phase angle at constant lift and flow angles.

With regard to the effect of mistuning, it was shown in Fig. 11 that blades 3 and 4 were much less responsive than blades 28 and 29 and that different interblade phase angles existed between blades 3 and 4 and between blades 28 and 29. It has been shown that mistuning can account for such behavior [6]. Since blades 3 and 4 were much less in tune than blades 28 and 29, as discussed earlier, it is concluded that mistuning is the reason for the difference in response between these two pairs of blades.

Table 1 Effect of IGV setting on blade loading and flow at 40°F (4°C) ambient temperature

IGV setting, deg	Elevation, ft*	Flow, lb/s**	Power, MW	Blade loading, kW
0	6922	668	88	47,500
0	0	860	113	62,800
19	0	763	100	47,500

*1 ft = 0.305 m
**1 lb/s = 0.455 kg/s

Corrective Action

In light of the operating experience associated with these failures, operating restrictions were defined and implemented to preclude further fatigue failure. These restrictions were relaxed somewhat after the telemetry test data were analyzed. Also, after the telemetry test, design criteria were formulated for the design of a new blade that could operate at maximum power conditions without suffering fatigue failure.

Derated Operation

Before Telemetry Test. As stated earlier, all of the failures occurred at relatively low ambients, well below 50°F (10°C); none of the failures occurred during the months of May through November, even though no operating restrictions were imposed. Also, the more lightly loaded units in Tula, Mexico, where mass flow is 22 percent less than at sea level, had operated unrestricted for two full years without any sign of fatigue failure. Thus, it appeared that further blade failures could be prevented by selecting a mode of operation that would produce last row blade loadings less than those experienced during trouble-free operation.

Figure 14 displays the effect of compressor inlet temperature (ambient temperature) on exhaust flow and power for various IGV settings. The effect of IGV setting on the fourth stage rotor blade loading is shown in Table 1.

Based on the information in Table 1 and the aforementioned operating experience, it was decided that a conservative operating mode would be to close the IGV's to limit mass flow and power output to approximate the successful summer operation and the operation at Mexico. The criterion selected was to limit power output to a maximum of 100 MW and to vary the IGV setting between 19 and 37 deg as ambient temperature changed. This maintained power and mass flow below that which occurs on an 80°F day at sea level with the IGV open (0 deg) and limited blade loading to 47,500 kW, the maximum loading experienced by the blades at full power in Mexico. The temporary mode of operation thus defined is shown in Fig. 14.

This restricted mode of operation was implemented and was completely successful in preventing any recurrence of the fatigue problem. This mode of operation was in effect during the three-month period preceding the telemetry test.

After Telemetry Test. After the telemetry test was completed, it became apparent that the initial restrictions could be relaxed somewhat. Based on Fig. 13, it was decided that the blade could operate safely if the reduced frequency to critical reduced frequency ratio was not less than 1.12. This permitted the added unrestricted region of operation shown in Fig. 14 (cross-hatched region).

This modified restricted mode of operation was implemented and has also been completely successful in preventing any recurrence of the fatigue problem during the period between the telemetry test and installation of the redesigned blades in the various units in service.

Blade Redesign and Verification. Various schemes have been employed to reduce the resonance response of turbine

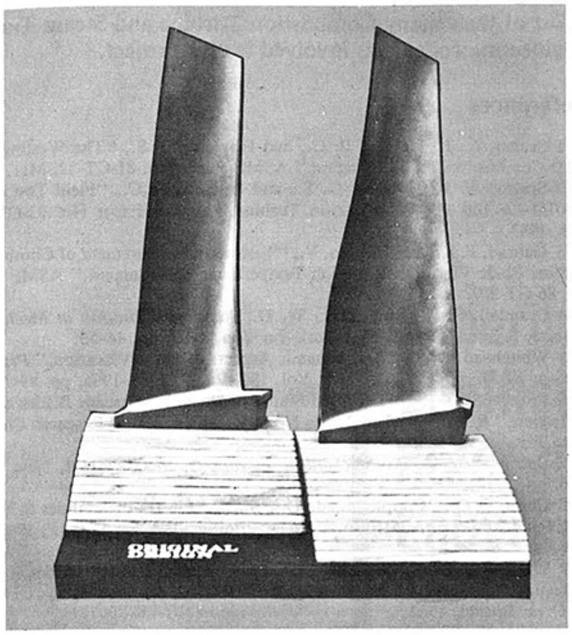

Fig. 15 Original and redesigned blades

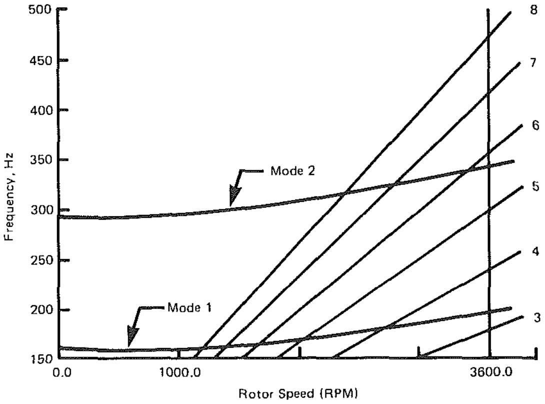

Fig. 16 Campbell diagram for the redesigned blade

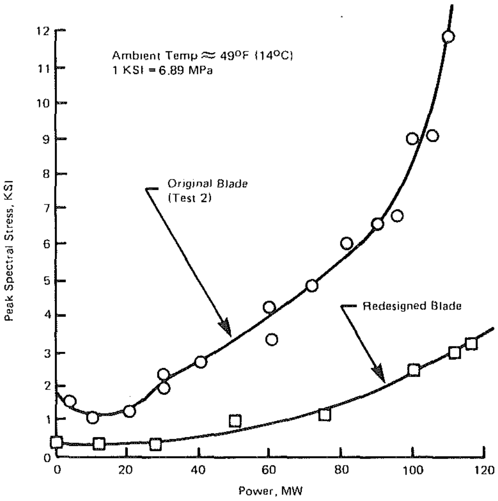

Fig. 17 Comparison of maximum first mode response measured in telemetry tests of the original and redesigned blades under similar operating conditions

blading that has experienced vibration failure in service. These include zig-zag tip shrouds, lacing wires, and loose pin dampers fitted in a zig-zag pattern between blades. While all of these approaches have merit, they also have drawbacks. Lacing wires and pin dampers require drilling holes through the blades, which weakens the blade cross section and introduces undesirable stress risers. They also introduce losses that reduce performance of the turbine. All three schemes are subject to fretting wear, and possibly fretting fatigue, and therefore require a degree of maintenance inconsistent with continuous duty industrial combustion turbine maintenance requirements. These approaches also add mass to the blade, especially the zig-zag shroud, thereby increasing CF (centrifugal force) stress and reducing creep life. Therefore, as stated at the outset of this paper, the most desirable solution to the problem from the point of view of optimum performance and reliability was a redesigned, free-standing, forged blade, providing, of course, such a blade could be designed and manufactured to meet design requirements.

In view of Fig. 13, it was decided that a 25 percent increase in the reduced frequency parameter results in an aerodynamically stable blade and an acceptably low level of vibratory stress. This could be accomplished by simply increasing the natural frequency of the blade by 25 percent. Moreover, the blade would still be tuned from EO excitation because the fundamental mode EO would increase from 2.6 to 3.3, and the blade vibratory stress would be substantially reduced, even if there were no benefit from increasing reduced frequency, due to the increased stiffness that results from adding material in the region where fundamental mode stress is maximum.

With these objectives in mind, a redesign effort was initiated. It was found that these objectives could be met and that the redesigned blade could be retrofitted in the units already in the field. A photograph of the redesigned blade next to the original blade is shown in Fig. 15. The substantial increase in stiffness in the lower half of the new blade can readily be seen in the photograph. A Campbell diagram for the redesigned blade is shown in Fig. 16.

The new blade was designed, manufactured, and telemetry tested in the same unit in less than one year after the first telemetry test. Sixteen of the 51 blades in the row were strain gaged for this test. The 16 instrumented blades were located in two groups 180 deg apart. Utilizing bench frequency test results for all 51 blades, one group was selected with the minimum possible mistuning and the other group was selected to maximize mistuning. The tuned group had a frequency spread of only 0.1 Hz, while the mistuned group had a spread of 2.6 Hz. In the latter group, the blades were generally arranged in an alternate high-low frequency pattern in an attempt to maximize the effect of mistuning. The response of the tuned group was, on the whole, somewhat higher than the mistuned group but in both cases the response was comparatively much lower.

The essential result from the verification test is summarized in Fig. 17, where maximum response of the new blade is compared to that of the original. It can be seen that maximum stress at 110 MW in the new blade is only 25 percent of that in the original design. It is estimated that approximately 50 percent of this reduction is due to the increase in blade stiffness, while the other 50 percent is attributable to increased aerodynamic damping. This estimate is based on the assumption that the excitation (power spectral density) at base load was the same in both tests, which is reasonable since the testing was conducted in the same turbine under nearly identical operating conditions, and also on the assumption that the positive amplitude distribution of the excitation is the same as the steady gas load distribution. With these assumptions, the $\bar{W}\bar{\sigma}/\bar{K}$ term in equation (1) can be evaluated, which gives an indication of how much stress reduction would be expected just from increasing the stiffness of the blade. This turned out to be approximately 50 percent. The other 50 percent, then, can be attributed to a substantial increase in minimum aerodynamic damping, which resulted from the 25 percent increase in reduced frequency for the redesigned blade.

Summary and Conclusions

A flow-induced nonsynchronous vibration, which caused fatigue failures in previous units, was measured in a telemetry field test of the last-stage turbine blade in a large industrial combustion turbine. The interpretation of the test data, the definition of temporary restricted modes of operation that prevented additional failures, blade redesign criteria, and telemetry test results which verified the redesign have been described.

This experience demonstrates that the design of future high-performance exhaust end combustion turbine blading must take into account the limitations imposed by nonsynchronous excitation (buffeting) and the aeroelastic interaction between the blade structure and flow, in addition to those imposed by the synchronous (EO) excitations allowed for in the traditional design process.

Acknowledgments

The authors gratefully acknowledge the support of the Dow Chemical Co. and, in particular, the cooperation and invaluable assistance of Mr. C. J. Barras and his staff at the Texas Division. The authors also acknowledge the dedicated effort of their many Combustion Turbine and Steam Turbine Engineering colleagues involved in this project.

References

1 Scalzo, A. J., Holden, P. C., and Howard, G. S., "The Westinghouse 501D Combustion Turbine Engine," ASME Paper No. 81-GT-32, Mar. 1981.

2 Scalzo, A. J., Howard, G. S., and Holden, P. C., "Field Test of the W501D-A 100 MW Combustion Turbine," ASME Paper No. 83-GT-174, Mar. 1983.

3 Gabriel, F. K., and Donato, V., "Telemetry Measurement of Combustion Turbine Blade Vibration in a High Temperature Environment," ASME Paper No. 86-GT-207.

4 Crandall, S. H., and Mark, W. D., *Random Vibration in Mechanical Systems*, Academic Press, New York-London, 1963, pp. 44-53.

5 Whitehead, D. S., "Aerodynamic Aspects of Blade Vibration," *Proc. Institution of Mechanical Engineers*, Vol. 180, Pt. 31, 1965-1966, pp. 49-60.

6 Whitehead, D. S., "Torsional Flutter of Unstalled Cascade Blades at Zero Deflection," Reports & Memoranda No. 3429, Aeronautical Research Council, Great Britain, 1964.

7 Den Hartog, J. P., *Mechanical Vibrations*, McGraw-Hill, New York, 1956, pp. 133-134.

8 Carta, F. O., "Coupled Blade-Disc-Shroud Flutter Instabilities in Turbojet Engine Rotors," ASME JOURNAL OF ENGINEERING FOR POWER, 1967, pp. 419-426.

9 Whitehead, D. S., "Bending Flutter of Unstalled Cascade Blades at Finite Deflection," Reports and Memoranda No. 3386, Aeronautical Research Council, Great Britain, 1962.

10 Smith, S. N., "Discrete Frequency Sound Generation in Axial Flow Turbine Machines," Reports and Memoranda No. 3709, Aeronautical Research Council, Great Britain, 1973.

11 Kovats, Z., "Dynamic Cascade Facility and Methods for Investigating Flow-Excited Vibration and Aerodynamic Damping of Model Low Pressure Blade Groups," ASME Paper No. 79-WA/GT-6.

D. W. Childs
Professor.

J. K. Scharrer
Research Assistant.

Mechanical Engineering Department,
Turbomachinery Laboratories,
Texas A&M University,
College Station, TX 77843

Experimental Rotordynamic Coefficient Results for Teeth-on-Rotor and Teeth-on-Stator Labyrinth Gas Seals

An experimental test facility is used to measure the rotordynamic coefficients of teeth-on-rotor and teeth-on-stator labyrinth gas seals. Direct damping coefficients are presented for these seals for the first time. The results are presented for the two seal configurations at identical operating conditions, and show that, in a rotordynamic sense, the teeth-on-stator seal is more stable than the teeth-on-rotor seal, for inlet tangential velocity in the direction of rotation.

Introduction

The design, development, and operation of the test apparatus and facility which have been developed to measure the leakage and rotordynamic coefficients of annular gas seals has been described by Childs et al. [1]. This apparatus has been designed and used to measure rotordynamic coefficients of plain annular seals, plain seals with honeycomb stators, and labyrinth seals. Nelson et al. [2] presented the results for plain annular seals with constant-clearance and convergent-tapered geometries. This paper presents the results for "see-through" labyrinth seals, as shown in Fig. 1, with teeth on the rotor and teeth on the stator.

As described in [1], the rotordynamic coefficients for a gas seal are defined by the following linearized force-displacement model

$$-\begin{Bmatrix}F_x\\ F_y\end{Bmatrix} = \begin{bmatrix}K_{xx} & K_{xy}\\ K_{yx} & K_{yy}\end{bmatrix}\begin{Bmatrix}X\\ Y\end{Bmatrix} + \begin{bmatrix}C_{xx} & C_{xy}\\ C_{yx} & C_{yy}\end{bmatrix}\begin{Bmatrix}\dot{X}\\ \dot{Y}\end{Bmatrix} \qquad (1)$$

where (X, Y) define the motion of the seal's rotor relative to its stator, (F_x, F_y) are the components of the reaction force acting on the rotor, and $(K_{xx}, K_{yy}, K_{xy}, K_{yx})$ and $(C_{xx}, C_{yy}, C_{xy}, C_{yx})$ are the stiffness and damping coefficients, respectively. Equation (1) applies for small motion of the rotor about an arbitrary eccentric position. For small motion about a centered position, the following simpler model applies

$$-\begin{Bmatrix}F_x\\ F_y\end{Bmatrix} = \begin{bmatrix}K & k\\ -k & K\end{bmatrix}\begin{Bmatrix}X\\ Y\end{Bmatrix} + \begin{bmatrix}C & c\\ -c & C\end{bmatrix}\begin{Bmatrix}\dot{X}\\ \dot{Y}\end{Bmatrix} \qquad (2)$$

Although the test apparatus has the capability of separately identifying the eccentric-position rotordynamic coefficients of equation (1), the results presented here are for the centered-position case only.

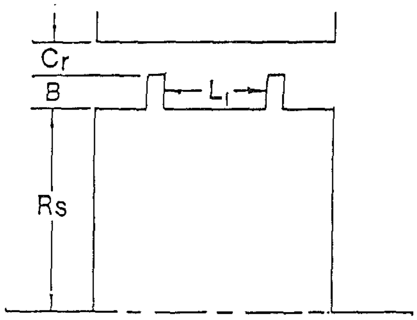

Fig. 1 A typical cavity

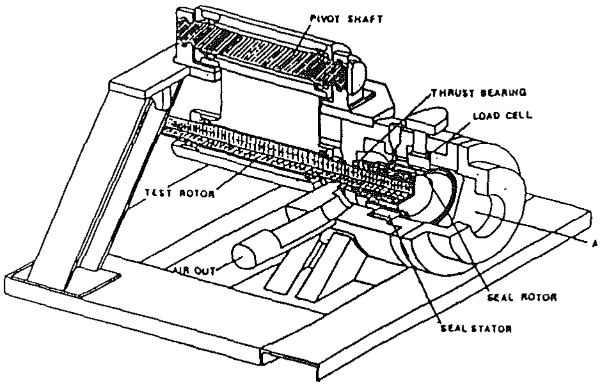

Fig. 2 Test apparatus

Previous Experimental Programs

A limited amount of experimental data have been published to date on the determination of the stiffness coefficients for labyrinth gas seals. However, no data have been published concerning the damping coefficients of labyrinth gas seals. The first published results for stiffness coefficients were those of Wachter and Benckert [3-5]. They investigated the following three types of seals: (*a*) teeth-on-stator, (*b*) interlocking

---

Contributed by the Gas Turbine Division of The American Society of Mechanical Engineers and presented at the 31st International Gas Turbine Conference and Exhibit, Düsseldorf, Federal Republic of Germany, June 8-12, 1986. Manuscript received at ASME Headquarters December 26, 1985. Paper No. 86-GT-12.

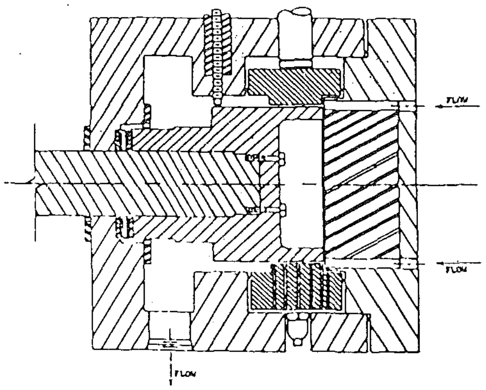

Fig. 3 Cross-sectional view of test section showing smooth stator

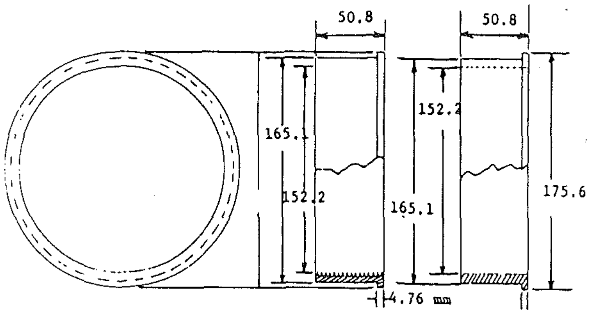

Fig. 4 Detail of smooth and labyrinth stator inserts

teeth on the rotor and stator, and (*c*) teeth on the stator and steps or grooves on the rotor. Seals were tested in the following two modes: (*a*) no seal rotation, but fluid prerotation, and (*b*) seal rotation but zero fluid prerotation. These results were limited in that the pressure drop was small, many of the data were for nonrotating seals, and no data were presented for teeth-on-rotor seals. The next investigation was carried out by Wright [6], whose results were for single-cavity teeth-on-stator seals with convergent, divergent, or straight geometries. Although this was a very limited and special case, these results did give insight into the effects of pressure drop, convergence or divergence of the clearance, and forward or backward whirl of a seal. The most recent investigation was that of Brown and Leong [7], who investigated various teeth-on-stator seal configurations. Their results include variations of pressure, geometry, rotor speed, and inlet tangential velocity.

In reviewing previous experimental programs, there is a clear need for extensive testing of seals with teeth on the rotor and results for measured damping coefficients. This paper presents some initial results for stiffness and damping coefficients for two nominally identical seals, differing only in that one is a tooth-on-rotor configuration and the other is a tooth-on-stator configuration. The test apparatus, facilities, and data-identification procedures used in this study are described in detail in [1, 2].

Table 1 Dimensions and parameters of seals tested in this study

	Teeth on rotor	Teeth on stator
Radius, cm	7.25	7.56
Length, cm	5.08	5.08
Tooth pitch, cm	0.3175	0.3175
Tooth height, cm	0.3175	0.3175
Clearance, cm	0.0406	0.0406
mr	−0.33	−0.33
nr	0.187	0.187
ms	−0.33	−0.33
ns	0.187	0.187
Average inlet temp., K	300.0	300.0

Experimental Results

Introduction. The test results reported here were developed as part of an extended, joint NASA-USAF funded research program for annular gas seal studies. Tests were on a labyrinth-rotor/smooth-stator seal. The test program had the initial objective of comparing the leakage and stability performances of a teeth-on-stator and a teeth-on-rotor labyrinth seal. Air is the test fluid.

Test Apparatus and Seal Configuration. The rotor shaft is suspended pendulum fashion from an upper, rigidly mounted pivot shaft, as shown in Fig. 2. This arrangement allows a side-to-side (horizontal) motion of the rotor. A cam within the pivot shaft allows vertical positioning of the rotor. The rotor is excited horizontally by a hydraulic shaker head which acts on the rotor-shaft bearing housing and works against a return spring mounted on the opposite side of the bearing housing. The design of the test rig (Fig. 3) permits the installation of various rotor/stator combinations. The stator is supported in the test section housing by three piezoelectric quartz load cells in a trihedral configuration. Different seal stator designs are obtained by the use of inserts.

The dimensions and pertinent data for each seal configuration are given in Table 1. The constants given in Table 1 for Fanning friction factor determination (*mr*, *nr*, *ms*, *ns*) are the same as those determined for the constant-clearance seal case as discussed by Nelson et al. [2]. The smooth and labyrinth stator inserts used for these tests are shown in Fig. 4. The labyrinth rotor and the tooth detail for both rotor and stator are shown in Figs. 5 and 6.

Test Variables. When shaking about the centered position, the dynamic seal apparatus is capable of controlling the following three independent variables: *pressure ratio, rotor speed,* and *inlet tangential velocity*. The actual test points for each of these three independent variables are shown in Table 2. When reviewing the following figures, Table 2 should be consulted for the definitions of all symbols used.

The *pressure ratios* achieved at the TAMU facility were up to 2.5 times larger than those published by Wachter and Benckert [3–5]. The reservoir pressures, as measured upstream of the flowmeter, are given in Table 2. These values differ from the actual inlet pressure, as given in the pressure distribution

Nomenclature

A = seal orbit radius, L; illustrated in Fig. 9
B = tooth height, L; illustrated in Fig. 1
C, c = direct and cross-coupled damping coefficients, FT/L
C_r = radial clearance, L; illustrated in Fig. 1
K, k = direct and cross-coupled stiffness coefficients, F/L
F = seal reaction-force, F
L = tooth pitch, L; illustrated in Fig. 1
P = seal inlet pressure, F/L^2
R_s = seal radius, L; illustrated in Fig. 1
X, Y = rotor-to-stator relative displacement components, L
Ω = shaking frequency, 1/T
ω = shaft angular velocity, 1/T

Subscripts

i = value in ith cavity
r = radial component
t = tangential component
x, y = rectangular coordinate directions

Table 2 Definition of symbols used in figures

Supply pressure	Rotor speeds	Inlet tangential velocities
1 3.08 bar	1 500 cpm	1 High velocity against rotation
2 4.46 bar	2 1000 cpm	2 Low velocity against rotation
3 5.84 bar	3 2000 cpm	3 Zero tangential velocity
4 7.22 bar	4 3000 cpm	4 Low velocity with rotation
5 8.25 bar	5 4000 cpm	5 High velocity with rotation
	6 5000 cpm	
	7 6000 cpm	
	8 7000 cpm	
	9 8000 cpm	

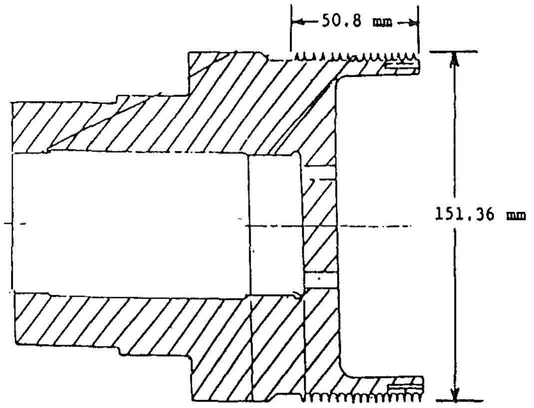

Fig. 5 Cross section of labyrinth rotor

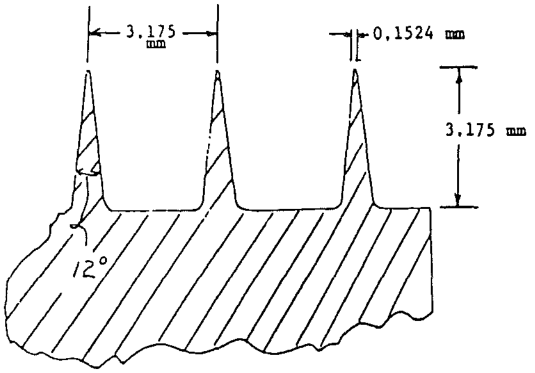

Fig. 6 Detail of labyrinth teeth for seals tested

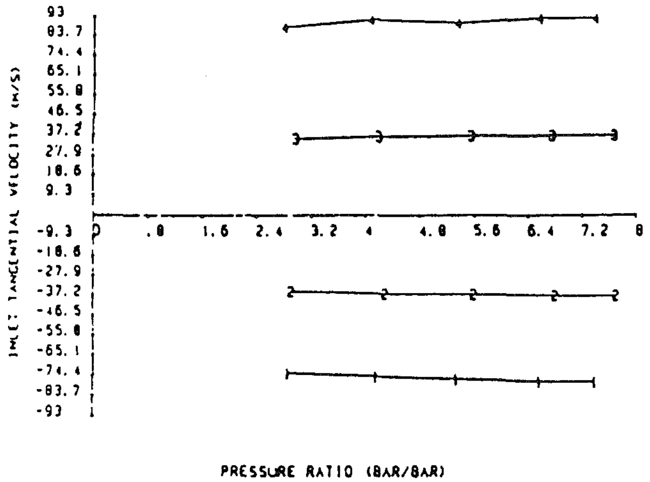

Fig. 7 Inlet tangential velocity versus pressure ratio for teeth-on-rotor labyrinth seal

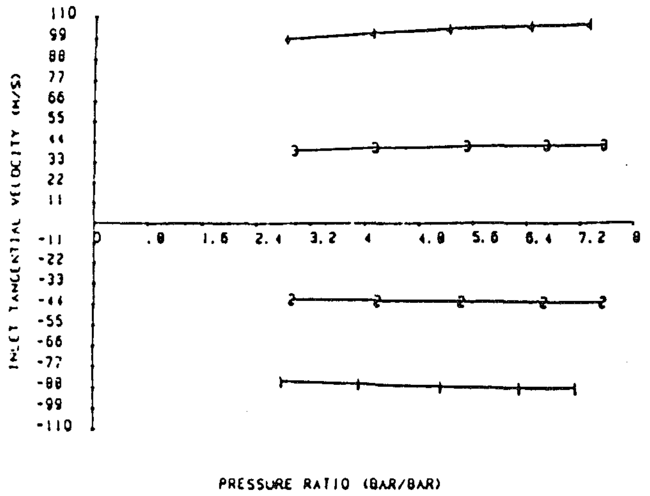

Fig. 8 Inlet tangential velocity versus pressure ratio for teeth-on-stator labyrinth seal

plots, because of frictional losses and an acceleration of the fluid due to the inlet guide vanes. No tests could be run at zero pressure difference, since a small pressure difference is necessary to keep the rotor from shifting axially and rubbing the inlet guide vanes.

The *rotor speeds* tested to date at the TAMU facility were comparable to those published by Wachter and Benckert. The surface velocities reached here were about half of those reported by Wachter and Benckert. However, Wachter and Benckert published very little data that combine rotor rotation and inlet fluid prerotation. In this study, all possible combinations of independent variables are given. For discussion purposes, the 3000 cpm rotor speed will be highlighted. The results showed little sensitivity to rotor speed and the 3000 cpm point tended to yield the clearest and most descriptive data. No zero rotor speed tests were run, since rotor rotation was necessary to prevent damage to the thrust bearing during shaking.

The *inlet tangential velocities* attained were up to 2.0 times those published by Wachter and Benckert. The inlet tangential velocities are given in Figs. 7 and 8 as a function of pressure ratio for both teeth-on-rotor and teeth-on-stator seals. The figures show that inlet tangential velocity remains fairly constant over the pressure ratios tested. There were five test points for inlet tangential velocity: two positive, two negative, and one at zero. The zero inlet tangential velocity point corresponds to the x axis in Figs. 7 and 8. The negative numbers shown in the figures mean that the inlet tangential velocity was opposed to the direction of rotor rotation. The positive numbers mean that the inlet tangential velocity was in the same direction as rotor rotation. The two different magnitudes of inlet tangential velocity, for each direction, correspond to the different inlet guide vane geometries, as discussed in [9]. The ratio of inlet tangential velocity to rotor surface velocity ranged from about -13 to about 16. Although the larger numbers are practically unrealistic, they

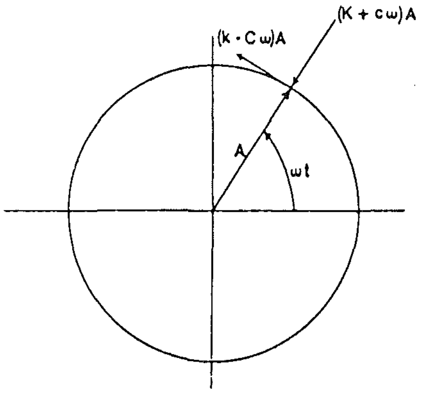

Fig. 9 Forces on a rotor

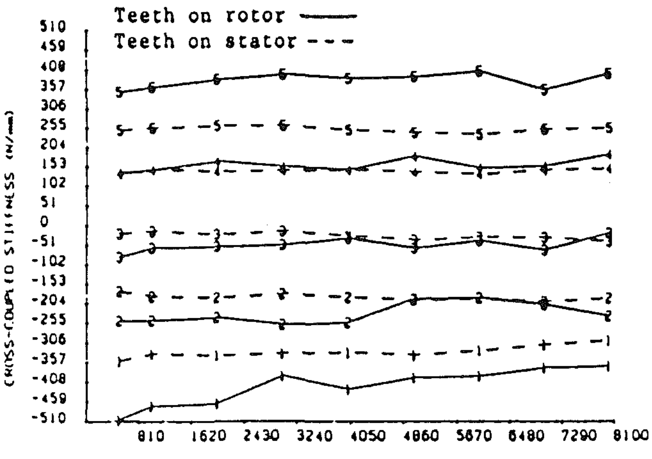

Fig. 10 Cross-coupled stiffness versus rotor speed

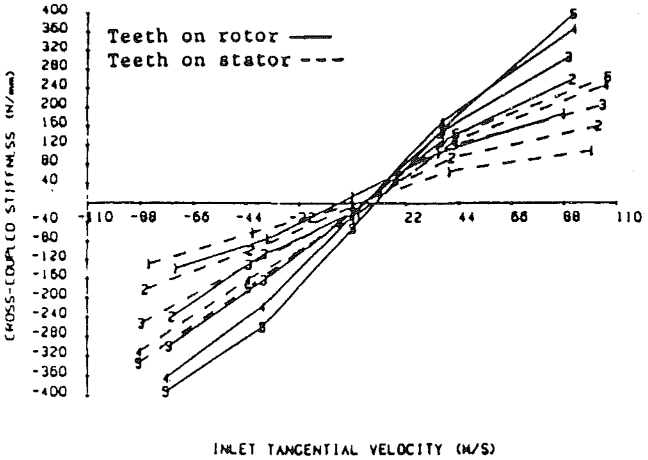

Fig. 11 Cross-coupled stiffness versus inlet tangential velocity

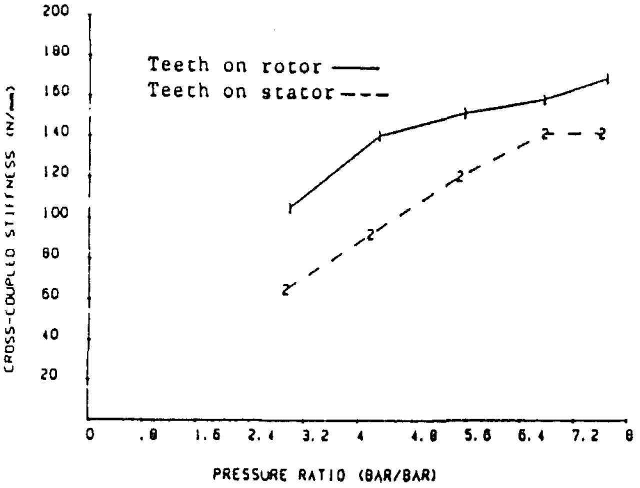

Fig. 12 Cross-coupled stiffness versus pressure ratio

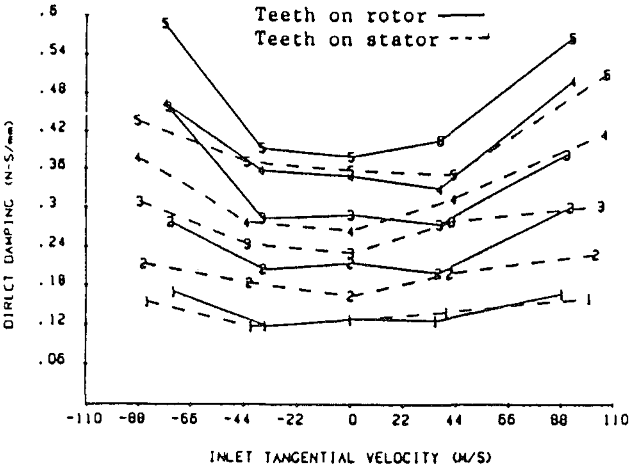

Fig. 13 Direct damping versus inlet tangential velocity

do give insight into the effects of inlet tangential velocity that would have otherwise gone unnoticed. This is most evident in the plots of direct damping versus inlet tangential velocity.

The effects of the three independent variables, *pressure ratio, inlet tangential velocity*, and *rotor speed*, on the dynamic (rotordynamic coefficients) results will be reviewed in order.

Dynamic Results. For a circular orbit of amplitude A, the resultant radial and tangential forces developed by the seal model of equation (2) are illustrated in Fig. 9 and defined by

$$-F_r/A = K + c\omega$$

$$F_t/A = k - C\omega$$

From a stability standpoint, the destabilizing tangential force F_t is of most interest. The destabilizing influence comes from the cross-coupled stiffness k, and the stabilizing influence comes from the direct damping C. The radial force usually has little influence on stability, except in rare cases involving multistage "back-to-back" centrifugal compressors with midspan seals where large negative direct stiffness values may reduce the natural frequencies. Since the focus of this study was on stability, the cross-coupled stiffness and direct damping results, which have the most influence, will be presented first. The direct stiffness will follow.

Relative Uncertainty. Before proceeding with the results, a statement must be made concerning the uncertainty present in the experimental results. Using the method described by Holman [8], the uncertainty in the dynamic coefficients can be determined. The uncertainty in the force, excitation frequency, and displacement measurements are 0.89 N (0.2 lb), 0.13 Hz, and 0.0013 mm (0.05 mils), respectively. The resulting calculated uncertainty in the stiffness coefficients is 7 N/mm (40 lb/in.) and 0.0875 N-s/mm (0.5 lb-s/in.) for the damping coefficients. Since the measured cross-coupled damping results were rarely greater than the uncertainty, test results are not provided here for this parameter; however data are available in [9].

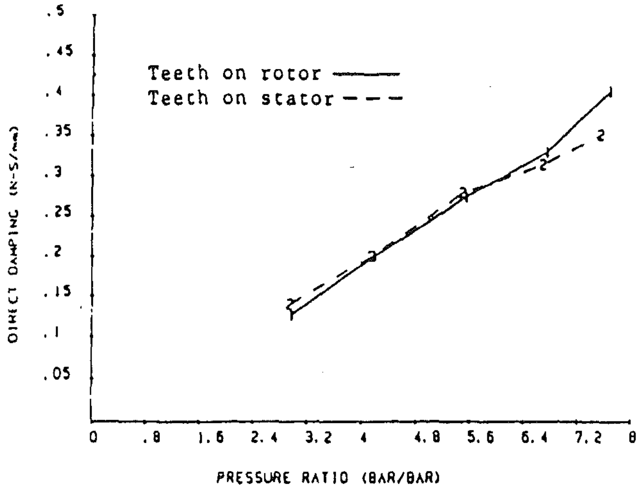

Fig. 14 Direct damping versus pressure ratio

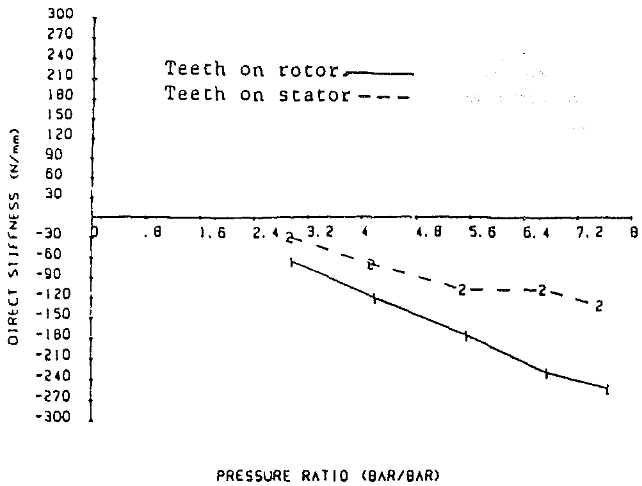

Fig. 17 Direct stiffness versus pressure ratio

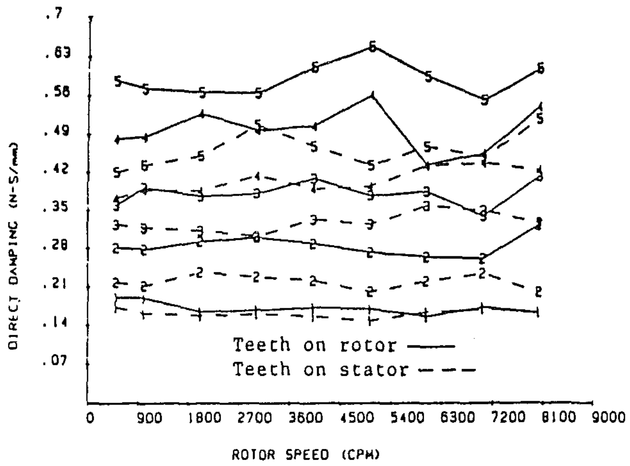

Fig. 15 Direct damping versus rotor speed

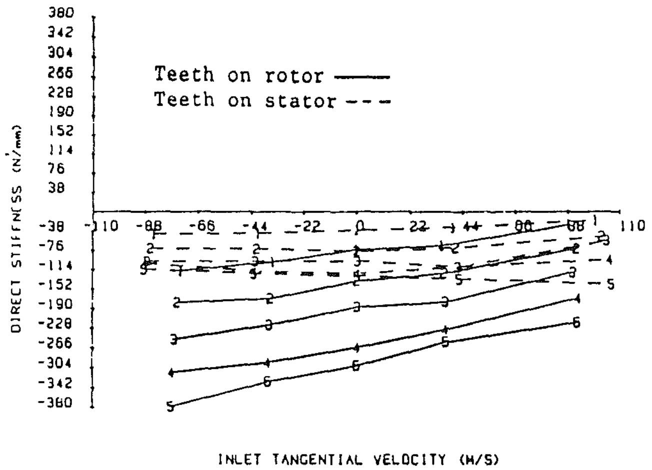

Fig. 18 Direct stiffness versus inlet tangential velocity

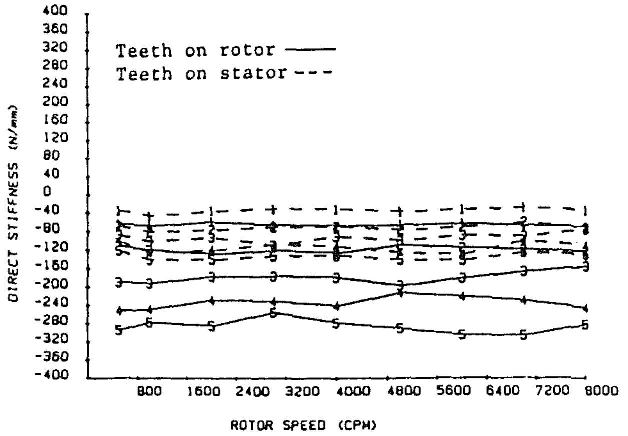

Fig. 16 Direct stiffness versus rotor speed

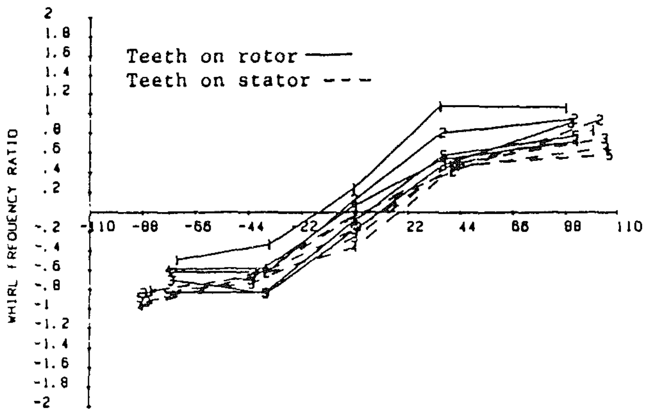

Fig. 19 Whirl frequency ratio versus inlet tangential velocity

Cross-Coupled Stiffness Comparison. Figure 10 shows a comparison of the cross-coupled stiffness versus rotor speed for the inlet tangential velocity set of Table 2. The figure shows that the teeth-on-rotor labyrinth develops a larger cross-coupled stiffness than the teeth-on-stator configuration. This figure also shows that cross-coupled stiffness results for the two seals were insensitive to rotor speed over the range of speeds tested (500-8000 cpm). Figure 11 shows the results for cross-coupled stiffness versus inlet tangential velocity for the two seals for the inlet pressure set of Table 2. This figure shows that the teeth-on-rotor seal develops consistently larger cross-coupled stiffness than the teeth-on-stator seal for all inlet tangential velocity values tested. Figure 12 shows a comparison of the cross-coupled stiffness of the two seals versus pressure ratio at 3000 cpm. This figure shows that the cross-coupled stiffness of both seals increases with pressure ratio. However, the cross-coupled stiffness for the teeth-on-stator seal levels off under choked conditions ($P > 5.84$ bar).

Direct Damping Comparison. Figure 13 shows a comparison of the direct damping versus inlet tangential velocity for the inlet pressure set of Table 2. The results show that the teeth-on-rotor case also develops larger direct-damping coefficients than the teeth-on-stator case. This figure also shows that the direct damping for both seals is very sensitive to inlet tangential velocity. Figure 14 shows a comparison of the direct damping versus pressure ratio at 3000 cpm. This figure shows that the direct damping for both seals increases with increasing inlet pressure. Figure 15 compares the direct damping versus rotor speed for the inlet pressure set of Table 2, and shows that direct damping is relatively insensitive to rotor speed.

Direct Stiffness Comparison. Figure 16 shows the results for direct stiffness versus rotor speed with the inlet pressure set of Table 2. The figure shows that the teeth-on-rotor case develops a substantially larger magnitude of direct stiffness than the teeth-on-stator case. Note that the direct stiffness is negative which would reduce the system's natural frequency and reduce the stability. Figure 17 shows a comparison of the direct stiffness for the two seals versus pressure ratio at 3000 cpm. This figure shows that the magnitude of direct stiffness increases with increasing pressure ratio for both seals. The direct stiffness for the teeth-on-stator seal seems to level off for choked exit conditions ($P > 5.84$ bar). Figure 18 shows a comparison of the direct stiffness versus inlet tangential velocity for the two seals for the inlet pressure set of Table 2. The figure shows that the direct stiffness for the teeth-on-stator seal increases with increasing inlet tangential velocity, while the direct stiffness for the teeth-on-rotor seal decreases with increasing inlet tangential velocity.

Whirl Frequency Ratio Comparison. Since a direct comparison of the coefficients of the two seals does not show any clear stability advantage, another method of comparison must be used. One method in which the dynamic coefficients of the two seals can be directly compared is through their respective nondimensional whirl frequency ratios. Whirl ratio is defined by

$$\text{Whirl ratio} = k/C\Omega$$

where Ω is the shaking frequency, and k/C is the ratio of the destabilizing influence of the cross-coupled stiffness and the stabilizing influence of direct damping. From a stability viewpoint, a minimum whirl ratio is desirable. Figure 19 shows a comparison plot of the whirl frequency ratios for the two seals versus inlet tangential velocity with the inlet pressure set of Table 2, and shows that the teeth-on-stator seal has a smaller whirl ratio than the teeth-on-rotor seal for *positive* inlet tangential velocities. This result is significant because most turbomachines have positive inlet tangential velocities for seals and teeth-on-stator seals are shown to be clearly superior to teeth-on-rotor seals from a stability viewpoint.

Conclusions

Test results have been presented for stiffness and damping coefficients of teeth-on-rotor and teeth-on-stator labyrinth seals which are geometrically similar. The seals were tested under identical operating conditions to investigate the influence of rotor speed, pressure ratio, and inlet tangential velocity on the rotordynamic coefficients.

The experimental results of the previous section support the following conclusions:

1 The stiffness and damping coefficients are insensitive to rotor speed for both seal configurations tested. This may be due to a lack of shear forces developed by the seals and may change as higher speeds are attained.

2 The stiffness and damping coefficients are very sensitive to inlet tangential velocity.

3 The stiffness and damping coefficients increase with increasing inlet pressure.

4 From a rotordynamic standpoint, the teeth-on-stator seal is more stable than the teeth-on-rotor seal for positive inlet tangential velocity.

As a point of interest, the theory of [10] was in reasonable agreement with the cross-coupled stiffness results presented here. However predictions for direct stiffness and damping are unsatisfactory. Details of the comparison are provided in [9].

Acknowledgments

This work was supported in part by NASA Grant NAS3-181 from NASA Lewis Research Center (Technical Monitor, Robert Hendricks) and AFOSR Contract F49620-82-K-0033 (Technical Monitor, Tony Amos).

References

1 Childs, D., Nelson, C., Nicks, C., Scharrer, J., Elrod, D., and Hale, K., "Theory Versus Experiment for the Rotordynamic Coefficients of Annular Gas Seals: Part 1, Test Facility and Apparatus," ASME *Journal of Tribology* (in press).

2 Nelson, C., Childs, D., Nicks, C., and Elrod, D., "Theory Versus Experiment for the Rotordynamic Coefficients of Annular Gas Seals: Part 2, Constant-Clearance and Convergent-Tapered Geometry," ASME *Journal of Tribology* (in press).

3 Wachter, J., and Benckert, H., "Querkrafte aus Spaltdichtungen—eine mogliche Ursache für die Laufunruhe von Turbomaschinen," *Atomkernenergie*, Vol. 32, No. 4, 1978, pp. 239–246.

4 Wachter, J., and Benckert, H., "Flow Induced Spring Coefficients of Labyrinth Seals for Applications in Rotordynamic," in: *Rotordynamic Instability Problems in High Performance Turbomachinery*, NASA CP 2133, 1980, pp. 189–212.

5 Benckert, H., "Stromungsbedinte Federkennwerte in Labyrinthdichtungen," Doctoral dissertation, University of Stuttgart, 1980.

6 Wright, D. V., "Labyrinth Seal Forces on a Whirling Rotor," *Rotor Dynamical Instability*, ASME, New York, 1983, pp. 19–31.

7 Brown, R. D., and Leong, Y. M. M. S., "Experimental Investigation of Lateral Forces Induced by Flow Through Model Labyrinth Glands," *Rotordynamic Instability Problems in High Performance Turbomachinery*, NASA CP 2338, 1984, pp. 187–210.

8 Holman, J. P., *Experimental Methods for Engineers*, McGraw-Hill, New York, 1978, p. 45.

9 Scharrer, J., "A Comparison of Experimental and Theoretical Results for Rotordynamic Coefficients for Labyrinth Gas Seals," TRC Report No. SEAL-2-85, Texas A&M University, May 1985.

10 Childs, D., and Scharrer, J., "An Iwatsubo-Based Solution for Labyrinth Seals—Comparison to Experimental Results," ASME JOURNAL OF ENGINEERING FOR GAS TURBINES AND POWER (in press).

Qihan Li
Lecturer.

Litang Yan
Professor.

Jet Propulsion Department,
Beijing Institute of Aeronautics &
Astronautics,
People's Republic of China

J. F. Hamilton
Professor.
School of Mechanical Engineering,
Purdue University,
West Lafayette, IN 47907

Investigation of the Steady-State Response of a Dual-Rotor System With Intershaft Squeeze Film Damper

This paper presents an analysis of the steady-state unbalance response of a dual-rotor gas turbine engine with a flexible intershaft squeeze film damper using a simplified transfer matrix method. The simplified transfer matrix method is convenient for the evaluation of the critical speed and response of the rotor system with various supports, shaft coupling, intershaft bearing, etc. The steady-state unbalance response of the rotor system is calculated for different shaft rotation speeds. The damping effects of an intershaft squeeze film damper with different radial clearances under various levels of rotor unbalance are investigated.

Introduction

Dual-rotor gas turbine engines often incorporate intershaft bearings to minimize shaft deflections caused by rotor unbalance and/or aircraft maneuvers. This method of rotor support eliminates the static support structure in the aerodynamic flowpath and thus improves engine efficiency, performance, and reliability. However, the intershaft bearing load sometimes is very large and will permit cross-exciting vibration between the inner and the outer shafts. An intershaft squeeze film damper could be used to decrease the loading and cross excitation vibration. Hibner et al. [1, 2, 3], Courage [4], and Gunter et al. [5, 6] have carried out analytical and experimental investigations respectively in this field.

The transfer matrix method, which was advanced first by Myklestad [7] and Prohl [8], is widely used to calculate critical speeds, unbalance response, and stability of rotor structures [2, 9, 10]. However, using this method to calculate the dynamic characteristics of a rotor system with rigid supports, hinged-joint, and intershaft bearings is troublesome due to the boundary conditions and shaft coupling.

In this paper a simplified transfer matrix method [11, 12] is used for calculating the steady-state unbalance response of a dual-rotor gas turbine engine equipped with a flexible intershaft squeeze film damper. The multispool rotor system is first divided into several components, which are represented by a series of lumped masses, called nodes, and the transfer relationships between nodes are developed individually for each component. Forces and angular displacement are used as initial parameters for the rigid supports, intershaft bearings, and hinged-joint, respectively. The total sets of linear equations are then coupled by applying the connecting and boundary conditions among the components.

The unbalance steady-state amplitude response and bearing forces of the rotor system are calculated for different shaft rotation speeds. The flexible intershaft damping effects of the damper with different radial clearances under various level of rotor unbalances are examined.

Computer Model of Dual-Rotor System

Figure 1 represents a schematic drawing of the jet engine dual rotor used for this analysis. The engine consists of two coaxial rotors. The inner rotor is the low-pressure rotor (LP rotor) and is supported by one main (rolling) bearing. The LP compressor is driven by the LP turbine. They are connected with each other by key coupling. The outer core rotor is called the high-pressure rotor (HP rotor) and is supported by two main (rolling) bearings. There are two intershaft bearings, front and rear rolling bearings, connecting the LP rotor and HP rotor. A flexible intershaft squeeze film damper (a flexible support structure in parallel with the damper) is added in series with the rear intershaft bearing.

Figure 2 represents the computer model. The rotor system is partitioned into two single systems which have a total of 45 nodes (lumped masses): 21 nodes in the LP rotor and 24 nodes in the HP rotor. A total of 12 stations are used to indicate the locations of the connecting and boundary points of the rotor system.

The axial and torsional motions of the rotor system are neglected and the structure of the rotor is assumed symmetric about the axis of rotation of the rotor system.

The inertia and gyroscopic effects of disks are considered. The three main bearing supports are assumed to be rigid.

The inner and outer ring of the squeeze film damper rotate with the LP rotor at the same speed and same direction. The damper has no end seals or oil grooves and has a length of 2.4

Contributed by the Gas Turbine Division and presented at the 1985 Beijing International Gas Turbine Symposium and Exposition, Beijing, People's Republic of China, September 1-7, 1985. Manuscript received at ASME Headquarters May 13, 1985. Paper No. 85-IGT-39.

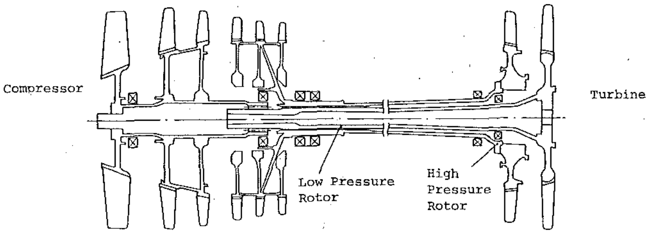

Fig. 1 A schematic drawing of the jet engine dual rotor

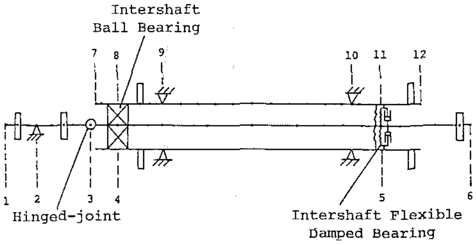

Fig. 2 Computer model of a dual rotor

cm, with an outer diameter of 6 cm. The flexible intershaft support is assumed to have a stiffness of 2.0×10^4 kg/cm.

A ratio of the rotating speeds of 1.1 between HP rotor and LP rotor is used in the analysis.

Calculating Approach

Computation of the Hydrodynamic Forces of the Intershaft Squeeze Film Damper [13, 14]. The basic bearing equation is the Reynolds equation, which is derived from the Navier-Stokes equation for incompressible flow using the short bearing approximation. The bearing forces are calculated using the rotating Cartesian coordinate system shown in Fig. 3.

The hydrodynamic force components in the rotating coordinate system are independent of time and can be written as follows:

$$F_r = \frac{\mu(\omega_b + \omega_j - 2\Omega)rL^3}{c^2}\left[\frac{\epsilon^2}{(1-\epsilon^2)^2}\right]$$

$$F_t = \frac{\mu(\omega_b + \omega_j - 2\Omega)rL^3}{2C^2}\left[\frac{\pi\epsilon}{2(1-\epsilon^2)^{3/2}}\right]$$

The equivalent stiffness is

$$K_0 = -\frac{\mu(\omega_b + \omega_j - 2\Omega)rL^3}{c^3}\left[\frac{\epsilon}{(1-\epsilon^2)^2}\right]$$

and the equivalent damping is

$$C_0 = -\frac{\mu(\omega_b + \omega_j - 2\Omega)rL^3}{2\Omega C^3}\left[\frac{\pi}{2(1-\epsilon^2)^{3/2}}\right]$$

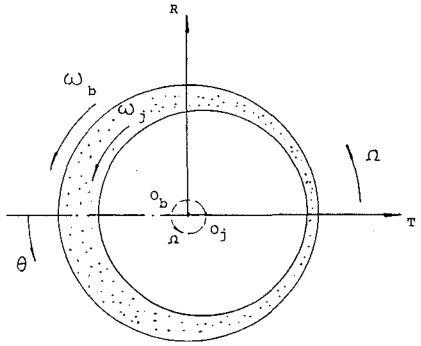

Fig. 3 Rotating coordinate system at intershaft damper

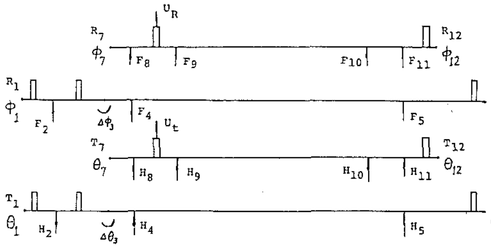

Fig. 4 Initial state parameters and connecting and boundary conditions of a dual-rotor system

where

$$\omega_b = \omega_j = \Omega_L$$

$$\Omega = \Omega_H$$

Initial Unknown State Parameters and the Connecting and Boundary Conditions of the Rotor System. Rotating coordinates are also used in the complete rotor system with the steady-state response characteristics of the rotor system calculated in the R-0-Z and T-0-Z planes respectively as shown in Fig. 4.

The initial unknown state parameters are: R_1, ϕ_1, F_2, $\Delta\phi_3$, F_4, R_7, ϕ_7, F_9, F_{10}, F_{11}, T_1, θ_1, H_2, $\Delta\theta_3$, H_4, T_7, θ_7, H_9, H_{10}, H_{11}.

It should be noted that the effects of the hinged-joint, the three main bearing supports, the front intershaft bearing, and the rear intershaft damper bearing are given as angular displacements and forces respectively.

The connecting and boundary conditions are:

$$R_2 = 0, M_{R_3} = 0, R_4 - R_8 = 0, R_5 - R_{11} + \frac{F_{11}}{K_S + K_0} = 0, M_{R_6} = 0,$$

$$Q_{R_6} = 0, R_9 = 0, R_{10} = 0, M_{R_{12}} = 0, Q_{R_{12}} = 0, T_2 = 0,$$

$$M_{T_3} = 0, T_4 - T_8 = 0, T_{11} = 0, M_{T_6} = 0, Q_{T_6} = 0, T_9 = 0,$$

$$T_{10} = 0, M_{T_{12}} = 0, Q_{T_{12}} = 0.$$

Nomenclature

c = damper clearance
EI = shaft stiffness
F_r, F_t = hydrodynamic forces in R and T direction
F, H = bearing forces in R and T direction
J_p, J_T = polar moment and transverse moment of inertia of a disk
K_i = stiffness at node i
K_0 = damper oil film stiffness
K_s = intershaft flexible support stiffness
l = length of the shaft section
L = damper length
m_i = mass at node i
m_d = disk mass
M_R, M_T = bending moments
N = resultant of bearing forces
Q_R, Q_T = shear forces
r = inner journal radius of the damper
R, T = radial and tangential displacement of the rotor
UN = unbalance force
α = direction angle of unbalance force
ϕ, θ = angular displacement of the rotor
ϵ = damper journal eccentricity
μ = damper viscosity
Ω = rotor precession speed
Ω_L = L-rotor spin speed
Ω_H = H-rotor spin speed
ω_b = outer ring spin speed of the damper
ω_j = inner journal spin speed of the damper
$\{p\}$ = state parameter vector
$[U]$ = unit transfer matrix

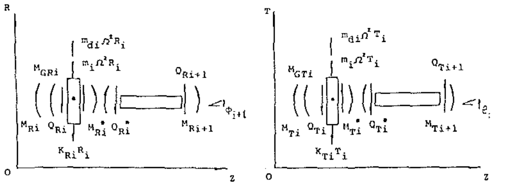

Fig. 5 Sign convention of unit transfer matrix

The unbalance components in R and T directions are $UN \cos \alpha$ and $UN \sin \alpha$. α indicates the angle between unbalance force and vibration displacement.

Unit Transfer Matrix. For node i, the sign convention for state parameters (radial displacement, angular displacement, bending moment, and shear force) is shown in Fig. 5.

The relation, called unit transfer matrix $[u_i]$, between the left end and the right end of the node i can be written as follows

$$(P_{i+1}) = [u_i](P_i)$$

where the state vectors are

$$(P_{i+1}) = (R\phi M_R Q_R T\theta M_T Q_T)^T_{i+1}$$
$$(P_i) = (R\phi M_R Q_R T\theta M_T Q_T)^T_i$$

and the transfer matrix is

$$[u_i] = \begin{bmatrix} 1+\frac{l^3}{6EI}A & 1-\frac{l^2}{2EI}B & \frac{l^2}{2EI} & -\frac{l^3}{6EI} & & & & \\ \frac{l^2}{2EI}A & 1-\frac{l}{EI}B & \frac{l}{EI} & -\frac{l^2}{2EI} & & & & \\ lA & -B & 1 & -1 & & & & \\ -A & 0 & 0 & 1 & & & & \\ & & & & 1+\frac{l^3}{6EI}A & 1-\frac{l^2}{2EI}B & \frac{l^2}{2EI} & -\frac{l^3}{6EI} \\ & & & & \frac{l^2}{2EI}A & 1-\frac{l}{EI}B & \frac{l}{EI} & -\frac{l^2}{EI} \\ & & & & lA & -B & 1 & -1 \\ & & & & -A & 0 & 0 & 1 \end{bmatrix}$$

The coefficients A and B are

$$A = (m_i + m_d)\Omega^2 - K_i$$
$$B = \left(1 - \frac{J_p}{J_T}\frac{\omega}{\Omega}\right) J_T \Omega$$
$$\omega = \Omega_L \text{ for LP rotor, } \omega = \omega_H \text{ for HP rotor}$$

Construction and Solution of the Sets of Linear Equations. The relation between any two stations can be represented using products of the transfer matrices as

$$P_j = U_{j-1} U_{j-2} \ldots U_{n-1} U_n P_n \qquad (j > n)$$

and

$$P_j^{Sq} = U_{j-1} U_{j-2} \ldots U_{n-1} U_n P_n^{Sq}$$

where Sq indicates the initial unknown state parameter at n station.

Successively letting one of the parameters such as $S1 = 1$, the others equal to zero, the P_j^{S1}, P_j^{S2}, ... P_j^{Sq} can then be calculated.

Applying linear superposition principle, the equation

$$P_j = P_j^{S1} S1 + P_j^{S2} S2 + \ldots + P_j^{Sq} Sq$$

can be obtained. For example, there are four unknown state parameters, R_1, ϕ_1, F_2, $\Delta\phi_3$, on the left side of fourth station in R direction, so the displacement of fourth station in the direction can be represented

$$R_4 = R_4^{R1} R_1 + R_4^{\phi 1} \phi_1 + R_4^{F2} F_2 + R_4^{\Delta\phi 3} \Delta\phi_3$$

Utilizing the connecting and boundary conditions, the sets of linear equations can be constructed as shown in Table 1. Written in matrix form

$$[P^{Sq}](Sq) = (C)$$

where

$$(Sq) = (R_1 \phi_1 F_2 \Delta\phi_3 F_4 F_{11} R_7 \phi_7 F_9 F_{10}$$
$$T_1 \theta_1 H_2 \Delta\theta_3 H_4 H_{11} T_7 \theta_7 H_9 H_{10})^T$$

$[P^{Sq}]_{20\times 20}$ coefficient matrix in the sets of equations, $(C) = -(C_1 C_2 C_3 \ldots C_{20})^T$ unbalance force vector in which $C_4 = -UN \cos \alpha$, $C_7 = C_8 = C_9 = C_{10} = UN \cos \alpha$, $C_{14} = C_{17} = C_{18} = C_{19} = C_{20} = UN \sin \alpha$, the others are equal to zero.

The vector (Sq) can be solved using the Gaussian elimination technique and after substituting the results into the sets of equations, the response of the rotor system at any node can be obtained.

It should be noted that for a given rotating speed, the magnitude of unbalance is known but its direction must be evaluated. In order to solve the sets of equations, the radial stiffness K_0 and damping force H of the damper is first calculated by assuming an eccentricity (the ratio between the relative displacement of the damper and the clearance of the damper) and an iteration program is used to compute the true response of the rotor.

Typical Calculation Results

The steady-state unbalance responses of the rotor system for different constant shaft speeds were calculated and the response characteristics including rotor amplitudes and bearing forces for different clearances of the intershaft squeeze film damper under different rotor unbalances were examined.

The LP rotor was taken to be balanced with the unbalance applied to the front stage compressor of the HP rotor. Except for the clearance, the other parameters of the squeeze film damper were kept unchanged.

Table 1

$$R_2 - C_1 + R_2^{R_1} R_1 + R_2^{\Phi_1} \Phi_1 = 0$$

$$M_{R_3} - C_2 + M_{R_3}^{R_1} R_1 + M_{R_3}^{\Phi_1} \Phi_1 + M_{R_3}^{F_2} F_2 = 0$$

$$R_4 - R_8 - C_3 + R_4^{R_1} R_1 + R_4^{\Phi_1} \Phi_1 + R_4^{F_2} F_2 + R_4^{\Delta\Phi_3} \Delta\Phi_3 - R_8^{R_7} R_7 - R_8^{\Phi_7} \Phi_7 = 0$$

$$R_5 - R_{11} + \frac{F_{11}}{K_S+K_o} - C_4 + R_5^{R_1} R_1 + R_5^{\Phi_1} \Phi_1 + R_5^{F_2} F_2 + R_5^{\Delta\Phi_3} \Delta\Phi_3 + R_5^{F_4} F_4 + \frac{1}{K_S + K_o} F_{11} - R_{11}^{R_7} R_7 - R_{11}^{\Phi_7} \Phi_7 - R_{11}^{F_9} F_9 - R_{11}^{F_{10}} F_{10} = 0$$

$$M_{R_6} = C_5 + M_{R_6}^{R_1} R_1 + M_{R_6}^{\Phi_1} \Phi_1 + M_{R_6}^{F_2} F_2 + M_{R_6}^{\Delta\Phi_3} \Delta\Phi_3 + M_{R_6}^{F_4} F_4 - M_{R_6}^{F_{11}} F_{11} = 0$$

$$Q_{R_6} - C_6 + Q_{R_6}^{R_1} R_1 + Q_{R_6}^{\Phi_1} \Phi_1 + Q_{R_6}^{F_2} F_2 + Q_{R_6}^{\Delta\Phi_3} \Delta\Phi_3 + Q_{R_6}^{F_4} F_4 - Q_{R_6}^{F_{11}} F_{11} = 0$$

$$R_9 - C_7 - R_9^{F_4} F_4 + R_9^{R_7} R_7 + R_9^{\Phi_7} \Phi_7 = 0$$

$$R_{10} - C_8 - R_{10}^{F_4} F_4 + R_{10}^{R_7} R_7 + R_{10}^{\Phi_7} \Phi_7 + R_{10}^{F_9} F_9 = 0$$

$$M_{R_{12}} - C_9 - M_{R_{12}}^{F_4} F_4 + M_{R_{12}}^{F_{11}} F_{11} + M_{R_{12}}^{R_7} R_7 + M_{R_{12}}^{\Phi_7} \Phi_7 + M_{R_{12}}^{F_9} F_9 + M_{R_{12}}^{F_{10}} F_{10} - 0$$

$$Q_{R_{12}} - C_{10} - Q_{R_{12}}^{F_4} F_4 + Q_{R_{12}}^{F_{11}} F_{11} + Q_{R_{12}}^{R_7} R_7 + Q_{R_{12}}^{\Phi_7} \Phi_7 + Q_{R_{12}}^{F_9} F_9 + Q_{R_{12}}^{F_{10}} F_{10} - 0$$

$$T_2 - C_{11} + T_2^{T_1} T_1 + T_2^{\theta_1} \theta_1 = 0$$

$$M_{T_3} - C_{12} + M_{T_3}^{T_1} T_1 + M_{T_3}^{\theta_1} \theta_1 + M_{T_3}^{H_2} H_2 = 0$$

$$T_4 - T_8 - C_{13} + T_4^{T_1} T_1 + T_4^{\theta_1} \theta_1 + T_4^{H_2} H_2 + T_4^{\Delta\theta_3} \Delta\theta_3 - T_8^{T_7} T_7 - T_8^{\theta_7} \theta_7 = 0$$

$$T_{11} - C_{14} - T_{11}^{H_4} H_4 + T_{11}^{T_7} T_7 + T_{11}^{\theta_7} \theta_7 + T_{11}^{H_9} H_9 + T_{11}^{H_{10}} H_{10} = 0$$

$$M_{T_6} - C_{15} + M_{T_6}^{T_1} T_1 + M_{T_6}^{\theta_1} \theta_1 + M_{T_6}^{H_2} H_2 + M_{T_6}^{\Delta\theta_3} \Delta\theta_3 + M_{T_6}^{H_4} H_4 - M_{T_6}^{H_{11}} H_{11} = 0$$

$$Q_{T_6} = C_{16} + Q_{T_6}^{T_1} T_1 + Q_{T_6}^{\theta_1} \theta_1 + Q_{T_6}^{H_2} H_2 + Q_{T_6}^{\Delta\theta_3} \Delta\theta_3 + Q_{T_6}^{H_4} H_4 - Q_{T_6}^{H_{11}} H_{11} = 0$$

$$T_9 - C_{17} - T_9^{H_4} H_4 + T_9^{T_7} T_7 + T_9^{\theta_7} \theta_7 = 0$$

$$T_{10} - C_{18} - T_{10}^{H_4} H_4 + T_{10}^{T_7} T_7 + T_{10}^{\theta_7} \theta_7 + T_{10}^{H_9} H_9 = 0$$

$$M_{T_{12}} - C_{19} - M_{T_{12}}^{H_4} H_4 + M_{T_{12}}^{H_{11}} H_{11} + M_{T_{12}}^{T_7} T_7 + M_{T_{12}}^{\theta_7} \theta_7 + M_{T_{12}}^{H_9} H_9 + M_{T_{12}}^{H_{10}} H_{10} = 0$$

$$Q_{T_{12}} - C_{20} - Q_{T_{12}}^{H_4} H_4 + Q_{T_{12}}^{H_1} H_{11} + Q_{T_{12}}^{T_7} T_7 + Q_{T_{12}}^{\theta_7} \theta_7 + Q_{T_{12}}^{H_9} H_9 + Q_{T_{12}}^{H_{10}} H_{10} = 0$$

Figures 6–10 and Table 2 present the steady-state amplitude response and bearing forces of the rotor system in the rotating coordinate system (radial and tangential directions) for different rotating speeds when the clearance is 0.018 cm and the unbalance is 0.5 kg-cm.

It can be seen that as the HP rotor speed is increased from 10,000 to 12,000 rpm, the phase angle of the amplitude response is changed by 180 deg, and when HP rotor speed is 11,000 rpm, both the amplitude and bearing loading are very large. These results indicate that the rotor system is passing through a resonant state at 11,000 rpm, in which the damper can be effective only if the unbalance is smaller and the damper clearance is larger. As shown in Table 2, when rotor unbalances exceeded 0.05, 0.1, and 0.12 kg-cm for clearances of 0.018, 0.024, and 0.03 cm, respectively, the rotor system was unstable and the bearing forces increased very rapidly with small speed changes.

When the HP rotor speed has reached 15,000 rpm, the rotor

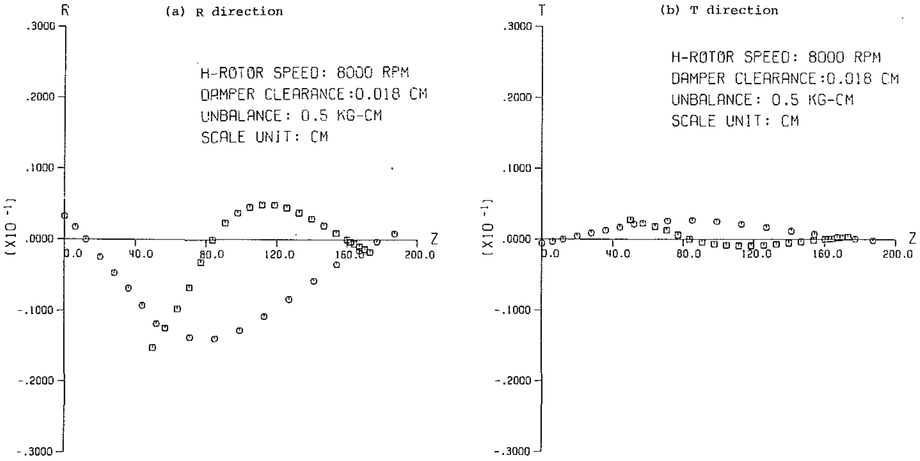

Fig. 6 Amplitude response of the rotor system at 8000 rpm

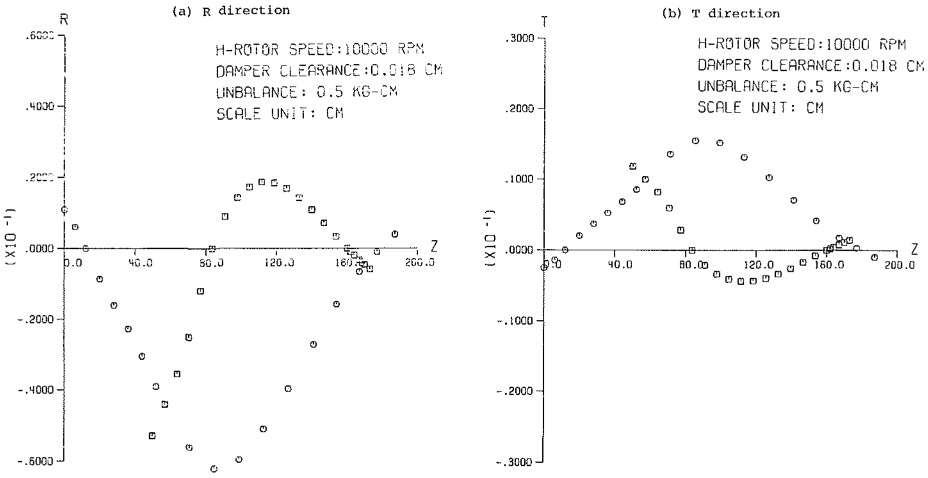

Fig. 7 Amplitude response of the rotor system at 10,000 rpm

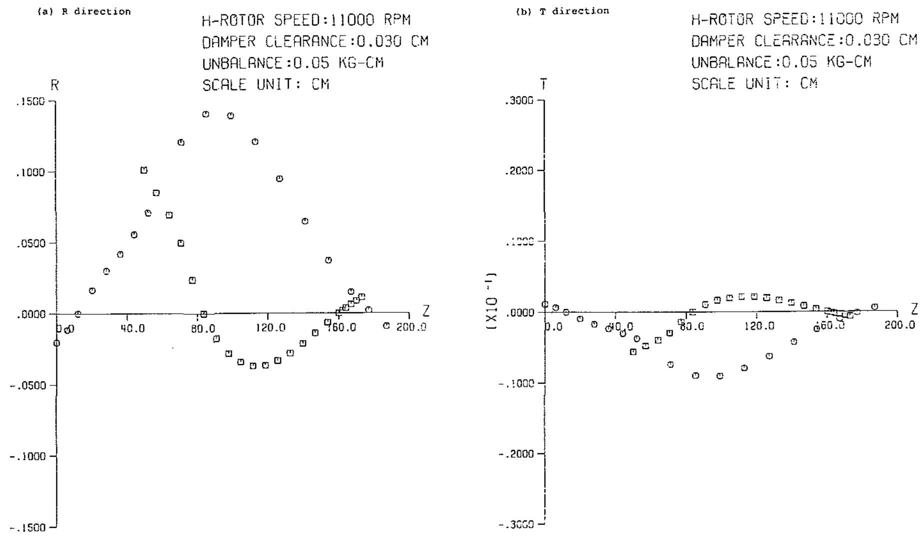

Fig. 8 Amplitude response of the rotor system at 11,000 rpm

system is always unstable which indicates the incorporation of an intershaft squeeze film damper into the rotor system produces an instability threshold speed.

Figures 11-13 present the steady-state amplitude response of the rotor system in the radial direction for an unbalance of 1.0 kg-cm and three values of damping clearance at 10,000 rpm and Fig. 14 presents the response of the rotor system for the same unbalance and rotating speed as above but having no intershaft squeeze film damper (rear intershaft bearing stiffness is assumed to be 2×10^6 kg-cm here).

Table 3 presents the resultant of bearing forces for different damper clearances and rotor unbalances at 10,000 rpm, and

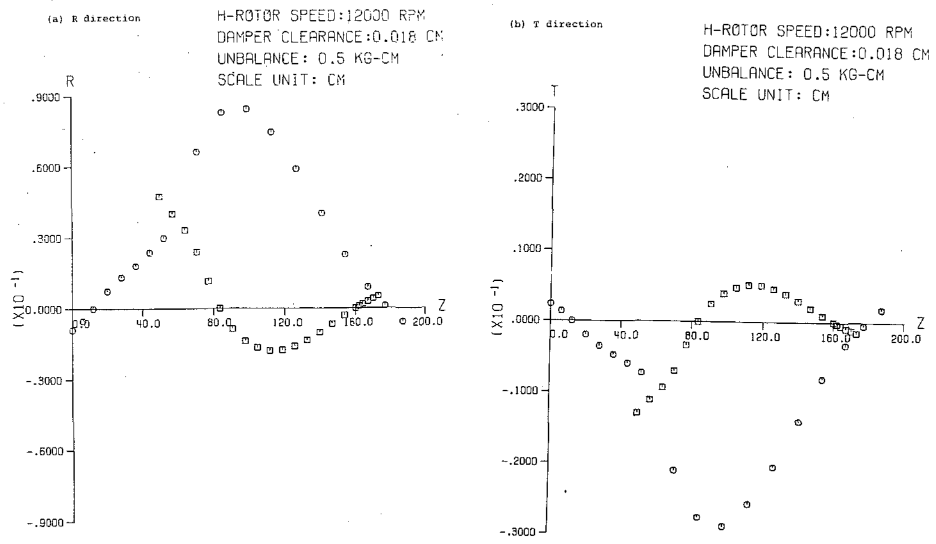

Fig. 9 Amplitude response of the rotor system at 12,000 rpm

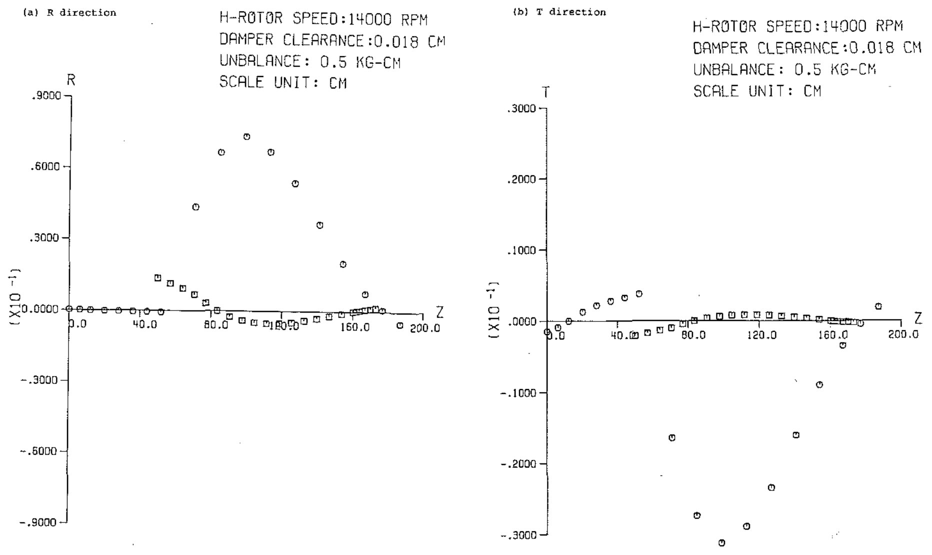

Fig. 10 Amplitude response of the rotor system at 14,000 rpm

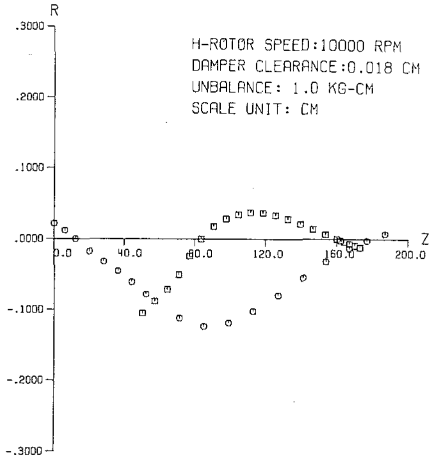

Fig. 11 Amplitude response of the rotor system for a damper clearance of 0.018 cm

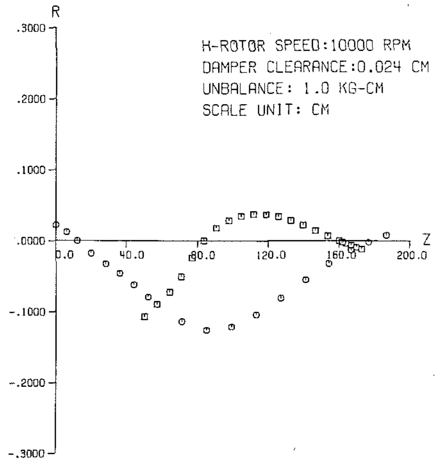

Fig. 12 Amplitude response of the rotor system for a damper clearance of 0.024 cm

shows the comparison with the bearing forces for the same cases except the rotor system is without flexible intershaft squeeze film damper.

The results of the calculation show that with the incorporation of a rear flexible intershaft squeeze film damper into the rotor system, the maximum values of amplitude

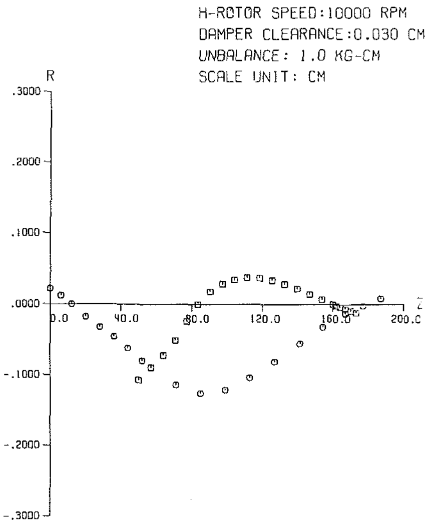

Fig. 13 Amplitude response of the rotor system for a damper clearance of 0.030 cm

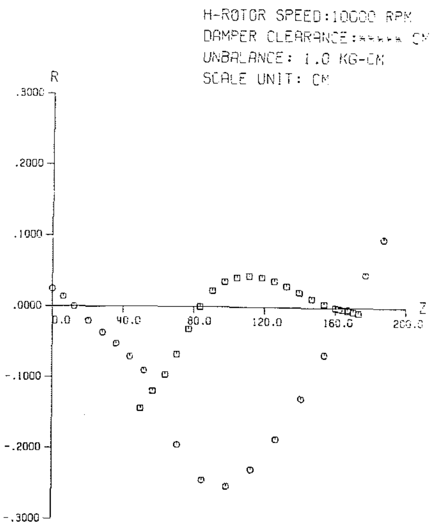

Fig. 14 Amplitude response of the rotor system without intershaft squeeze film damper

Table 2 Bearing forces of the rotor system for different rotating speeds ($C = 0.018$ cm, $UE = 0.5$ kg·cm)

HP rotor Speed (rpm)	Bearing Forces (kg)									
	R Direction					T Direction				
	F_2	F_4	F_{11}	F_9	F_{10}	H_2	H_4	H_{11}	H_9	H_{10}
8000	-58.9	16.1	5.0	-390.1	32.9	3.5	-2.3	-0.8	55.8	-4.5
9000	-108.2	24.3	7.0	-628.8	43.6	17.7	-3.9	-1.4	102.0	-6.9
10000	-949.6	14.8	71.1	-4388.7	137.1	217.6	1.4	-19.3	979.3	-28.5
11000 (a)	1987.9	211.2	-118.5	8938.9	-236.8	-97.7	0.64	75.8	-378.3	-74.7
(b)	3873.1	418.3	-194.6	17439.9	-506.2	-145.2	-0.95	112.6	-562.1	-111.0
(c)	4956.3	521.4	-323.6	22266.6	-555.4	-102.2	-0.67	19.3	-395.8	-78.2
12000	985.6	287.9	-98.1	4488.5	-37.7	-259.3	-106.0	46.9	-1196.3	-12.9
13000	442.1	329.6	-35.6	2369.5	38.9	-72.5	-119.2	40.9	-553.9	-33.8
14000	-30.1	491.2	-101.6	1073.3	98.3	186..3	-201.4	66.4	-146.0	-78.9
15000	Rotor System Unstable									

(a) C = 0.018 cm, UE = 0.5 kg-cm (b) C = 0.024 cm, UE = 0.1 kg-cm
(c) C = 0.03 cm, UE = 0.12 kg-cm

Table 3 Resultant for bearing forces of the rotor system for different clearances and unbalances (HP rotor speed 10,000 rpm)

Damper Clearance (cm)	Rotor Unbalance (kg-cm)	Bearing Forces (kg)				
		N_2	N_4	N_{11}	N_9	N_{10}
0.018	0.1	-194.7	2.9	13.9	-899.1	28.4
	0.3	-584.1	8.8	42.9	-2697.2	85.5
	0.5	-974.6	14.9	73.6	-4496.6	140.4
	1.0	-1956.4	31.8	162.4	-9018.7	263.5
	1.5	-2972.7	53.7	219.4	-13060.6	346.9
	2.0	-4131.5	91.0	545.8	-18837.3	353.8
	2.5	Rotor System Unstable				
0.024	0.1	-192.9	2.8	13.6	-892.2	29.0
	0.3	-578.9	8.7	41.0	-2676.5	86.5
	0.5	-965.2	14.6	69.0	-4460.6	143.3
	1.0	-1930.4	29.7	141.9	-8921.3	282.0
	1.5	-2897.9	45.8	222.8	-13386.3	412.1
	2.0	-3872.3	64.3	321.1	-17649.4	521.2
	3.0	-6081.4	153.1	914.5	-27713.7	424.1
	4.0	Rotor System Unstable				
0.030	0.1	-192.9	2.9	13.5	-891.1	29.0
	0.3	-578.1	8.7	40.6	-2673.2	86.8
	0.5	-963.5	14.5	67.8	-4454.8	144.4
	1.0	-1927.1	29.1	137.1	-8909.7	287.0
	1.5	-2890.7	44.1	208.6	-13363.8	426.9
	2.0	-3855.0	59.6	284.1	-17817.9	562.1
	3.0	-5792.0	96.5	478.0	-26736.4	782.1
	4.0	-8139.0	245.3	1506.9	36932.8	548.8
	5.0	Rotor System Unstable				
No Damper, Intershaft Bearing Stiffness $K_s = 2\times10^6$ (kg-cm)	0.5	-1091.4	-273.3	-1952.7	-6160.9	2646.6
	1.0	-2182.8	-546.6	-3905.3	-12321.8	5293.2
	2.0	-4365.6	-1093.1	-7810.7	-24643.7	10586.5
	3.0	-6548.4	-1639.8	-11716.2	-36965.4	15879.6

response of the LP rotor and HP rotor can be reduced to less than 50 and 80 percent, respectively, the front and rear intershaft bearings and HP rotor rear support loading can be reduced to less than 10 percent, and the HP rotor front support loading can be reduced to less than 70 percent of the levels reached by the rotor system without the flexible intershaft squeeze film damper. But the LP rotor front main support loading is reduced very small.

For a given rotor unbalance and three values of damper clearances (within the clearance range in which the damper is effective to reduce amplitiude and loading), the damping effects are basically the same. However, for any given damper clearance, if rotor unbalance is too large, the radial stiffness of damper will increase at a much faster rate than the damping and will produce a highly nonlinear rotor system which is unstable. It is shown clearly in Table 3 that the larger the damper clearance, the greater the upper limit of rotor unbalance.

The results also indicate that the relation between bearing loading and rotor unbalance is linear for smaller unbalances. In this case, the rotor system can be considered to be linear and it is convenient to evaluate unbalance response of the rotor system.

Conclusion

The use of the simplified transfer matrix method is a convenient and accurate method to determine the critical speed, steady-state unbalance response, and stability of the rotor system, especially those that have complicated boundary supports and intershaft coupling.

The introduction of a flexible intershaft squeeze film damper into the rotor system is effective in reducing amplitude response and bearing loading, especially for the bearing loading at the location of the intershaft bearings and adjacent rotor bearing supports. The effectiveness of the damper depends on the configuration, position and parameters of the damper and the unbalance levels of the rotor. If other factors of the damper are kept unchanged, a definite damper clearance corresponds to a definite upper limit of rotor unbalance. If the upper limit of rotor unbalance is exceeded, the rotor system will be unstable.

An instability threshold speed will be produced with the introduction of an intershaft squeeze film damper into the rotor system. In designing intershaft squeeze film damper, it should be necessary to consider the operating speed of the rotor below the threshold speed of the rotor system.

References

1 Hibner, D. H., Kirk, R. G., and Buono, D. F., "Analytical and Experimental Investigation of the Stability of Intershaft Squeeze Film Dampers—Part 1: Demonstration of Instability," ASME JOURNAL OF ENGINEERING FOR POWER, Jan. 1977.

2 Hibner, D. H., Bansal, P. N., and Buono, D. F., "Analysis and Experimental Investigation of the Stability of Intershaft Squeeze Film Dampers—Part 2: Control of Instability," ASME *J. of Mech. Design*, Vol. 100, July 1978.

3 Hibner, D. H., "Dynamic Response of Viscous-Damped Multi-Shaft Jet Engines," *J. of Aircraft*, Vol. 12, Apr. 1975.

4 Courage, J. B., "Experimental Study of an Inter-Shaft Squeeze Film Bearing," The Second International Vibration of Rotating Machinery Conference, 1980.

5 Gunter, E. J., Li, D. F., and Barrett, L. E., "A Dynamic Analysis of Multispool Gas Turbine Helicopter Engine," *Proceedings of the Conference on Stability and Dynamic Response of Rotors in Squeeze Film Bearings*, 1979.

6 Li, D. F., and Gunter, E. J., "Component Mode Synthesis of Large Rotor System," ASME JOURNAL OF ENGINEERING FOR POWER, Vol. 104, July 1982.

7 Myklestad, N. O., "A New Method of Calculating Natural Modes of Uncoupled Bending Vibration of Airplane Wings and Other Types of Beams," *J. of the Aeronautical Sciences*, Apr. 1944.

8 Prohl, M. A., "A General Method for Calculating Critical Speeds of Flexible Rotors," ASME *J. of Applied Mechanics*, Vol. 67, 1945.

9 Lund, J. W., "Stability and Damped Critical Speeds of a Flexible Rotor in Fluid Film Bearings," ASME *Journal of Engineering for Industry*, May 1974.

10 Li, D. F., and Gunter, E. J., "A Study of the Modal Truncation Error in the Component Mode Analysis of a Dual-Rotor System," ASME JOURNAL OF ENGINEERIONG FOR POWER, Vol. 104, July 1982.

11 Litang Yan, "A Simplified Transfer Matrix Method for Calculating Critical Speeds and Response of Multispool Rotor System," Beijing Institute of Aeronautics & Astronautics, China, 1982.

12 Baolin Hong, "Calculation of Critical Speeds and Response of Dual-Rotor System With Squeeze Film Damper Using Simplified Transfer Matrix Method," MSE dissertation, Beijing Institute of Aeronautics & Astronautics, China, 1983.

13 Barrett, L. E., and Gunter, E. J., "Steady-State and Transient Analysis of a Squeeze Film Damper Bearing for Rotor Stability," NASA CR-2548, May 1975.

14 Gunter, E. J., Barrett, L. E., and Allaire, P. E., "Design of Nonlinear Squeeze-Film Dampers for Aircraft Engines," ASME *Journal of Lubrication Technology*, Jan. 1977.

Investigation of the Transient Response of a Dual-Rotor System With Intershaft Squeeze-Film Damper

Qihan Li
Lecturer,
Jet Propulsion Department,
Beijing Institute of Aeronautics
& Astronautics,
People's Republic of China

J. F. Hamilton
Professor,
School of Mechanical Engineering,
Purdue University,
West Lafayette, IN 47907

A method is presented for calculating the dynamics of a dual-rotor gas turbine engine equipped with a flexible intershaft squeeze-film damper. The method is based on the functional expansion component synthesis method. The transient response of the rotor due to a suddenly applied imbalance in the high-pressure turbine under different steady-speed operations is calculated. The damping effects of the intershaft damper and stability of the rotor system are investigated.

Introduction

Dual-rotor gas turbine engines often incorporate intershaft bearings to minimize shaft deflections caused by rotor imbalance and/or aircraft maneuvers. This method of rotor support eliminates the static support structure in the aerodynamic flowpath and improves engine efficiency, performance, and reliability. However, the intershaft bearing load sometimes is very large and will permit cross-exciting vibration between the inner and the outer shafts. An intershaft squeeze-film damper could be used to decrease the loading and cross excitation vibration. Hibner et al. [1, 2], Courage [3], and Gunter et al. [4] have carried out analytical and experimental investigations, respectively, in this field. However, to this date, this damping device has not been successfully incorporated into the real gas turbine engine.

The component mode synthesis method has been extensively applied to the analysis of large rotor systems. Childs [5], Gunter et al. [4, 6], and Nelson et al. [7] have utilized this method. In the component mode synthesis method, the large rotor-case system is first subdivided into smaller components and the component modes for each are individually derived. The total system is then characterized in the modal coordinates using a reduced number of component modes from each component.

In this paper, the functional expansion component synthesis method is used for calculating the transient response of a dual-rotor gas turbine engine equipped with a flexible intershaft squeeze-film damper. The dual-rotor system is first divided into several parts. In each part the model character is determined by a modal expansion. The total structure is then constructed by applying the constraint and/or connecting conditions among the components.

The transient response of the rotor system due to a suddenly applied imbalance in the high-pressure turbine is calculated for different steady-speed operations. The damping effects of the intershaft damper and stability of the rotor system are investigated.

Computer Model of Dual-Rotor System

Figure 1 represents a schematic drawing of the jet engine dual rotor used in this analysis. The engine consists of two coaxial rotors. The inner core rotor is called the low-pressure rotor (LP rotor) and is supported by one main (rolling) bearing. The low-pressure compressor is driven by a low-pressure turbine. They are connected with each other by key coupling. The outer core rotor is called the high-pressure rotor (HP rotor) and is supported by two main (rolling) bearings. There are two intershaft bearings, front and rear rolling bearings, connecting the LP rotor and HP rotor. A flexible intershaft squeeze film damper is added into the rear intershaft bearing.

Figure 2 represents the computer model. The rotor system is partitioned into three components. The LP rotor is composed

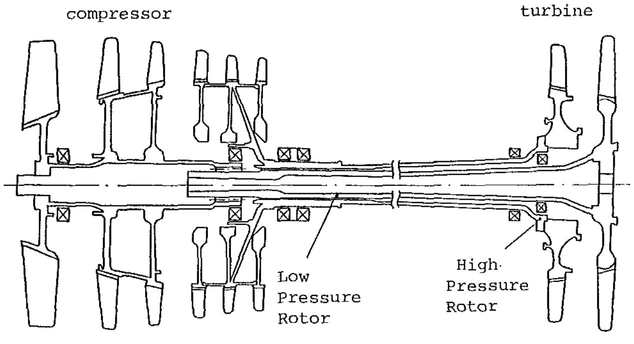

Fig. 1 Schematic drawing of the jet engine dual rotor

Contributed by the Gas Turbine Division and presented at the 1985 Beijing International Gas Turbine Symposium and Exposition, Beijing, People's Republic of China, September 1-7, 1985. Manuscript received at ASME Headquarters May 13, 1985. Paper No. 85-IGT-38.

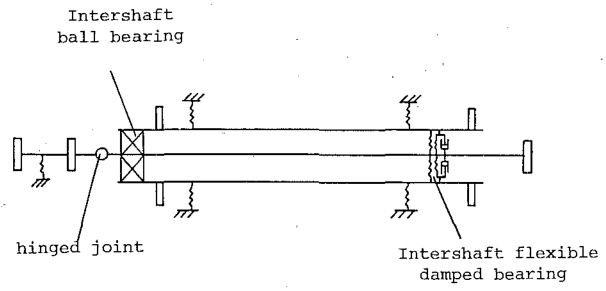

Fig. 2 Computer model of the dual-rotor jet engine

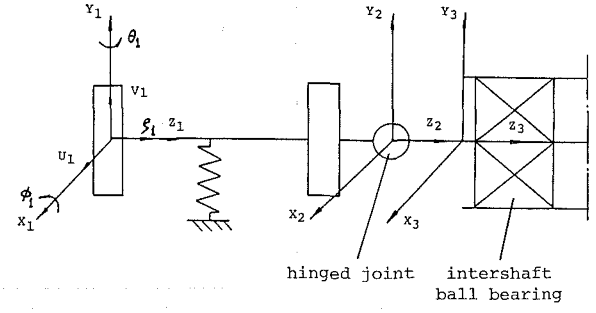

Fig. 3 Coordinate systems for rotor analysis

of two components, 1 and 2, which are separated by a hinged joint. The HP rotor is considered as one component (3).

The axial and torsional motions of the rotor system are neglected, and the motions of the two translational directions and the two rotational directions are assumed symmetric, respectively.

The gyroscopic effects of disks are considered. The stiffnesses of the case are represented by three sets of isotropic bearing support stiffness which were assumed to have a stiffness of 2.0 × 10^4 kg/cm each. The three main support bearings were taken to have damping of 0.2 kg-s/cm.

The inner journal and the outer ring of the squeeze film damper rotate with the LP rotor at the same speed and same direction. The damper has no end seals or oil grooves and has a length of 2.4 cm, and an outer diameter of 6 cm. The flexible intershaft support is assumed to have a stiffness of 2.0 × 10^4 kg/cm.

A ratio of the rotating speeds of 1.1 between HP rotor and LP rotor is used in the analysis.

Calculating Approach

Coordinate Systems. The x_1-y_1-z_1, x_2-y_2-z_2, x_3-y_3-z_3 coordinate systems are Cartesian coordinate systems fixed in space as shown in Fig. 3. They are located at the left end of LP rotor, at the hinged-joint position, and at the left end of HP rotor, respectively.

The lateral displacement of shafts along the x_i, y_i, z_i directions are indicated by u_i, v_i, ζ_i, respectively. The angular displacements about x_i, y_i are given by ϕ_i, θ_i, respectively. The index i is equal to 1, 2, 3, which correspond to three sets of component coordinate systems.

Assuming the motion of the rotor system is separable in space and time, the lateral displacement fields $u(\zeta, t)$ and $v(\zeta, t)$ can be written as an expansion of truncated sets of shape functions, $\beta_1, \beta_2, \ldots, \beta_n$, and n generalized coordinates, $\eta_1, \eta_2, \ldots, \eta_n$. The shape function terms are functions of the displacement along the shaft, while the generalized coordinates are the time-dependent functions to be evaluated.

The expansions can be written in a matrix form which is applicable for an expansion containing any number of terms as follows:

$$u(\zeta, t) = [\beta_u](\eta_u)$$
$$v(\zeta, t) = [\beta_v](\eta_v) \qquad (1)$$

Using Euler beam theory, the angular displacements can be written as follows:

$$\phi(\zeta, t) = [\beta_v'](\eta_v)$$
$$\theta(\zeta, t) = [\beta_u'](\eta_u) \qquad (2)$$

Equations (1) and (2) are combined to form a single matrix expression as follows:

$$\begin{bmatrix} u \\ v \\ \phi \\ \theta \end{bmatrix} = \begin{bmatrix} [\beta_u] & \\ & [\beta_v] \\ & [\beta_v'] \\ [\beta_u'] & \end{bmatrix} (\eta) = [H_z](\eta) \qquad (3)$$

The matrix $[H_z]$ is then a transformation matrix from Cartesian to generalized coordinates at any point along the shaft. For this procedure, the first three mode shapes of the

Nomenclature

b = support damping
c = clearance of the damper
D = damper outer diameter
EI = shaft stiffness
F_x, F_y = hydrodynamic forces in x and y direction
J_p, J_T = polar moment and transverse moment of inertia of a disk
l = shaft length
L = damper length
m_d = disk mass
m_r = shaft mass per unit length
R = inner journal radius of the damper
U, V = lateral displacement of the shaft
θ, ϕ = angular displacement of the shaft
μ = damper viscosity
Ω = rotor spin speed
Ω_L = LP rotor spin speed
Ω_H = HP rotor speed
ω_b = outer ring spin speed of the damper
ω_j = inner journal spin speed of the damper
$[C]$ = support damping matrix
$[C_Q]$ = generalized damping matrix of the coupled system
$(\mathbf{F})$ = discrete force vector
$[G]$ = generalized gyroscopic matrix of disks
$[G_Q]$ = generalized gyroscopic matrix of the coupled system
$[H_Z]$ = transformation matrix at point z
$[K_R]$ = generalized stiffness matrix of the shaft
$[K_S]$ = generalized stiffness matrix of the support
$[K_Q]$ = generalized stiffness matrix of the coupled system
$[M_R]$ = generalized mass matrix of the shaft
$[M_D]$ = generalized mass and moment of inertia matrix of disks
$[M_Q]$ = generalized mass matrix of the coupled system
$(\mathbf{N})$ = generalized forces vector
$(\mathbf{N}_Q)$ = generalized forces vector of the coupled system
$(\mathbf{q})$ = generalized independent coordinate vector
(η) = generalized collection vector
$[\alpha]$ = transformation matrix relating $(\mathbf{q})$ and (η)
$[\beta]$ = shape function matrix

dual-rotor system components were first evaluated using a numerical transfer matrix method. The three sets of polynomials (six for each) were then fitted and used as shape functions, $\beta_{u_{i1}}, \beta_{u_{i2}}, \beta_{u_{i3}}, \beta_{v_{i1}}, \beta_{v_{i2}}, \beta_{v_{i3}}$, for each component.

Equations of Motion for Single Component. The equations of motion for each component are developed in terms of generalized coordinate and take a general form:

$$[M_R + M_D]_{6\times 6}(\ddot{\eta})_{6\times 1} + [G + C]_{6\times 6}(\dot{\eta})_{6\times 1} + [K_R + K_S]_{6\times 6}(\eta)_{6\times 1} = (\mathbf{N})_{6\times 1} \tag{4}$$

The kinetic energy of the shaft is

$$T = \frac{1}{2}\int_0^1 m_r(\dot{u})^2 d\zeta + \frac{1}{2}\int_0^1 m_r(\dot{v})^2 d\zeta \tag{5}$$

Replacing the velocities with their expansions in the generalized coordinates

$$\begin{aligned}[\dot{u}] &= [\beta_u](\dot{\eta}_u)\\ [\dot{v}] &= [\beta_v](\dot{\eta}_v)\end{aligned} \tag{6}$$

and integrating yields

$$T = \frac{1}{2}(\dot{\eta})^T[M_R](\dot{\eta}) \tag{7}$$

where $[M_R]$ is the shaft inertia matrix. The potential energy for the shaft is

$$P = \frac{1}{2}\int_0^1 EI(u'')^2 d\zeta + \frac{1}{2}\int_0^1 EI(v'')^2 d\zeta \tag{8}$$

Replacing the displacement derivatives with their expansions in the generalized coordinates

$$\begin{aligned}[u''] &= [\beta_u''](\eta_u]\\ [v''] &= [\beta_v''](\eta_v]\end{aligned} \tag{9}$$

and integrating yield

$$P = \frac{1}{2}(\eta)^T[K_R](\eta) \tag{10}$$

where $[K_R]$ is the shaft stiffness matrix.

The inertial and gyroscopic forces of the disk applied on the shaft in the Cartesian fixed coordinate can be expressed as follows:

$$\begin{bmatrix} f_x \\ f_y \\ M_x \\ M_y \end{bmatrix} = \begin{bmatrix} m_d & & & \\ & m_d & & \\ & & J_T & \\ & & & J_T \end{bmatrix} \begin{pmatrix} \ddot{x} \\ \ddot{y} \\ \ddot{\phi} \\ \ddot{\theta} \end{pmatrix} + \begin{bmatrix} & J_p\Omega \\ -J_p\Omega & \end{bmatrix} \begin{pmatrix} \dot{x} \\ \dot{y} \\ \dot{\phi} \\ \dot{\theta} \end{pmatrix} \tag{11}$$

Converting this to generalized coordinates by use of the transformation matrix yields

$$(N_D) = [M_D](\ddot{\eta}) + [G](\dot{\eta}) \tag{12}$$

Similarly, the generalized stiffness and damping matrices of supports and generalized forces matrix at any point along the shaft can be obtained by using transformation matrix $[H_Z]$.

$$[K_S] = [H_Z]^T \begin{bmatrix} K_S & & & \\ & K_S & & \\ & & 0 & \\ & & & 0 \end{bmatrix} [H_Z] \tag{13}$$

$$[C] = [H_Z]^T \begin{bmatrix} b & & & \\ & b & & \\ & & 0 & \\ & & & 0 \end{bmatrix} [H_Z] \tag{14}$$

$$(\mathbf{N}) = [H_Z]^T(\mathbf{F}) \tag{15}$$

Calculating the Hydrodynamic Forces of the Squeeze-Film Damper Bearing. The basic bearing equation is the Reynolds equation, which is derived from the Navier-Stokes equation for incompressible flow. The short bearing approximation is used here.

The total force components in the x and y directions in fixed coordinates are obtained by integrating the pressure over the entire journal surface. The force expressions [8] are as follows:

$$\begin{bmatrix} F_x \\ F_y \end{bmatrix} = \frac{-\mu R L^3}{2} \int_0^{2\pi} \frac{(\omega_b + \omega_j)(x\sin\theta - Y\cos\theta) - 2(\dot{x}\cos\theta + \dot{y}\sin\theta)}{(c - x\cos\theta - Y\sin\theta)} \times \begin{bmatrix} \cos\theta \\ \sin\theta \end{bmatrix} d\theta \tag{16}$$

It should be noted that for the intershaft squeeze-film damper, $\omega_b = \omega_j = \Omega_L$ (the rotating speed of LP rotor) and the force components in the x and y directions acting on the inner journal and the outer ring of damper bearing are equal and opposite to each other.

As described previously, the hydrodynamic forces can be converted from the Cartesian fixed coordinate into the generalized coordinate by using the transformation matrix $[H_Z]$ at the location of intershaft damper.

Combining and Coupling System: Equations of Motion [9]. Using three component equations of motion, the equations of motion for the collection of components can be written in the form

$$\begin{bmatrix} [M_1] & & \\ & [M_2] & \\ & & [M_3] \end{bmatrix}_{18\times 18} (\ddot{\eta})_{18\times 1} + \begin{bmatrix} [G_1 + C_1] & & \\ & [G_2 + C_2] & \\ & & [G_3 + C_3] \end{bmatrix}_{18\times 18} (\dot{\eta})_{18\times 1} + \begin{bmatrix} [K_1] & & \\ & [K_2] & \\ & & [K_3] \end{bmatrix}_{18\times 18} (\eta)_{18\times 1} = \begin{bmatrix} (N_1) \\ (N_2) \\ (N_3) \end{bmatrix}_{18\times 1} \tag{17}$$

Equation (17) represents a set of disconnected component equations. The implication is that the vector (η) must contain a certain number of redundant degrees of freedom. These redundant degrees of freedom correspond to various constraints. In order to eliminate the redundant coordinates the constraint conditions among the components must be used.

In this dual-rotor system there is a flexible spring in the rear intershaft damper position between component 2 and component 3. The generalized coupling forces can be added directly into the stiffness terms of the combined system equations of motion by using the transformation matrix $[H_Z]$ to convert from the discrete coordinates into the generalized coordinates at the location of intershaft damper. The expressions are as follows:

$$\begin{bmatrix} [K_1] & & \\ & [K_2 + K_{C2}] & [K_{C23}] \\ & [K_{C32}] & [K_3 + K_{C3}] \end{bmatrix}$$

There are two constraint conditions between component 1 and component 2, i.e., the displacements in the x and y directions at the hinged-joint position are equal across the hinge.

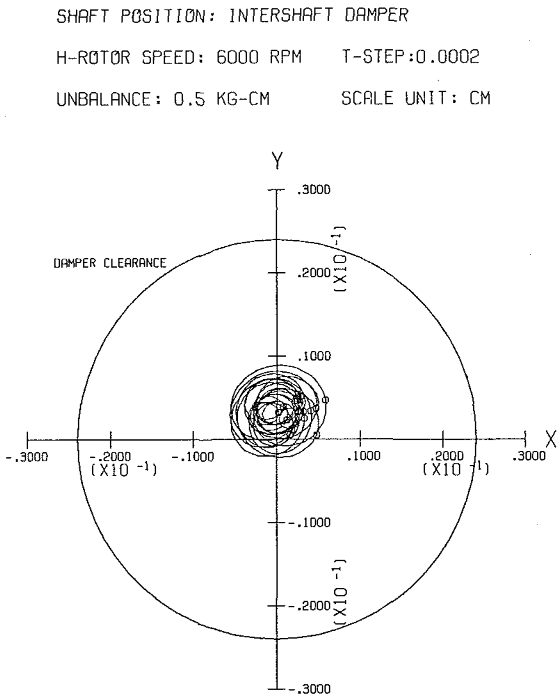

Fig. 4 Relative motion orbit at intershaft damper speed = 6000 rpm, clearance = 0.024 cm, imbalance = 0.5 kg·cm

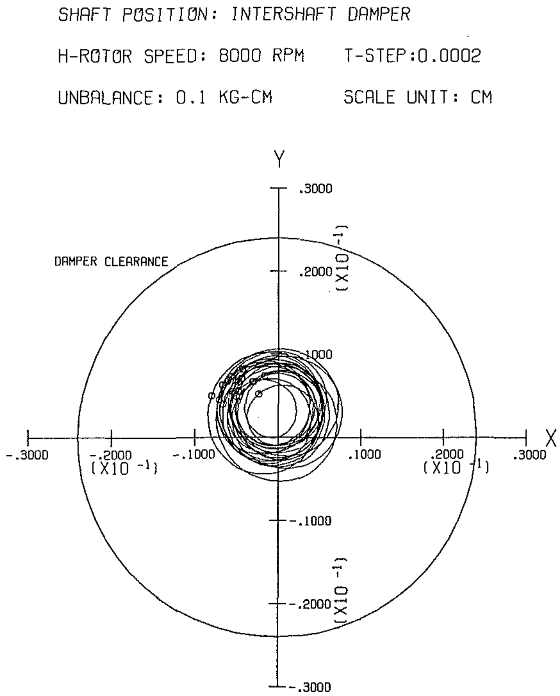

Fig. 5 Relative motion orbit at intershaft damper speed = 8000 rpm, clearance = 0.024 cm, imbalance = 0.1 kg·cm

There are two constraint conditions between component 2 and component 3, i.e., the displacements in x and y direction at the front intershaft bearing position are equal.

The constraint equations can be written in the matrix form

$$[S](\eta)=0 \tag{18}$$

where $[S]$ is a 4×18 matrix. Divide the vector η into the 14-dimensional vector $\mathbf{q}$ of independent variables and four-dimensional vector η_c of dependent variables and partition the matrix $[S]$ as follows:

$$[S]=[A\ B] \tag{19}$$

where B is a nonsingular 4×4 matrix and A is a 4×14 matrix. Equation (23) can be then written as

$$[A](\mathbf{q})+[B](\eta_c)=0 \tag{20}$$

Equation (20) yields

$$(\eta_c)=-[B]^{-1}[A](\mathbf{q}) \tag{21}$$

so that

$$(\eta)_{18\times1}=\frac{\mathbf{q}}{\eta_i}=\left[\frac{[I]}{-[B]^{-1}[A]}\right](\mathbf{q})=[\alpha]_{18\times14}(\mathbf{q})_{14\times1} \tag{22}$$

where $[\alpha]$ is a transformation matrix which represents the relation between $\eta(t)$ and $\mathbf{q}(t)$. Therefore, the coupled system equations of motion can be obtained as follows:

$$\begin{aligned}
&[\alpha]^T\begin{bmatrix}[M_1] & & \\ & [M_2] & \\ & & [M_3]\end{bmatrix}[\alpha](\ddot{\mathbf{q}})\\
&+[\alpha]^T\begin{bmatrix}[G_1+C_1] & & \\ & [G_2+C_2] & \\ & & [G_3+C_3]\end{bmatrix}[\alpha](\dot{\mathbf{q}})\\
&+[\alpha]^T\begin{bmatrix}[K_1] & & \\ & [K_2+K_{C2}] & [K_{C23}]\\ & [K_{C32}] & [K_3+K_{C3}]\end{bmatrix}[\alpha](\mathbf{q})\\
&=[\alpha]^T\begin{Bmatrix}(N_1)\\ (N_2)\\ (N_3)\end{Bmatrix}
\end{aligned} \tag{23}$$

Written in simpler notation this is

$$[M_Q]_{14\times14}(\ddot{\mathbf{q}})_{14\times1}+[G_Q+C_Q]_{14\times14}(\dot{\mathbf{q}})_{14\times1}+[K_Q]_{14\times14}(\mathbf{q})_{14\times1}=(\mathbf{N}_Q)_{14\times1} \tag{24}$$

Solving Transient Response of Dual-Rotor Systems. In order to examine the nonlinear characteristics of the intershaft squeeze-film damper, it is necessary to investigate the transient response of the system.

The transient response of the whole dual-rotor system under the effect of the system forces can be determined by integrating the coupled system equations of motion (24) forward in time where the squeeze-film hydrodynamic forces are calculated at each time interval by an integration of the Reynolds equation.

In this procedure, both Runga-Kutta and modified Newmark predictor-corrector methods are used to integrate the coupled equations of motion.

Typical Calculation Results

The transient responses of the rotor system due to a suddenly applied imbalance under different steady-speed operations were calculated and the response characteristics for different clearances of the intershaft squeeze-film damper under different rotor imbalance levels were examined.

The LP rotor was taken to be balanced and the imbalance was applied on the front stage compressor of HP rotor. Except for the clearance, the other parameters of the damper were kept unchanged.

The rotating speeds of HP rotor were 6000, 8000, 10,000, and 12,000 rpm, respectively. The transient motion was started initially at zero displacement and zero velocity.

The transient orbits of the outer ring and damper relative to the inner journal of damper are plotted in the reference clearance circle where the time marks on the orbits indicate one spin revolution of the HP rotor. The results of these calculations are shown in Table 1 and Figs. 4-9.

Figure 4 shows the response orbits for the last 20 cycles in a total of 80 cycles of simulation. The rotating speed of the HP rotor, the clearance of the damper, and the imbalance level of the rotor are equal to 6000 rpm, 0.024 cm, and 0.5 kg-cm,

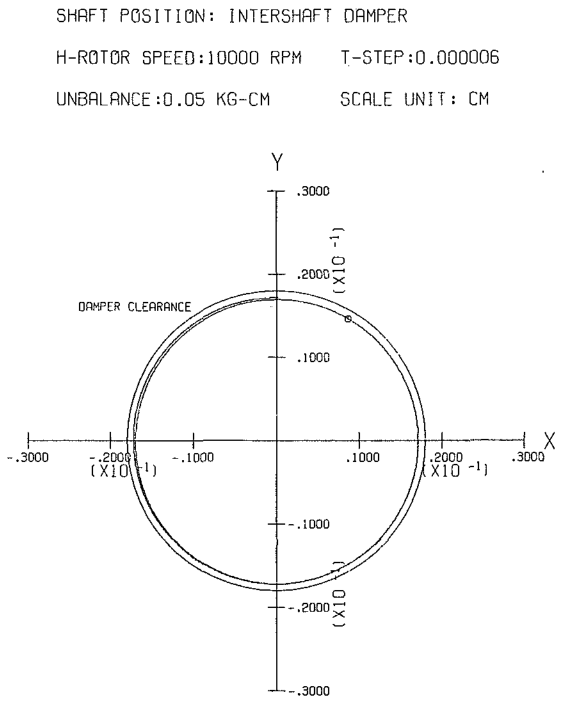

Fig. 6 Relative motion orbit at intershaft damper speed = 10,000 rpm, clearance = 0.018 cm, imbalance = 0.05 kg·cm

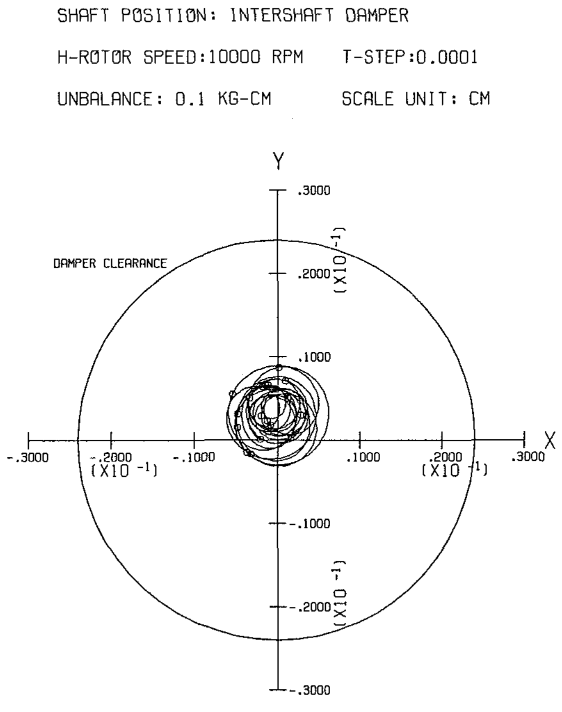

Fig. 7 Relative motion orbit at intershaft damper speed = 10,000, clearance = 0.024 cm, imbalance = 0.1 kg·cm

respectively. It can be seen that the rotor system is stable and a steady-state circular orbit is developed after 80 cycles.

Figure 5 shows the response orbits for the last 20 cycles in a total of 80 cycles of simulation. The clearance of the damper is the same as above, while the rotating speed of HP rotor is increased from 6000 to 8000 rpm. The imbalance level of the rotor is reduced from 0.5 to 0.1 kg-cm.

The rotor system is again stable and the orbits have spiraled into an equilibrium eccentricity. The maximum response amplitude observed during the initial transient motion is about 1.5 times the size of the steady-state orbit.

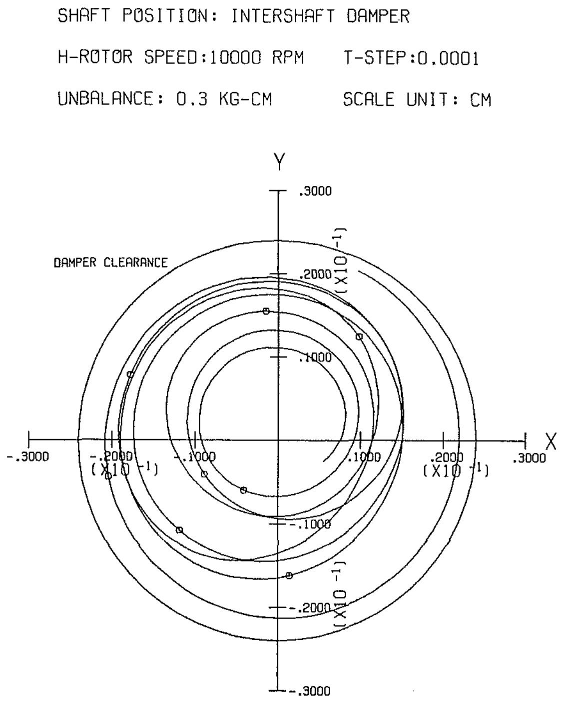

Fig. 8 Relative motion orbit at intershaft damper speed = 10,000 rpm, clearance = 0.024 cm, imbalance = 0.3 kg·cm

Comparing the orbits of Fig. 4 with the orbits of Fig. 5, it can be seen that the phase angle of vibration is changed near 180 deg, which indicates that there is a critical speed between 6000 and 8000 rpm. A comparison of this result with an eigenvalue calculation of a rotor system gives good agreement.

Figures 6 and 7 represent the transient orbits at 10,000 rpm under different clearances of the damper and different imbalance levels. Shown clearly in these figures are both stable orbits (a stable equilibrium position is reached) and unstable orbits (a limit cycle is formed). Which type appears is dependent on the clearance of the damper and the imbalance level of the rotor.

Figure 6 shows the system is unstable when the clearance is 0.018 cm (c/D = 0.15 percent) and the imbalance is 0.05 kg-cm. After 30 cycles the orbits spiral outward and produce a large eccentricity. Six cycles later a limit cycle is formed in which approximately 95 percent of bearing clearance is taken up.

It should be noted that at high eccentricities very small integration time steps are required to retain high accuracy in the solution because of the rapid variation in the bearing damper forces.

Figures 7 and 8 show the system is stable for the clearance of 0.024 cm (c/D = 0.2 percent) and an imbalance of 0.1 kg-cm. However an increase of imbalance to 0.3 kg-cm produces unstable orbits (will form a limit cycle).

In the above cases, when the eccentricity ratio (the ratio between the relative motion orbit of the damper and the clearance of the damper) are greater than a certain value (such as 0.4) [8, 10], the radial stiffness of damper bearing increases at a much faster rate than the damper and it produces a highly nonlinear rotor system which will result in system instability and limit cycles will be formed at a large eccentricity ratio. In this case the damper is usually undesirably overloaded.

Figure 9 shows the transient response at 12,000 rpm for different clearances of the damper and different imbalance levels of the rotor. It is seen that the system is always unstable even if the rotor imbalance is equal to zero. It is shown clearly in these figures that the orbits are spiraling outward at a whirl

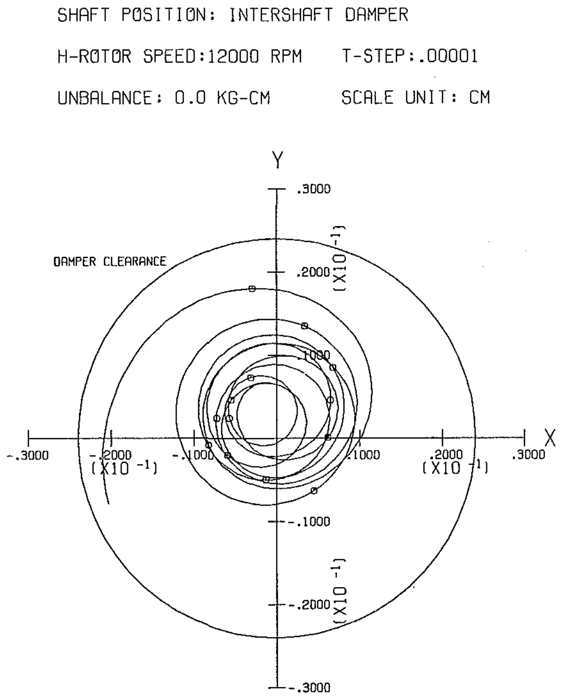

Fig. 9 Relative motion orbit at intershaft damper speed = 12,000 rpm, clearance = 0.024 cm, imbalance = 0.0 kg·cm

rate close to one-half operating speed indicating oil whirl. This result indicates that when HP rotor speed reaches 12,000 rpm, it has already exceeded the threshold speed of the rotor system.

Conclusions

The use of the component modal expansion technique with interconstraints is a convenient method to model the complete dynamic characteristics of a large twin-shaft rotor system. The component modes can be determined by a convenient transfer matrix method (or other methods). The resulting model is suitable for propagation solutions using numerical integration.

The introduction of an intershaft squeeze-film damper into the rotor system produces an instability threshold speed where the whirling speed is nonsynchronous with the shaft speed.

At shaft speeds below the threshold speed the intershaft squeeze-film damper is effective in reducing the synchronous whirl vibration due to the rotor imbalance. An important parameter was the damper clearance with larger clearance permitting greater imbalance (it should be noted that there will be an upper limit to effective clearance increase).

If the shaft imbalance is too large the effectiveness of the squeeze-film damper is lost and the rotor system becomes unstable with the whirling speed becoming nonsynchronous with the shaft speed.

Acknowledgments

The authors would like to thank Professor Litang Yan for his help and encouragement.

References

1 Hibner, D. H., Kirk, R. G., and Buono, D. F., "Analytical and Experimental Investigation of the Stability of Intershaft Squeeze Film Dampers—Part 1: Demonstration of Instability," ASME Journal of Engineering for Power, Vol. 99, Jan. 1977.

2 Hibner, D. H., Bansal, P. N., and Buono, D. F., "Analysis and Experimental Investigation of the Stability of Intershaft Squeeze Film Dampers—Part 2: Control of Instability," ASME *Journal of Mechanical Design*, Vol. 100, July 1978.

3 Courage, J. B., "Experimental Study of an Inter-Shaft Squeeze Film Bearing," The Second International Vibration of Rotating Machinery Conference, 1980.

4 Li, D. F., and Gunter, E. J., "Component Mode Synthesis of Large Rotor System," ASME Journal of Engineering for Power, Vol. 104, July 1982.

5 Childs, D. W., "High-Pressure Fuel Turbopump Rotor-Dynamic Instability Problem," ASME Journal of Engineering for Power, Vol. 100, No. 1, 1978.

6 Li, D. F., and Gunter, E. J., "A Study of the Modal Truncation Error in the Component Mode Analysis of a Dual-Rotor System," ASME Journal of Engineering for Power, Vol. 104, July 1982.

7 Nelson, H. D., and Meachan, W. L., "Transient Analysis of Rotor-Bearing Systems Using Component Mode Synthesis," ASME Paper No. 81-GT-110.

8 Barrett, L. E., and Gunter, E. J., "Steady-State and Transient Analysis of a Squeeze Film Damper Bearing for Rotor Stability," NASA CR-2548, May 1975.

9 Meirovitch, L., *Computational Methods in Structural Dynamics*, Sijthoff & Noordhoff, Alphen aan den Rijn, The Netherlands, Rockville, USA, 1980, pp. 384-401.

10 Gunter, E. J., Barrett, L. E., and Allaire, P. E., "Design of Nonlinear Squeeze-Film Dampers for Aircraft Engines," ASME *Journal of Lubrication Technology*, Jan. 1977.

Xuehai Li[1]
Graduate Research Assistant.

D. L. Taylor
Associate Professor.

Sibley School of Mechanical and
Aerospace Engineering,
Cornell University,
Ithaca, NY 14853

Perturbation Solutions for Eccentric Operation of Squeeze Film Damper Systems

The study focuses on the effect of a small unidirectional load such as comes from imperfect balance between preloading on centering springs and gravitational load on squeeze film dampers. A rigid rotor-squeeze film damper system is considered, and a thorough study of the synchronous motion of the system is performed. Two perturbation solutions are developed: one for large speed and one for small speed. The perturbation solutions are shown to be in good agreement with numerical simulation and published experimental results.

Introduction

Squeeze film dampers have been widely used in high-speed rotating machinery, principally because of their ability to suppress the resonent forced response of rotor dynamic systems. The schematic of a simplified model for a rigid-rotor-squeeze film damper is shown in Fig. 1. The rotating shaft is mounted in a rolling element so that the rotary motion of the journal about its center can be eliminated. Usually radial retainer springs are used to support the journal and to provide static load capacity of the system. In most cases the springs are preloaded vertically so that the equilibrium position of the rotor, under a gravity load, is centered in the clearance space.

This simplified model has been investigated for at least twenty years. Especially since the 1970s, many theoretical and experimental works have been published on various aspects of the problem [1]. Mohan [2] studied the system with π-film pressure distribution. He pointed out the existence of three possible stable modes. Two of them are synchronous circular orbits. The third mode is a noncircular and nonsynchronous orbit, which is observed with appropriate initial conditions and low values of bearing parameter. He also pointed out the occurrence of a jump phenomenon. Simansiri [3] verified the synchronous motion and the jump phenomenon by experiment. Taylor [4, 5] studied the transient and steady-state behavior of the synchronous motion and gave a closed-form solution for centered circular orbits given arbitrary system parameters.

Practically, it is very difficult to perfectly balance out the gravity load by preloading springs. A few researchers have considered this more realistic system. Tonnesen [6] showed experimentally the synchronous noncircular orbit at low frequency with large offset and the tendency of self-centering and circularizing of the orbits with increasing frequency and amplitude of unbalance force. Pan's work [7] seems to be the only theoretical treatment of the subject. He tried to use an analytical method to interpret the experimental results by Tonnesen.

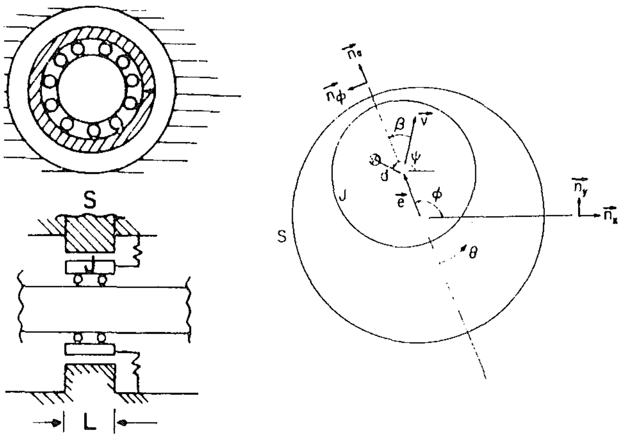

Fig. 1 A squeeze film damper system

Most theoretical work has focused on the synchronous motion of perfectly preloaded systems. The phenomenon has been studied thoroughly, and the theoretical predictions are confirmed by both experiments and numerical simulation. Although there have been some experiments on the imperfectly preloaded system, there is no appropriate theoretical interpretation of the phenomenon even though the imperfectly preloaded system is a more realistic model.

The objective of this research is an analytical description of the response of the imperfectly preloaded system. A perturbation method is applied, assuming that the gravitational residual is "small." The perturbation solutions for the behavior of the system are derived, evaluated, and verified by numerical simulation and published experimental evidence of other researchers.

Derivation of the Perturbation Solutions

The equations of motion for the system are taken directly from [5] with the additional consideration of a gravitational

---

[1] Currently Senior Research Engineer, Power Systems Research Department, General Motors Research Laboratories, Warren, MI 48090-9055.

Contributed by the Gas Turbine Division of The American Society of Mechanical Engineers and presented at the 31st International Gas Turbine Conference and Exhibit, Düsseldorf, Federal Republic of Germany, June 8–12, 1986. Manuscript received at ASME Headquarters February 7, 1986. Paper No. 86-GT-164.

residual. The assumptions in the derivation of equations of motion are:

1 The π-film pressure distribution and short bearing approximation are valid;
2 effects of the rolling element of the bearing are negligible;
3 the damper is open ended, and the ambient pressure is taken as zero;
4 there is no external pressurization;
5 the gyroscopic effect is negligible.

Using the polar coordinate system given in Fig. 1, it can be shown that the equations of motion of the system are

$$\begin{aligned} \epsilon'' &= -\lambda(\epsilon' I_3 + \epsilon\phi' I_1) - \epsilon(1-\phi'^2) \\ &\quad + \delta\Omega^2 \cos(\Omega t - \phi) - \alpha \sin\phi \qquad (1) \\ \phi'' &= \frac{1}{\epsilon}\,[-\lambda(\epsilon' I_1 + \epsilon\phi' I_2) - 2\epsilon'\phi' \\ &\quad + \delta\Omega^2 \sin(\Omega t - \phi) - \alpha\cos\phi] \end{aligned}$$

where

$$\begin{aligned} I_1 &= \int_{\theta_1}^{\theta_1+\pi} \frac{\sin\theta\cos\theta}{(1+\epsilon\cos\theta)^3}\,d\theta \\ I_2 &= \int_{\theta_1}^{\theta_1+\pi} \frac{\cos^2\theta}{(1+\epsilon\cos\theta)^3}\,d\theta \qquad (2) \\ I_3 &= \int_{\theta_1}^{\theta_1+\pi} \frac{\sin^2\theta}{(1+\epsilon\cos\theta)^3}\,d\theta \\ \theta_1 &= -\tan^{-1}\left(\frac{\epsilon'}{\epsilon\phi'}\right) \end{aligned}$$

The equations have been nondimensionalized as shown in the Nomenclature. The rotating unbalance is given by δ, and the gravitational residual by α.

The I are known as journal-bearing integrals (JBI), and can be integrated by recursive formulas. In general, JBI are very complicated functions of eccentricity, the rate of change of eccentricity, and the rotational speed of the journal center.

With $\alpha = 0$, one solution for the synchronous motion of the system can be shown to be a centered circular orbit. In this case, equation (2) reduces to $J_i = \int_{\pi}^{2\pi}(\ )\,d\theta$ which can be evaluated in closed form as

$$J_1 = \frac{2\epsilon}{(1-\epsilon^2)^2}$$

$$J_2 = \frac{\pi}{2(1-\epsilon^2)^{3/2}} \qquad (3)$$

$$J_3 = \frac{\pi(1+2\epsilon^2)}{2(1-\epsilon^2)^{5/2}}$$

Another convenient coordinate system is described by the transformation of $\gamma = \Omega - \phi$. Effectively, this is a change from a fixed reference frame to a rotating reference frame, and consequently, equation (1) becomes

$$\begin{aligned} \epsilon'' &= -\lambda(\epsilon' I_3 + \epsilon(\Omega-\gamma')I_1) \\ &\quad - \epsilon(1-(\Omega-\gamma')^2) + \delta\Omega^2\cos\gamma - \alpha\sin(\Omega t - \gamma) \\ \gamma'' &= \frac{1}{\epsilon}[\lambda(\epsilon' I_1 + \epsilon(\Omega-\gamma')I_2) \\ &\quad + 2\epsilon'(\Omega-\gamma') - \delta\Omega^2\sin\gamma + \alpha\cos(\Omega t-\gamma)] \qquad (4) \end{aligned}$$

Note that equation (4) has an autonomous form when $\alpha = 0$.

If α is "small," its effect on the synchronous motion of the perfectly perloaded system can be viewed, from the rotating reference frame, as a periodic excitation about the fixed points of the system, which are circular orbits. Applying the perturbation method to the problem, the first-order approximation to the solution of the equations of motion is

$$\begin{aligned} \epsilon &= \epsilon_0 + \alpha\epsilon_1 \\ \gamma &= \gamma_0 + \alpha\gamma_1 \end{aligned} \qquad (5)$$

The usual perturbation technique is followed by substituting equation (5) into equation (2), and expanding in equation (2) as a Taylor series about $\alpha = 0$. Considering the synchronous case, and retaining terms through the first order, the I_i have the forms of

$$\begin{aligned} I_1 &= J_1 + \alpha J_{11}\epsilon_1 \\ I_2 &= J_2 + \alpha J_{21}\epsilon_1 \\ I_3 &= J_3 + \alpha J_{31}\epsilon_1 \end{aligned} \qquad (6)$$

where J_{i1} is the derivative of J_i with respect to ϵ evaluated at ϵ_0.

Substituting equations (5) and (6) into equation (4), two sets of equations can be obtained in terms of order α^0 and α^1

$$\begin{aligned} O(\alpha^0):\quad \epsilon_0'' &= -\lambda(\epsilon_0' J_3 + \epsilon_0(\Omega-\gamma_0')J_1) \\ &\quad - \epsilon_0(1-(\Omega-\gamma_0')^2) + \delta\Omega^2\cos\gamma_0 \\ \gamma_0' &= \frac{1}{\epsilon_0}\,[\lambda(\epsilon_0' J_1 + \epsilon_0(\Omega-\gamma_0')J_2) \\ &\quad + 2\epsilon_0'(\Omega-\gamma_0') - \delta\Omega^2\sin\gamma_0] \qquad (7) \end{aligned}$$

Nomenclature

a, A, b, B = coefficients of perturbed equations
C = bearing clearance, m
d = offset of mass center of journal, m
e = offset of journal center, m
f = approximated fluid film force
F = fluid film force, kgm/s^2
h = film thickness, m
I_i = journal-bearing integrals
J_i = journal-bearing integrals for synchronous circular orbit
k = stiffness of retainer spring, kg/s^2
L = length of bearing, m
m = mass of rotor, kg
R = radius of journal, m
t = $\omega_1\tau$ = time
α = $\Delta mg/kC$ = gravitational residual
γ = $(\Omega t - \phi)$
δ = d/C = amplitude of unbalance on journal
Δmg = gravitational residual, kgm/s^2
ϵ = e/C = eccentricity of journal center
λ = $\mu L^3 k'/C^3 m\omega_1$ = bearing parameter
μ = coefficient of viscosity of fluid, kg/ms
τ = time, s
ϕ = precession angle of journal center
ω_1^2 = k/m for rigid rotor system
ω = external excitation frequency, 1/s
Ω = ω/ω_1 = external excitation frequency
Ωt = position of unbalance on journal
$(\dot{\ })$ = $d/d\tau$ = operator, 1/s
$(\ )'$ = d/dt = operator

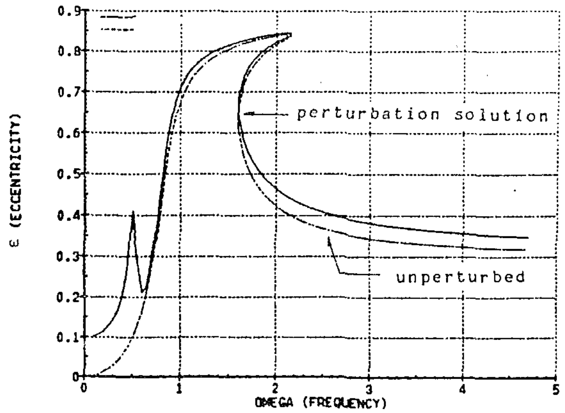

Fig. 2 Speed response by perturbation scheme, $\alpha = 0.1$, $\delta = 0.3$, $\lambda = 0.072$

$$O(\alpha^1): \quad \epsilon_1'' = a_1\epsilon_1 + a_2\epsilon_1' + a_3\gamma_1 + a_4\gamma_1' - \sin(\Omega t - \gamma_0)$$

$$\gamma_1'' = b_1\epsilon_1 + b_2\epsilon_1' + b_3\gamma_1 + b_4\gamma_1' + \cos(\Omega t - \gamma_0) \qquad (8)$$

where a_i and b_i are functions of the $O(\alpha^0)$ solution, derived in [8] and given in the Appendix.

Equation (7) is the unperturbed equations, which are the equations of motion for the perfectly preloaded system; and equation (8) is a set of differential equations linearized about the solution of equation (7) subject to a harmonic excitation from the projection of gravitational residual in the (ϵ, γ) coordinate system. Since a synchronous centered orbit for the unperturbed system is constant, the coefficients of (8) are constants, and the perturbed solution is a simple harmonic function with the external excitation frequency. The total solution is the superposition of a constant plus a harmonic function of time, and is still synchronous with the external excitation.

Figure 2 is the frequency response obtained by the perturbation method described above. It shows that this method encountered some problems. The amplitude of the unperturbed solution approaches zero at low frequencies. Therefore, no matter how small α is, there is always an Ω below which the unperturbed solution is smaller than the perturbed one. That violates the basic principle of the perturbation method. In addition, equation (8) exhibits a pseudo-resonance, at about $\Omega = 0.5$, which does not exist in the original system. Thus the perturbation solution gives false results around half frequency.

To complement the preceding perturbation solution, another perturbation scheme is used. In the fixed reference frame, Ω^2 is actually a small parameter at low frequencies, and the unbalance force can be viewed as an external disturbance which is small relative to the gravitational residual. Two different sets of equations are obtained in terms of order $(\Omega^2)^0$ and $(\Omega^2)^1$

$$O(\Omega^2)^0: \quad \epsilon_0'' = -\lambda(\epsilon_0' J_3 + \epsilon_0\phi_0' J_1) - \epsilon_0(1 - \phi_0'^2) - \alpha \sin\phi_0$$

$$\phi_0'' = \frac{1}{\epsilon_0}\left[-\lambda(\epsilon_0' I_{10} + \epsilon_0\phi_0' I_{20}) - 2\epsilon_0'\phi_0' - \alpha\cos\phi_0\right] \qquad (9)$$

$$O(\Omega^2)^1: \quad \epsilon_1'' = A_1\epsilon_1 + A_2\epsilon_1' + A_3\phi_1 + A_4\phi_1' + \delta\cos(\Omega t - \phi_0)$$

$$\phi_1'' = B_1\epsilon_1 + B_2\epsilon_1' + B_3\phi_1 + B_4\phi_1' + \delta\sin(\Omega t - \phi_0) \qquad (10)$$

The only equilibrium point for equation (9) is $(\alpha, -\pi/2)$, which is the static equilibrium position of the system. The solution of equation (10) can be interpreted as a perturbation by the unbalance around the static equilibrium of the system. Analogous to equation (8), A_i and B_i are functions of (ϵ_0, γ_0), given in the Appendix.

Results and Discussion

Several computer programs were written to evaluate equations (7)–(10), which give the analytical solutions. Meanwhile, a numerical simulation by direct numerical integration of the complete nonlinear differential equations was used to verify the analytical solution. Major subroutines used in the programs are called from computer package IMSL [9]. Those programs provide both analytical and numerical solutions of the speed responses and the orbits in the configuration space.

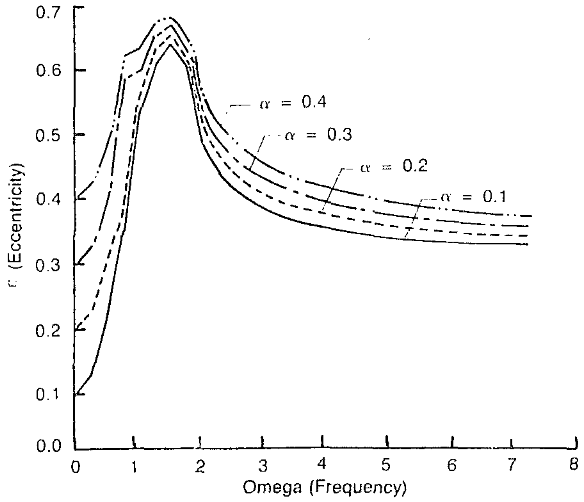

(a) Analytical

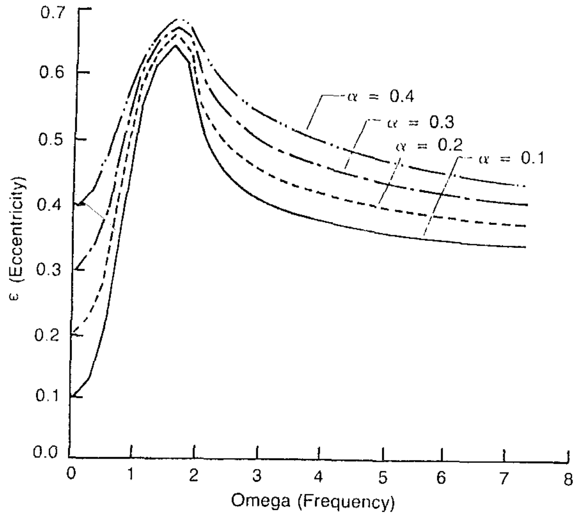

(b) Numerical

Fig. 3 Comparison of analytical and numerical solution with varying α, $\delta = 0.3$, $\lambda = 0.072$

Since the perturbed solution is based on the unperturbed solution, no qualitative change was expected for the system during the eccentric operation.

Figure 3 displays the analytical and numerical speed response (maximum eccentricity) with different values for gravitational residual. The analytical solutions are obtained by combining two perturbation schemes. In Fig. 3(*a*), Ω^2 is taken as the small parameter below $\Omega = 0.8$, and the static equilibrium is the unperturbed solution; above $\Omega = 0.8$, α is the small parameter, and the centered orbit of the system is the unperturbed solution. The comparison between the analytical and numerical results shows that the entire speed range can be divided into four regions: (1) low speed; (2) transition region; (3) the region around the resonance; (4) high speed. The boundary values of the regions depend upon the gravitational residual.

Within the transition region, which is approximately $\Omega = 0.5$ in Fig. 3, neither perturbation scheme gives correct predic-

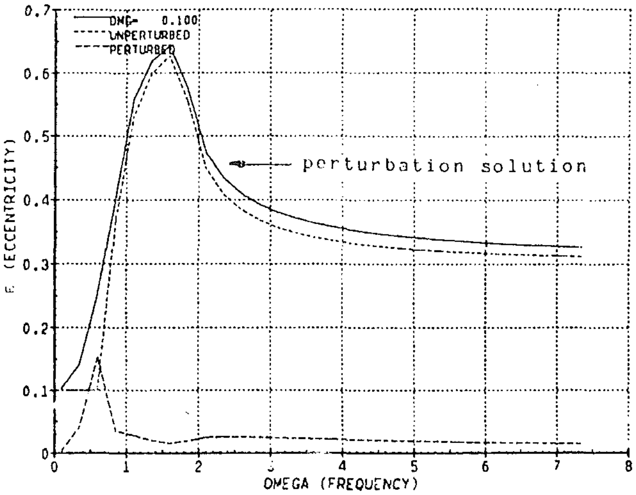

Fig. 4 Speed response by two perturbation schemes combined, $\alpha = 0.1$, $\delta = 0.3$, $\lambda = 0.22$

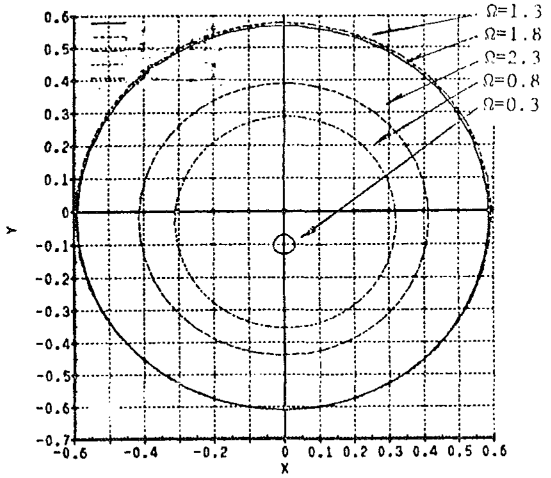

(a) Analytical

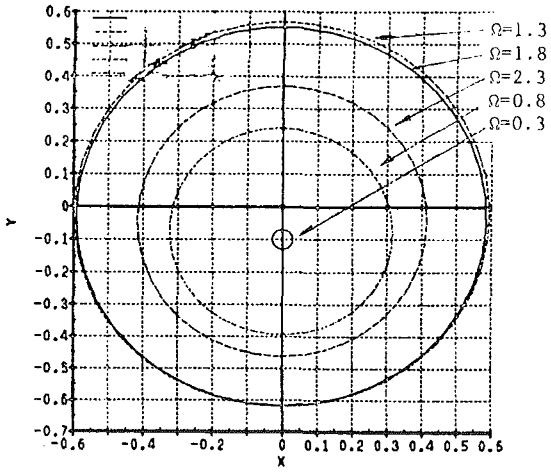

(b) Numerical

Fig. 5 Orbits with varying Ω, $\alpha = 0.1$, $\delta = 0.3$, $\lambda = 0.22$

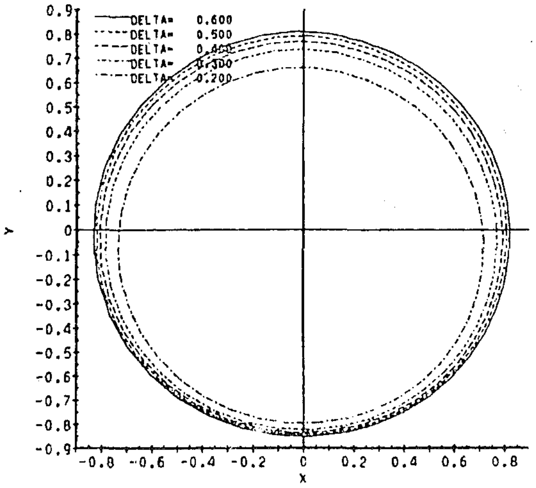

(a) Analytical

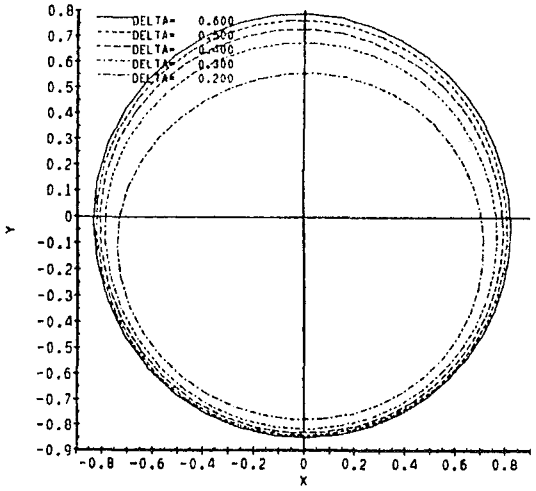

(b) Numerical

Fig. 6 Orbits with varying δ (around resonance), $\alpha = 0.3$, $\Omega = 1.3$, $\lambda = 0.072$

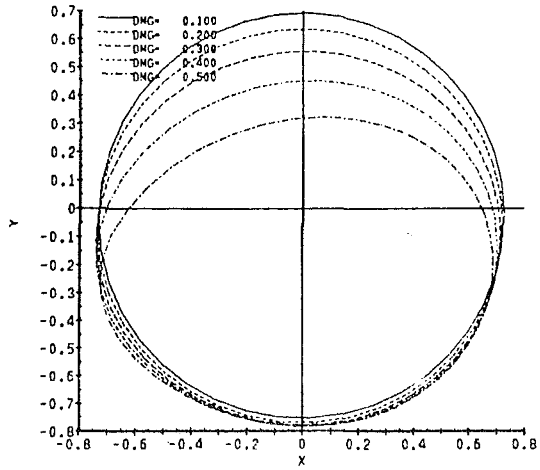

Fig. 7 Distortion of orbits

tions. Although the maximum eccentricity appears to match the numerical solution very well for $\alpha = 0.1$, the orbits are still away from the real ones. In Fig. 4, the unperturbed and perturbed solutions are plotted, separately. Between $\Omega = 0.45$ and 0.7, the zeroth solution is smaller than the first-order perturbation. This means that the perturbation solution cannot be expected to yield a good result. The actual orbit (predicted by simulation) is shifted up by the fluid film forces which push the orbit center away from the static equilibrium of the system for sufficiently large Ω. This transition orbit is not "close" to either of the perturbation solutions.

In the high-speed region, the error of the analytical solution grows with increasing α. The discrepancy of the perturbation solution mainly comes from the relative magnitudes of δ and α. Since the unperturbed solution approaches δ with increasing Ω, α larger than δ generates a larger error in the analytical solution. This is expected by the perturbation method.

In regions 1 and 3 the perturbation solutions are in very good agreement with numerical solutions because the unperturbed solutions are always larger than the small parameters. Figures 5 and 6 are results obtained both analytically and numerically for comparison. Figure 5 shows the orbits for varying Ω. It can be seen that the orbit center exactly locates at the static equilibrium of the system at low speeds; with increasing Ω the orbit center tends to relocate to the center of the clearance space. Figure 6 is the response for changing δ. The phenomenon of orbit self-centering is exactly as found by Tonnesen's experiment [6]. Figure 4 demonstrates the phenomenon more clearly. The perturbed solution is decreasing as the unperturbed solution is approaching its maximum. As a result, a series of solutions show the tendency of self-centering.

Beyond the interpretation of Tonnesen's experiment, Fig. 4 shows that the self-centering of the orbits is related to the increase of the unperturbed solution. When ϵ_0 decreases, the perturbed solution increases. This means that the self-centering phenomenon does not persist at high frequency. The orbit center actually drops down after the maximum ϵ_0. Furthermore, the self-centering of the orbits is dependent on the relative magnitudes of α and δ. Simulation has shown that the orbit can actually be completely off center over the whole speed range if α is much larger than δ. The analytical solution cannot give a good prediction under this condition.

Another phenomenon found by Tonnesen is distortion of the circular orbits. As far as the first-order approximation is concerned, the perturbation method cannot provide a correct solution. Figure 7 shows (by numerical integration) the direction of the orbits for large values of α.

Conclusions

The analytical and numerical results produce the following conclusions for the behavior of the system under eccentric operation:

1 Basically the synchronous orbit of the system under the effect of small gravitational residual is circular; the center of the orbit is on the vertical axis and its location is dependent upon the parameters of the system. At low speed, the center of the orbit is close to the static equilibrium of the system, which is α; at high speed, it is located at $\epsilon_0/2$.

2 Self-centering phenomena occur below the resonance speed. Within this range, increasing speed or increasing unbalance tends to move the center of the orbit toward the center of bearing. After the resonance, the orbit center is away from the bearing center. With α relatively larger than the unbalance of the system, the orbits may be never centered.

3 As far as the synchronous motion is concerned, there is no qualitative change for the system under the effect of small gravitational residual.

4 Large α causes distortion of the circular orbits.

5 The system can be operated without retainer springs for sufficiently large rotating speed and proper system parameters.

6 Numerical simulation confirms that by combining two perturbation schemes the perturbation method gives a simple, explicit, and qualitatively correct result over the whole speed range for a squeeze film damper system under the effect of a small gravitational residual. At low speeds and around resonances the results are most accurate. The method can be used in flexible models of squeeze film damper systems, and the system has a similar behavior [8].

References

1 Dogan, M., Holmes, R., "Squeeze-Film Damping of Rotor-Dynamic Systems," *The Shock and Vibration Digest*, Vol. 15, No. 9, Sept. 1983, pp. 3–8.

2 Mohan, S., and Hahn, E. J., "Design of Squeeze Film Damper Supports for Rigid Rotors," ASME *Journal of Engineering for Industry*, Aug. 1974, pp. 967–982.

3 Simandiri, S., and Hahn, E. J., "Experimental Evaluation of the Predicted Behavior of Squeeze-Film-Bearing-Supported Rigid Rotors," *Journal of Mechanical Engineering Science*, Vol. 21, No. 6, p. 419.

4 Taylor, D. L. and Kumar, B. R. K., "Nonlinear Response of Short Squeeze-Film Dampers," ASME *Journal of Lubrication Technology*, Jan. 1980, pp. 51–58.

5 Taylor, D. L., and Kumar, B. R. K., "Closed-Form, Steady-State Solution for the Unbalance Response of a Rigid Rotor in Squeeze Film Damper," ASME JOURNAL OF ENGINEERING FOR POWER, July 1983, pp. 551–559.

6 Tonnesen, J., "Experimental Parametric Study of a Squeeze Film Bearing," ASME *Journal of Lubrication Technology*, Apr. 1976, pp. 206–213.

7 Pan, C. H. T., "Eccentric Operation of the Squeeze-Film Damper," ASME *Journal of Lubrication Technology*, July 1978, pp. 369–377.

8 Li, X., "Nonlinear Analysis of Squeeze Film Damper Systems," Ph.D. dissertation, Cornell University, June 1985.

9 *IMSL User's Manual*, IMSL, Inc., revised Nov. 1984.

APPENDIX

Coefficients of Equations for Synchronous Motions

The following are coefficients of equations (8) and (10) which describe the small synchronous eccentric motion of the squeeze film damper system

$$a_1 = \Omega^2 - 1 - \lambda\Omega(J_1 + \epsilon_0 J_{11})$$

$$a_2 = -\lambda J_3$$

$$a_3 = -\delta_0 \Omega^2 \sin \gamma_0$$

$$a_4 = \epsilon_0(\lambda J_1 - 2\Omega)$$

$$b_1 = \lambda\Omega J_{21} + \delta_0 \Omega^2 \sin \gamma_0 / \epsilon_0^2$$

$$b_2 = (2\Omega + \lambda J_1)/\epsilon_0$$

$$b_3 = -\delta_0 \Omega^2 \cos \gamma_0 / \epsilon_0$$

$$b_4 = -\lambda J_2$$

$$J_{11} = \frac{2(1 + 3\epsilon_0^2)}{(1 - \epsilon_0^2)^3}$$

$$J_{21} = \frac{3\pi\epsilon_0}{2(1 - \epsilon_0^2)^{5/2}}$$

$$A_1 = -1$$

$$A_2 = -\lambda J_3$$

$$A_3 = 0$$

$$A_4 = -\lambda\epsilon_0 J_1$$

$$B_1 = 0$$

$$B_2 = -\lambda J_1/\epsilon_0$$

$$B_3 = -\delta/\epsilon_0$$

$$B_4 = -\lambda J_2$$

Effect of Control Algorithms on Magnetic Journal Bearing Properties

R. R. Humphris
Research Professor.

R. D. Kelm[1]
Research Associate.

D. W. Lewis
Professor.

P. E. Allaire
Professor.

Department of Mechanical
and Aerospace Engineering,
University of Virginia,
Charlottesville, VA 22901

Magnetic journal bearings are coming into increasing use in industry today. They are primarily used to replace either rolling element or fluid film bearings in rotating machinery. The major advantages are elimination of oil systems and associated seals, expected very long life, very low power losses, and great potential for vibration reduction. Disadvantages include lack of field experience, unknown reliability over a long time, high cost (so far primarily due to the small quantity being made for a given application), and advanced automatic control design required. This paper discusses the design of a magnetic journal bearing with four electromagnets arranged radially around a shaft to fully support a rotor. Each electromagnetic is connected to a controlling electronics circuit which regulates the current to the magnet. For the measurements presented here, only the top magnet was tested and the shaft was not rotating. Thus a single control algorithm was isolated from other effects. This paper compares two control algorithms with differing circuit band widths of 1.2 kHz and 50 kHz. The wider bandwidth algorithm produced approximately a sixfold increase in magnetic bearing stiffness and a much greater stable operating region compared to the lower bandwidth algorithm. Overall, the calculated effective stiffness and damping coefficients were within 20 to 30 percent of the measured values.

Introduction

Most turbomachines such as gas turbines, jet engines, pumps, and compressors operate at high speeds to achieve required efficiencies. Currently, speeds are limited because of bearing problems such as wear, lubrication difficulties, and large vibrations. Usually rolling element bearings have a relatively short lifespan compared to the turbomachines they operate in so that they have to be replaced at regular intervals. Fluid film bearings usually have long life but have high horsepower loss and require extensive oil supply systems and seals to keep the oil out of the working fluid.

A recent high-technology development in the turbomachinery field is that of the magnetic bearing, which can replace the rolling element or fluid film bearing. The design of such bearings has been reported on by Schwitzer and Lange [1–5] for example. Several electromagnets are arranged radially around the shaft. Figure 1 illustrates the geometry. In each magnet around the shaft, the current, and thus the force, is adjusted continuously by an automatic control electronics package [1, 2]. Noncontacting sensors located in the fixed part of the bearing continuously monitor the shaft position. The output from these is used as input for the feedback control.

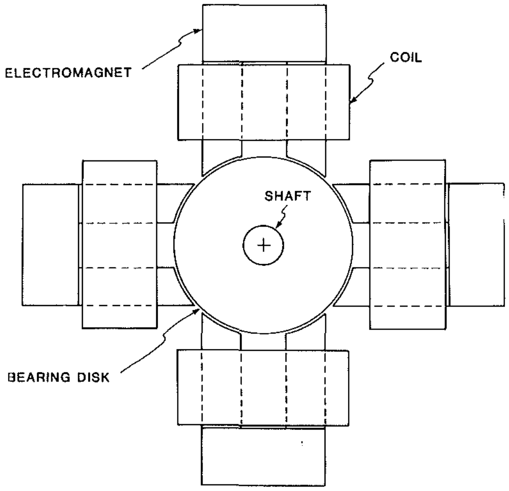

Fig. 1 Magnetic bearing geometry

An electromagnet is inherently attractive. As current is fed through the coils, the magnet would simply attract the shaft until contact is made. The automatic control algorithm acts to reduce the current, and thus the force, as the shaft approaches the magnet. Similarly, the current (force) is increased as the shaft moves away from the magnet. This creates an effective stiffness of the bearing, tending to hold the shaft in a centered position. Typically there are four or eight magnets, each with two poles, around the shaft, which force the shaft to operate in the centered position vertically and horizontally. The

---

[1] Currently at Technical Resources, Dow Chemical USA, Houston, TX 77253

Contributed by the Gas Turbine Division of THE AMERICAN SOCIETY OF MECHANICAL ENGINEERS and presented at the 31st International Gas Turbine Conference and Exhibit, Düsseldorf, Federal Republic of Germany, June 8–12, 1986. Manuscript received at ASME Headquarters Jaunary 10, 1986. Paper No. 86-GT-54.

automatic control can either be connected to all of the sensors and magnets [4] or only locally connected. The overall control system produces a positive stiffness and damping [5] which can be changed over a wide range of parameters to minimize rotor vibrations. The force in the magnets acting on the shaft is produced by signals proportional to a combination of the shaft displacement and velocity, producing the desired values of stiffness and damping.

Some details of magnetic bearing design were discussed by Ulbrich and Anton [6]. Nikolajsen et al. [7] and Gondhalekar and Holmes [8] reported on the design of magnetic bearings for long flexible shafts. Allaire et al. [9] presented a comparison of a theoretical model and experimental measurements of a magnetic support system. Hebble [10] has even carried out a nonlinear theoretical analysis of a magnetic bearing.

A number of works have looked at the general concept of control of vibrations in a rotor-bearing system. Allaire et al. analyzed a single mass flexible rotor on rigid bearings [14] and flexible bearings [15]. An experimental test rig with automatic controls placed on the ball bearing supports for a flexible three-mass rotor was reported by Lewis et al. [16]. Stanway and Burrows [17] discussed general control algorithms for rotors. Stanway and O'Reilly [18] considered eigenvalue reassignment methods for flexible shaft rotors.

The purpose of this paper is to report on the correlation between the experimental magnetic support bearing constructed for the rotor and the theoretical model. Our earlier work [9] discussed a support system consisting of a single pole (solenoid) magnetic support and its associated control components. The use of a single pole system resulted in a very inefficient magnetic circuit but still supported the weight desired. Further, it responded well to changes in the system due to external inputs. This work reports on the extension to a two-pole, U-shaped magnet support system to support a nonrotating disk on a rotor. The geometry now matches the configuration suitable for use in rotating machinery.

Perhaps the most difficult part of the design of magnetic bearings is the control algorithm. The main part of this paper discusses two control algorithms. The primary difference between the two is observed in the electronic circuit bandwidth. One produces a magnetic bearing with poor stability characteristics while the second has rather good stability. Finally the overall bearing effective stiffness and damping coefficients (important for rotor dynamics) are evaluated both experimentally and theoretically.

Experimental Setup

Magnetic Bearing Geometry. The magnetic bearing used in this study has four electromagnets distributed radially around a 12.7 mm (0.5 in.) diameter shaft. This small shaft does not allow sufficient space around the shaft for the magnets and the steel shaft is not a good magnetic material. A soft iron disk 58.4 mm (2.3 in.) in diameter and 25.4 mm (1.0 in.) long was placed over the shaft at the normal bearing location. Each magnet consisted of a solid soft iron core forming a horseshoe, with two pole faces cut to a diameter of 60.5 mm (2.38 in.). This gives a nominal radial clearance of 1.0 mm (0.040 in.). Each leg of the magnet was wound with 920 turns of wire. All magnets were the same. The shaft weight, including the soft iron bearing disk, was supported by having a larger steady-state current in the top magnet. The other three electromagnets had a steady-state current in them to provide a value about which a set of linearized properties was determined. Appendix A gives sample calculations.

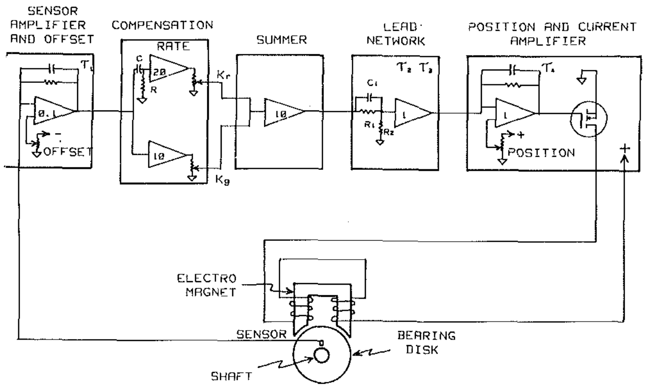

Fig. 2 Block diagram of magnetic support system

Position Sensors. Two position sensors were located vertically and horizontally on the shaft a short axial distance away from the magnetic bearing. These were standard induction (eddy-current) probes of the type normally used to monitor rotating equipment in the field. Various tests were conducted to insure that the magnetic fields from the bearing did not affect the readings of the two probes, which were located about 25 mm (1 in.) from the bearing disk.

Bandwidth Considerations. As noted previously, an attractive magnetic support system is fundamentally unstable and requires some type of controller for stable operation. Two controllers, denoted A and B, were considered in this study. The difference between the two was the bandwidth of the electronic circuit.

One definition of bandwidth is the frequency at which the transfer function for the system is down 3 db from its low-frequency value [19]. This single number is not an all-exclusive parameter. With lower and lower damping, a system may exhibit unduly large responses near critical speeds, an undesirable characteristic. Yet the reverse of this, increasing the damping, can reduce the peak (critical speed) responses and would also cut down the bandwidth of the system. This implies that the control system will not track the shaft response at a rate sufficiently fast to maintain control. This can be visualized as trying to prevent large oscillations of a mass by supplying a force in opposition to the motion, away from a desired equilibrium position. If the response term of the controlled force is too slow (too low a bandwidth), it may lose its effectiveness. In the extreme, the phase of the controlled force may approach 180 deg and instead of reducing the mass oscillations, it will increase them.

Circuit Description. A block diagram of the control circuit for one magnet is given in Fig. 2. The control circuit is the same for each magnet. The circuit basically operates as follows:

Nomenclature

A = area of magnetic pole (one)
C = capacitance
F_g = force in magnetic gap
F_{ext} = external force
h = gap thickness
i = current in coil
K_p = sensor amplifier gain
K_a = current amplifier gain
K_g = proportional gain
K_i = current stiffness
K_r = rate (derivative) gain
K_y = position stiffness
m = mass
N = number of turns (per pole)
R = resistance
W = weight
y = position
ϕ = magnetic flux
μ_0 = permeability of free space
τ = time constant = RC

The signal from the eddy-current induction probe, which senses the position of the shaft, goes to the sensor amplifier. This amplifier has a fixed gain, along with a low pass filter, and a reference or offset adjustment to bring the average signal voltage to a zero value for the normal operating position. With a sensor amplifier constant K_p, the transfer function for this block is $K_p/1+\tau_1 s$, where the $1+\tau_1 s$ term represents the low pass filter.

The compensation consists of two parallel paths of signal conditioning. These paths allow for a position or proportional gain adjustment and a rate or velocity adjustment. These adjustments affect the stiffness and damping, respectively, of the supported mass. C and R are the rate circuit capacitance and resistance. K_g is the gain constant and K_r is the rate constant. Then the transfer function for the compensation is

$$\frac{K_g+(K_g+K_r)RCs}{1+RCs}$$

After going through the summing amplifier with a gain of 10, the signal passes through a lead network, consisting of R_1, R_2, and C_1, which helps to control the stability by providing a phase lead component into the control loop. The transfer function for the lead network is

$$\frac{s+1/\tau_2}{s+1/\tau_3}$$

where $\tau_2=R_1C_1$; $\tau_3=[(R_1+R_2)/R_1R_2]C_1$.

The signal then passes through the position amplifier, which has an adjustment to set the bias level of the current amplifier. This determines the steady-state current provided by the current amplifier to the electromagnet and hence the normal operating position of the shaft. This block also has a low pass filter to prevent undesirable current spikes and oscillation of the current amplifier-magnet coil combination. The transfer function is $K_a/1+\tau_4 s$, where K_a is the current amplifier gain constant in amps per volt and τ_4 is the RC time constant of this low pass filter.

Control Diagram. The dynamics of the electromagnet-mass system, as derived in Appendix A, is combined with the circuit operating characteristics, as described in Appendix B. The complete control diagram of a stable magnetic bearing support system can be assembled as shown in Fig. 3. This is the basic diagram from which the overall control algorithm is obtained, as shown below.

$$\frac{y(t)}{F(t)}=\frac{(1+\tau_4 s)(s+1/\tau_3)(1+RCs)(1+\tau_1 s)}{(ms^2+K_y)(1+\tau_4 s)(s+1/\tau_3)(1+RCs)(1+\tau_1 s)-K_iK_aK_p(s+1/\tau_2)(K_g+(K_g+K_r)RCs)}$$

The system characteristic equation is

$$(ms^2+K_y)(1+\tau_4 s)(s+1/\tau_3)(1+RCs)(1+\tau_1 s)$$
$$-K_iK_aK_p(s+1/\tau_2)(K_g+(K_g+K_r)RCs)=0$$

The method of derivation of this equation is given in [9].

Test Circuits. In the following tests, the bottom magnet was turned off to permit a detailed evaluation of a single magnet with its control circuit. The two side magnets were turned on but only served to keep the shaft motions vertical. It was experimentally observed that horizontal shaft motions were largely independent of vertical motions. The shaft was not rotating during the testing. Other effects, such as eddy currents due to shaft rotation (which would produce heating losses in the solid iron cores used in this work, but not in normal laminated construction), were avoided.

In the evolution of testing to obtain a good stable magnetic bearing operation with ample stiffness and damping characteristics, many different circuit changes and variations were tried. Results of two different control circuits are presented in the next section. The numerical values for the parameters of the horseshoe-shaped magnetic bearing which gave the "best" operation to date are those used in test Circuit B (see Table 1).

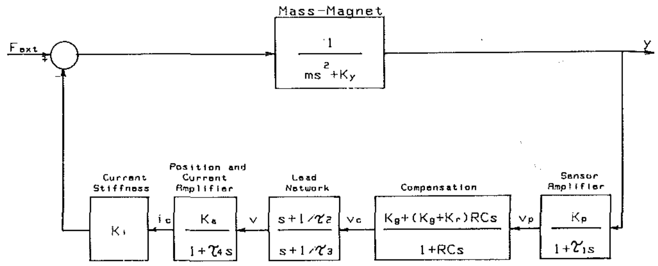

Fig. 3 Control diagram of stable magnetic support system

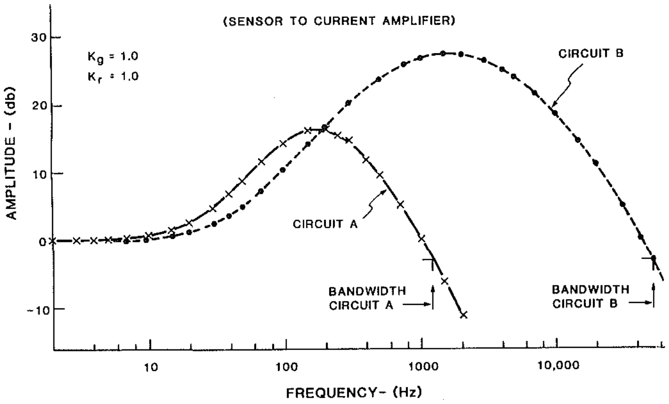

Fig. 4 Frequency response—Circuits A and B

However, to demonstrate the effect of a reduced bandwidth and an approximate factor of three change in the location of the pole-zero combination of the lead network on the bearing operation, results of test Circuit A are compared to those of Circuit B. The only changes in the A circuit (from those listed in Table 1) are as listed in Table 2.

The effect of the reduced-time constants of Circuit B on the experimental frequency response of just the electronics portion of the control loop is shown in Fig. 4. There is excellent agreement (± 2 db) between the theoretically predicted curve and the experimentally measured response for these circuits. In particular, note the increase in the bandwidth or frequency at which the response has decreased to -3 db. The bandwidth of the B circuit is about 50 kHz whereas it is only 1.2 kHz for the A circuit with the same settings for the position and rate constants. This difference greatly affects the stability and operational limitations of the supported magnetic bearing, as presented in the next section.

Experimental Results

Stable Regions. It was found that both Circuits A and B had various combinations of rate and position constant settings which would cause the magnetic bearing to go into a limit cycle oscillation or to go completely unstable. The frequency of oscillation varied from about 20 Hz to over 100 Hz, depending on the constants. The regions of safe stable operation for Circuits A and B are shown in Fig. 5. From these, it is obvious that Circuit B offers a much wider range of rate and gain variation.

Table 1 Parameters for best magnetic bearing control system (Circuit B)

A	(magnetic face area) = 342 mm^2 (0.53 in.^{2})
c	(rate circuit capacity) = 0.015 μf
h	(gap separation) = 0.9 mm (35 mils)
i	(coil current) = 0.120 A
K_a	(current amplifier gain) = 0.45 A/v
K_g	(position gain) = 0 to 10
K_r	(rate gain) = 0 to 20
K_p	(sensor amplifier constant) = 0.79 v/mm (20 v/in.)
m	(mass) = 2 lb
N	(coil turns/leg) = 920
R	(rate circuit resistance) = 100 KΩ
τ_1	(time constant) = 0 s
τ_2	(time constant) = 1.8×10^{-3} s (85 Hz)
τ_3	(time constant) = 1.8×10^{-4} s (870 Hz)
τ_4	(time constant) = 5.0×10^{-5} s (3200 Hz)

Table 2 Changed parameters for alternative control system (Circuit A)

$\tau_1 = 6.2 \times 10^{-4}$ s (259 Hz)
$\tau_2 = 5.0 \times 10^{-3}$ s (32 Hz)
$\tau_3 = 5.0 \times 10^{-4}$ s (320 Hz)
$\tau_4 = 1.2 \times 10^{-3}$ s (133 Hz)

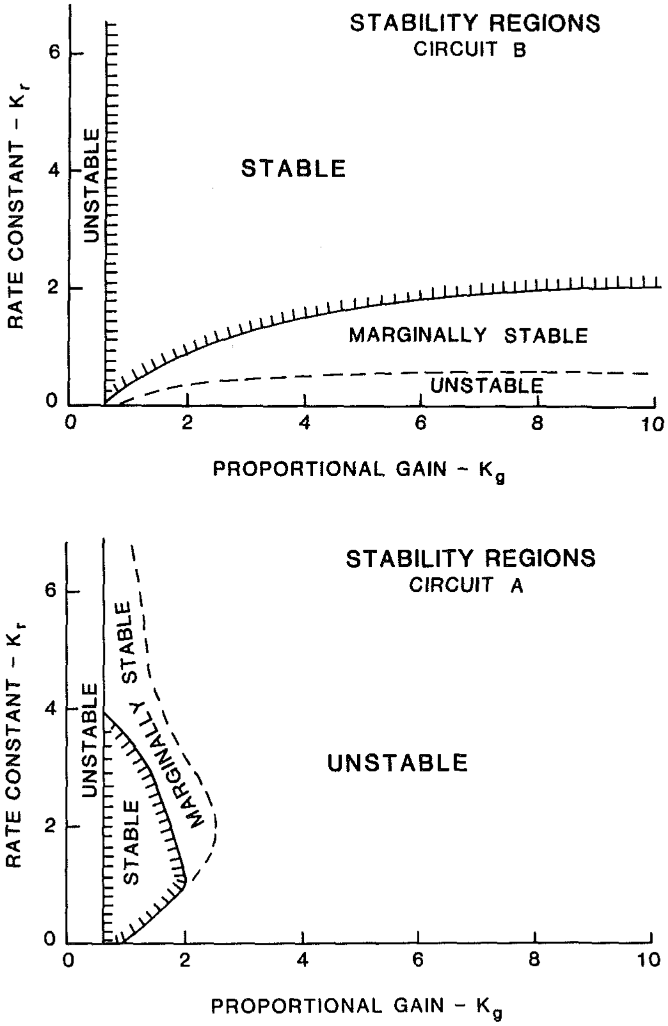

Fig. 5 Stability regions

Step Reponse. One of the standard methods of testing automatic control devices is the application of a step input to the system. In this case a very low-frequency step function from a signal generator was applied to the control system at the position amplifier location, so that the step function would not be affected by the compensation or lead network. The overall system response to a step function gives much insight

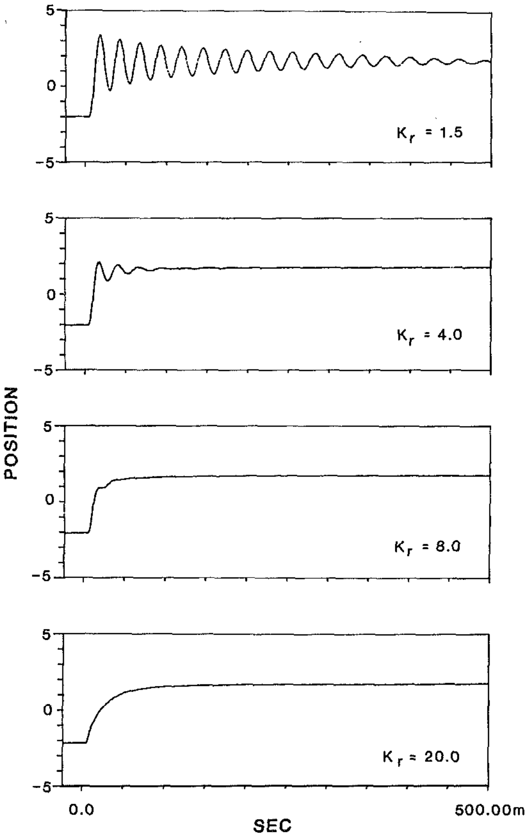

Fig. 6 Experimental step response for various values of K_r with $K_g = 2.0$

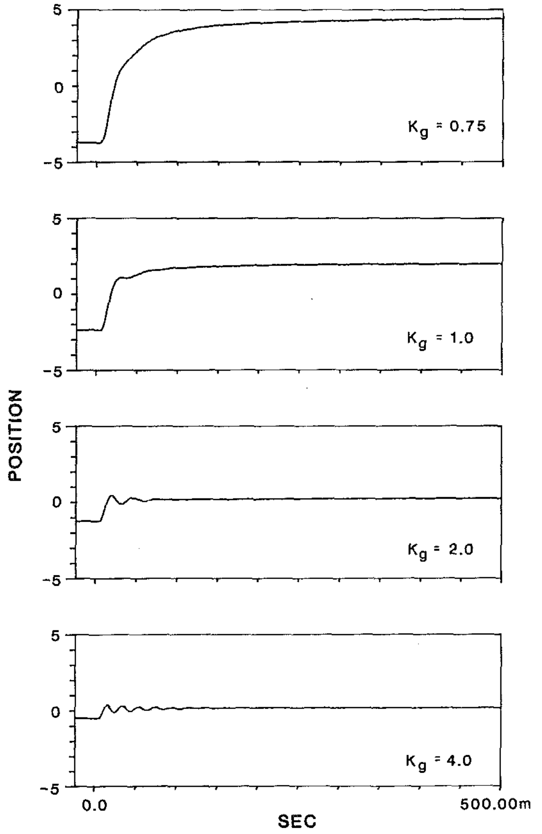

Fig. 7 Experimental step response for various values of K_g with $K_r = 4.0$

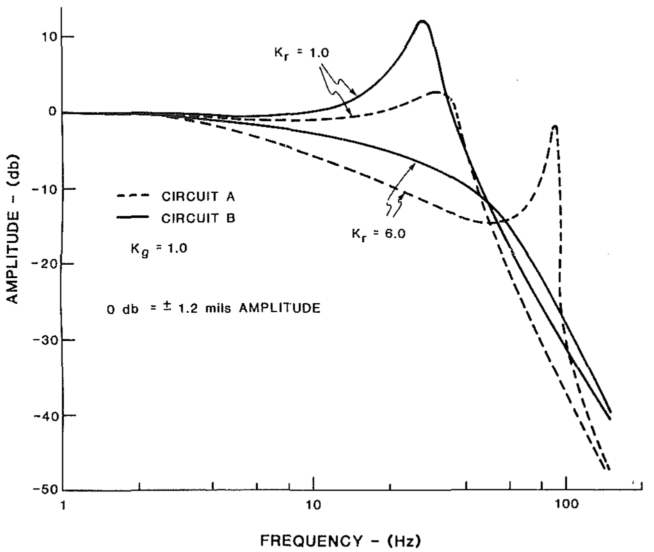

Fig. 8 Closed-loop frequency response (experimental)

into the system stability or damping characteristics. It can also be used to determine a value for the effective stiffness and damping coefficients.

Figures 6 and 7 give the response of the two-pole, one-electromagnet, bearing support to a step input. The vertical scale represents the shaft position and the horizontal scale is time.

The proportional or position gain K_g was kept constant in Fig. 6, while the rate gain constant K_r has values of 1.5, 4.0, 8.0, and 20.0. Inspection shows that the response varies from a highly underdamped system with a damping ratio of less than 0.1 to a greatly overdamped system with a damping ratio of approximately 2.7. The optimum value of K_r, for rapidly reaching the new steady-state position, would appear to be slightly less than 8.0.

For Fig. 7, the rate gain K_r was kept at a constant value of 4.0, while the proportional gain was set at values of 0.75, 1.0, 2.0, and 4.0. Here the optimum value of proportional gain appears to be near a value of 2.0. It should also be noted that the magnitude of the position step decreases as the proportional gain is increased, even though the input step voltage remained constant. This just reflects the fact that the system stiffness increases as the proportional gain increases and thus the deflection for a given disturbance is decreased. Indeed, with proper calibration, a stiffness curve versus gain setting could be generated from this figure.

Closed-Loop Frequency Response. The electronic circuit frequency response shown previously in Fig. 4 indicated that Circuit B had a 3-db bandwidth of about 40 times that of Circuit A. It is of interest to compare the closed-loop frequency response for the same rate and proportional gain settings. This is given in Fig. 8. It is obvious that the closed-loop bandwidths are not very different for the two test circuits. The closed-loop bandwidth is mainly determined by the dynamics of the magnet-mass component. The large peak at about 90 Hz for Circuit A with $K_r = 6.0$ illustrates clearly why this circuit is marginally stable at these settings as shown in Fig. 5.

The closed-loop response did not change as dramatically as the electronic circuit response for the two circuits. However, it is clear that the increased bandwidth and new location of the pole-zero combination of the lead network have greatly increased the range of stable proportional gain and rate settings. Thus control system B yields a more stable operation of the magnetic bearing.

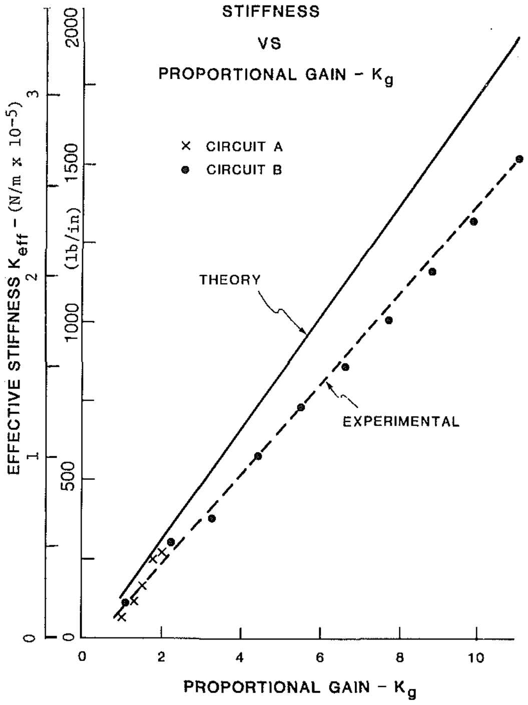

Fig. 9 Theoretical and measured effective stiffness of magnetic bearing

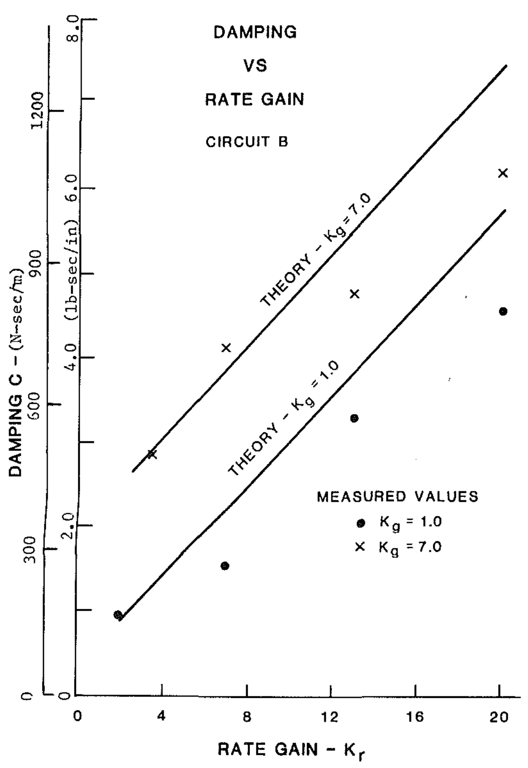

Fig. 10 Theoretical and measured damping of magnetic bearing

In addition, the closed-loop frequency response of Circuit B in Fig. 8 can be compared to the corresponding step response as given in Fig. 6. It is seen that the peaked response curve for $K_r = 1.0$ results in a fast rise, but very oscillatory step response. The nonpeaked closed-loop response for $K_r = 6.0$ produces a nonoscillatory, but slower exponential rise step response.

Stiffness. One of the important defining characteristics of most any type of bearing is its stiffness value. The operational behavior of a magnetic bearing is largely determined by the control algorithm. Within the stable region, the stiffness may be varied over a certain range by changing the proportional gain K_g. A theoretical analysis of the stiffness coefficient is given in Appendix C and a plot of this theoretical stiffness as a function of the proportional gain K_g is shown in Fig. 9, along with experimentally measured values for the two test circuits. From this figure, it is noted that Circuit A, with the smaller bandwidth, has a very limited range of effective stiffness, compared to that of Circuit B. Circuit A had a maximum stiffness value of about 4.5E4 N/m before it became unstable (as the proportional gain was increased). In contrast, stiffness values of over 2.7E5 N/m were obtained with Circuit B at a maximum K_g setting. This stiffness value of 2.7E5 N/m could be increased even more by electronically increasing the maximum gain of the position gain amplifier in the compensation block.

The experimental data are linear, with a slightly lower slope than the theoretical values. Over the range of K_g from 1 to 11, the measured values differ from the theory by about 20 percent.

Thus the stiffnesses obtainable using Circuit B are much greater, more than a factor of 6, over those using Circuit A. This was made possible due to the greater bandwidth and relocation of the lead network pole-zero combination of Circuit B.

Damping. Another of the important defining characteristics of a bearing is its damping value, which determines the speed and shape of the response of a shaft to a sudden change in force or excitation. With a magnetic bearing, the damping is mainly determined by the amount of velocity or rate signal present in the overall control system. A theoretical analysis of the damping coefficient is presented in Appendix C and the method used to determine the experimental values of damping from the system response to a step input is given in Appendix D. Results for Circuit B of both the theory and experimentally determined values of damping for two values of proportional gain are shown in Fig. 10.

Again, it is noted that the theory predicts a linear increase of damping with increasing rate and proportional gain settings. The measured values are somewhat scattered, but are within 30 percent of the predicted values. The maximum damping measured was about 1.1E3 N-s/m for $K_g = 7.0$.

Summary and Conclusions

A magnetic journal bearing was designed, constructed, measured, and analyzed. For the measurements here, the lower magnet was turned off so that only the top magnet was actually tested. Both side magnets were activated but served merely to keep the shaft from undergoing any horizontal motion. Also the shaft was not rotating during testing. All of the above insured that the primary testing was of the control algorithm for a single magnet rather than other effects.

The objective was to determine the effect of two different control algorithms on the bearing performance. It was found that an electronic circuit with one set of time constants produced an electronic circuit frequency response with a much higher bandwidth, 50 kHz, compared to the alternative of 1.2 kHz. The increased bandwidth circuit gave a much wider range of stable bearing operation than the low bandwidth circuit. A comparison of measured versus calculated values of frequency response gave agreement to within 2.0 db for the circuits (without the magnets).

Response of the system to a step function was also measured. Responses ranged from damping ratios of 0.1 to about 2.7. The optimum value of proportional gain for $K_r = 4.0$ was found to be about 2.0 for the 50 kHz bandwidth circuit. However, for any given proportional gain setting, which determines a certain effective stiffness value of the magnetic bearing, there is a corresponding rate or velocity gain setting which would provide optimum damping characteristics.

It was found that the magnetic component of the system largely governed the closed-loop frequency response plot and its associated bandwidth. Thus the increased bandwidth of the electronic circuit was not immediately obvious in the closed-loop response. However, one could infer stability and damping behavior from the curve shape.

A method was developed for both measuring and calculating the effective stiffness and damping coefficients of the magnetic bearing. It includes the magnetic component itself plus the control circuit. Overall, the effective stiffness was found to be quite linear with the proportional gain K_g. The measured results were consistently about 20 percent below the calculated values. This could be due to losses in the magnetic circuit which were not taken into account in the analysis. Measured effective damping coefficients were linear with increasing derivative gain K_r. Measured results were within 30 percent of calculated values.

The final and perhaps most important of the results was the upper value of stiffness which could be obtained in the bearing before a control system instability was reached. The 1.2 kHz bandwidth system gave an upper stiffness of 4.6E4 N/m (260 lb/in.) while the 50 kHz bandwidth system produced an upper stiffness of 2.7E5 N/m. This represents an approximately sixfold increase. A greater stiffness value could be obtained by increasing the maximum gain of the proportional gain amplifier. The increase gives much more flexibility to the designer of rotating machines when flexible shafts must be considered.

References

1 Schweitzer, G., and Lange, R., "Characteristics of a Magnetic Rotor Bearing for Active Vibration Control," First International Conference on Vibrations in Rotating Machinery, Institution of Mechanical Engineers, Cambridge, Sept. 1976, Paper No. C239/76.

2 Schweitzer, G., and Ulbrich, H., "Magnetic Bearings – A Novel Type of Suspension," Sec. Intern. Conf. on Vibrations in Rotating Machinery, Institution of Mechanical Engineers, London, Cambridge, 1980.

3 Schweitzer, G., Traxler, A., Bleuler, H., Bauser, E., and Koroknay, P., "Magnetische Lagerung einer Epitaxie-Zentrifuge bei Hochvakuumbedingungen," *Vakuumtechnik, 32. Jahrgang, Heft 3*, 1983, pp. 70–74.

4 Bleuler, H., and Schweitzer, G., "Decentralized Control," Applied Control and Identification Symposium, IASTED, Copenhagen, 1983.

5 Salm, J., and Schweitzer, G., "Modeling and Control of a Flexible Rotor With Magnetic Bearings," Third International Conference on Vibrations in Rotating Machinery, Institution of Mechanical Engineers, York, Sept. 1984, Paper No. C277/80.

6 Ulbrich, H., and Anton, E., "Theory and Application of Magnetic Bearings With Integrated Displacement and Velocity Sensors," Third International Conference on Vibrations in Rotating Machinery, Institution of Mechanical Engineers, York, Sept. 1984, Paper No. C299/84.

7 Nikolajsen, J. L., Holmes, R., and Gondhalekar, V., "Investigation of an Electromagnetic Damper for Vibration Control of a Transmission Shaft," The Institution of Mechanical Engineers, Vol. 193, No. 31, 1979, pp. 331–336.

8 Gondhalekar, V., and Holmes, R., "Design of an Electromagnetic Bearing for the Vibration Control of a Flexible Transmission Shaft," Rotor Dynamics Instability Problems in High Performance Turbomachinery, Texas A&M University, May 1984.

9 Allaire, P., Humphris, R., and Kelm, R., "Magnetic Bearings for Vibration Reduction and Failure Prevention," *Proceedings of Mechanical Failures Prevention Group*, National Bureau of Standards, Apr. 1985.

10 Hebbale, K. V., "A Theoretical Model for the Study of Nonlinear Dynamics of Magnetic Bearings," Ph.D. Thesis, Cornell University, Jan. 1985.

11 Haberman, H., and Liard, G. L., "Practical Magnetic Bearings," *IEEE Spectrum*, Sept. 1979, pp. 26–30.

12 Haberman, H., and Liard, G. L., "An Active Magnetic Bearing System," *Tribology International*, Apr. 1980, pp. 85–89.

13 Haberman, H., and Brunet, M., "The Active Magnetic Bearing Enables Optimum Damping of Flexible Rotor," ASME Paper No. 84-GT-117.

14 Allaire, P. E., Lewis, D. W., and Jain, V. K., "Feedback Control of a Single Mass Rotor on Rigid Supports," *Journal of the Franklin Institute*, Vol. 312, 1981, pp. 1–11.

15 Allaire, P. E., Lewis, D. W., and Knight, J. D., "Active Vibration Control of a Single Mass Rotor on Flexible Supports," *Journal of the Franklin Institute*, Vol. 315, 1983, pp. 211–222.

16 Lewis, D. W., Moore, J. W., Bradley, P. L., and Allaire, P. E., "Vibration Limiting of Rotors by Feedback Control," *Proceedings of NASA/ARO Workshop on Rotor Dynamic Instability*, 1982, pp. 434–437.

17 Stanway, R., and Burrows, C. R., "Active Vibration Control of a Flexible

Rotor on Flexibly-Mounted Journal Bearings," ASME *Journal of Dynamic Systems, Measurement and Control*, Vol. 103, 1981, pp. 383-388.

18 Stanway, R., and O'Reilly, J., "State-Variable Feedback Control of Rotor-Bearing Suspension Systems," Third International Conference on Vibrations in Rotating Machinery, Institution of Mechanical Engineers, York, Sept. 1984, Paper No. C274/84.

19 Dorf, R. C., "Modern Control Systems," 3rd ed., Addison Wesley, New York, 1983.

APPENDIX A

Theoretical Model of Magnetic Bearing

The purpose of this appendix is to develop a theoretical model of the magnetic bearing. It is useful for both designing future bearings and comparing to the experimental results obtained in this paper. Only a single magnet is considered. Also a small motion about some centered position is assumed so that linearized analysis can be used. It is assumed that the flux levels are well below saturation in the core material.

The total magnetic flux in an air gap is

$$\phi = \frac{\mu_0 A N i}{h}$$

Here fringing and leakage effects are neglected for simplicity. The force exerted on the weight by the magnet is

$$F_g = \frac{\phi^2}{2\mu_0 A}$$

Substituting for ϕ above gives the force per air gap as

$$F_g = \frac{\mu_0 A N^2 i^2}{2\,h^2}$$

For both air gaps, the total force is simply doubled or

$$F = 2F_g = \frac{\mu_0 A N^2 i^2}{h^2} \qquad \text{(A1)}$$

The magnet supports the steady-state downward load so $F = W$. Thus the load capacity is

$$W = \frac{\mu_0 A N^2 i_s^2}{h_s^2} \qquad \text{(A2)}$$

where i_s and h_s are the steady-state current and gap thickness, respectively.

Two independent parameters can change: position y and current i. Define the position and current stiffnesses

$$K_y = -\frac{\Delta F}{\Delta y} = \text{Position stiffness}$$

$$K_i = -\frac{\Delta F}{\Delta i} = \text{Current stiffness}$$

Assume that the change in position Δy is a change about the steady-state gap thickness h_s. Here Δy is small compared to h_s and Δi is small compared to i_s. Then the actual gap clearance h and current i have the form

$$h = h_s - \Delta y$$

$$i = i_s + \Delta i$$

The negative sign occurs because as the mass moves up (and Δy is positive), the gap clearance decreases.

Equation (A1) for the force expression gives

$$F = \frac{\mu_0 A N^2 (i_s + \Delta i)^2}{(h_s - \Delta y)^2}$$

Both Δy and Δi are small, so this can be approximated by the binomial expansion to yield

$$F = \frac{\mu_0 A N^2 i_s^2}{h_s^2}\left(1 + 2\frac{\Delta y}{h_s} + 2\frac{\Delta i}{i_s}\right)$$

First, setting Δi to zero

$$F = W - K_y \Delta y = \frac{\mu_0 A N^2 i_s^2}{h_s^2} + \frac{2\mu_0 A N^2 i_s^2}{h_s^3}\Delta y$$

and the position stiffness is

$$K_y = -\frac{2\mu_0 A N^2 i_s^2}{h_s^3} \qquad \text{(A3)}$$

As is well known, the position stiffness is negative. A positive displacement Δy toward the magnet increases the force. Conversely, an actual spring would apply a force tending to restore the position of the mass to h_s. Second, setting Δy to zero

$$F = W - K_i \Delta i = \frac{\mu_0 A N^2 i_s^2}{h_s^2} + \frac{2\mu_0 A N^2 i_s}{h_s^2}\Delta i$$

and the current stiffness is

$$K_i = -\frac{2\mu_0 A N^2 i_s}{h_s^2} \qquad \text{(A4)}$$

It is also negative, indicating that an increase in current tends to force the mass away from the steady-state value (toward the magnet).

APPENDIX B

Block Diagram Model of System

A block diagram of all the components was generated for further use with simulation methods. The block diagram consists of six blocks: mass dynamics, sensor amplifier, compensation, lead-network, current and position amplifier, and current stiffness as shown in Fig. 3.

The force equation can be written as

$$mg + \Delta F = \frac{\mu_0 A N^2 i_s^2}{h_s^2} + K_i \Delta i + m\,\frac{d^2 y}{dt^2} + K_y \Delta y \qquad \text{(B1)}$$

using the equations derived in Appendix A. Since

$$mg = W = \frac{\mu_0 A N^2 i_s^2}{h_s^2} \qquad \text{(B2)}$$

then

$$\Delta F = K_i \Delta i + m\,\frac{d^2 y}{dt^2} + K_y \Delta y \qquad \text{(B3)}$$

Assuming $i = i_s + i_c$ (steady + control current) and $y = 0$ at $h = h_s$, then $\Delta i = i_c$ and $\Delta y = y$. So, using the Laplace transform

$$\Delta F = K_i i_c + (ms^2 + K_y) y \qquad \text{(B4)}$$

From this equation, the mass dynamics and the current stiffness component blocks can be constructed.

Position sensing can be described by a constant K_p, which describes the gain used to produce a voltage proportional to position change. Typical units are volts/mm. A low pass filter is also incorporated into the sensor circuit to make the transfer function

$$\frac{v_p}{y} = \frac{K_p}{1 + \tau_1 s}$$

The output from the sensor amplifier is a position voltage v_p. A voltage offset is used to set this position voltage to zero at the center of the bearing, so $y = 0$ for $h = h_s$.

The compensation circuit involves position and velocity signals with variable gains in parallel. K_g is the position constant and K_r is the velocity constant. These gains are adjustable and affect the stiffness and damping acting on the supported mass. The transfer function is

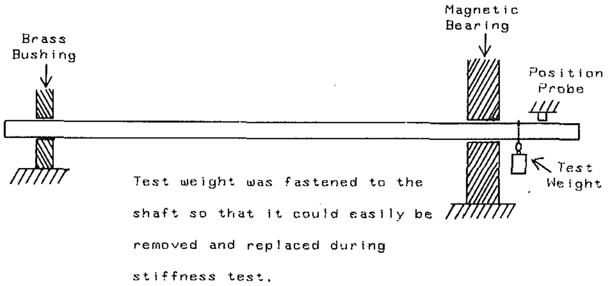

Test weight was fastened to the shaft so that it could easily be removed and replaced during stiffness test.

Fig. 11 Experimental stiffness set-up

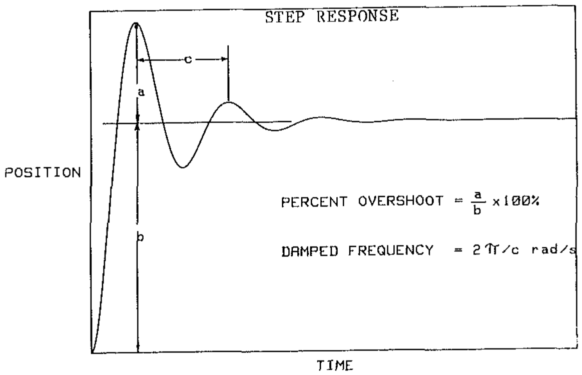

Fig. 12 Sample underdamped response for damping calculation

$$\frac{\text{control voltage}}{\text{position voltage}}=\frac{v_c}{v_p}=K_g+\frac{K_r RCs}{1+RCs}$$

$$=\frac{K_g+(K_g+K_r)RCs}{1+RCs} \tag{B5}$$

The lead network is a simple pole-zero combination used for stabilization. The transfer function is

$$\frac{\text{applied voltage}}{\text{control voltage}}=\frac{v}{v_c}=\frac{s+1/\tau_2}{s+1/\tau_3} \tag{B6}$$

Current amplification is described by a constant and a low pass filter to attenuate stray voltage spikes and noise as

$$\frac{i_c}{v}=\frac{K_a}{1+\tau_4 s} \tag{B7}$$

A block diagram can now be formed as shown in Fig. 3, using force as the input and position as output.

APPENDIX C

Theoretical Analysis of Stiffness and Damping Coefficients

To analyze the stiffness and damping properties of the magnetic bearing, it is useful to write appropriate equations describing the dynamics and then compare the results to a lumped second-order model.

Using the block diagram in Fig. 3, an equation can be written involving y and i_c as

$$\frac{K_p[K_g+(K_g+K_r)RCs][s+1/\tau_2]K_a}{(1+\tau_1 s)(s+1/\tau_3)(1+RCs)(1+\tau_4 s)}\,y=i_c \tag{C1}$$

Using equation (B4), a 2 × 2 matrix can be formed as

$$\begin{bmatrix} A & B \\ C & D \end{bmatrix}\begin{Bmatrix} y \\ i_c \end{Bmatrix}=\begin{bmatrix} \Delta F \\ 0 \end{bmatrix} \tag{C2}$$

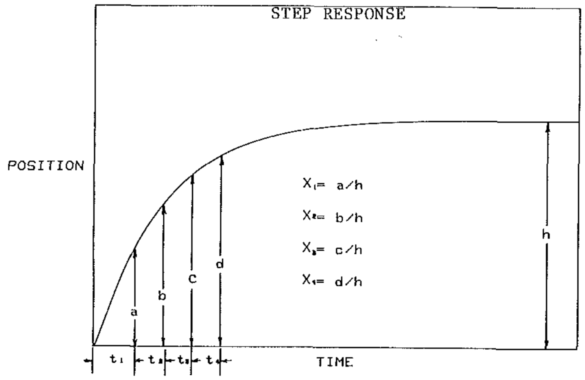

Fig. 13 Sample overdamped response for damping calculation

where

$$\begin{aligned} A &= ms^2+K_y \\ B &= K_i \\ C &= \frac{K_p[K_g+(K_g+K_r)RCs][s+1/\tau_2]K_a}{(1+\tau_1 s)(s+1/\tau_3)(1+RCs)(1+\tau_4 s)} \\ D &= -1 \end{aligned}$$

Solving the matrix for y

$$y=\frac{\Delta FD}{(A\,D-B\,C)}=\frac{\Delta F}{(B\,C-A\,D)} \tag{C3}$$

Let $s=j\omega$, where $j=\sqrt{-1}$ and compare equation (C3) to

$$y=\frac{f(\omega)}{(K-m\omega^2)+j\omega c} \tag{C4}$$

yielding

$$\begin{aligned} K_{\text{equivalent}} &= K_y+\text{Re}\{BC\} \\ C_{\text{equivalent}} &= Im\{BC\}/\omega \end{aligned}$$

Evaluating the equivalent stiffness and damping quantities above will yield lumped stiffness and damping quantities for the magnetic bearing.

APPENDIX D

Experimental Determination of Stiffness

This appendix describes the methods used to measure values for effective stiffness and damping coefficients from the test rig described in this paper. Stiffness was measured by adding small weights to the shaft assembly near the bearing and calculating stiffness from deflection data. Damping was determined by analyzing step response plots for the magnetic bearing in comparison to second order theory for a step response.

Stiffness data were collected by hanging a small weight on the shaft near the bearing, then recording the deflection of the shaft as near to the bearing as practical (see Fig. 11). It was quickly noticed that the measured stiffness was dependent on the magnitude of the test weight; a hardening spring effect was noticed. Analysis of data showed the optimum test weight for our rig to be 30 g. Using this test weight, the effective stiffness was calculated as

$$K_{\text{eff}}=-\frac{\Delta F}{\Delta y}$$

Damping values were determined by analyzing step response plots. The analysis falls into two classes, underdamped and overdamped. In the underdamped case the response overshoots and after several oscillations approaches its final value.

The percent overshoot was measured from the plot, which yields a damping ratio (xi) by the relation

$$\text{percent os} = \exp\left(\frac{\xi \ \pi}{\sqrt{1-\xi^2}}\right) \times 100 \text{ percent}$$

Next the damped frequency of oscillation ω_d was calculated from the period. The natural frequency ω_n was then estimated by the relation

$$\omega_n = \omega_d / \sqrt{1-\xi^2}$$

The effective damping was then estimated as

$$C_{\text{eff}} = 2\xi m \omega_n$$

where m is the mass of the rotor at the bearing. For the overdamped case, the step heights for five instants in time were measured as the fraction of final value of each response curve. Each height and time combination was fed into a numerical search routine to solve the following equation for the damping ratio

$$C(t) = \frac{y(t)}{\text{final } ht} = 1 + [2(\xi^2 - \xi\sqrt{\xi^2-1} - 1)]^{-1} e^{-(\xi - \sqrt{\xi^2-1})\omega_n t}$$

$$+ [2(\xi^2 + \xi\sqrt{\xi^2-1} - 1)]^{-1} e^{-(\xi + \sqrt{\xi^2-1})\omega_n t}$$

An approximate damping ratio was assumed to be the average of the five measured xis. The natural frequency was assumed to be

$$\omega_n = \sqrt{K_{\text{eff}}/m}$$

where the measured stiffness and mass were used. The effective damping was estimated as

$$C_{\text{eff}} = 2\xi m \omega_n$$

Figures 12 and 13 give examples of the method used.

E. Bazan[1]
Paul C. Rizzo Associates, Inc.,
Pittsburgh, PA 15235

J. Bielak
Department of Civil Engineering,
Carnegie-Mellon University,
Pittsburgh, PA 15213

J. H. Griffin
Department of Mechanical Engineering,
Carnegie-Mellon University,
Pittsburgh, PA 15213

An Efficient Method for Predicting the Vibratory Response of Linear Structures With Friction Interfaces

A simple methodology to study the steady-state response of systems consisting of linear elastic substructures connected by friction interfaces is presented. Assuming that only the first Fourier components of the friction forces contribute significantly to the system response, the differential equations of motion are transformed into a system of algebraic complex equations. Then, an efficient linearized procedure to solve these equations for different normal loads in the friction interfaces is developed. As part of the solution procedure, a criterion to determine the slip-to-stuck transitions in the joint is proposed. Within the assumption that the response is harmonic, any desired accuracy can be obtained with this methodology. Selected numerical examples are presented to illustrate practical applications and the relevant features of the methodology. Due to its simplicity, this methodology is particularly appropriate for performing parametric studies that require solutions for many values of normal loads.

1 Introduction

One important consideration in the design of gas turbine engines is limiting the amplitudes of steady-state vibrations of its components in order to prevent failures due to high cycle fatigue. The most widely used damping devices incorporate specially designed friction interfaces which dissipate energy and reduce high frequency vibrations to an acceptable level. The study of steady-state vibrations of structures with so-called frictional dampers has attracted the attention of many investigators. The first analytical solution for a single-degree-of-freedom system with a Coulomb frictional joint was presented by Den Hartog [4]. The most relevant contributions until 1979 are discussed by Plunkett [10]. More recently, further analytical and experimental research has been reported by Griffin and co-workers [6, 12, 3], Muszynska et al. [9], Srinivasan et al. [16], Dominic et al. [5], and Soni and Bogner [13], among others.

Most of the analytical studies are limited to cases with one friction joint only, mainly due to the difficulties of solving the nonlinear differential equations which result from the mathematical models. The available mathematical models and methods of solution cannot be easily extended to problems with several friction joints, and their results do not explain completely all the experimentally observed phenomena. For these reasons, a more efficient and rational utilization of friction dampers still requires additional experimental and analytical research.

In this paper we present a simple, approximate, yet accurate, methodology for studying the steady-state response of structures containing friction interfaces, but which are otherwise linear. The procedures that are developed result in systems of nonlinear equations that would be prohibitively expensive to solve if the global problem were formulated directly. This difficulty was avoided by exploiting the linearity of the individual subsystems utilizing finite element substructuring techniques. The substructuring approach has been widely used in mechanics to solve static problems [11], as well as dynamic problems [7, 8]. In fact, this approach was used to analyze shrouded blades in [15]. The work described in our paper is significantly different in that we incorporate friction constraints at the interfaces. In linear analyses it is possible to back calculate a coefficient of viscous or structural damping to produce the same peak response as that obtained with friction damping. This value, however, will depend on the level of excitation and on the normal force at the interface; it cannot be obtained directly from the physics of the problem and can only be calculated once the response is known. For example, in a structure that contains a friction interface no damping occurs if the excitation is small since the joint does not slip. However, for larger levels of excitation, the static friction in the joint can be overcome and rubbing can dissipate a significant amount of energy. Clearly, both conditions cannot be represented by a single value of equivalent viscous or structural damping. In the approach presented here, the nonlinear damping dissipated by friction is calculated directly by the procedure for any level of excitation without resorting to "calibrating" the model.

The organization of the paper is as follows. First, the differential equations governing the motion of the system under study are formulated in terms of the complete set of system displacements. A methodology to obtain approximate solu-

---

[1] Formerly, Department of Civil Engineering, Carnegie-Mellon University, Pittsburgh, PA 15213, while on leave from the National University of Mexico.

Contributed by the Gas Turbine Division of THE AMERICAN SOCIETY OF MECHANICAL ENGINEERS and presented at the 31st International Gas Turbine Conference and Exhibit, Düsseldorf, Federal Republic of Germany, June 8–12, 1986. Manuscript received at ASME Headquarters January 17, 1986. Paper No. 86-GT-88.

tions of these equations is presented next, based on the assumption that only the first Fourier component of the tangential forces in the friction joints has a significant participation in the system response. The problem is eventually reduced to the solution of an algebraic system of equations relating the complex variable representation of the relative displacements and the tangential forces in the friction joints. The use of a complex variable approach allows the development of simple and efficient algorithms to systematically formulate the equations. A procedure to solve the equations for several levels of normal loads in the friction joints is also presented. It only requires that systems of real linear equations be solved. Any degree of accuracy can be obtained by applying this procedure iteratively. In addition, a criterion is established for determining the transition of a joint from a slipping to a fully stuck condition.

Relevant computational issues are discussed, with emphasis on the interaction of the methodology with finite element programs. Selected examples are presented to illustrate applications of the methodology in practical problems as well as the most relevant feature of the solution procedure.

2 Equations of Motion

We will consider a structural system consisting of several elastic substructures connected by friction interfaces and subjected to prescribed harmonic loads, as shown in Fig. 1. An appropriate finite element discretization of each substructure can be carried out, shown schematically in Fig. 2. Thus, the system is represented as a set of elastic substructures with a finite number of degrees of freedom and connected by friction joints at some of their nodes. We will also consider that the normal loads in the friction joints are independent of the displacements and are given as a vector of positive constants times a positive scalar parameter, and that only displacements in the tangential direction can occur in those joints.

A typical substructure has stiffness matrix K, mass matrix M, damping matrix C, and applied nodal loads Q, obtained by standard finite element techniques. Let X be the vector of displacements, which can be divided into two mutually exclusive vectors: X_1, corresponding to the degrees of freedom not connected to friction joints, and X_2, corresponding to the degrees of freedom connected to friction joints. The stiffness, mass, and damping matrices and the vector of nodal loads can be partitioned accordingly.

Newton's second law yields the following equations of motion for the substructure

$$M_{11}\ddot{X}_1 + M_{12}\ddot{X}_2 + C_{11}\dot{X}_1 + C_{12}\dot{X}_2 + K_{11}X_1 + K_{12}X_2 = Q_1 \quad (1)$$

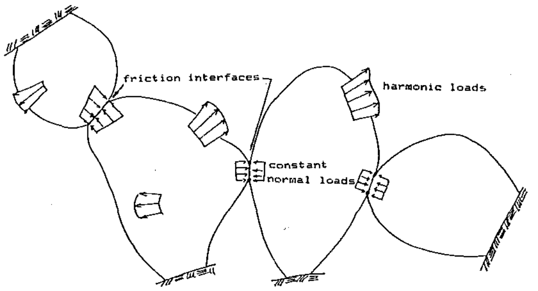

Fig. 1 System of elastic substructures connected by friction interfaces

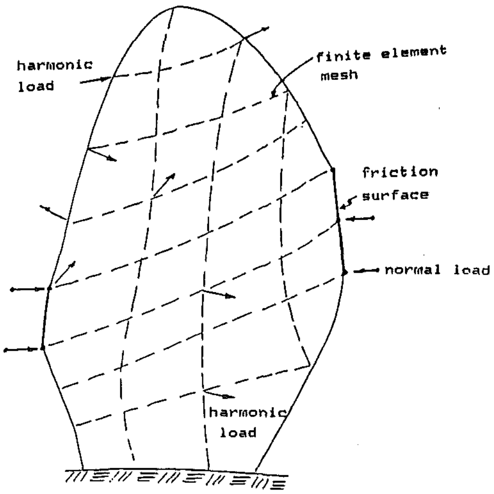

Fig. 2 Finite element model of a substructure

$$M_{21}\ddot{X}_1 + M_{22}\ddot{X}_2 + C_{21}\dot{X}_1 + C_{22}\dot{X}_2 + K_{21}X_1 + K_{22}X_2 = Q_2 + F \quad (2)$$

where dots denote derivatives with respect to time, and F is a vector containing the forces in the friction joints, with an appropriate sign that will be discussed later. These equations can be written for each substructure of the system, and are coupled by the friction forces F.

The behavior of a friction joint can be described in terms of the relative displacement (difference between the displacements of the connected nodes) and the tangential force in the joint. Here, joints of Coulomb type are considered. This implies that when a joint j is sliding, its tangential force f_j

Nomenclature

A = diagonal matrix with entries a_j
a_j = ratio d_j/f_j
B_i = imaginary part of $\hat{U}^*\hat{K}\hat{U}$
B_r = real part of $\hat{U}^*\hat{K}\hat{U}$
C = damping matrix
D = vector of relative displacements
d_j = relative displacement in joint j
e_j = factor for normal force in joint j
F = vector of friction forces
f_j = friction force in joint j
G = diagonal matrix with entries f_j
H = diagonal matrix with entries d_j
i = unit of imaginary numbers
K = stiffness matrix
M = mass matrix
N = parameter defining normal forces
N_j = normal force in joint j
Q = vector of applied nodal forces
q_j = load applied at node j
R = reduced flexibility matrix
r = condensed flexibility matrix
t = time
U = complex unit diagonal matrix
X = vector of total displacements
x_j = total displacement of node j
Z = reduced vector of displacements
z = condensed vector of displacements
α = ratio of force amplitudes
β = phase angle
Δ = increment of
θ = vector of phase angles
θ_j = phase angle in joint j
μ = friction coefficient
ω = excitation frequency

Superscript

caret ($\hat{}$) = denotes a complex quantity must satisfy the condition $f_j = \mu_j N_j$, where μ_j and N_j are, respectively, the friction coefficient and the normal force in the joint. The sign of the force must be opposite to that of the relative velocity. These conditions hold until a change in the sign of the relative velocity occurs, causing the joint to become stuck or start sliding in the opposite direction. When the joint is locked its relative displacement remains constant and its tangential force is unknown, its value being a result of the analysis.

Exact analytical solutions for the total set of differential equations of motion are difficult to obtain because it is necessary to know, at any time, which joints are sliding and which are stuck. This information, however, is part of the solution of the problem rather than part of the data. In general, for each joint, an unknown number of incursions in both conditions can take place during a period of vibration. Hence, any attempt to develop an exact solution in terms of piecewise linear solutions would lead to a problem which would have to be approached numerically and whose solution would require excessive computer resources.

Several well-known step-by-step time integration schemes can be used to solve approximately the equations of motion [1]. The main advantage of these procedures is that any number of slip-to-stick changes and vice versa can be considered without difficulty. However, for nonlinear steady-state problems the integration has to be carried out for a long time, enough to reach the periodic state, i.e., until the effect of the initial disturbances becomes negligible. Besides, to obtain accurate results in multiple-degree-of-freedom problems, the time step has to be several times smaller than the lowest relevant period of the system or any of the substructures. For these reasons numerical integration can become impractical even for systems with a moderate number of degrees of freedom.

3 Approximate Method of Solution

In view of the difficulties of obtaining analytical or numerical exact solutions, approximate methods have been used by several researchers [13, 5, 9]. The most widely used method is the so-called harmonic balance method which finds the best approximation of the response in the space of the harmonic functions with the same frequency as that of the excitation. This method is completely equivalent to the linearization technique proposed by Caughey [2]; its theoretical foundations have been thoroughly studied by Spanos and Iwan [14].

The following assumptions are made in the harmonic balance method:

1 All the responses are harmonic with the same frequency as that of the excitation forces;

2 the friction force in each joint has the same direction as the relative velocity in the joint, but opposite sign;

3 only the first Fourier component of the friction force in each joint has a significant participation in the response of the system, i.e., the effects of higher components are negligible.

Another classical assumption is that the friction joints are always sliding, i.e., no stuck conditions are considered. Since in many practical cases the joints are only partially sliding, or even completely stuck, this assumption may lead to erroneous results. A criterion to determine the slip-to-stuck limiting loads is presented here, permitting the actual states of the joints to be considered correctly in the dynamic analysis.

3.1 Equations of Motion for a Typical Substructure. The harmonic excitation forces in the nodes of a typical substructure can be expressed as

$$q_j(t) = \hat{q}_j \exp(i\omega t), \qquad j = 1, \text{ndf}$$

where a caret ($\hat{}$) denotes a complex quantity, t = time, $i = \sqrt{-1}$, and ndf = the number of degrees of freedom of the substructure.

According to assumptions (1) and (3) the elements $x_j(t)$ of the displacement vector and $f_j(t)$ of the friction force vectors are also harmonic, i.e., $x_j(t) = \hat{x}_j \exp(i\omega t)$ and $f_j(t) = \hat{f}_j \exp(i\omega t)$, where $\hat{x}_j$ is an unknown complex constant. For a totally sliding joint, the friction force has the shape of an alternating square wave. Consequently, $\hat{f}_j$ is a complex constant with modulus $(4/\pi)\mu_j N_j$, where μ_j is the friction coefficient and N_j the normal load on joint j.

By substituting these expressions into (1) and (2) and dropping the factor $\exp(i\omega t)$, the following complex algebraic equations are obtained for the substructure

$$(K_{11} - \omega^2 M_{11} + i\omega C_{11})\hat{X}_1 + (K_{12} - \omega^2 M_{12} + i\omega C_{12})\hat{X}_2 = \hat{Q}_1 \tag{3}$$

$$(K_{21} - \omega^2 M_{21} + i\omega C_{21})\hat{X}_1 + (K_{22} - \omega^2 M_{22} + i\omega C_{22})\hat{X}_2 = \hat{Q}_2 + \hat{F} \tag{4}$$

Define

$$\begin{aligned} &\hat{K}_{ij} = K_{ij} - \omega^2 M_{ij} + i\omega C_{ij} \qquad (i, j = 1, 2) \\ &\hat{r}^s = (\hat{K}_{22} - \hat{K}_{21}\hat{K}_{11}^{-1}\hat{K}_{12})^{-1} \\ &\hat{z}^s = \hat{r}^s(\hat{Q}_2 - \hat{K}_{21}\hat{K}_{11}^{-1}\hat{Q}_1) \\ &\hat{X}^s = \hat{X}_2 \\ &\hat{F}^s = \hat{F} \end{aligned} \tag{5}$$

where the superscript s indicates that these matrices correspond to the sth substructure.

With the above definitions, (3) and (4) lead, after solving for $\hat{X}_2$, to

$$\hat{X}^s = \hat{z}^s + \hat{r}^s \hat{F}^s \tag{6}$$

which is an equation relating the displacements of the degrees of freedom of substructure s to the tangential forces in its joints. Vector $\hat{z}^s$ contains the part of the displacements produced by the external harmonic loads. $\hat{r}^s$ is called the compliance or dynamic flexibility matrix; its elements are displacements in the direction of the degrees of freedom associated with the joints, due to unit loads applied in the same directions.

Defining now $\hat{F}$ as the vector containing the friction forces in all the joints, the displacement of a generic degree of freedom j of the substructure s can be expressed as

$$\hat{x}_j^s = \hat{z}_j^s + \hat{r}_j^s \hat{F} \tag{7}$$

$\hat{x}_j^s$ and $\hat{z}_j^s$ are the corresponding elements of $\hat{X}^s$ and $\hat{z}^s$; $\hat{r}_j^s$ contains the corresponding terms of $\hat{r}^s$ and, in order to match the dimension of $\hat{F}$, contains zeros in the places corresponding to friction forces not related to the degree of freedom j. $\hat{r}_j^s$ also includes appropriate signs to account for the correct direction of the friction forces, as discussed in the next section.

3.2 Equations for the Complete System. We now derive the equations for a typical system, like the one depicted in Fig. 1. The first step is to define the relative displacements in the joints, as follows

$$\hat{d}_j = \hat{x}_i^m - \hat{x}_l^n \tag{8}$$

The superscript m can be assigned arbitrarily to any of the substructures connected by the joint j; n denotes the other connected substructure. The relative velocity is positive from m to n. Therefore, the friction force from joint j is negative for substructure m, and positive for substructure n. This rule is used when writing equations (7). Replacing $\hat{x}_j^s$ $(s = m, n)$ into (8) we obtain

$$\hat{d}_j = (\hat{z}_i^m - \hat{z}_l^n) - (\hat{r}_l^n - \hat{r}_i^m)\hat{F}$$

One equation can be written for each degree of freedom in the friction interfaces obtaining the following system of complex algebraic equations

$$\hat{D} + \hat{R}\hat{F} = \hat{Z} \tag{9}$$

for the relative displacements in the friction joints in terms of the corresponding friction forces and known displacements $\hat{Z}$. The number of unknowns in these equations is twice the number of equations. To complete the formulation, it is necessary to make use of the relationships between the joint displacements and forces $\hat{D}$ and $\hat{F}$. For the dry friction (Coulomb) joints and steady-state response considered in this work, the relative displacement in a joint is

$$(\hat{x}_l^m - \hat{x}_l^n)\exp(i\omega t) = \hat{d}_j \exp(i\omega t) \tag{10}$$

$\hat{d}_j$ is a complex constant that can be expressed as $d_j \exp(i\theta_j)$, where d_j and θ_j are the corresponding amplitude and phase angle. According to assumption (2), the phase angle of the friction force is opposite to that of the relative velocity; therefore, $\hat{f}_j = -if_j \exp(i\theta_j)$, where f_j is the amplitude of the friction force in the jth joint. Defining $a_j = d_j/f_j$ we have

$$\hat{d}_j = i(d_j/f_j)\hat{f}_j = ia_j\hat{f}_j \tag{11}$$

The ratio a_j is always positive and can vary between zero and infinity. Both limiting values lead to special linear problems. a_j equal to zero means that there is no relative displacement in the jth joint. On the other hand, a_j equal to infinity corresponds to the case of no normal force (and as a consequence, no friction force) in the joint.

Equation (9) can be now written as

$$[\hat{R} + iA]\hat{F} = \hat{Z} \tag{12}$$

where A is a real diagonal matrix with entries a_j.

For prescribed values of A, (12) is a linear system of complex equations for the friction forces $\hat{F}$. We are, however, interested in solutions for prescribed normal forces in the joints, i.e., for prescribed amplitudes of $\hat{F}$ and not of A. In this case, a_j cannot be calculated directly because the d_j are still unknown. This problem is addressed in the next section, as part of the proposed solution methodology.

4 An Efficient Solution Procedure

4.1 General. In the cases of interest for this paper, the normal loads in the joints are prescribed as a vector of real constants times a scalar parameter N, i.e., as

$$\begin{Bmatrix} N_1 \\ N_2 \\ \cdot \\ \cdot \\ \cdot \\ N_n \end{Bmatrix} = N \begin{Bmatrix} e_1 \\ e_2 \\ \cdot \\ \cdot \\ \cdot \\ e_n \end{Bmatrix} \tag{13}$$

In practical design problems, it is desired to find the solution for different values of N, and, eventually, to calculate the N for which the response controlling the design (displacement, stress, etc.) is a minimum. This is the optimum value of the parameter N.

If the joint j, with friction coefficient μ_j, is sliding, the amplitude of the friction force in that joint is $f_j = (4/\pi)\mu_j N_j$. In this joint, the relative displacement has an unknown amplitude d_j.

In general, for a given value of N, some joints will be sliding, and the rest will be locked. There are two limiting conditions. The first one occurs for high values of normal forces, preventing any slip of the joints. In this case the governing equation (9) reduces to $\hat{R}\hat{F} = -\hat{Z}$, which can be solved directly. The other limiting case corresponds to no normal forces ($N = 0$) and, consequently, no friction forces in the joints. All the joints are slipping, and the relative displacements $\hat{D}$ are given by $\hat{Z}$.

It can be easily shown that Gaussian elimination of the equations corresponding to the locked joints (using the condition that the relative displacements are zero) yields a reduced system of equations of the same form as (9), but containing only terms related to the sliding joints. As pointed out before, it cannot be asserted that the amplitude of all of the forces is $f_j = (4/\pi)\mu_j N_j$, because this in acceptable only for joints that are at least partially sliding. For a locked joint the value of f_j is completely unknown and must be determined as part of the solution.

4.2 The Basic Step. The solution algorithm developed in this work is summarized in this section. It essentially consists of finding the solution when all the joints are slipping, and then progressively calculating the solutions as the normal loads are increased. The basic step of the algorithm is presented next.

Equation (9) can be written as

$$\hat{F} + \hat{K}\hat{D} = \hat{F}_0 \tag{14}$$

where $\hat{K} = \hat{R}^{-1}$ and $\hat{F}_0 = \hat{K}\hat{Z}$. Assume that solution vectors $\hat{F}$ and $\hat{D}$ for normal forces defined by $N = N_0$ are known. The solution for another, close, value of $N = N_0 + \Delta N$ is desired. Let $\hat{F}_1$ and $\hat{D}_1$ denote the new solution vectors, and define $\Delta\hat{F}$ and $\Delta\hat{D}$ so that

$$\hat{F}_1 = \hat{F} + \Delta\hat{F} \text{ and } \hat{D}_1 = \hat{D} + \Delta\hat{D} \tag{15}$$

Since $\hat{F}$ and $\hat{D}$ satisfy (14) we can write

$$\Delta\hat{F} + \hat{K}\Delta\hat{D} = 0 \tag{16}$$

Note that this is an exact relationship between the complex increments of friction forces and relative displacements. Recalling that the elements of $\hat{F}$ and $\hat{D}$ in the known solution are $\hat{d}_j = d_j \exp(i\theta_j)$ and $\hat{f}_j = if_j \exp(i\theta_j)$, the increments can be approximated by truncated Taylor's series expansions as follows

$$\Delta\hat{d}_j = \exp(i\theta_j)\Delta d_j + i\hat{d}_j \Delta\theta_j$$
$$\Delta\hat{f}_j = i\exp(i\theta_j)\Delta f_j + i\hat{f}_j \Delta\theta_j$$

Substitution into (16), after algebraic manipulations, yields the following system of linear equations for the increments of amplitudes and phase angles of the relative displacements

$$B_i \Delta d + B_r H \Delta\theta = \Delta f \tag{17}$$

$$B_r \Delta d + (G - B_i H)\Delta\theta = 0 \tag{18}$$

where B_r and B_i are the real and imaginary parts of the complex matrix product $\hat{U}^*\hat{K}\hat{U}$. $\hat{U}$ is a unit complex diagonal matrix with nonzero elements $u_{jj} = \exp(i\theta_j)$. Δd and $\Delta\theta$ are real unknown vectors of amplitudes and phase angles of the relative displacements. H and G are real diagonal matrices with nonzero elements d_j and f_j, respectively. ΔF is the known vector of increments in the amplitudes of the friction forces. Note that the matrices defining the coefficients of the system (17) and (18), which are used to estimate the solution each time N is increased, are expressed in terms of the known solution.

Solving for Δd and $\Delta\theta$ we have an approximation for ΔF that can be used to compute F_1 and D_1. The accuracy of this approximate solution can be verified by computing $F_2 = F_0 - KD_1$, and comparing F_2 with F_1. If the comparison is not satisfactory, it is possible to compute a new starting solution that satisfies (14) calculating the ratios $a_j = d_j/f_j$ with D_1 and the desired values of the amplitudes of the tangential forces. Introducing the estimated a_j into (12), another vector of forces F_3 is obtained. In general, F_3 will be different from F_1. The difference $F_3 - F_1$ can be taken as a new vector ΔF using F_3 to compute the coefficients of equations (17) and (18). The steps can be repeated iteratively in the following manner until a desired accuracy is reached.

1 Solve the system under the assumption that all the joints are slipping, and define the initial values of f_j, f_j^0.

2 Increase the value of μN.

  2.1 Compute Δf, vector of increments of the amplitudes of the tangential forces, $\Delta f_j = f_j^1 - f_j^0$.

  2.2 Compute Δd, vector of increments of the amplitudes of the relative displacements.

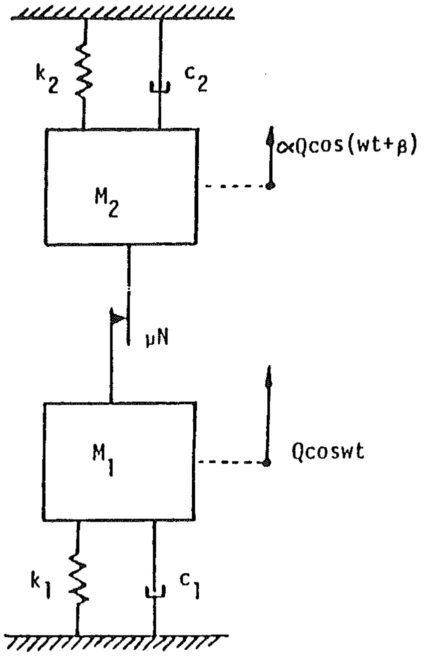

Fig. 3 Two-body system with a friction joint

2.3 Calculate the new relative displacements, $d_j^1 = d_j^0 + \Delta d_j$, and the ratios $a_j = d_j^1/f_j^1$.
2.4 Solve equations (12) and compute f_j^2.
2.5 If $f_j^2 = f_j^1$ continue with 2.6. If not, set $f_j^0 = f_j^2$ and start 2.1 again.
2.6 Verify if all the joints are actually slipping, i.e., if all d_j^1 are positive. Yes, define $f_j^0 = f_j^2$ and look for the next value of μN (go to 2). No, eliminate equations corresponding to the locked joints (negative amplitudes) and start 2.1 again.

3 The procedure finishes when all the joints are locked.

4.3 Slip-to-Stick Transitions. In the previous section it was assumed that all the joints are slipping. This assumption is certainly valid when the joint normal loads are small but must be checked as N increases. As N increases, the amplitudes of the relative joint motions decrease. When the calculated amplitude of a joint's relative motion becomes zero (or negative) that joint is considered locked for subsequent analyses, the amplitude of its relative motion is set identically equal to zero, and the associated degree of freedom may be eliminated from the set of nonlinear algebraic equations. Thus, the number of nonlinear equations that must be solved becomes progressively smaller as the normal loads are increased and the joints lock. When a joint is considered locked, the force transmitted by friction through it may be calculated as a result of the analysis. The joint is actually locked if the amplitude of the force is smaller than $\mu N e_j$. The slipping and stuck models are then said to be compatible and there is no transition region where the simple harmonic assumption breaks down.

In solving the numerical example described in the next section, it was found that convergence to negative values of the relative displacements is possible. In fact, examining equation (18), it can be observed that no restrictions are imposed on the values of Δd. The physical meaning of zero or negative values for the relative displacements is that the corresponding joints are already locked. On the other hand, the condition of zero relative displacements can be used to eliminate the locked joints from the system of equations for subsequent (higher) normal loads. For this reason, it is important to have an accurate criterion for establishing at what normal loads each joint becomes stuck. Such a criterion can be formalized in the following manner.

Table 1 Comparisons of results for the system of Fig. 3

a) dimensionless frequency ω = 0.707

$\mu N/Q$	relative displacement		displacement of mass 1	
	exact	approx.	exact	approx.
0.20	149.1	149.1	149.0	149.1
0.40	98.0	97.9	98.0	97.9
0.60	46.9	47.2	46.9	47.2
0.80	2.1	-5.6	2.5	2.1
1.00	0.0	0.0	2.0	2.0

b) dimensionless frequency ω = 1.

$\mu N/Q$	relative displacement		displacement of mass 1	
	exact	approx.	exact	approx.
1.00	3.40	3.61	5.35	6.38
2.40	2.76	3.06	10.93	12.73
6.91	1.36	1.30	30.49	35.24
10.00	0.57	0.12	42.61	50.87
12.50	0.05	0.00	50.93	51.76

We start with the solution for $\mu N = \mu N_0$, for which all the joints under consideration are sliding. The friction forces and the relative displacements are $f_{0j} = (4/\pi)e_j\mu N_0$ and d_{0j}, respectively. The desired solution corresponds to an unknown value of μN for which $f_j = (4/\pi)e_j\mu N$. Therefore, the differences in the amplitudes of the friction forces are

$$\Delta f_j = (4/\pi)(f_j - f_{0j}) = (4/\pi)(e_j)(\mu N - \mu N_0) = (4/\pi)(e_j)(\Delta\mu N) \tag{19}$$

Solving (17)-(18) for a unit increment in μN, i.e., for $\Delta f_j = 4/\pi e_j$, we obtain increments Δd_j for the relative displacements. The total values are

$$d_j = d_{0j} + \Delta\mu N \Delta d_j \tag{20}$$

For $\Delta\mu N$ yielding $d_j = 0$ the joint j will become locked. Applying this condition to each joint, n values of μN are obtained, where n is the number of joints under consideration. The important value is the smallest value of normal load increment for which lockup occurs since it is the corresponding joint which will be the first to stop slipping.

5 Numerical Results

To verify the accuracy and applicability of the methodology, the solution of the one-joint problem depicted in Fig. 3 was computed using the approximate method calculated over a range of values of the system parameters and the results compared with exact solutions. The exact solution was developed by exploiting the piecewise linearity of the differential equation, i.e., when the joint is slipping the friction force is constant and the solution can be represented by one set of harmonic functions with unknown coefficients, and when the joint is stuck the system is also linear and can be represented by another set of harmonic functions with unknown coefficients. The coefficients are calculated (along with the time at which transition occurs between slipping and sticking) by forcing the solutions to satisfy the appropriate continuity and periodicity conditions. In general, the results from the approximate procedure compared quite well with exact solutions. Representative results are shown in Table 1 for $M_1 = M_2 = 0.5$, $k_1 = 0.25$, $k_2 = 0.75$, $Q = 1.0$, $\alpha = 0.0$, and $c_1 = c_2 = 1$ percent of critical. The two cases shown in the table are for excitation frequencies of $\omega = 0.707$ and $\omega =$

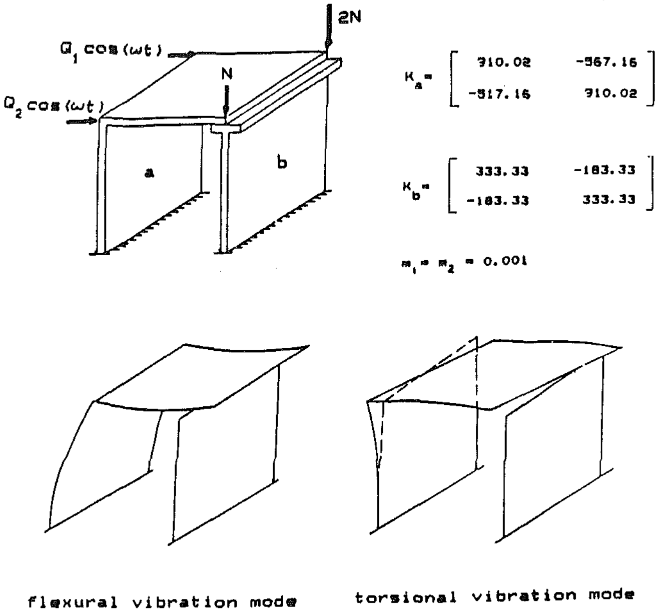

Fig. 4 Two-joint plate system

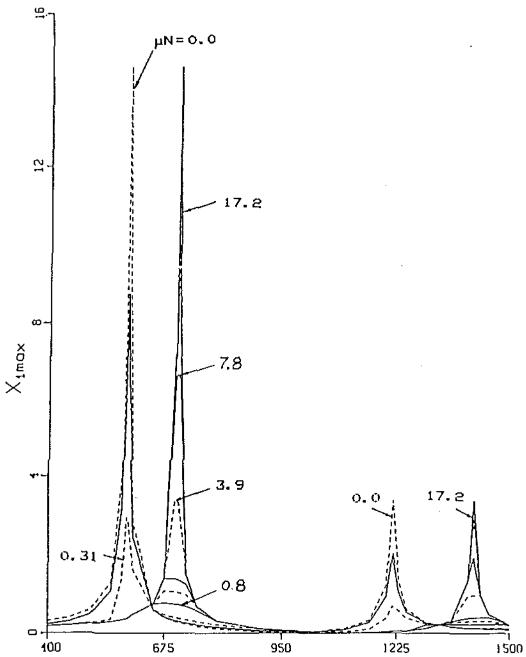

Fig. 5 Maximum response curve for system of Fig. 4

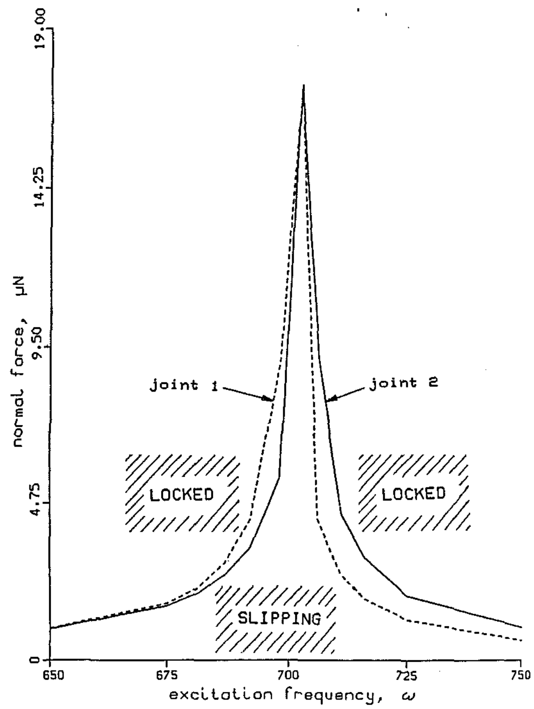

Fig. 6 Slip-to-stuck transitions for system of Fig. 4

1.0. These frequencies are particularly interesting since the first corresponds to the resonant frequency that the system would have if the damper were slipping all the time, while the second is the resonant frequency of the system when the damper is stuck all the time. Consequently, these two frequencies turn out to be the frequencies of most interest in the limit for either very large or small excitations, respectively.

Part (*a*) of the table shows exact and approximate results for $\omega = 0.707$. As is indicated by the table the approximate method provides an excellent method of estimating the solution for excitations at this frequency. Part (*b*) of the table shows exact and approximate results for $\omega = 1.0$. In this case the approximate procedure was less accurate, but still adequately predicted the absolute displacement of the masses. The absolute displacements of the masses were of comparable magnitude, consequently, small errors in their values resulted in relatively large percentage errors in the relative displacement as it approached zero. This is a limitation of the approximation caused by the fact that if slip occurs the Fourier coefficient of the friction force is taken to be $4/\pi$, independent of the amplitude of the relative motion. In fact, this value must go to 1.0 as the relative motion goes to zero and it is this discrepancy that induces the errors previously cited. A number of procedures were tried for approximating this transition of the Fourier coefficient from $4/\pi$ to 1.0 as the amplitude of the relative motion went to zero. In general, none of the approaches worked (on the average after taking all frequencies of excitation into consideration) any better than the simple one utilized here of setting the Fourier coefficient equal to $4/\pi$ when the joint slips.

In summary the approximate approach used in this paper proved to be a relatively accurate method for calculating the absolute and relative motions of the vibrating masses except for small relative motions at an excitation frequency near the natural frequency of the locked system. Under these conditions, it adequately predicted the absolute motion of the masses and qualitatively predicted the correct trends, but yielded significant percentage errors in values of relative motion between the masses. This is a limitation of the approach that should be taken into consideration in its use.

To demonstrate the applicability of the methodology in design problems we have analyzed the system with two substructures and two friction joints system shown in Fig. 4. Plate finite elements (including only bending deformations) were used to calculate the stiffness and mass properties of each substructure and structural damping was set at 1 percent of critical damping. The stiffness matrices are also presented in Fig. 4. External loads $Q_1 = 1$ and $Q_2 = 2$ were considered. The normal forces in the friction joints are the same, i.e., $e_1 = 1 = e_2$.

The natural frequencies and modes of vibrations for the system with the joints locked, and for substructure 1 isolated were calculated (substructure 2 was considered massless). The mode shapes for the isolated substructure are shown in Fig. 4. The mode shapes for the total system are similar, but correspond to higher frequencies. In both cases, the first mode is flexural, and the second one, torsional.

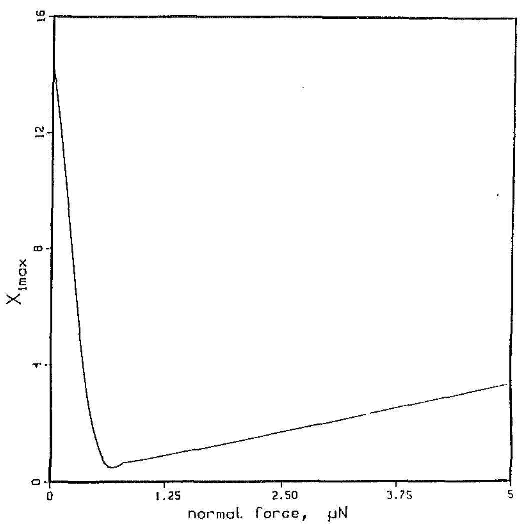

Fig. 7 Optimization curve for system of Fig. 4

In the dynamic analysis the excitation frequency was varied between 400 and 1500 rad/s to include the four possible resonant conditions (see values below). Several values of the normal force in the joints were considered.

Results are summarized in Figs. 5–7. In Fig. 5 the maximum horizontal displacement of substructure 1 in joint 1 is presented as a function of the excitation frequency. The first peak in Fig. 5 corresponds to the first natural frequency of substructure 1 ($\omega = 586$ rad/s) and occurs when there are no forces, and consequently no energy dissipation, in the joint. If the normal forces increase, the response for that particular frequency decreases quickly. However, for frequencies close to the first natural frequency of the complete system ($\omega = 702$ rad/s) the response increases very rapidly, and a second peak is reached. This peak has its maximum value when the normal forces are high enough to keep the joints locked, preventing energy dissipation by friction. Peak responses also occur for the corresponding second natural frequencies ($\omega = 1215$ and 1412 rad/s), but their values are only 23 percent of the former ones.

Figure 6 shows values of the normal forces for which a change from the stuck to the sliding condition (or vice versa) occurs in each friction point. For a prescribed frequency, a joint is locked for normal forces that exceed the value given in the corresponding curve. For given normal loads, a horizontal line can be drawn in Fig. 6 to find the limiting frequencies for which each joint is either always stuck or always sliding. The slip-to-stuck curve has a peak at $\omega = 702$, the first resonant frequency when the joints are locked. The reason is that the largest tangential forces in the joints under harmonic excitation occur for this resonant condition, requiring the maximum normal loads to prevent slipping.

Results presented in Fig. 7 can be useful for design purposes. This figure shows the maximum value $x_{1\max}$ of the displacement at node 1, as a function of the parameter μN defining the normal forces in the joints. It was obtained by considering all the possible values of the excitation frequency, i.e., by taking the peak values of the response curves of Fig. 5. The optimum value of the mentioned parameter is that giving the minimum value of $x_{1\max}$ (0.6 in this case). A similar curve was developed for the displacement in node 2, and the same optimum value of μN was obtained. Curves corresponding to any other response of interest can be easily constructed. Naturally, it is highly desirable to design the friction joints to have values of the normal forces close to the optimum ones.

6 Conclusions

A simple methodology for analyzing the steady-state vibrations of linear structures containing friction interfaces was presented. The numerical problem is reduced to the solution of systems of linear algebraic equations. Well-known, efficient algorithms can be used for this purpose. The main hypotheses are that the response is harmonic with the same period as that of the excitation, and that only the first Fourier components of the friction forces have a relevant participation in the dynamic response. It can be noted that, for the simple Coulomb model of friction used here, the Fourier series for the nonlinear forces would contain only odd integer multiples of the fundamental frequency, and that the amplitudes of the terms decrease at least as fast as their frequencies increase. Consequently, one would expect relatively minor contributions from the higher order harmonics that have been neglected. As a result, we expect the solution procedures presented here to be reasonably accurate under most circumstances.

Within the frame of the above assumptions, the complex variable approach presented here is an efficient and systematic tool which can be utilized to derive the equations governing the motion of the friction joints in terms of their relative displacements and tangential forces. In fact, it is possible to formulate the equations in a manner similar to the direct stiffness method, taking advantage of the topological and storage procedures devised for such a method.

The comparison of numerical results for the single-joint problem of Fig. 3 shows that the approximate methodology can yield very good estimates of the exact results. The major discrepancies occur when the joints are partially sliding, because in these cases the first Fourier coefficients of the friction forces are closer to one and not $4/\pi$. The errors could be reduced by using some rules to calculate the Fourier coefficient as a function of the normal forces in the joints. These rules can be easily incorporated in the methodology; however, their general applicability must be carefully verified first.

The linearization concepts proposed in this work can be used for systems with friction interfaces obeying different constitutive laws. In general, assuming that the response is harmonic, the differential equations can be transformed into a system of algebraic nonlinear equations relating relative displacements and friction forces in the joints. The equations can be linearized by considering truncated Taylor expansions in terms of the increments of the unknowns.

A criterion to determine the slip-to-stuck transitions in the joints is required to correctly formulate the problem under study, whatever method of solution is employed. It can be appreciated in Table 1 that it is mathematically possible to obtain negative amplitudes for the relative displacements in the joints. Similar results were obtained in the two-joint problem. Physically, this would correspond to friction forces with the same, not opposite, direction as the relative velocities. In reality, the joints are locked, and that physical fact must be incorporated into any solution procedure one may use to calculate the response for high joint normal loads.

The inclusion of possible locked joints allows a direct extension of the methodology to systems comprising substructures continuously connected, like the bladed disks of turbine engines or similar circumferentially periodic structures. The continuous interfaces can be treated as friction interfaces with the joints always locked.

The methodology presented here constitutes a good compromise between numerical effort and accuracy. This is particularly true when a large number of cases have to be solved. For instance, the derivation of optimization curves, as depicted in Fig. 7, requires solutions for a wide range of frequencies, for each set of normal load values. In this case, the methodology takes advantage of the already known solutions to find additional ones. In addition, if an exact solution is required, the approximate results could be used as initial conditions to solve the differential equations of motion using finite difference methods. This would significantly reduce the time for which integration has to be carried out, since the initial guess would be close to the steady-state solution.

7 Acknowledgments

This work was supported by the Aero Propulsion Laboratory, Wright-Patterson Air Force Base, Contract No. F33615-K-2316, under the direction of Dr. James C. MacBain and Mr. William Stange.

8 References

1 Bathe, K.-J., and Wilson, E. L., *Numerical Methods in Finite Element Analysis*, Prentice Hall, Englewood Cliffs, NJ, 1976.

2 Caughey, T. K., "Sinusoidal Excitation of a System With Bilinear Hysteresis," ASME *Journal of Applied Mechanics*, Vol. 27, 1960, pp. 640-643.

3 Menq, C.-H., and Griffin, J. H., "A Comparison of Transient and Steady State Finite Element Analyses of Forced Response of a Frictionally Damped Beam," ASME Paper No. 83-DET-24.

4 Den Hartog, J. P., "Forced Vibrations With Combined Coulomb and Viscous Friction," *Trans. ASME*, 1931, pp. 107–115.

5 Dominic, R. J., Graf, R., and Raju, B. B., "Analytical and Experimental Investigation of Turbine Blade Damping," University of Dayton Publication No. UDR-TR-82-39, Aug. 1982.

6 Griffin, J. H., "Friction Damping of Resonant Stresses in Gas Turbine Airfoils," ASME JOURNAL OF ENGINEERING FOR POWER, Vol. 102, Apr. 1980, pp. 329–333.

7 Hurty, W. C., "Dynamic Analysis of Structural Systems Using Component Modes," *AIAA Journal*, Vol. 3, No. 4, Apr. 1965, pp. 678–685.

8 Mahalingam, S., "The Synthesis of Vibrating Systems by Use of Internal Harmonic Receptances," *Journal of Sound and Vibration*, Vol. 40, No. 3, 1975, pp. 337–350.

9 Muszynska, A., Jones, D. I. G., Lagnese, T., and Whitford, L., "On Nonlinear Response of Multiple Blade Systems," *Shock and Vibration Bulletin*, Vol. 51, No. 3, May 1981, pp. 88–110.

10 Plunkett, R., "Friction Damping in Damping Applications for Vibration Control," *AMD*, Vol. 38, 1980.

11 Przemieniecki, J. S., *Theory of Matrix Structural Analysis*, McGraw-Hill, New York, 1968.

12 Sinha, A., and Griffin, J. H., "Friction Damping of Flutter in Gas Turbine Engine Airfoils," *AIAA Journal of Aircraft*, Vol. 20, No. 4, Apr. 1983, pp,. 372–376.

13 Soni, M. L., and Bogner, F. K., "Finite Element Vibration Analysis of Damped Structures," *AIAA Journal*, Vol. 20, No. 8, 1982, pp. 700-707.

14 Spanos, P.-T. D., and Iwan, W. D., "On the Existence and Uniqueness of Solutions Generated by Equivalent Linearization," *Int. J. Non-Linear Mechanics*, Vol. 13, 1978, No. 71–78.

15 Srinivasan, A. V., Lionberger, S. R., and Brown, K. W., "Dynamic Analysis of an Assembly of Shrouded Blades Using Component Modes," ASME *Journal of Mechanical Design*, Vol. 100, July 1978, pp. 520–527.

16 Srinivasan, A. V., Cutts, D. G., and Shidhar, S., "Turbojet Engine Blade Damping," NASA Contract Report 165406, July 1981.

The Production of Jet Fuel From Alternative Sources

H. R. Lander, Jr.
Air Force Wright Aeronautical Laboratories,
Aero Propulsion Laboratory,
Wright-Patterson Air Force Base, OH

H. E. Reif
Sun Refining and Marketing Company,
Marcus Hook, PA

The most significant potential source of aviation gas turbine fuels in the continental United States is the western oil shale located in the Rocky Mountain States of Colorado, Utah, and Wyoming. Nearly 600 billion barrels of recoverable oil is located in this area. This paper discusses the availability of oil shale and reviews the recovery, upgrading and refining schemes necessary to produce fuel which can be used in present-day aircraft. Other synthetic fuels are discussed with regard to the processing necessary to produce suitable fuels for today's high-performance aircraft. Heavy oil and tar sand bitumen are likely to be refined in the next decade. Methods for producing suitable fuels are discussed. The chemical structure of these sources, which is basically cyclic, leads to the potential for heavier fuels with more energy per given volume and therefore longer range for certain aircraft. This exciting possibility is reviewed.

Introduction

Today, the refining industry finds itself in a state of transition. Light paraffin crude oils are diminishing worldwide, while heavier, sour (high-sulfur) crudes are becoming more commonplace. No longer can these difficult refinery feedstocks be handled and lost in a refinery by means of blending with lighter crudes. They must be refined in concentrated forms. Besides this emerging trend in crude type, changes in overall availability, quality and cost, coupled with changes in refinery technology, the introduction of syncrudes and changes in the relative demands for the major products, gasoline and diesel fuel, all contribute to a perplexing and sometimes confusing future. Aviation gas turbine fuels represent only about 7 percent of the refinery production in the United States. As of October 1984, the domestic production of kerosene-type fuels (Jet A, JP-5, Jet A-1) was reported to be 922,000 barrels per day (bpd) [1]. The total crude processed in the United States last year was approximately 16 million bpd. The growing scarcity of light sweet petroleum could impact the future availability of a minor product such as jet fuels. Of course, the industry will have technology for handling the more difficult feedstocks and will produce the required gasoline and/or diesel fuel for ground transportation. This paper looks at alternative refinery feedstocks of the future and evaluates their potential for producing aviation gas turbine fuels. Oil shale, tar sands, and heavy oils are discussed. The potential for modifying fuel specifications, making them more identifiable with the basic feedstocks, and improving aircraft performance is reviewed for the current refining situation and the evolving future.

Aircraft Fuels. Almost exclusively, aviation gas turbine fuels have been produced from petroleum crude. These jet fuels are the most critical product, in terms of quality, produced by the refining industry. The naturally occurring hydrocarbons in petroleum can be essentially fractionated with little additional processing to produce highly stable jet fuels. There are instances where fuels are mildly hydrotreated to remove sulfur but for the most part, chemical conversion processes are not necessary.

In 1951, the United States Air Force (USAF) standardized aircraft operations on JP-4 jet fuel in order to optimize performance and availability. "Average" typical properties are shown in Table 1. This fuel can be characterized as a "wide-cut" fuel with a boiling range between 150°F and 480°F. This range optimizes the requirement for a vapor pressure between 2 and 3 psi at 100°F and a maximum freeze point of −72°F. These properties are required for high-altitude operations and low ambient temperature conditions at certain air bases. Although made up of many different hydrocarbons, jet fuels consist essentially of four general types of compounds. These hydrocarbons can be grouped into the following series: the paraffins (including isoparaffins); cycloparaffins or naphthenes; aromatics; and olefins. The proportion of each compound type varies with the different types of crude oils and the processing needed to produce the fuel. A typical fuel will contain hundreds of different compounds. Except for restrictions on aromatics and olefins, the

Table 1 Typical properties of aviation fuels

	JP-4	JP-8 (Jet A-1)
Specific gravity, 60°F	0.764	0.800
Boiling range, °F	150-480	350-520
Heat of combustion, Btu/lb	18,700	18,500
Hydrogen content, wt. percent	14.4	13.8
Viscosity, cs @		
−40°F	2.6	10.0
0°F	1.6	3.8
40°F	1.4	2.0
Flash point, °F	−22	128
Freezing point, °F	−75	−62

Contributed by the Gas Turbine Division and presented at the 1985 Beijing International Gas Turbine Symposium and Exposition, Beijing, People's Republic of China, September 1-7, 1985. Manuscript received at ASME Headquarters May 31, 1985. Paper No. 85-IGT-67.

Table 2 Typical hydrocarbon composition of jet fuels (modified ASTM method D-2789)

Hydrocarbon type	JP-4 composition, wt. percent	Jet A-1 composition, wt. percent
Paraffins	66.0	44.5
Cycloparaffins	16.7	36.2
Alkybenzenes	15.8	16.5
Indans and tetralins	1.0	2.3
Naphthalenes	0.5	0.5
	100.0	100.0

majority of the hydrocarbons is not directly controlled. The requirements on density, energy content, freeze point, and hydrogen content favor paraffinic or isoparaffinic-based fuel. The hydrocarbon constituents of most JP-4 fuels are primarily normal or isoparaffins (50-70 volume percent) and cycloparaffins (20-40 volume percent). Typically, these fuels have energy levels and hydrogen contents well in excess of the specification limits. The hydrocarbon-type composition of a typical petroleum JP-4 is depicted in Table 2. The refiner produces JP-4 from a blend of 60-70 percent light naphtha and 30-40 percent kerosene in terms of crude oil fractions.

Most of the world's airlines and many foreign military services use a kerosene-type fuel. This fuel is designated by the American Society for Testing and Materials (ASTM) as Jet A-1 fuel and is similar to its military counterpart, JP-8, as outlined in Table 1. The basic difference between Jet A-1 and JP-8 is the additives required for military operations. The "average" boiling range for Jet A-1 is between 350°F and 520°F where volatility is limited by a flashpoint minimum of 100°F. This fuel has a freeze point maximum limit of -54°F. The hydrocarbon constituents in this fuel are, in general, denser than JP-4 and are outlined for a typical fuel in Table 2. The properties of a typical JP-8 (Jet A-1) fuel are compared to JP-4 (Jet B) in Table 1.

Oil Shale. Oil shales are an abundant resource, occurring in many parts of the world. It is estimated and projected that worldwide oil shale reserves are equivalent to approximately two quadrillion barrels of oil. This includes estimates of future discoveries. These deposits of varying quality are found on every continent, with Asia having the largest reserves of nearly 850 trillion barrels and Australia and New Zealand having the smallest reserves at 120 trillion barrels [2]. There has been a small oil shale industry in various parts of the world for the last century [3].

Oil shale is a fine-grained sedimentary rock which contains an organic solid material commonly referred to as kerogen. Upon heating, this kerogen will pyrolyze to yield liquid shale oil, gases, and residual carbon. The proportions of inorganic material in shale vary with location and grade of the shale. Commonly occurring minerals are dolomite, calcite, quartz, illite, and sometimes nahcolite and dawsonite [4].

The largest active shale oil industry in the world is located in Northeastern China in the Liaoning Province near the city of Fuchun in Mau. A 300 to 650 foot thick lean (10 gal per ton) oil shale deposit exists as overburden on a thick coal seam. The ore is approximately 18 km long and 2 km wide. The oil shale must be removed to facilitate open-pit mining of the coal. Pilot scale operations were begun in 1924 and operations were expanded to a processing level of 1.4 million tons in 1929, using German Pintsch technology. In 1941, a new plant was completed and operations increased to 4.7 million tons per year (1.3 million barrels per year) in 1943. The People's Republic of China completed a new plant in 1954 and continued to expand this operation until the 1970s. Production in 1978 was 1.4 million barrels. In all likelihood, there will be major changes in the Fuchun operation; first the underlying coal bed dips, making its recovery more amenable to underground mining, and also the discovery of the Taching Oil Field north of Fuchun places the shale plants in direct competition with petroleum operations. A second oil shale operation in the Guangdong Province near Maoming in southern China has been reported. The operation, which includes producing minerals, has been mentioned in United States visits to Fuchun [3]. Production in 1978 was reported to be 570,000 barrels. Current recovery technology at Maoming is believed to be an earlier generation of Lurgi retorts. Chinese geologists estimate the current oil reserves in the Guangdong Province alone to be in excess of 25 billion barrels of recoverable oil.

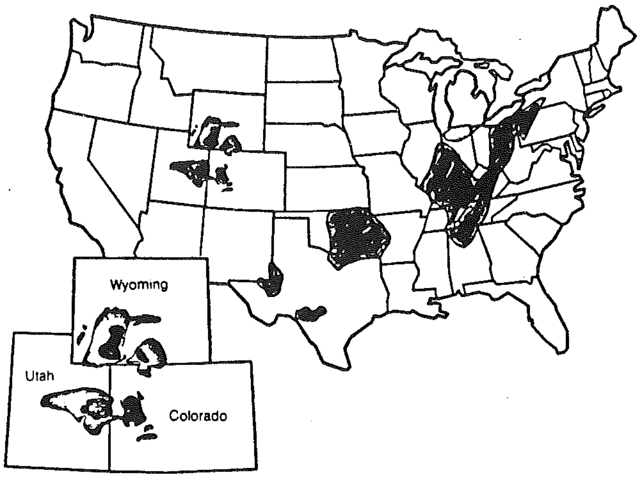

Fig. 1 Location of U.S. oil shale deposits

Oil shale could possibly be the biggest alternative source of hydrocarbon fuel and replacement for petroleum in the United States. To date, the world's largest deposit of recoverable oil shale is the Green River Formation, located in the Rocky Mountain area, specifically in the states of Colorado, Utah, and Wyoming. It has been estimated that this deposit alone contains the equivalent of nearly 2.0 trillion barrels of oil. Of this, 600 billion barrels of recoverable oil is high-grade shale containing between 25 and 100 United States gallons per ton of oil. It is estimated that 80 billion barrels of oil equivalence could be recovered using current technology. This alone would replace the total domestic requirement for oil for 20 years [5].

Locations of major United States oil shale deposits are shown on the map in Fig. 1. The oil shale deposits of the Green River Formation are the richest and are being developed commercially. There are less rich and extensive deposits underlying much of the east central part of the country. These beds are generally thin, yielding low-grade oil. Because of their proximity to the eastern industrial complex, there is some interest in developing the eastern shale, also. In general, western shale has higher carbon/hydrogen ratios (weight); for instance, western shale oil is generally 8.0 while eastern (New Albany) shale oil is of the order of 11.0. In simplistic terms, eastern oil shale will require more hydrogen addition to produce transportation fuels to current specifications. There has been some development work expended in recovering the oil under hydrogen pressure. This could improve eastern oil shale yields and quality. Currently, the richest eastern deposits are on the order of 10-15 gal per ton using conventional retorting techniques.

Research on the production of shale oil has been carried out in the United States on a large scale since the late 1940s. Much of the early work concentrated on the mining of the oil-bearing rock and on processing of rock above ground to produce the shale oil. The extraction of oil from the shale is straightforward. The shale is heated to a temperature above 900°F at which the kerogen decomposes into oil and light hydrocarbon gases. Figure 2 is a schematic of a typical aboveground facility [6]. In this operation, the shale is mined,

Table 3 Properties of Green River formation shale oil

	Union "B"	Paraho	Occidental	Geokinetics
API gravity, 60°F		22.7	20.6	23.0
Chemical analysis, wt. percent				
Carbon	84.8	83.83	84.82	84.48
Hydrogen	11.61	11.72	12.04	11.96
Sulfur	0.81	0.75	0.52	0.48
Nitrogen	1.74	2.13	1.46	1.66
Oxygen	0.90	1.31	1.18	1.75
Trace metals, parts per million				
Iron	–	90	–	60
Arsenic	–	34	33	20
Pour point, °F	60	–	65	–

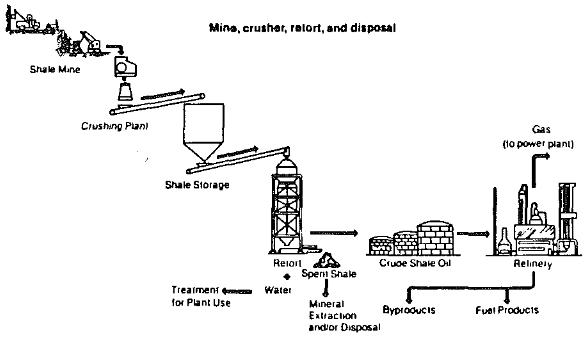

Fig. 2 Aboveground oil shale recovery and processing facility

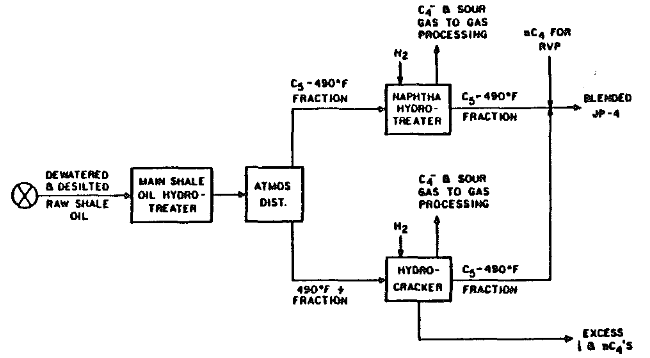

Fig. 3 Schematic flow diagram of process to maximize shale JP-4

brought out to an aboveground facility where it is crushed, and heated in a vessel called a "retort."

Aboveground technology is presently considered to be workable on a modular scale with plants ranging in size between 5,000 and 10,000 barrels per day. The Union Oil Company of California and Paraho Development Corporation have developed aboveground retorts and intend to proceed with commercialization. The Union Oil project is proceeding with a price guarantee from the United States Synthetic Fuels Corporation on their upgraded oil (syncrude). The United States Synthetic Fuels Corporation is a quasi-government organization established by the Energy Security Act of 1980 to provide financial incentives for the merging synthetic fuels industry.

The Occidental Petroleum Company and Geokinetics Oil Shale Project in Colorado and Utah, respectively, have developed in-place (*in-situ*) technologies for recovering shale oil. These techniques minimize the problems and cost of mining, handling, and disposing of large quantities of materials inherent in surface methods. Occidental's process is "modified *in situ*" which uses a combination of underground recovery together with a limited amount of mining. About 20 to 25 percent of the total shale is removed to create a series of individual rooms underground. The rock formation adjacent to a room is explosively expanded into the room to form an underground retort. This technique has been demonstrated on a commercial scale with recoveries in the retort of nearly 70 percent. The removed shale is brought to the surface where the oil could be extracted using an "aboveground" process. The Geokinetics' process is "true *in situ*" where a section of shale is rubblized and heated in place, and the released oil is collected and pumped to the surface. This technology has been demonstrated on a small commercial scale. These two processes are being supported by the United States Synthetic Fuels Corporation with loan and price guarantees.

A complete description of these recovery technologies and others can be found in the literature and will not be discussed here.

Shale Oil Jet Fuel. Crude shale oil from the Western United States offers a significant potential source of middle distillate fuels. Table 3 compares the characteristics of crude shale oil produced by the various recovery technologies.

In order to produce jet fuel, particularly a wide-cut product such as JP-4, at least two things must be accomplished; namely, lower boiling fractions must be increased. The refiner is concerned about the high gravity, high pour point, and the nitrogen, sulfur, and trace metal contents. Shale oil has a narrower boiling range than most petroleum crudes. Fewer than 10 percent of the shale oil crudes boil above 1000°F. Shale oil contains arsenic which is not normally found in petroleum. Before the crude shale oil can be sent to conventional downstream processes, it must be upgraded by removing unstable compounds and catalyst poisons, such as nitrogen and arsenic.

Figure 3 is a schematic diagram of the process studied to maximize production of JP-4 fuel for the United States Air Force. Dewatered and desalted shale oil is hydrotreated to a level of 100 parts per million (ppm) nitrogen in the effluent which is fed to an atmospheric distillation unit where a JP-4 fraction and fractions boiling above 490°F were produced. The JP-4 fraction (150°F to 490°F) from the fractionator is cleaned up in a naphtha hydrotreater while the 490°F+ fractions are charged to a hydrocracker. The 150°F to 490°F products from the naphtha hydrotreater and the hydrocracker are combined for the final jet fuel blend.

Paraho shale oil was processed according to the schematic flow diagram in Fig. 3. An initial hydrotreating step is commonly used to upgrade the raw shale oil and its severity will depend on the amount and types of products the refiner wishes to produce [7]. The nitrogen content was reduced to the 100 ppm target. The hydrogen content of the shale oil was increased to 13.65 weight percent and the sulfur level is reduced to only 14 ppm. The arsenic level, which is detrimental to the hydrotreating, was reduced by a "guard" reaction section at the entrance to the reactor where an alumina catalyst was incorporated for this purpose.

Next the hydrotreated or ungraded shale oil was fractionated and yielded 22.2 volume percent of JP-4 boiling range material. This fraction was further hydrotreated to clean up some of the characteristics. The resulting material will be used in the final JP-4 blend.

Table 4 Specification analyses on Paraho shale JP-4

	Paraho shale JP-4	MIL-T-5624L specification limit
Gravity, °API @ 60°F	56.7	45-57
Distillation, °F (ASTM D-86)		
IBP	153	report
20 vol. percent	214	293 (max)
50 vol. percent	279	374 (max)
End point	498	518 (max)
Net heat of combustion, Btu/lb	18,794	18,400 (max)
Freezing point, °F	−80	−72 (max)
Aromatics, vol. percent	5.2	25.0 (max)
Olefins, vol. percent	1.4	5.0 (max)
Sulfur, wt. percent	0.0003	0.4 (max)
Nitrogen, ppm	0.1	NA
Vapor pressure, Reid (100°F)	2.7	2.0-3.0
Copper strip corrosion	1B	1B (max)
Thermal stability		
Pressure drop, mm Hg	0	25 (max)
Heater deposit	0	3 (max)
Hydrogen, wt. percent	14.4	13.6 (max)
Carbon, wt. percent	85.4	NA
Oxygen, wt. percent	0.1	NA

Table 5 Estimated world oil in place

Total hydrocarbons:	
5000×10^9 bbl conventional	
6000×10^9 bbl heavy oil and bitumen	
Heavy oil and bitumen in place:	
Venezuela	38 percent
Canada	22 percent
USSR	22 percent
Nigeria and Mexico	8 percent
USA	3 percent
All others	7 percent

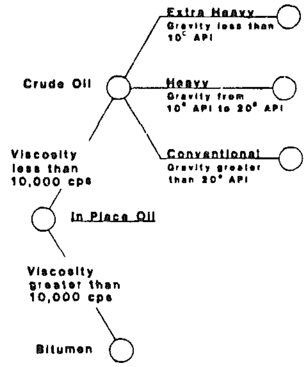

Fig. 4 Oil nomenclature criteria

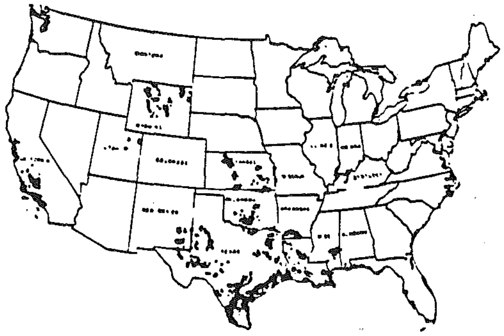

Fig. 5 Heavy oil deposits in the U.S.

The gas oil (490°F+) fractions produced from the hydrotreated shale oil were further hydrotreated and hydrocracked to produce additional stable lower boiling fractions. The overall yield of liquid products from this process was 110 volume percent of the total gas oil feed. The hydrocracking step essentially changed the molecular structure of the 675°F+ fraction to heavy naphtha and middle distillate materials suitable for use in transportation fuels. Economic evaluations of the costs of producing complete slates of transportation fuels from shale oil indicated that the cost of the shale fuels would not be competitive with petroleum-derived products at this time. Recent reduction in the price of world petroleum crude have reduced JP-4 prices by 40 percent over the last four years.

A sample of JP-4 jet fuel was produced from a blend containing 27 volume percent hydrotreated naphtha and 73 volume percent hydrocracked gas oil. The analyses on this fuel are given in Table 4. A very high-quality fuel was produced which exceeded all the requirements of the MIL-T-5624L specification and would be considered above average compared to the fuels produced today from conventional petroleum. The aromatic content was low and the energy and hydrogen values were high. Thermal stability was excellent and the nonspecification nitrogen level was in the parts per billion area. Because of the hydrorefining required to produce this fuel, there is a strong possibility of some lubricity problems associated with fuel-wetted close-tolerance components, i.e., fuel pumps, controls, etc. The USAF routinely uses surface-active corrosion inhibiting materials to reduce this problem and a ball-on-cylinder lubricity test is being standardized to test for the property.

In the early 1980s, the USAF sponsored a number of bench-scale and pilot plant studies to ascertain the suitability of western shale oil to produce acceptable JP-4, meeting the current specifications. These efforts were with Sun Marketing and Refining Company, Ashland Petroleum, UOP Process Division, and Amoco Oil Company. Using different refining approaches, it was concluded that western shale oil derived from a number of different recovery techniques was an excellent source of heavy naphtha and middle distillate materials. The cost of producing fuels at that time was competitive with those from conventional petroleum.

Tar Sands and Heavy Oils. Tar sands and heavy crude oil are a major potential source of transportation fuels. These materials are widespread around the world. There is no common definition of these materials; however, there is an excellent set of criteria presented by Meyer [8]:

1 Low API gravity (<20°API)
2 Poor reservoir mobility
3 Viscosities greater than 60 centipoise
4 Dark color
5 Metal content as high as 500 ppm
6 Sulfur content 3 weight percent or higher
7 Asphaltene content up to 50 weight percent
8 High thermal sensitivity
9 Frequent occurrence of water-wettable particulates

Another attempt at defining and differentiating between bitumen and heavy oil was presented by Byramjee [10] and is reproduced in Fig. 4.

Heavy crudes are found throughout the world with the largest deposits being in Canada and Venezuela. Current production from these sources is estimated to be at 5 percent of the total annual world crude production [9]. This production is normally from crudes nearer the 20° API definition and is quite often diluted with lighter crude. Direct use of truly heavier crudes (10° API or less) and bitumen is very small at present. The incentive for developing these resources is obvious: Meyer [10], et al. estimated that the world has nearly 6×10^9 barrels of heavy oil in place while conventional oil was estimated at 5×10^9 barrels. This information is depicted in Table 5.

Of particular interest are the reserves of these materials in the United States. Major known tar sand resources are located in the states of Utah, California, Kentucky, and Texas. In-

Table 6 Typical properties of heavy oils and bitumens

	California heavy oil	Utah resin bitumen	South Texas bitumen
Gravity, °API @ 60°F (specific gravity)	13° (098)	9.3 (1.005)	– 1.0 (1.08)
Distillation, vol. percent @			
600°F	18	5	4
1000°F	60	36	35
Pour point, °F	45	140 (est)	175
Elemental analysis, wt. percent			
Carbon	87.2	86.3	80.4
Hydrogen	10.6	11.1	8.98
Nitrogen	0.7	0.94	0.36
Sulfur	1.2	0.45	10.25
Oxygen	0.3	1.20	1.40
Compound types, wt. percent			
Asphaltenes	6	20	37.4
Saturates	–	40	–
Aromatics	–	15	–
Polars	18	25	–
Metals, parts per million			
Iron	25	200	–
Nickel	70	85	24
Vanadium	32	20	85
Characterization factor, *K*	11.6	11.3	10.6

place resources of heavy oil could be as much as 200 billion barrels (primarily in California) and more than 50 billion barrels of bitumen. This estimate is based on a 10 percent conversion of the in-place reserves. Heavy oil deposits in the United States are outlined in Fig. 5.

Currently, Canada has the most advanced oil and tar sands recovery processing program. In Alberta Province, there are two commercial plants producing synthetic crude from tar sands bitumen having gravities in the range of 8-12° API. The first commercial extraction and upgrading plant, Great Canadian Oil Sands (GCOS), Ltd., started operation in 1967. Currently, the production capacity is about 58,000 barrels per day of synthetic crude. The second plant, Syncrude Ltd., started commercial production in 1976 and is designed to recover about 125,000 barrels per day of synthetic crude.

Both tar sands plants use a hot water extraction process developed by Sun Marketing and Refining Company to separate bitumen from the tar sands. The bitumen is upgraded to synthetic crude via coking followed by hydrogenating the distillation fractions. The hydrogenated streams are recombined to produce synthetic crude. These synthetic crudes are not usually used as the exclusive feed to a refinery, but are combined with conventional petroleum crudes before conversion to a full product slate of transportation fuels. Typical properties of heavy oil and bitumen are shown in Table 6. The UOP characterization factor (*K*) is used by the refiner to evaluate crude. One of its primary uses is to determine the principal hydrocarbon type in the crude. For instance, *K* factors between 12.2 and 12.9 indicate paraffin base while factors less than 11.5 signify naphthene-based crude. *K* factors between 11.5 and 12.2 indicate intermediate base. For the syncrude with a 11.70 *K* factor, we have an intermediate base, while the two fractions definitely are naphthenes. Another clue to the cyclic structure of these fractions is the low freeze/pour points for the high boiling fraction. Therefore, the cyclic structures must be cracked to produce specification fuels or specifications might have to be modified to accommodate a denser hydrocarbon structure.

The many heavy crudes that are produced in California and other states, in general, have gravities in the 14-20° API range. These crudes are currently being processed into transportation fuels by domestic refineries designed to handle them. Refined products consist of motor gasoline as the major product and generally minor volumes of turbine fuels. In most cases, the initial upgrading step is coking to remove carbon from the hydrogen-deficient crude. The coker distillate fractions are then hydrogenated to remove sulfur and nitrogen compounds and to saturate olefins before being charged to downstream processing units for conversion into finished products via catalytic reforming, catalytic hydrocracking, and fluid catalytic cracking. Average production of heavy crude from the three major California deposits totaled about 350,000 barrels per day in 1982.

Table 6 outlines the characteristics of representative heavy oils and bitumens. There are several problems that must be considered in processing these oils. They have a large residual fraction as shown by the percentage of oil boiling above 1000°F. In addition, the asphaltene content is high and the hydrogen contents are low. Again, the characterization factor *K* indicates that the primary constituents of these materials are naphthenic in nature.

Between the tar sands and heavy crude resources, there would appear to be ample potential domestic production to meet future transportation fuel requirements. Current refinery processing routes employed are not yet geared to produce these fuels, which are heavily concentrated on products in the naphtha/middle distillate boiling range. Most often, these feedstocks are combined with more conventional petroleum crudes, so the finished products might include only a small proportion of these materials. With the disappearance of paraffin-based light crudes, though, these heavier, more difficult crudes will play ever-increasing roles in the production of transportation fuels. The USAF is currently evaluating the potential of producing jet fuels from these sources.

Future Jet Fuels. The ability of the refining industry to produce a variety of high-quality products from the heaviest sour crudes, bitumens, and tar sands has been demonstrated. Many domestic refiners are upgrading their facilities, anticipating ever-increasing amounts of heavy feedstocks.

In general, JP-4 jet fuel is a blend of naphtha and kerosene distillation fractions. Producing JP-4 from heavier feed components by hydrocracking or catalytic cracking followed by hydrogenation could increase the potential volume of components for blending into JP-4. The anticipated closing of additional antiquated refineries would not be expected to have any significant impact on the availability of JP-4 since most domestic refineries are operating well below their capacities.

Western oil shale is an excellent source of conventional jet fuel. Studies indicated that with sufficient hydrorefinement, raw shale oil can be converted entirely into high-quality transportation fuels. The commercialization of this industry could have a positive impact on the future availability of paraffin-based jet fuels. At the moment, with the worldwide availability of crude oil, the domestic synthetic fuel production will not proceed at a rate commensurate with impacting fuel requirements before the year 2000.

It has already been discussed that tar sand bitumen and heavy oil are potential large sources of the cyclic paraffins needed to increase the range potential of jet fuels; however, these materials are not being produced in large quantities today and would not have a serious impact on the jet fuel market. Certainly in the future they could provide the feedstock for naphthenic-based fuel, but this impact is several decades away depending on the availability of lighter crudes.

Worldwide there is a variety of crudes that might be characterized by the dominant hydrocarbon types present in the mixtures. All crudes contain mixtures of paraffins, naphthenes, and aromatics in varying concentrations, but one hydrocarbon type may be dominant. Crudes also contain varying amounts of heteroatoms (sulfur, nitrogen, and metals) which are partially removed or concentrated in the refining and conversion processes. For example, paraffinic crudes are generally waxy, hence, they are selected for the manufacture of paraffinic lubricants. Naphthenic-type crudes are relatively low in paraffin content. They are selected for special applications or for the manufacture of aromatics and gasoline. Aromatic rich crudes may be high in asphaltene content. They are used for manufacturing gasoline and asphalt. In the United States, the production of low-sulfur naphthenic crude is declining rapidly and it will soon become a scarce commodity. Hence, this raw material cannot be considered to be a major supply source for manufacturing higher density jet fuels.

However, most refineries have at least one conversion process to produce gasoline from heavier distillate feedstock and a catalytic dehydrogenation process for octane improvement in addition to the crude distillation facilities. Petroleum refiners utilize thermal, catalytic, and physical separation processes to manufacture high-quality fuels from crude oils. In the refinery conversion processes where large molecules are cracked either thermally or catalytically, fractions rich in aromatic rings are produced. These fractions can be converted to naphthenes by various additional hydrogenation processes. Potential streams for use in manufacturing naphthenic fuels could be obtained from crude distillation, coking, catalytic cracking and/or catalytic hydrocracking. The yields of internal refinery streams were estimated based on normal process yields. The total potential volumes of candidate streams were determined and, using a 78 percent utilization factor and 90 percent operating factor, the total amount of heavy naphtha available was 0.82 million bpd and that of hydrotreated gas oils was 0.87 million bpd. In most cases, these streams would require additional hydrogen processing to make them suitable for use as a turbine fuel component, for example, desulfurization, denitrogenation, olefin saturation, and some conversion of aromatic rings to naphthene rings. The potential demand of 200,000 to 250,000 bpd of these streams for use in preparing a naphthenic turbine fuel would only represent a small fraction of the total volumes available.

The published hydrorefining and hydrotreating facilities in domestic refineries as of January 1984 were reviewed [11]. Only hydrorefining units for upgrading catalytic light cycle oils and light gas oils and hydrotreating units for desulfurizing and stabilizing heavy naphthas and kerosenes were considered. The total hydrorefining and hydrotreating plant capacities identified are 1.06 and 1.11 million bpd, respectively. From these specific refineries and their hydroprocessing capacities, the potential volume of naphthenic fuel that could be blended from these plants was estimated to be 1,771,700 bpd. This potential volume is far in excess of any demand. The resulting quality and characteristics of these fuel components would have to be determined. This effort should be completed in early 1986.

In 1980, a naphthenic fuel was produced from an aromatic stream under a research contract with Stone and Webster Engineering Corporation [12]. A light pyrolysis fuel oil produced from the steam cracking of a petroleum gas oil fraction was converted into jet fuel. The raw aromatic fuel oil was converted into naphthenic products by hydrogenation in a pilot plant operation carried out at the Institut Français de Pétrole at Rueil-Malmaison, France. Table 7 presents the critical fuel properties and compares them with the starting feedstock. The naphthenic fuel produced (JP-8X) has the same volatility as JP-8 or Jet A-1, essentially a kerosene. The high density JP-8 fuel is 93.6 percent naphthenic (cycloparaffins) with the remainder of the fuel being aromatic. The hydrocarbon composition of a typical JP-8 from Table 3 is about 36.2 weight percent naphthene and 19.3 weight percent aromatics. The JP-8X has a density which is higher than now permitted for JP-8. This increased density, however, results in approximately an 8 percent increase in volumetric heating value. When comparing the volumetric heating value of JP-8X to conventional JP-4, the energy increase is nearly 12.5 percent. The JP-8X has excellent low-temperature properties, with a freeze point of less than −100°F and a viscosity of 21 centistokes at −40°F. Other characteristics such as hydrogen content and gravimetric heat of combustion are slightly below the values now permitted in JP-8. The thermal stability of the fuel was excellent, exceeding the specification limits, and the storage stability was good after five years. JP-8X is a prototype fuel which offers promise as a range extender for aircraft. Future efforts by the USAF will ascertain the extent to which the JP-8 specification (MIL-T-83133A) can be modified. Such properties as viscosity might be too high for conventional aircraft. However, such future engine and aircraft designs will incorporate the ability to fly on a denser fuel, like JP-8X.

Table 7 High-density jet fuel production

	Feedstock pyrolysis fuel oil	High-density JP-8 (JP-8X)
Specific gravity, 60°F	0.978	0.872
Net heat of combustion		
Btu/lb	16,881	18,271
Btu/gal	138,060	135,425
Hydrogen, wt. percent	8.33	13.25
Flash point, °F	175	134
Boiling range, °F	392-562	369-500
Freezing point, °F	–	−100
Thermal stability	–	Excellent
Viscosity, cs @ −40°F	74	21

Table 8 Projected properties of broadened specification and high-density fuels

	JP-4	Broad spec	High density
Specific gravity, 60°F	0.764	0.826	0.888
Boiling range, °F	150-480	150-650	360-650
Heat of combustion			
Btu/lb (percent of decrease)	18,700	18,400 (−0.8 percent)	18,300 (−1.3 percent)
Btu/lb (percent of increase)	118,000	127,000 (8 percent)	136,000 (15 percent)
Viscosity cs @ −40°F	2.6	8.5	40
Freezing point, °F	−75	−80	−80
Flash point, °F	−22	0	140

Recalling that JP-4 has approximately 40 percent kerosene, it is conceivable that a high-density, higher-boiling kerosene fraction could replace the present fraction, thus extending the range for JP-4 powered aircraft. Possible properties of both a broadened specification JP-4 and a maximized high-density fuel for future systems are depicted in Table 8. The broad specification fuel incorporates maximum potential availability and substantial increases in range while the high-density fuel would maximize density increase while maintaining low costs and availability. These fuels would be derived from many of the refinery feedstocks of the future, such as heavy oils, tars, bitumens, and eventually such sources as coal liquids. The cyclic natures of these materials make them ideal for a higher-density product if the hydrocarbon ring is preserved in the processing. In addition, these fuels can be produced from various by-product streams such as light cycle oils, pyrolysis oils, and others. Processes and catalysts for producing these fuels are currently available to the refining industry.

Conclusions

Alternative hydrocarbon sources, such as shale oil, heavy oils, and tar sand bitumen, will begin to play ever-increasing roles in the world's energy picture. Refining technology is in hand to upgrade and process shale oil into high-quality conventional fuels. Recovery technology is now being developed on a commercial scale, with the cost of the raw shale oil being slightly higher than crude prices. The United States Air Force will become the first customer in the United States to use shale jet fuel on a continuing basis. Shale oil, through hydrotreating and hydrocracking processes, can be entirely converted into a high-quality syncrude for fractionation into a broad range of transportation fuels.

Heavy oils and bitumens are difficult to refine, but eventually will play bigger roles in the refining industry. Their basic structure, cyclic hydrocarbons, could result in jet fuels of higher density and volumetric heating values which could increase the range of certain aircraft. These cyclic structures could be cracked and processed into conventional paraffinic-based fuels. Current research efforts are evaluating these concepts with regard to fuel quality and economics.

Currently, the United States refining industry has the capacity to produce a wide cut jet fuel, JP-4, and a kerosene fuel, such as JP-8 from straight distilled petroleum or by the blending of special refinery streams. The changing crude quality projected for the future could require some major processing steps to meet current specifications. Research efforts are currently evaluating the possible use of broadened specification fuels with relaxation, if possible, of certain characteristics.

Higher density fuels for current aircraft will have characterization similar to current fuels, except for higher densities and volumetric heating values. These fuels, which have been designated as JP-8X, are currently being evaluated by the United States Air Force. Future fuels will also make maximum benefit of the general characteristics of naphthenic hydrocarbons to increase density and lower freeze point. A broadened specification wide boiling range jet fuel would maximize availability and provide for some range increase. Maximum density-energy fuels will also be evaluated so that future aircraft can take maximum advantage of increased density.

In summary, the aviation industry must recognize the overall refinery situation both with regard to aircraft fuels and fuel candidates of the future. The refiner can and will continue to produce conventional fuels from a variety of sources. The near-term use of higher density fuels is a distinct possibility. The desirability of increasing range and availability of future fuels must be addressed now in order to design aircraft systems capable of using these fuels in the future.

References

1 Coordinating Research Council (CRC), Inc., *Handbook of Aviation Fuel Properties*, CRC Report No. 530, 1983.

2 Duncan, D. C., and Swanson, V. E., U.S. Geological Survey Circ. 523, 1965.

3 Petzrick, P. A., "Historical Utilization of Oil Shale," 188th National American Chemical Society Meeting, 1984.

4 Baughman, G. L., *Synthetic Fuels Data Handbook*, Cameron Engineers, Inc.

5 Yen, T. F., ed., "Science and Technology of Oil Shale," Ann Arbor Science, 1976.

6 Occidental Petroleum Corporation Brochure, Shale Oil.

7 Schwedock, J. P., Reif, H. E., and Macris, A., "Manufacture of Aviation and Distillate Fricle From Raw Shale Oil," AIChE, 1982 Summer National Meeting.

8 Meyer, R. F., and Dietzman, W. D., "World Geography of Heavy Crude Oils," New York, 1981.

9 Byramjee, R. J., "Heavy Crudes and Bitumen Categorized to Help Assess Resources, Techniques," *Oil to Gas Journal*, Vol. 81, No. 27, pp. 78–82.

10 Meyer, et al., "World Resources of Heavy Oil and Tar Sands," *Synthetic Fuel From Oil Shale and Tar Sands Symposium*, Chicago, IL, July 1983.

11 *Oil and Gas Journal*, Vol. 82, No. 13, pp. 111–112.

12 Korosi, A., and Rubin, J. N., "Hydroprocessing of Light Pyrolysis Fuel for Kerosene Type Jet Fuel," AFWAL-TR-80-2012, Feb. 1980.

Thermal Decomposition of Aircraft Fuel

P. J. Marteney

L. J. Spadaccini

United Technologies Research Center,
East Hartford, CT 06108

A test program has been conducted to determine the thermal stability and heat transfer characteristics of JP-5 and several other kerosene-type fuels which vary in composition and tendency to form deposits. Tests were conducted in small-diameter, resistively heated tubes at typical aircraft engine operating conditions. A detailed mapping of the thermal decomposition characteristics of JP-5 was performed to evaluate the importance of key environmental factors—such as temperature, pressure, flowrate, and test duration—and to establish a data base for estimating the relative performance of new fuels. Tests were conducted over the temperature range 425 to 870 K for durations up to 32 hr. Fuel deposition rates varied among fuels, and the relationship between the "breakpoint temperature" (determined according to ASTM D3241) and the rate of fuel deposition was investigated.

Introduction

Anticipated increases in the thermal loadings applied to the fuel systems of high-performance aircraft and uncertainty regarding the future quality of aircraft fuel have prompted investigation of the stability of gas turbine fuels under thermal stress. At severe heat fluxes, fuel will undergo thermal decomposition, resulting in the formation and accumulation of deposits (coke). This insoluble material can reduce heat exchanger efficiency, obstruct valves and filters, and degrade the atomization and spray characteristics of injection nozzles [1]. Thus, the high-temperature stability of both current and future aviation fuels is of great interest, and additional data are required to determine the maximum thermal loading a fuel can tolerate to support the design of advanced technology engines.

Hydrocarbon fuel thermal stability has been studied for many years by numerous investigators, who have employed a variety of test methods [1]. However, the chemistry of fuel thermal decomposition is very complex, and there is presently only a limited understanding of the mechanisms involved. It is generally believed that deposits are produced by free radical autoxidation of hydrocarbon molecules, involving hydroperoxide formation and decomposition, and are condensed from the fuel in a stepwise manner. The rate of deposit formation on heated surfaces is primarily affected by the local temperature and the fuel composition; however, the flow velocity and the wall material can also play important roles.

The purpose of this study was to investigate the deposit formation characteristics of several fuels thought to have a relatively wide range of thermal stability, to evaluate changes in the heat transfer characteristics due to deposit formation, and to relate these results to the standard fuel-thermal-oxidation stability specification test (ASTM D3241, JFTOT Procedure). The detailed chemistry of the deposit-formation mechanisms was considered beyond the scope of the present effort; therefore, no attempt was made to systematically vary fuel composition.

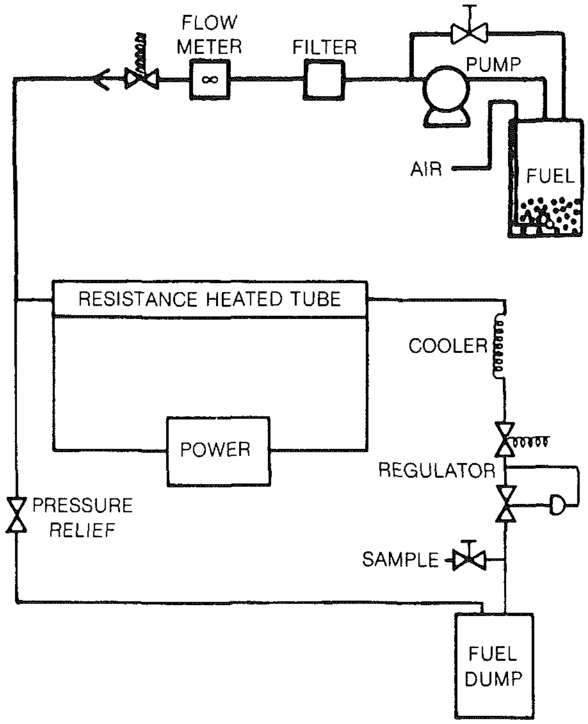

Fig. 1 Aircraft fuel deposit test apparatus

A detailed mapping of the thermal decomposition characteristics of JP-5 was performed to evaluate the importance of key environmental factors, such as temperature, pressure, flowrate (expressed as velocity and Reynolds number), and test duration, and to establish a comprehensive data base for estimating the relative performance of new fuels.

Contributed by the Gas Turbine Division of THE AMERICAN SOCIETY OF MECHANICAL ENGINEERS and presented at the 31st International Gas Turbine Conference and Exhibit, Düsseldorf, Federal Republic of Germany, June 8–12, 1986. Manuscript received at ASME Headquarters January 8, 1986. Paper No. 86-GT-36.

Table 1 Selected Properties of Test Fuels

	JP-5	Sun Tech A	Sun Tech B	NDF
Aromatics (vol. percent)	17	37.1	30.7	23.5
Olefins (vol. percent)	0.8	0.6	0.9	1.0
Sulfur (wt. percent)	0.008	0.21	0.07	0.37
Nitrogen (ppm)	5	178	78	0.67
Hydrogen (wt. percent)	13.7	12.2	12.9	13.3
API gravity (288 K)	40.9	32.5	36.3	35.3
Viscosity (cSt) (273 K)	3.3	4.9	4.5	7.2
Distillation (K)				
IBP	457	448	445	459
10 percent	472	469	476	497
20 percent	476	479	486	513
50 percent	489	514	513	549
90 percent	515	581	556	606
EP	534	600	593	625
Breakpoint (K), ASTM D3241	531	538*	536	517

*Varied during storage

Time-dependent wall temperatures, which can be used in conjunction with measured deposit thickness to estimate heat-transfer parameters, were also obtained. Additional tests were conducted to study deposit formation in three other fuels which varied significantly in composition and properties, and were expected to differ greatly in thermal stability. These fuels were: Sun Tech A, Sun Tech B, and Naval Distillate Fuel (NDF). The Sun Tech A and Sun Tech B fuels are petroleum distillates that were mixed with high-aromatic blending stock to increase the aromatic concentration without significantly increasing the heavier components. Chemical and physical properties of the test fuels (all determined by standard ASTM methods) are listed in Table 1.

Test Apparatus and Experimental Procedure

The method utilized for determining fuel thermal stability and heat transfer characteristics was described in an earlier paper [2], and consists of exposing air-saturated fuel to a thermal environment which closely simulates engine operating conditions. The test apparatus, shown schematically in Fig. 1, is used to conduct continuous, steady-flow experiments over a wide range of temperatures, flow rates, and durations. In this method, fuel flows through a 2.4-m length of thin-walled metal tubing (0.317-cm o.d. × 0.040-cm wall) that is heated by an electric current passing through it. Because the tube is an electrically resistive material (316 stainless steel), it acts as a resistance heater, converting the electrical energy to heat. Since the electrical resistance of the tube material does not vary significantly with temperature, the local heat flux is approximately constant along the tube. Insulating the outside of the tube minimizes external heat loss and results in essentially all of the heat being absorbed by the fuel. Thermocouples attached to the tube permit determination of the temperature at the fuel-surface interface. From the measurement of the inlet and outlet fuel temperatures, the electric power dissipated in the tube (the heat generation) and the fuel flow rate and pressure, sufficient information is available to compute the heat transfer characteristics at any environmental condition being simulated. In a single test, generic data are obtained over a wide range of temperatures. If the simulated conditions are severe enough to cause thermal decomposition of the fuel by any mechanism (viz., thermal reaction, oxidation, or pyrolysis) and are maintained for a sufficient period of time, deposits accumulate on the tube surface. Since the deposit presents a finite thermal resistance, the outer wall temperature will increase locally if the electrical power being dissipated is held constant (i.e., if the fuel outlet temperature is held constant). After completion of the test, the tube is cut into short sections and the deposits are subjected to quantitative and qualitative analyses.

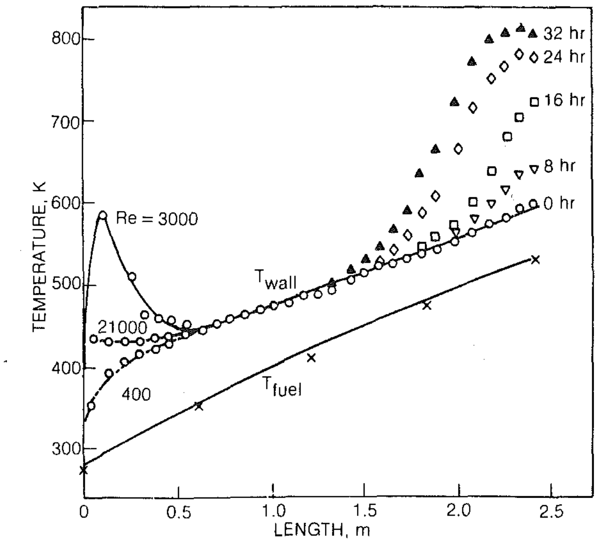

Fig. 2 Effect of test duration on tube temperature for JP-5

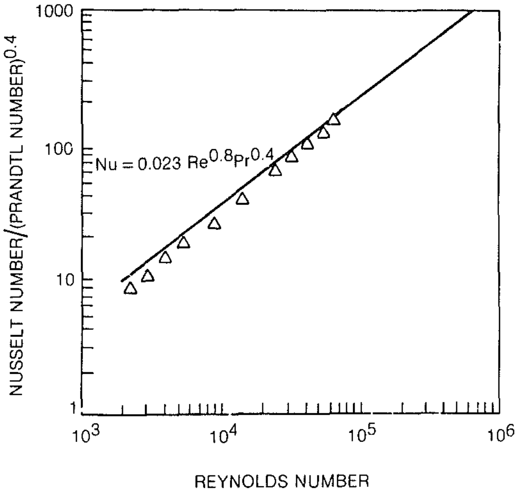

Fig. 3 Heat transfer characteristics of JP-5

The quantity of carbon deposited in each tube specimen is measured by oxidizing the deposit and analyzing the product gases using nondispersive infrared analyzers. Prior to analysis, specimens are vacuum dried at 400 K for a minimum of 16 hr to remove any residual liquid fuel. The tube sections are then installed in a high-temperature (approximately 850 K) laboratory furnace and each deposit is reacted with a separately metered flow of oxygen directed through the inside of the tube. At the conclusion of the burnoff, the total mass and average composition of the product gases collected from individual tube specimens are determined, and the mass of carbon in each deposit specimen is calculated from a mass balance. The deposition data are normalized with respect to the inside lateral surface area of the tube specimens, and reported as average rates of carbon formation over the total test time, i.e., as $\mu g/cm^2 \cdot hr$. The minimum carbon deposition rate that could be accurately measured from a standard 5-cm-long tube specimen was 26 $\mu g/cm^2$ (or approximately 3 $\mu g/cm^2 \cdot hr$ for a typical 8-hr test).

Results and Discussion

The test matrix for JP-5 fuel comprised flow velocities of

0.3, 2.1, and 15 m/s (tube entrance Reynolds numbers of 400, 3000, and 21,000), fuel exit temperatures of 475, 535, and 615 K, wall temperatures of 420 to 675 K, and test times of 8, 16, and 32 hr. Overlap of test conditions was provided within the matrix to permit an assessment of the accuracy and repeatability of the deposition and heat transfer data acquired.

Heat Transfer. Since tests were conducted over a range of inlet Reynolds numbers, laminar, transitional and fully developed turbulent flows were established within the tubes. In all cases, the initial (i.e., 0 hr) wall and fuel temperature distributions downstream of the entrance region were identical for laminar or turbulent flow and nearly linear, increasing from inlet to outlet (see Fig. 2). At the transitional flow condition (Re = 3000), a tube length of approximately 30 cm was required for the establishment of fully developed turbulent flow. With increasing run time, there is a continuous increase in outer wall temperature of the tube, due to deposit formation, which is first evident at high temperatures near the outlet, and later can be detected at progressively lower initial temperatures located farther upstream.

Constant input heat fluxes ranging from 34 to 1420 kW/m^2 were required to achieve the desired temperatures. Voltage drops measured across 60-cm sections of the tube remained uniform and approximately constant throughout the tests, thereby verifying that the local heat flux was constant. Because the fuel axial temperature profiles also remained constant throughout the tests, the temperature at the interface between the fuel and the deposit layer which forms inside the tube was always considered to be approximately equal to the initial inner-wall temperature of a clean tube, provided the local convective heat transfer coefficients also remained constant (a reasonable assumption in view of the near-linear rise in wall temperature with increasing time). Consequently, the initial wall temperature was selected as the correlating parameter for the deposit formation rates.

The turbulent flow heat transfer characteristics of JP-5 are presented in Fig. 3. The experimentally determined forced convection heat transfer coefficients are nondimensionalized to form the Nusselt number, and correlated with the Prandtl and Reynolds numbers. As shown in the figure, the data are very consistent, and can be satisfactorily correlated by a simple Dittus-Boelter equation (i.e., $\mathrm{Nu} = 0.023\ \mathrm{Re}^{0.8}\mathrm{Pr}^{0.4}$).

Deposit Formation in JP-5. The average rates of carbon deposition (determined from the burnoff analysis of selected 5-cm-long tube sections) are correlated with the average local, initial wall temperature (i.e., the interface temperature) in Fig. 4. As shown in the figure, the overlapping data merge and form a characteristic profile that is strongly dependent on the initial wall temperature and not affected by pressure variations above the critical point. The deposition rate varies from a measurement threshold value of approximately 3 μg/cm^2•hr at an initial wall temperature of 420 K, to a maximum value of approximately 1000 μg/cm^2•hr at an initial wall temperature of 645 K. Furthermore, the rate of deposit formation accelerates rapidly as wall temperature is increased above 533 K, the ASTM thermal stability specification temperature for aviation turbine fuels. The apparent decrease in deposit formation at initial wall temperatures above 645 K is consistent with the results obtained in [2], wherein tests were conducted at much higher tube wall temperatures (typically 810 K at the outlet). Although this behavior at elevated temperatures is not presently understood due to the complexity of the chemical mechanisms involved, a similar trend was observed by Taylor [3]. Despite the lack of a complete understanding of this behavior, it is widely agreed that fuel thermal decomposition reactions usually begin with oxidation (promoted by dissolved air) and propagate by the formation of hydroperoxides. Therefore, the sudden decrease in deposit formation at temperatures above 645 K may be indicative of a depletion of oxygen in the fuel, related to the known decomposition of hydroperoxides at elevated temperatures [4], or to competing mechanisms (e.g., liquid-phase pyrolysis) in which specific reactions become the rate-limiting steps.

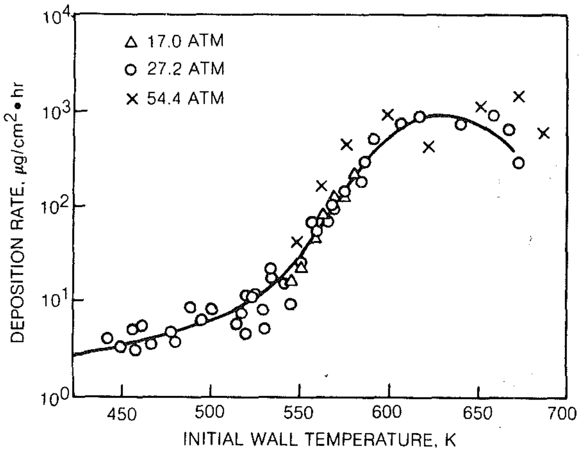

Fig. 4 Effect of wall temperature and pressure on deposition rates in JP-5

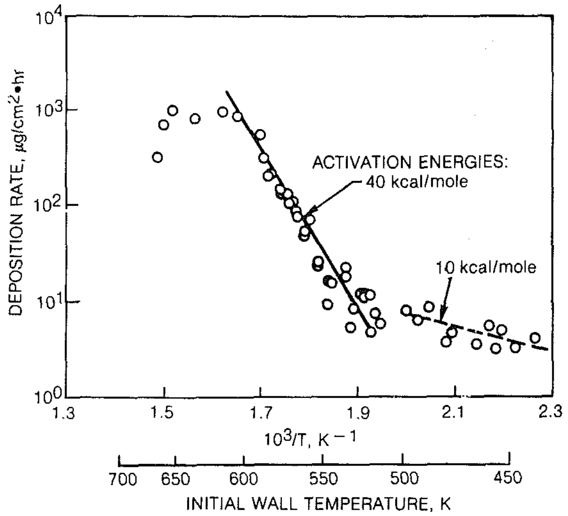

Fig. 5 Arrhenius plot of deposition rates in JP-5

The deposition rate data for JP-5 are replotted versus the reciprocal of the initial wall temperature in Fig. 5 to permit evaluation of a global activation energy for the entire decomposition process. Determination of an activation energy indicates the sensitivity of the reaction rate to changes in temperature, but does not necessarily denote a relative deposition rate or a specific reaction path. In fact, it is likely that an encompassing one-step or "global" scheme comprises a series of parallel reactions which would require very detailed study to decouple or isolate. The activation energy determined according to the Arrhenius approximation is 40 kcal/mole. Activation energies of this magnitude suggest a homogeneous (liquid phase) reaction system, rather than a heterogeneous mechanism such as might occur at a wall. In Fig. 5, the low-temperature data (below 535 K) are fitted by a broken line representing an activation energy of approximately 10 kcal/mole. These data are subject to a greater uncertainty as a consequence of reduced deposition, approaching the measurement threshold of the present work. The assumption may be made that the two reactions (or systems of reactions) indicated in Fig. 5 occur at all times, but there are specific temperature regimes in which each is important. Hazlett [4] has studied free-radical reactions related to fuel thermal decomposition

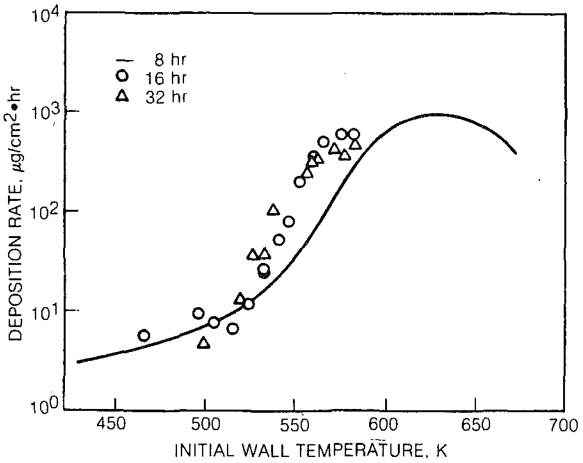

Fig. 6 Effect of test duration on deposition rates in JP-5

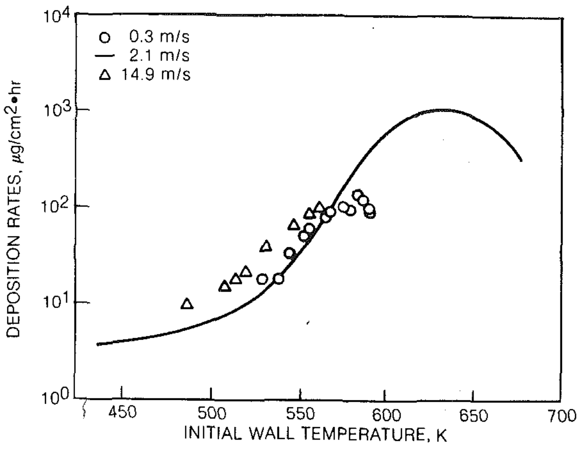

Fig. 7 Effect of flow velocity on deposition rates in JP-5

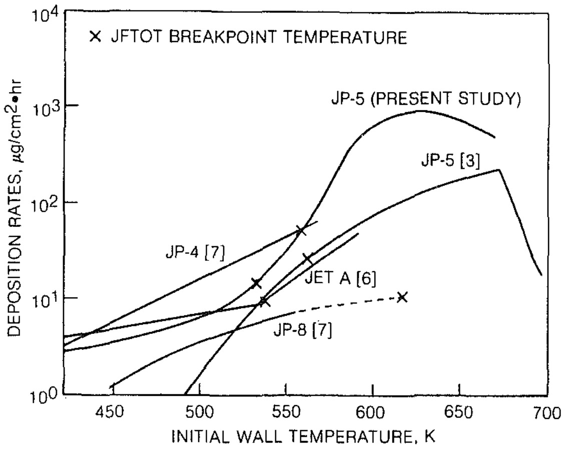

Fig. 8 Comparison of deposition rates in several aviation fuels

and concluded that autoxidation via hydroperoxides is the dominant chemical mechanism for temperatures up to approximately 535 K. At higher temperatures, approaching the region of hydrocarbon pyrolysis, dissociation of oxygenated products (e.g., hydroperoxide decomposition) may play an important role. Therefore, changes in activation energy may be the result of different rate-controlling reactions at low, intermediate, and high temperatures.

Deposit density is difficult to evaluate because of the very thin and sometimes irregular deposit layer produced during an 8-hr test. Therefore, an optical comparator was used to photograph transverse sections of selected tube specimens at 10× magnification. Deposit thicknesses were measured from the photographs and, together with the rate correlations, an average density of 1 g/cm^3 was determined. However, it is generally believed that lower density deposits can be produced, particularly at very low flow velocities [5].

Effect of Test Duration. The effect of test duration on fuel deposit formation was investigated through a series of runs conducted for 8, 16, and 32 hr. Tests of varying duration can provide insight into the type of reaction (i.e., homogeneous versus heterogeneous) and changes in deposit morphology (e.g., density). If the wall significantly influences reactions, long-duration tests should show a decrease in deposition rates as the wall is covered by deposit. If the deposition rate is found to increase with time, an interaction with existing deposit may be suspected. The results, shown in Fig. 6, indicate that the rate of deposition is progressively greater as the run time is increased. In conjunction with an increase in rate, the tube position corresponding to the thickest deposit is located farther upstream, i.e., at a lower initial wall temperature. Since fuel can permeate deposits, decomposition could be accelerated by the increased residence time and higher local temperature and surface area within the deposit matrix. Also prominent in Fig. 6 is the lagging of deposition rates near the end of the tube. Both Taylor [3] and Hazlett [4] have concluded that oxygen-coupled species are principally responsible for fuel decomposition at low and moderate temperatures and that depletion of oxygenated species will lead to a reduction in deposition rates. Therefore, the falloff of deposition rate near the tube exit may reflect a depletion of the available dissolved oxygen or hydroperoxide species. With regard to the effect of run time on the deposit character, no significant changes in morphology were apparent after 32 hr; however, longer test durations (perhaps hundreds of hours) may be required to produce sufficiently thick deposits.

Effect of Velocity and Residence Time. The influence of simultaneous variations in flow velocity, residence time, and quantity of fuel stressed was determined by conducting tests at several different fuel flow rates while maintaining the tube length, run time, and discharge temperature constant. The fuel flow rates selected for these tests engendered laminar, transitional, and fully developed turbulent flows; the velocities and heat fluxes varied in direct proportion to changes in the flow rate, while the residence time varied inversely with the flow rate. Changes in fuel deposition induced by a maximum flow variation of approximately 50 times were evaluated and the results are compared in Fig. 7. As shown in the figure, the deposition rates for laminar and transitional flows were essentially the same at all temperatures up to 560 K. However, the peak deposition rate occurred at a lower temperature in laminar flow, suggesting that the reaction became mixing-limited at elevated temperatures (i.e., governed by the rate of transport of reactants to the wall rather than by chemical kinetics), or that there was a depletion of oxygenated species precipitated by the increased residence time and reduced flow rate. On the other hand, the very-high-velocity, turbulent flow resulted in a greater deposition rate at temperatures below 535 K due to increased mixing and a greater quantity of fuel heated. Although only a few high-velocity data points were obtained above 535 K, the deposition rate profiles for the transitional and turbulent flows appear to converge.

Fuel Bulk Temperature Effects. Insight into the relative importance of wall and bulk-fuel temperatures was obtained from analysis of deposition data obtained from a test in which the wall temperature profile was nearly constant (540 ± 15 K). Although the fuel temperature increased from 390 K to 505 K, the deposition rate did not increase with increasing fuel temperature, but remained approximately constant at 20

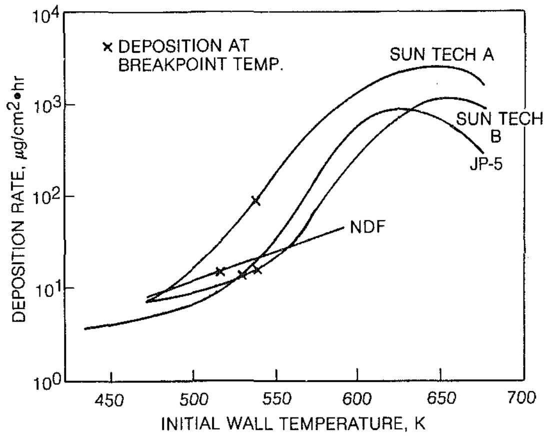

Fig. 9 Comparison of deposition rates in broad-specification fuels

$\mu g/cm^2 \cdot hr$. In addition, the deposition rates in the inlet sections of transitional flow tests rose and fell in correspondence with the wall temperature profile, further demonstrating the greater influence of the wall temperature on deposit formation. Therefore, in the present heated-tube apparatus, the deposition rates are influenced primarily by the higher temperatures near the fuel-wall interface, and secondarily by the lower bulk-fuel temperatures.

Comparison of Results for Aviation Fuels. Comparison of the present deposition rate results for JP-5 with published data is difficult due to the wide variety of fuels, test apparatus, and correlating parameters used by previous investigators. However, in Fig. 8 the results of several aircraft fuel thermal stability studies are compared to demonstrate the general agreement in the magnitude of the deposition rates and the trend with increasing temperature. The prior deposit rate correlations that are shown in the figure were reported by Taylor [3] for JP-5 using a heated-tube apparatus, Vranos and Marteney [6] for Jet A using an isothermal-wall, steady-flow reactor, and Purvis [7] for JP-4 and JP-8 using a vapor-phase static reactor. The breakpoint temperatures for these fuels differ significantly, ranging from 530 to 613 K, and are indicated in Fig. 8.

Deposition in Broad-Specification Fuels. A goal of this study was to establish the degree of correspondence between the JFTOT breakpoint temperature (thermal stability rating) and observed deposition in the heated-tube tests. Therefore, the deposition characteristics of all of the fuels tested are compared in Fig. 9. As shown in the figure, the relative deposition rates among fuels are strongly dependent on the local wall temperature. Furthermore, several of the fuels have similar deposition rates close to the JFTOT breakpoint temperatures (516 to 538 K). However, at wall temperatures slightly above or below the respective breakpoint temperatures of these fuels the deposition rates diverge, indicating that the JFTOT ranking may be valid only over a relatively narrow span of temperatures. Thus, the fuel with the greatest tendency to form deposits (i.e., the lowest thermal stability) is not necessarily the fuel that produces the largest amount of deposit.

Application of Results

In order to demonstrate a methodology for assessing fuel and engine compatibility and for identifying the components of an aircraft fuel system that are most likely to incur significant deposit accumulation, the fuel deposition data acquired can be utilized to predict the deposit buildup. Estimates of the deposit thickness can be made by determining the fuel passage wall temperatures, applying the deposition rate correlations developed, and integrating over the time spent at each flight condition, i.e.,

$$\text{Deposit thickness} = \frac{\text{Formation rate} \times \text{Time}}{\text{Deposit density}}$$

The local wall temperatures in the fuel system may be measured, or calculated using appropriate thermal models. Assumptions which are implicit in the analysis are that any time dependence of deposit formation rate or deposit density is known, and that one temperature (e.g., the wall temperature) is sufficient to define the rate. Also, the possible effects on deposit buildup of fuel system transient operation (i.e., shear and thermal stress) and wall material or geometry (e.g., composition, roughness, shape) are neglected.

For the simplest case, where the deposition rate remains constant, the deposition characteristics of JP-5 (Fig. 4) were used to calculate a map of the growth of deposit thickness as a function of wall temperature and test duration. The results, shown in Fig. 10, are presented in two ways: (*a*) the deposit thickness versus wall temperature for specific times of 10, 100, and 1000 hr, and (*b*) the time versus wall temperature for accumulating deposit thicknesses of 2.5, 25, and 250 μm. The strong dependence of deposit buildup on wall temperature is clearly illustrated in the figure. For example, roughly the same thickness of deposit would be produced by heating JP-5 for 10 hr at 575 K as by heating it for 100 hr at 525 K. Furthermore, if a 25-μm-thick deposit is the maximum allowable after 500 hr, a wall temperature below 485 K would have to be assured.

The above results assume a constant heat flux. For a component subjected to a constant external temperature condition, the heat flux would reduce as a deposit layer builds on the internal surface due to its insulating properties. In this case, the temperatures at the deposit/fuel interface would

(a) EFFECT OF TIME ON THICKNESS

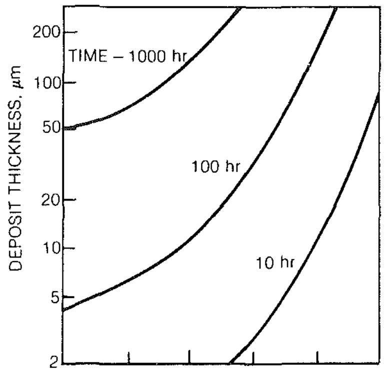

(b) ALLOWABLE TIME FOR SPECIFIED THICKNESS

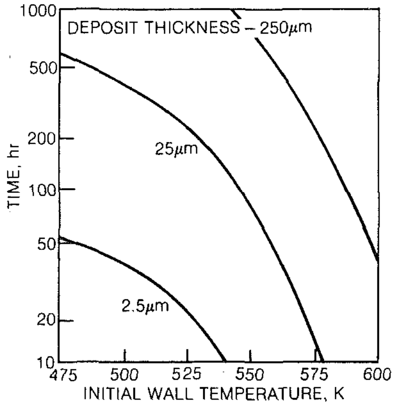

Fig. 10 Growth of deposit thickness in JP-5

decrease as deposit accumulates, tending to slow the rate of deposit buildup with time.

Concluding Remark

The major conclusions that can be drawn from this study are:

- The heated-tube methodology provides very good resolution of the fuel deposition rates over a wide range of aircraft operating conditions and results in a high degree of repeatability.
- Local surface temperature is the key variable affecting the deposit formation. Velocity and test duration are also important physical factors, while fuel bulk temperature and pressure (above the critical point) have a secondary influence on deposition rates.
- Fuel deposition rates increase with increasing test time, presumably as a result of fuel being retained and reacted in the deposit matrix, but long-duration tests are required to define the specific temperature-time dependence.
- The fuel thermal degradation process appears to occur in two stages that are characterized by unique activation energies. The first-stage reactions occur at temperatures below 535 K, and are probably limited to autoxidation, while the second-stage reactions occur in the temperature range 535 to 615 K, between autoxidation and hydrocarbon pyrolysis.

The key benefit derived is the quantitative assessment of the carbon deposition rates and the associated heat transfer characteristics of several aircraft fuels as functions of parameters that are typically specified in engine design. Through careful analysis of engine operating conditions in conjunction with the observed deposition rates, realistic estimates of deposit buildup are possible. These estimates, coupled with the observed heat transfer characteristics of the fuel and the deposit, permit evaluation of the effects of deposit formation throughout an aircraft engine fuel system.

Acknowledgments

This study was performed with the support of the Naval Air Propulsion Center, under Contract N00140-83-C-9119, C. J. Nowack and R. A. Kamin, Project Managers.

References

1 Coordinating Research Council, Inc., "Thermal Oxidation Stability of Jet Fuels – A Literature Survey," CRC Report No. 509, Apr. 1979.

2 TeVelde, J., et al., "Thermal Stability of Alternative Aircraft Fuels," AIAA Paper No. 83-143, June 1983.

3 Taylor, W. F., "Deposit Formation From Deoxygenated Hydrocarbons, Part I – General Features," *Ind. & Eng. Chem., Prod. Res. & Devel.*, Vol. 13, No. 2, 1974, pp. 133–138.

4 Hazlett, R. N., et al., "Reactions of Aerated n-Dodecane Liquid Flowing Over Heated Metal Tubes," *Ind. & Eng. Chem., Prod. Res. & Devel.*, Vol. 16, No. 2, 1977.

5 Szetela, E. J., and Giovanetti, A. J., "Fuel Deposit Characteristics at Low Velocity," ASME Paper No. 85-IGT-130, Sept. 1985.

6 Vranos, A., and Marteney, P. J., "Experimental Study of the Stability of Aircraft Fuels at Elevated Temperatures," NASA CR165165, Dec. 1980.

7 Purvis, W. J., "Investigation of Thermal Coking Rates of Air Force Jet Fuels," Air Force Aeropropulsion Laboratory Report AFWAL-TR-84-2004, Mar. 1984.

The Autoignition and Combustion of Coal-Water Slurry Under Simulated Diesel Engine Conditions

D. L. Siebers

T. M. Dyer

Combustion Applications Division,
Sandia National Laboratories,
Livermore, CA 94550

The combustion characteristics of a coal-water slurry spray were examined under diesel engine conditions. A two-stage combustion process was used to simulate the diesel engine conditions in a constant-volume combustion bomb. The combustion characteristics investigated were ignition delay, ignition site, combustion development, combustion duration, and combustion completeness. The results show that the ignition delay of the coal-water slurry fuel is temperature and pressure dependent. Also, the coal slurry ignition delay is approximately a factor of five longer and the energy release rate is significantly slower in comparison to the ignition delay and energy release rate for conventional No. 2 diesel fuel. The combustion of the slurry spray was incomplete for all test conditions due to the impingement and the adherence of the coal slurry on the wall. This fundamental testing provides insight into engine design parameters which must be considered if coal-water slurry is to be used in practice.

Introduction

Coal-derived fuels are being considered as alternative fuels for diesel engine applications. Their use would result in less dependence on imported oil and greater reliance on abundant domestic coal supplies. Coal-derived fuels include synthetic liquid fuels, dry powdered coal, and coal slurries. For slow- to medium-speed and medium- to large-scale diesel engine applications, such as locomotives, ships, and stationary industrial power plants, the most energy efficient means of using coal appears to be as a coal slurry, if total energy usage from production to combustion in a diesel engine is considered [1]. Furthermore, coal-water slurry appears to be the most economical of the possible coal slurry fuels. However, the use of a fuel containing pulverized coal in a diesel engine will not be an easy task. There are many problems to be solved with the production and the transportation of coal slurry fuels and with their combustion and emissions.

The purpose of this study was to examine experimentally the combustion characteristics of coal-water slurry fuel under simulated diesel engine conditions in a combustion bomb. This study will help develop the base of combustion-related information needed to design diesel engines which will accept these alternative fuels. The characteristics which were examined were ignition delay, ignition site, combustion development, combustion duration, and combustion completeness.

The use of coal in diesel engines is not a new idea. Research on the subject began with Rudolf Diesel, the inventor of the diesel engine, in the late 1800s and proceeded at various levels of effort to the present, with much of the research being carried out in Germany just prior to World War II. Thorough reviews of much of the previous research have been conducted by Caton and Rosegay [1], Soehngen [2], and Robben [3]. These reviews identified three major problem areas associated with the use of coal slurry fuels in diesel engines: wear of engine components, injection of the coal into the engine, and complete combustion of the coal in the residence time available in a given diesel engine. A fourth problem should be added to this list as a result of present emission regulations, namely, minimization of pollutant emissions.

In addition to the works covered in the three previous reviews a few very recent articles have appeared in the literature which should be noted. Gurney et al. [4], and Clingenpeel et al. [5], describe a program at the National Institute for Petroleum and Energy Research (NIPER) to examine the use of coal slurries in diesel engines. These works examine diesel engine performance, emissions, and wear resulting from various coal slurries: coal-DF-2 (No. 2 diesel fuel), coal-methanol, coal-methanol-water, and coal-water. Some of the important combustion-related conclusions from these works were that (*a*) the engine speed is limited by the need to completely burn the coal and control particulate emissions, (*b*) the engine performed better when hot, (*c*) ignition assists consisting of a glowplug and pilot injection of DF-2 were needed to burn the methanol and water slurries, and (*d*) there was greater energy consumption for all slurry fuels in comparison to DF-2.

Robben et al. [6], using an approach similar to ours, present some preliminary results on the combustion of a

---

Contributed by the Diesel and Gas Engine Power Division and presented at the Energy-Sources and Technology Conference and Exhibition, Dallas, Texas, February 17–21, 1985. Manuscript received at ASME Headquarters November 19, 1984. Paper No. 85-DGP-15.

Table 1 The predicted equilibrium combustion products for three mixtures of $H_2/O_2/N_2$ initially at 10 atm and 420 K (species with mole fractions less than 0.001 are not listed)

Reactants (mole fractions)			
Equivalence ratio	0.230	0.260	0.290
N_2	0.627	0.600	0.570
O_2	0.255	0.263	0.272
H_2	0.118	0.137	0.158
Products			
Pressure, atm	35.59	38.92	42.30
Equil. temp., K	1588	1755	1932
MW, gm/gmole	27.60	27.38	27.13
N_2	0.665	0.642	0.615
O_2	0.208	0.207	0.207
H_2O	0.125	0.147	0.171
NO	0.002	0.003	0.006

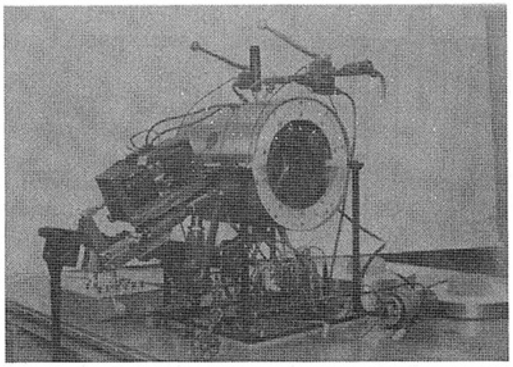

Fig. 1 Photograph of the combustion bomb

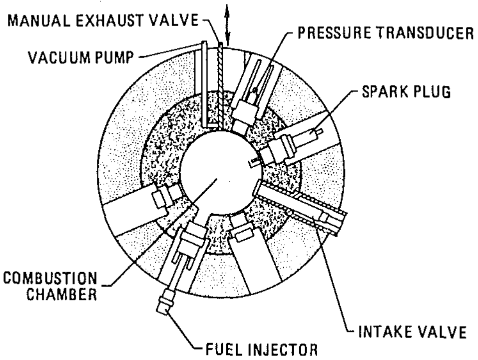

Fig. 2 Cross section of the combustion bomb

coal–water slurry obtained in a rapid compression machine. Their main conclusion is that high compression temperatures are necessary to achieve reasonably satisfactory combustion of the slurry. They used the same low-ash coal–water slurry we used in our work.

Ryan and Dodge [7] conducted tests with various slurries of coal, charcoal, and coke in DF-2. Their work consisted of spray studies in an inert nitrogen atmosphere and engine tests with a single cylinder CLR research engine. The work indicated that the combustion performance of properly formulated slurry fuels should be very similar to DF-2.

Diesel Simulation

The diesel simulation consisted of two main steps. First, pressures and temperatures that occur near top dead center (TDC) in a cylinder of a diesel engine were generated in a constant-volume combustion bomb. Second, the coal–water slurry was injected with a conventional liquid fuel injector into the simulated engine environment. The fuel spray then autoignited and burned as if it were a single isolated plume from a spray in an open-chamber diesel engine.

The pressures and temperatures necessary to simulate diesel engine conditions were achieved with the procedure proposed by Oren et al. [8]. A premixed charge of a very lean gaseous fuel/oxidizer/diluent mixture was ignited and burned in the combustion bomb. The combustion products of this burn formed a high-pressure, high-temperature environment. Since the premixed charge was lean, there was excess oxygen remaining in its combustion products. A liquid fuel spray injected into these hot, high-pressure combustion products autoignited and burned.

The premixed charge used in these experiments was a lean mixture of $H_2/O_2/N_2$. Depending upon the temperature and pressure desired for the simulation, one of three equivalence ratios was used for the premixed charge, 0.23, 0.26, or 0.29. Table 1 gives the predicted equilibrium temperatures, pressures, molecular weights, and compositions of the combustion products for the three equivalence ratios. These equilibrium computations are based on the assumption of constant internal energy and constant volume.

Table 1 shows that the products of combustion have about 21 percent O_2, like air, but that they have more water vapor and a lower molecular weight than air. We have found that the water acts as a diluent and poses no problem. The lower molecular weight means that the density of a mixture for a given pressure and temperature will be slightly less than for air at the same pressure and temperature.

This procedure resulted in a chamber environment with temperatures and pressures in the 700 K to 1400 K range and the 10 atm to 32 atm range, respectively. This procedure also allowed the combustion bomb walls to be heated to realistic engine wall temperatures, independent of the temperature of the gases in the chamber. In previous combustion bomb studies of diesel combustion processes, the compressed air in the bomb was either electrically heated or the bomb was placed in a furnace to generate the necessary temperatures, both of which result in wall temperatures as high as the compressed air temperature. These high wall temperatures are unrealistic for conventional diesel engines, and the resulting reduced material strengths cause serious engineering design problems for an experiment.

Experimental Apparatus and Instrumentation

Facility. A single-event, constant-volume combustion bomb designed and fabricated by Volkswagen Research in West Germany has been used for this study. The combustion bomb was designed to closely simulate the combustion processes occurring near TDC in various types of piston engines. Detailed discussion of the apparatus regarding simulation of homogeneous-charge combustion in engines is found in an earlier paper by Dyer [9]. Our discussion of the apparatus focuses on the simulation of spray combustion in diesel engines.

Figure 1 is a photograph of the combustion bomb. The combustion chamber is a cylindrical pressure vessel, fitted on each end with glass windows 25 mm thick, permitting a clear optical path through the combustion chamber. The cylindrical chamber is 80 mm in diameter and 29 mm wide between the windows. The windows are pressure and vacuum sealed with ribbed, annealed copper washers wrapped with a single layer of Teflon tape. A high-strength bayonet fitting on each window allows easy removal of the windows for cleaning or replacement. The walls of the combustion bomb are surrounded by a layer of high-temperature insulation and can be electrically heated to approximately 500 K to simulate actual operating wall temperatures in engines. For these tests the walls were heated to 420 K.

A schematic cross section of the combustion chamber is shown in Fig. 2. The figure shows four important features needed to simulate diesel engine operating conditions: (*a*) a fast-response, shrouded poppet intake valve for induction of the premixed charge into the initially evacuated combustion chamber, (*b*) a conventional spark ignition system for igniting

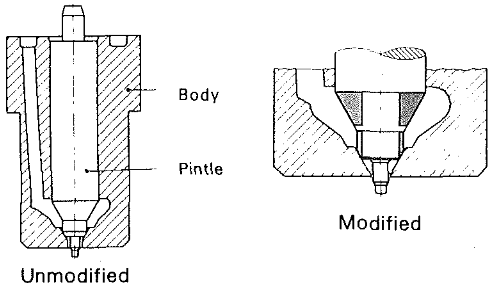

Fig. 3 Cross section of the fuel injector

the premixed charge, (*c*) a single-shot, high-pressure liqiud fuel injector, and (*d*) temperature-regulated walls. Also shown in the figure are a port for evacuating the combustion chamber prior to a test, ports for additional diagnostics, and a pressure transducer for measuring the pressure history of the combustion event.

The intake valve is actuated by two opposing solenoids; one opens the valve and the other ensures fast closing. When the solenoids are not energized, the valve is held shut with a preloaded spring. The intake valve is shrouded to provide a flow directed tangential to the walls producing swirl.

A high-pressure reservoir supplies the desired premixed charge to the intake valve manifold. The charge is synthesized in the reservoir by control of the partial pressure of each component as it is added. An explosion-proof, electrically driven fan stirs the mixture for at least 5 min before intake to insure a homogeneous mixture. Tests of this system showed that equivalence ratios of the premixed charge prepared in this manner were reproducible to better than ± 2 percent.

The liquid fuel injector pump is a jerk-type pump. The driving force for the pump is supplied by a spring that is manually loaded prior to each test. The pump is actuated at the desired time by releasing the spring with a solenoid. The solenoid is set to operate when the pressure and temperature in the combustion bomb drop to preset values after the premixed charge combustion.

The fuel injector used was a modified American Bosch ADN-12SD-12 fuel injector and AKB 35S5790A nozzle holder. The injector was recessed 32 mm into the wall of the combustion bomb in a port with a diameter equal to the outer diameter of the injector tip, 14 mm. The injector tip was water cooled, allowing for control of the injection temperature of the fuel. The modifications to the injector tip consisted of removing the darkened regions shown on the pintle in the schematic in the right of Fig. 3. These modifications resulted in a repeatable, hollow-cone spray pattern. For these tests the injector opening pressure, the quantity of slurry injected, and the injector temperature were 110 atm (approximately the opening pressure used by Gurney et al. [4]), 20 mg, and 38°C, respectively.

Timing for the various events such as intake valve operation for introducing the premixed charge, ignition of that charge, start of the high-speed movie camera, and start of the data acquisition by the minicomputer are programmed in advance on digital counters. Thus, once the experiment is initiated, all events are sequenced automatically.

Test Procedure. The combustion bomb and windows are thoroughly cleaned and washed with methanol. The desired premixed charge of $H_2/O_2/N_2$ is prepared in the reservoir at the desired pressure. The combustion chamber is evacuated by means of the vacuum pump through a manual exhaust valve (see Fig. 2) which provides a vacuum baseline for all of the pressure traces. The exhaust valve is closed, and the test sequence is initiated. The digital counters then control the start of data acquisition, and the induction and ignition of the premixed charge. Once the $H_2/O_2/N_2$ charge burns, the resulting high pressure and temperature begin to decrease due to heat transfer to the walls. When the desired pressure and temperature is achieved in the bomb, a signal is sent to actuate the liquid fuel injector. The liquid fuel injected then autoignites and burns. Immediately after the test, the bomb is evacuated.

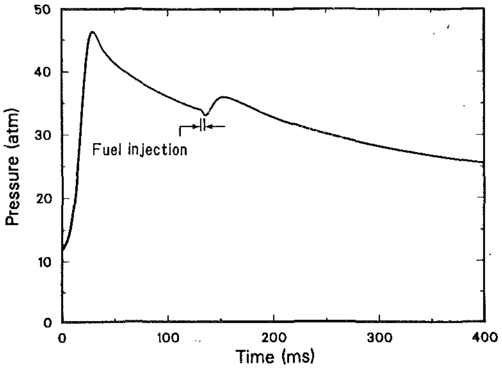

Fig. 4 Pressure history of a diesel combustion simulation

The time of ignition of the $H_2/O_2/N_2$ mixture determines to a large extent the state of fluid motion in the bomb. For these coal-water slurry tests, there was no significant fluid motion at the time of injection. Ignition of the premixed charge was set to occur 3 s after the valve operation sequence, since this has been shown to be an adequate time for mixture motion to decay to negligible values. For injection into a highly swirling turbulent environment, ignition of the premixed charge would have been set to occur shortly after closure of the intake valve.

Figure 4 shows a pressure history in the combustion bomb for a typical diesel combustion simulation. The combustion bomb is initially charged with 12.9 atm of $H_2/O_2/N_2$ with an equivalence ratio of 0.26. The mixture is spark ignited at time zero. The pressure rises as the premixed charge burns, reaching a peak at 26 ms. Some heat transfer occurs from the bomb so the predicted peak equilibrium pressure of 50.2 atm is not achieved. After the premixed charge combustion, the pressure decays due to further heat transfer to the walls. The bulk temperature of the cooling gaseous mixture can be calculated accurately at any instant prior to the slurry injection using perfect gas relations coupled with the measured pressure and the predicted peak temperature and pressure for the particular $H_2/O_2/N_2$ mixture. Once the desired pressure and temperature are achieved, the coal slurry is injected. In Fig. 4 this occurs at a pressure of 34.0 atm and a temperature of 1190 K. The slurry then autoignites and burns as indicated by the second pressure rise in the figure.

Instrumentation. The combustion bomb facility is instrumented so that proper functioning of the apparatus can be monitored as previously discussed by Dyer [9]. Pressure in the mixer reservoir is measured with a calibrated Heise gage in parallel with a diaphragm pressure transducer equipped with a digital readout.

The diagnostics used in these experiments are pressure histories of the combustion event measured with a piezoelectric pressure transducer, combustion luminosity histories measured with a photodiode, high-speed shadowgraph movies, and high-speed movies of the luminosity emitted during combustion, the injection pressure, and the fuel injector pintle movement.

The transducer used for pressure history of the combustion event is a water-cooled Kistler Model 601H. The transducer diaphragm was coated with a high-temperature silicone rubber compound (GE RTV 630) after having been primed and solvent cleaned. This procedure was undertaken to reduce sensitivity drift due to thermal strain during calibration and

Table 2 The composition and particle size distribution of the coal used in the coal-water slurry: The composition is by weight percent and the particle distribution is by weight percent less than a certain size in microns (assuming spherical particles)

Composition

55.9 percent fixed carbon
40.7 percent volatile
12.9 percent N_2/O_2
5.9 percent H_2
2.7 percent H_2O
0.68 percent ash
0.60 percent sulfur

Particle Size Distribution

1 percent $< 1.6\ \mu m$
5 percent < 2.6
10 percent < 2.9
20 percent < 3.5
30 percent < 3.7
40 percent < 4.0
50 percent < 4.1
60 percent < 4.6
70 percent < 5.0
80 percent < 5.9
90 percent < 8.1
95 percent < 11.0
99 percent < 17.8
Largest size $= 21.9$

Table 3 Composition of the coal-water slurry by weight percent

49.0 percent water
45.8 percent coal
2.0 percent Surfynol 485
2.0 percent Ucon 50-HB5100
1.0 percent A-23
0.2 percent CW11

operation in combustion environments. The transducer is coupled to a Kistler charge amplifier Model No. 504E4. The pressure transducer is dynamically calibrated by charging the combustion bomb to various pressures.

The fuel injection pressure was measured with an AVL 8QP500c pressure transducer and Kistler charge amplifier Model No. 504E4. The pressure transducer and charge amplifier were calibrated with a dead weight tester. The pressure measurement was made in the fuel supply line just as it entered the nozzle holder.

The luminosity during the combustion event was measured with a United Detector Technologies photodiode, Model PIN-8LC. The photodiode was placed near one of the combustion bomb windows where it was exposed to the entire combustion chamber. These luminosity measurements are used only in a relative sense to determine the start of combustion and combustion duration.

The time of fuel injector opening is determined from the motion of the fuel injector pintle. When the fuel pressure in the nozzle rises to a preset value, the pintle opens pushing back the spring-loaded spindle in the nozzle holder that is used to set the injector opening pressure. An extra stem connected to the spindle in the nozzle holder moves through the beam of He/Ne laser as the pintle opens, blocking a portion of the beam directed at a photodiode (United Detector Technologies model PIN-8LC). The photodiode signal gives the injector opening time, the length of time open, and the rate at which the fuel injector opens.

The pressure history, the combustion luminosity history, the fuel injector pintle opening, and the fuel injection pressure data are acquired and stored with an LSI 11/23 minicomputer and storage oscilloscope. The minicomputer is equipped with an a/d convertor capable of multiplexing several input channels with a single channel digitization rate of 40 kHz. The transient data are recorded in core memory and then transferred to disc and stored for later detailed analysis.

Fuel. The coal-water slurry used in this experiment was supplied by NIPER. It is the same as the low-ash coal-water slurry that was shown by Gurney et al. [4] to be a promising fuel. The composition of the coal and the particle distribution, as analyzed by NIPER, are given in Table 2. The largest particle was found to be approximately 22 μm. The coal-water slurry composition is given in Table 3. The slurry is nominally a 50/50 mix of coal and water by weight. Small percentages of surfactants, lubricants, and dispersants were found necessary to make the slurry compatible with fuel injection equipment [4]. The gross heating value of the coal, the heating value of the coal-water slurry, and a typical heating value for DF-2 are 32,500 kJ/kg, 14,700 kJ/kg, and 42,500 kJ/kg, respectively.

Results and Discussion

Fuel Injection. Several problems were encountered while developing a repeatable method for injecting the coal-water slurry into the combustion bomb. One of the major problems was that the coal-water slurry tended to dry and harden quickly when exposed to room temperature air. This meant that fuel loading had to be carried out quickly and that the slurry had to be kept in airtight containers. Another problem was that the coal and water in the slurry separated easily. As a result, the slurry in storage had to be continuously stirred with a magnetic mixer and the slurry in the combustion bomb fuel reservoir had to be changed every 1 to 2 h. The slurry was also found to be abrasive and corrosive. Smooth machined surfaces in the fuel injector nozzle were pitted and corroded after completion of these tests.

Fuel injector plugging was also a problem. All outward-opening poppet fuel injectors that we tried were found to plug rapidly. The inward-opening pintle fuel injector we used had to be cleaned with each loading of the fuel reservoir and water-cooled to 38°C to ensure that it did not plug. If the fuel injector was allowed to equilibrate with the combustion bomb wall temperature of 147°C, the slurry in the injector nozzle hardened. The mechanism for hardening of the fuel in the heated injector nozzle is not known. The pressure in the fuel line was maintained at 7 atm which is above saturation pressure of water at 147°C. A final problem that arose was the failure of the intake valve used for injecting the premixed charge. Coal eventually worked its way into the mechanism causing it to seize; this damaged the connecting rod between the valve and the actuating solenoids.

Combustion of the Coal-Water Slurry. The combustion of a coal-water slurry spray is shown in Figs. 5 and 6. Figure 5 shows a sequence of frames from a high-speed movie taken at 4000 frames per second. The movie combines both a shadowgraph image and an image of the luminosity emitted from the burning coal. The lower curve in Fig. 6 shows the corresponding pressure history from the start of injection. The pressure plotted is the pressure rise from the time of injection. Figures 5 and 6 represent a case where the coal-water slurry was injected into a temperature of 1350 K and a pressure of 29 atm. The equivalence ratio 0.26 premixed charge in Table 1 was used to generate these conditions. The wall temperature, quantity of fuel injected, and injector opening pressure were 420 K, 20 mg, and 110 atm, respectively. Also shown in Fig. 6 is the pressure rise caused by 20 mg of DF-2 injected into the same pressure and temperature conditions. (It should be remembered that the DF-2 has a heating value 2.9 times that of the coal-water slurry.)

As seen in the upper left frame in Fig. 5, the spray of coal-water slurry emerges from the injector port at 0.8 ms after the injector opens. At 2.0 ms after the start of injection, the spray has traveled 2/3 of the way across the combustion chamber and ignition has occurred near the base of the spray as indicated by the bright spots in the photo. Figure 6 shows that the pressure is still decreasing due to evaporation of water at this time. At 3.0 ms, the combustion has progressed around the spray toward the tip and the spray has almost reached the opposite wall of the chamber. Figure 6 shows that the pressure is still decreasing due to water evaporation. By 4.0 ms, the spray has hit the wall and combustion nearly engulfs the whole spray. At this point the pressure begins to increase due to significant heat release, and by 8.0 ms, the pressure loss due to water evaporation is recovered. After the spray hits the opposite wall, combustion continues for about another 40 ms

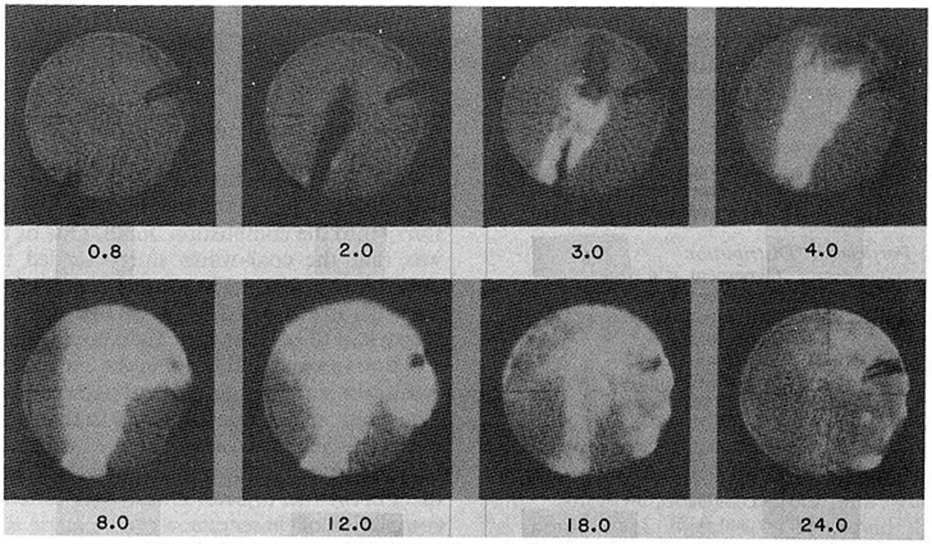

Fig. 5 A sequence of high-speed movie frames of coal-water slurry combustion (time in ms)

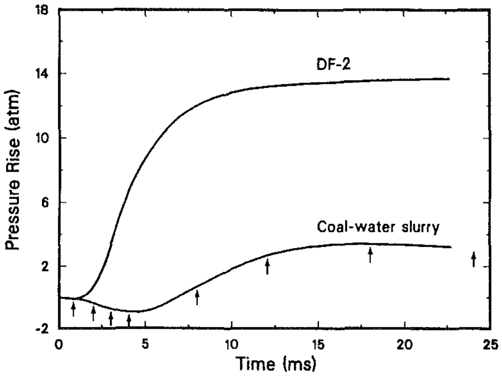

Fig. 6 Pressure rise relative to the start of injection versus the time from injection for the combustion of 20 mg of coal-water slurry and DF-2 under the same conditions (the arrows on the coal slurry curve indicate the frame locations in Fig. 5)

as evidenced by the luminosity, but the major portion of the pressure rise is completed between 15 and 20 ms. Near the end of the combustion event, small luminous spheres are visible floating around the combustion chamber, some of which are seen in the frame corresponding to 24 ms.

For coal-water slurry the ignition site near the injector is similar to that noted for other liquid fuels tested in this apparatus. We hypothesize that it is the location of the first fuel to enter the chamber, mix with the ambient oxygen, and reach the flammability limit and the autoignition temperature.

The individual luminous spheres noted near the end of the combustion event are believed to be particles of burning coal. The spheres have a luminous, semitransparent outer region surrounding a bright yellow core. They resemble burning coal particles observed by others in much lower oxygen concentration environments where the coal particles and the ambient fluid had a relatively large differential velocity [10, 11]. The major difference is that there is no tail protruding from the sphere as noted in previous works. The lack of a tail is most likely due to a higher oxygen concentration in this work and a negligible velocity differential between the coal particles and the gases in the chamber this late in the combustion event. The inability to discern the burning of individual particles early in the combustion event is most likely due to the large number of particles burning.

Comparison of the coal-water slurry and DF-2 pressure histories shown in Fig. 6 points out some important differences in the combustion of the two fuels. It is seen that the combustion of 20 mg of each fuel results in significantly different pressure rises, energy release rates, and ignition delay times. For all conditions studied the slurry burned slower, released less energy, and had a longer ignition delay than DF-2. Furthermore, the magnitude of the evaporative pressure loss from the slurry injection is significantly larger than that for DF-2. The coal-water slurry takes almost 7 ms to recover the evaporative pressure loss, while the DF-2 recovers the pressure loss within about 1 ms.

The difference in the total pressure rise of the fuels shown in Fig. 6 is due primarily to the difference in heating values. The DF-2 has a heating value 2.9 times larger than that of the coal-water slurry. However, incomplete combustion of the coal also contributed to the lower total pressure rise for the slurry. Using the difference in energy contents and the pressure rise for the DF-2, a pressure rise for coal-water slurry can be estimated. This estimate indicates that 5 to 15 percent of the coal did not burn for the case illustrated in Fig. 6. Incomplete combustion of the coal was confirmed by the observation of coal adhering to the chamber wall opposite the injector.

Incomplete combustion of the coal was found for all the test conditions of this experiment, and the lower the chamber temperature, the larger the quantity of unburned coal that appeared on the wall after a test. This observation is consistent with greater portions of the spray hitting the wall before the coal ignites for the lower temperature (i.e., longer ignition delay) cases. DF-2 under the same test conditions also impinged on the wall, but unlike the coal it evaporated and burned.

The difference in ignition delay between the coal-water slurry and the DF-2 noted in Fig. 6 is even more pronounced at lower temperatures which are more representative of current diesel engine designs. Ignition delay based on three definitions was determined from the pressure and luminosity histories for each coal-water slurry test and compared to the ignition delay for DF-2 under the same conditions. Figures 7 and 8 schematically illustrate the three ignition delay definitions used. The luminosity ignition delay, defined in Fig. 7, is the time from injector opening until the first illumination from the coal combustion is measured with a photodiode. (The ignition delay measured in this manner agreed with the luminous ignition delay noted on the high-speed movies.) The pressure-based ignition delay definitions are based on the fact that the pressure in the combustion chamber drops initially after injection as a result of the evaporation of the fuel. The subsequent combustion of the

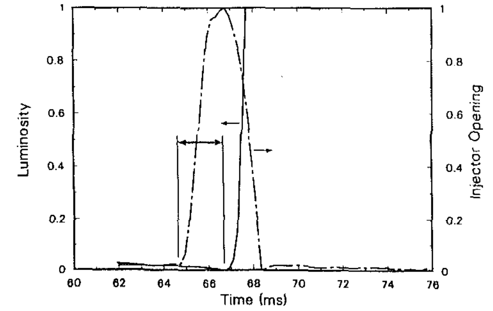

Fig. 7 Definition of luminous ignition delay

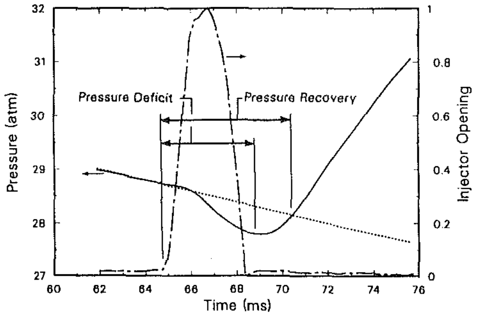

Fig. 8 Definitions of pressure deficit and pressure recovery ignition delays

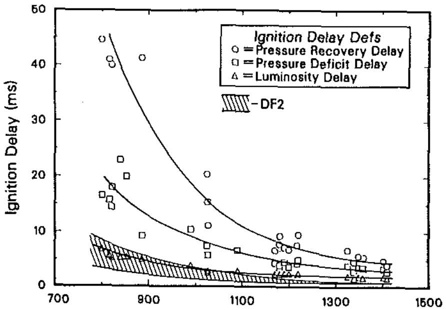

Fig. 9 Ignition delay of the coal-water slurry versus chamber temperature

fuel causes the pressure to increase. The pressure recovery ignition delay, defined in Fig. 8, is the time from injector opening until the pressure regains the value it would have had if no fuel had been injected. The pressure deficit ignition delay, also defined in Fig. 8, is the time from injector opening until the pressure loss from evaporation reaches a maximum.

Figure 9 shows ignition delay versus temperature for the coal-water slurry based on the three definitions. Also shown is the range of the three measures of ignition delay for DF-2 tested under the same conditions as part of this experiment. The figure illustrates several features about the ignition properties of the coal-water slurry. First, the ignition delay is a strong function of the ambient temperature in the combustion bomb, decreasing as the temperature increases. Second, as the temperature increases the three measures of ignition delay converge. Third, the ignition delay based on luminosity is the shortest, followed by the pressure deficit, and pressure recovery ignition delays. Finally, the ignition for the coal slurry is significantly longer than the ignition delay for DF-2 under the same conditions. There is about a factor of five difference between the pressure recovery ignition delays for the two fuels, which is the most important definition for diesel engines. (The pressure recovery ignition delay data for DF-2 are represented by the upper boundary of the cross-hatched region in Fig. 9.)

The ordering from shortest to longest of the ignition delays based on each definition is also different for the two fuels. The pressure deficit ignition delay is the shortest for the DF-2 followed by the luminosity and pressure recovery ignition delays. This is most likely due to the fact that particles which can radiate energy must be formed in the DF-2 combustion process (i.e., soot), whereas such particles already exist in the coal slurry.

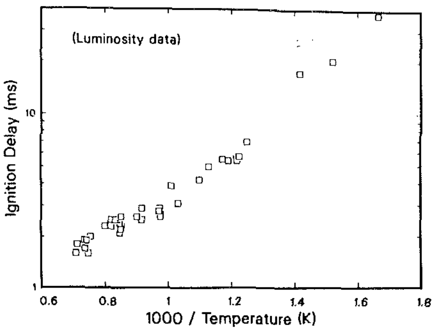

Fig. 10 Luminous ignition delay exhibits an Arrhenius-type temperature dependence

A plot of the log of the luminous ignition delay versus the inverse of the chamber temperature, as shown in Fig. 10, shows that the ignition delay has an Arrhenius-type dependence on the temperature. The effective activation energy is approximately 20 kJ/mole for temperatures greater than about 800 K (or $1000/T \leq 1.25$). This compares with a typical chemical activation for coal of 150 kJ/mole [12]. For temperatures less than 800 K, the data appear to have a higher effective activation energy. For these cases pressure histories and luminosity measurements indicated that there was very insignificant combustion of the coal. One possible explanation for this is that a typical ignition temperature for the coal is around 700 K [12]. If only coal particles near the outer edge of the spray reach this temperature while the spray core remains relatively cool, there may be insufficient energy release to maintain combustion. Another explanation is that a combination of effects is important, namely, the long ignition delay for these low temperatures and spray impingement on the wall. Below 800 K the ignition delay based on luminosity is greater than 7 ms, which is equivalent to the time needed for the entire body of the spray to travel completely across the combustion chamber and impinge on the opposite wall. Since much of the coal adheres to the wall, it probably cools rapidly to the wall temperature of 420 K, and therefore cannot ignite even though the chamber temperature is above the coal ignition temperature.

The scatter in the pressure-based ignition delay data plotted in Fig. 9 can be explained by a dependence of the pressure-based ignition delay definitions on density or pressure. In Fig. 9 the ignition delays for all densities at each temperature were plotted versus temperature. However, in Figs. 11 and 12 the ignition delay data for nominal temperatures of 1025 K and 1200 K, respectively, are plotted versus density in the combustion chamber, which for a given temperature is directly related to pressure. The pressure-based ignition delays are observed to decrease with increasing density or pressure. This dependence is strongest for the pressure recovery ignition delay. A comparison of Figs. 11 and 12 indicates that this density or pressure dependence decreases with increasing temperature. The figures also show that the luminous ignition delay has no such pressure or density dependence.

The slower combustion rate noted earlier for the coal-water slurry relative to DF-2 in Fig. 6 is also evident in Fig. 9. Comparing the spread of the three ignition delays for DF-2 to those for the coal-water slurry indicates that the rate of energy release for the coal-water slurry is significantly slower. For example, the time between the pressure deficit and

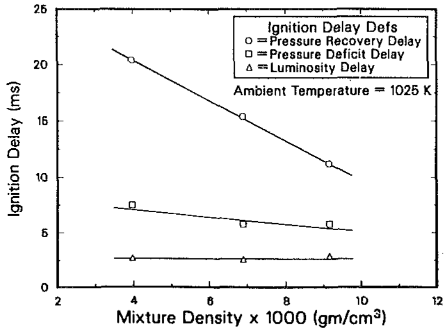

Fig. 11 Ignition delay versus pressure for a chamber temperature of 1025 K

pressure recovery ignition delays for the coal-water slurry is significantly longer than the same time difference for DF-2.

From the movies and pressure histories and from additional tests using these fuels, it was noted that while some of the DF-2 injected would burn very rapidly in a premixed mode for the longer ignition delay cases, none of the coal-water slurry did. The coal appeared to burn in a mixing controlled mode for all conditions. It was also determined that the combustion duration of the fraction of the 20 mg of slurry that burned for each test was similar to the combustion duration of all 20 mg of DF-2 injected into the same conditions.

Implications of These Tests

Although the absolute value of ignition delay measurements acquired in our combustion bomb may vary with mixture turbulence, fuel injection parameters affecting atomization, properties of the raw coal, and composition of the additive package, we feel that our data provide insight into diesel engine design issues related to using coal-water slurry as a fuel. First, the cylinder chamber design should minimize wall impingement, possibly through swirl. Second, the fuel injector should provide a well-atomized, soft spray to minimize wall impingement and maximize the combustion rate and completeness. Atomization of coal slurry fuels similar to those used in our tests has also been shown to be important in steady flow tests by Holve [11]. Third, the combustion chamber temperatures should be higher than in conventional engines through reduced heat losses, preheated air, or higher compression ratios to achieve the maximum combustion rate and combustion completeness combined with the minimum ignition delay. Finally, engine speeds need to be on the low end of conventional diesel engine speeds to allow adequate residence time for complete combustion of the coal.

Summary and Conclusions

The autoignition and combustion characteristics of a coal-water slurry were examined under simulated diesel engine conditions in a constant-volume combustion bomb. A two-stage combustion process was used to generate high-pressure, 10 to 32 atm, and high-temperature, 700 K to 1400 K, quiescent environments into which the coal-water slurry was injected with a conventional liquid-fuel injector. The coal slurry spray under these conditions autoignited and burned as it would in a diesel engine. The combustion characteristics of interest were determined from measured pressure and combustion luminosity histories and from high-speed movies of the combustion event.

The major conclusions about the combustion of coal-water slurry drawn from this work are:

- The pressure recovery ignition delay for the coal-water slurry was approximately a factor of five longer than the pressure recovery ignition delay for No. 2 diesel fuel (DF-2) under the same conditions.

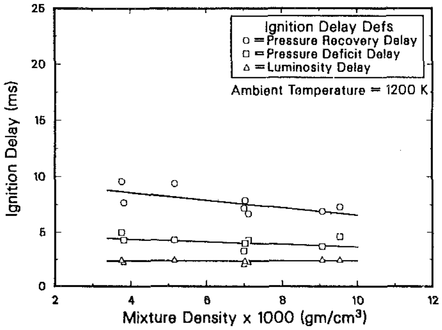

Fig. 12 Ignition delay versus pressure for a chamber temperature of 1200 K

- Luminosity appears before a pressure rise when coal burns, which is opposite to the trend for DF-2.
- The ignition delay has an Arrhenius-type dependence on temperature.
- The rate of energy release during the coal combustion is significantly slower than that for DF-2.
- For the conditions tested the combustion of the coal-water slurry was incomplete due mostly to wall impingement by the spray.
- The pressure-based ignition delays decrease as the ambient density or pressure increases.
- The minimum temperature for which a significant portion of a spray of the coal-water slurry burned was approximately 800 K.

Acknowledgments

The authors would like to acknowledge the continued funding by the Department of Energy: Morgantown Energy Technology Center, Mr. L. K. Carpenter; and the Division of Energy Conversion and Utilization Technologies, Mr. M. E. Gunn, Jr. We greatly appreciate the technical support of our industrial partners as an essential aspect helping to guide this work, especially Volkswagen Research and the Motor Vehicle Manufacturers Association.

References

1 Caton, J. A., and Rosegay, K. H., "A Review and Comparison of Reciprocating Engine Operation Using Solid Fuels," SAE Paper No. 831362, SAE International Off-Highway Meeting, Milwaukee, WI, Sept. 1983.

2 Soehngen, E. E., "Development of Coal-Burning Diesel Engines in Germany," Energy Research and Development Administration Report FE/WAPO/3387-1, Aug. 1976.

3 Robben, F., "Coal-Fueled Diesel Engines," SAE Paper No. 831747, presented at the 1983 SAE Fuels and Lubricants Meeting, San Francisco, CA, Nov. 1983.

4 Gurney, M. D., Clingenpeel, J. M., and Eccleston, D. B., "A Program to Examine the Use of Coal Slurry Fuels in Diesel Engines," ASME Paper No. 84-DGP-9.

5 Clingenpeel, J. M., Gurney, M. D., and Eccleston, D. B., "A Combustion and Wear Analysis of a Compression-Ignition Engine Using Coal Slurry Fuels," ASME Paper No. 84-DGP-8.

6 Robben, F., Brehob, D. D., Namazian, M., Sawyer, R. F., and Sherman, P., "Coal-Fueled Diesel Engines," The 6th Intl. Symp. on Coal Slurry Comb. and Techn., Orlando, FL, 1984.

7 Ryan, T. W., and Dodge, L. G., "Diesel Engine Injection and Combustion of Slurries of Coal, Charcoal, and Coke in Diesel Fuel," Paper No. 840119, SAE International Congress and Exposition, Detroit, MI, Feb. 1984.

8 Oren, D. C., Wahiduzzaman, S., and Ferguson, C. R., "Diesel Combustion Bomb: Proof of Concept," Paper No. 841358, SAE Fuel and Lubricants Meeting, Baltimore, MD, Oct. 1984.

9 Dyer, T. M., "Characterization of One- and Two-Dimensional Homogeneous Combustion Phenomena in a Constant Volume Bomb," *Trans. SAE*, Vol. 88, 1979, pp. 1196-1216.

10 McLean, W. J., Hardesty, D. R., and Pohl, J. H., "Direct Observations of Devolatilizing Pulverized Coal Particles in a Combustion Environment," *18th Symp. (Intl.) on Comb.*, 1980, p. 1239.

11 Holve, D. J., "Combustion Studies of Coal/Water Slurries," presented at the 1984 Spring Meeting of the Combustion Institute, University of Colorado, Boulder, CO, Apr. 2-3, 1984.

12 Field, M. A., Gill, D. W., Morgan, B. B., and Hawksley, P. G. W., *Combustion of Pulverised Coal*, The British Coal Utilization Research Association, Leatherhead, Surrey, England, 1974.

Numerical Simulations of Two-Stroke Cycle Engines Using Coal Fuels

S. Kishan
Engineering and Environmental
Analysis Division,
Radian Corporation,
Austin, TX 78766

S. R. Bell

J. A. Caton

Department of Mechanical Engineering,
Texas A&M University,
College Station, TX 77843

An analytical model of a two-stroke cycle, reciprocating, compression ignition engine was used to investigate the ignition and combustion characteristics of coal/water slurry fuels. The engine cycle simulation was based on a thermodynamic analysis of the cylinder contents and consisted of models for the injection, ignition, combustion, mixing, heat transfer, work, and scavenging processes. The thermodynamic analysis resulted in a set of first-order nonlinear, ordinary differential equations which were numerically integrated to obtain instantaneous cylinder gas, droplet, and particle conditions. The simulation results were first compared to experimental data from a large, slow-speed (120 rpm) engine using a coal/water slurry fuel. Complete validation of the model was not possible due to the lack of detailed experimental data, but comparisons are presented which indicate general agreement between measured and computed values. The model was then used to predict the performance of an engine representative of a locomotive medium-speed engine. Engine and fuel parameters were varied to study their effect on ignition and combustion of the coal/water slurry fuel and on the indicated engine performance. Increases in the inlet air temperature improved the ignition and combustion characteristics. Lower equivalence ratios or smaller particle sizes resulted in higher thermal efficiencies. Also, higher reactive coal led to increased cylinder pressures and higher thermal efficiencies due to faster burning rates.

Introduction

The need for developing alternative fuels for reciprocating, internal-combustion engines has been growing in recent years. This is primarily the result of the depletion of petroleum supplies and has led to the consideration of fueling engines with coal fuels. Interest in coal fuels is motivated by the economic and strategic advantages of coal relative to petroleum fuels [1, 2]. Applications of coal-slurry-fueled engines would be especially suited for low- and medium-speed engines since the difficult problems of fuel handling, wear prevention, and low burning rates are accentuated as engine speed increases. Specific applications which would be especially suitable for solid-fueled engines consist of stationary power plants, marine propulsion systems, and railroad locomotives. Many of these large engines are based on two-stroke cycle designs to provide favorable power-to-weight ratios.

Recent work has shown that reasonable success with coal fuels in reciprocating engines can be achieved. In some cases, performance of coal-fueled engines has been reported to be the same as that of oil-fueled engines [3]. Past work has identified several areas of concern, however, with the combustion of coal fuels in engines. In particular, the ignition of coal fuels in engines has been shown to be sensitive to the cylinder gas conditions [4, 5].

This investigation used a cycle simulation [6, 7] for two-stroke cycle engines which was developed for diesel or coal slurry fuel. The simulation was modified to include a more representative combustion process [8, 9] which will be described in a subsequent section. Two different engines were modeled: a very large, slow-speed (120 rpm) engine and a large, medium-speed (900 rpm) engine. The slow-speed engine was selected primarily because the only published experimental data of successful coal-fueled engine op eration were obtained from a Sulzer Brothers' 1 RSA 76 engine [3]. The medium-speed engine was selected since a major thrust for utilizing coal slurry fuels is for locomotive applications. One such two-stroke cycle, medium-speed engine is the General Motors' EMD 710 engine.

The specific objectives of this investigation were to develop simple models of the dominant processes, to integrate these models into a complete engine cycle simulation, and to use the simulation to explore the combustion and engine performance characteristics of the two engines using coal/water slurry fuel. Due to the lack of some experimental details, definitive validations of the cycle simulation were not possible, but comparisons are presented which indicate general agreement between measurements and computations.

Model Description

An engine cycle simulation has been developed [6, 7] for a conventional open chamber, direct-injected, compression-

---

Contributed by the Internal Combustion Engine Division and presented at the *Energy-Sources and Technology Conference and Exhibition*, New Orleans, Louisiana, February 23-27, 1986. Manuscript received at ASME Headquarters April 30, 1986. Paper No. 86-ICE-13.

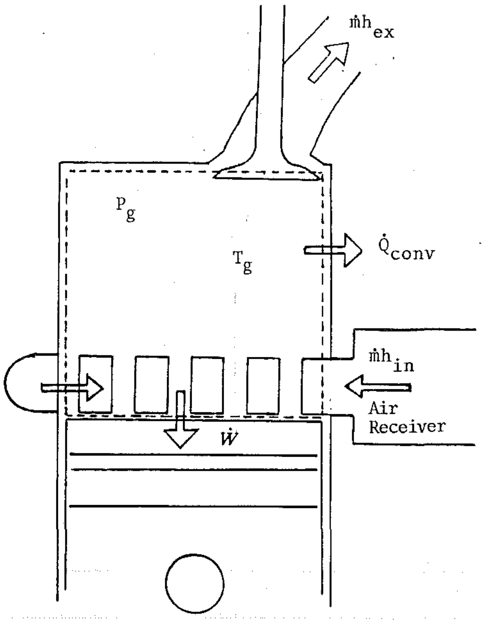

Fig. 1 A schematic diagram of the engine piston and cylinder with the thermodynamic components denoted

ignition, two-stroke cycle engine. The simulation was structured to model both loop- and uniflow-scavenged, two-stroke cycle engines. The simulation models the scavenging, compression, expansion, combustion, and exhaust processes of the two-stroke cycle. The various processes are modeled on the basis of a thermodynamic analysis of the cylinder gas by utilizing submodels for scavenging, wall heat transfer, intake, and exhaust processes and a detailed model for combustion. The original combustion model has been enhanced and now includes cylinder gas mixing as well as solid coal particle combustion, coal devolatilization, and liquid fuel evaporation and combustion.

To obtain the instantaneous cylinder gas thermodynamic state, the first law of thermodynamics was applied to the control volume illustrated in Fig. 1. The energy equation for the cylinder contents is

$$\frac{dE_g}{dt} = -\dot{W} + \sum_i \dot{Q}_i - \sum_j \dot{m}_j h_j \qquad (1)$$

The cylinder contents were divided into individual regions and zones which are described below. Equation (1) is applied to each of the regions during scavenging, to each of the zones during combustion, and to all the cylinder contents during compression and expansion. The change in the gas energy may also be expressed in terms of internal energy as

$$\frac{dE_g}{dt} = m_g C_v \dot{T}_g + \dot{m}_g C_v T_g \qquad (2)$$

From equations (1) and (2) an expression for the change in gas temperature is obtained as

$$\dot{T}_g = \frac{1}{m_g C_v}\left(-\dot{W} + \sum_i \dot{Q}_i - \sum_j \dot{m}_j h_j - \dot{m}_g C_v T_g\right) \qquad (3)$$

This equation is then integrated for each region during scavenging and for each zone during combustion to yield the instantaneous local temperature. The next few paragraphs describe the submodels.

The scavenging model is based on the experimental work of Dedeoglu [10] and the analytical work of Benson [11], but was developed here for both uniflow- and loop-scavenged systems. The details of the overall scavenging model are described elsewhere [6, 7] and are only summarized here. The first part of scavenging was modeled as exhaust blowdown which occurred when the exhaust ports/valves opened and then proceeded in three phases while both the intake ports and exhaust ports/valves were open. The three scavenging phases are: a displacement phase, a mixing phase, and a short circuiting phase. Figure 2 is a schematic illustration of the exhaust blowdown, the three scavenging phases, and the regions used to model the scavenging process for a uniflow-scavenged process. The cylinder was divided into three regions: one for air, one for combusted gas, and one for mixed gas (air and combusted gas). The mixed gas region is determined by using a mixing ratio based on the incoming jet velocity, which specifies the amount of incoming air and combusted gas that form the mixed zone at each crank angle [6].

Nomenclature

aTDC = after top dead center
aBDC = after bottom dead center
bTDC = before top dead center
bBDC = before bottom dead center
CA = crank angle
CIE = coal slurry injection end
CIS = coal slurry injection start
C_v = constant volume specific heat of cylinder gas
D = diameter
DIE = diesel injection end
DIS = diesel injection start
E_g = internal energy of the cylinder gas
E = activation energy
F = pressure correction factor (see [13])
h = enthalpy of cylinder gas
$k_{1,2}$ = reaction rate constant
m = mass
$\dot{m}$ = time derivative of mass; mass flow rate
P_g = cylinder gas pressure
$\dot{Q}_{comb}$ = heat release from combustion
$\dot{Q}_{conv}$ = convective heat transfer rate
$\dot{Q}_i$ = heat transfer or heat release from zone i
$\dot{Q}_{rad}$ = radiation heat transfer rate
$\dot{Q}_{sr}$ = heat release from surface reactions
R = gas constant
t = time
T_g = temperature of cylinder gas
T_{packet} = temperature of packet gas
$\dot{T}_g$ = time derivative of temperature
V = instantaneous evolved volatile mass fraction
V_{max} = maximum volatile yield
$\dot{W}$ = rate of piston work
$\alpha_{1,2}$ = rate constant multiplier
α_g = thermal diffusivity of gas
η = engine thermal efficiency
θ_b = entrainment constant
ρ = density
τ = ignition delay time parameter
ϕ = equivalence ratio

Subscripts

a = air
d = droplet
ea = entrained air
ex = exhaust
g = gas
i = heat transfer zone
j = flow surface
l = liquid
p = particle
s = solid
v = volatiles

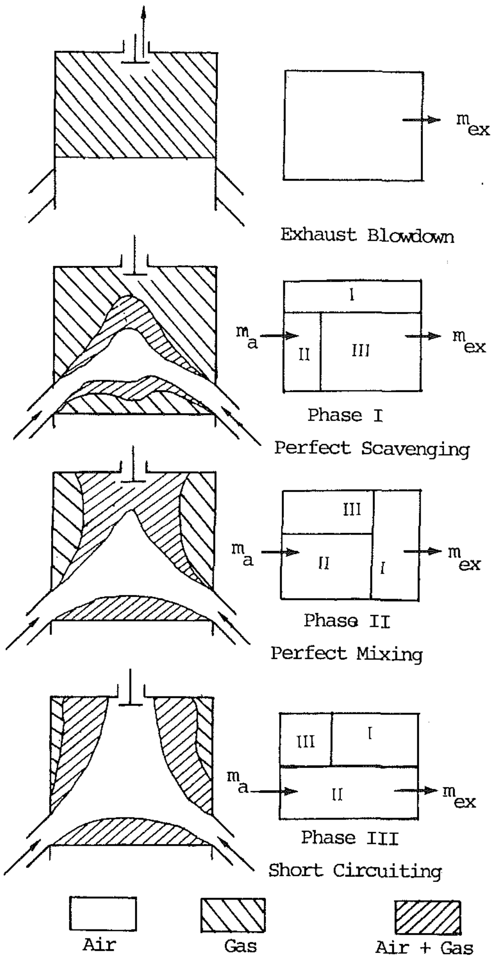

Fig. 2 A schematic of the scavenging model

Scavenging proceeds as the intake ports open and fresh air "jets" into the cylinder and displaces the combusted gas toward the exhaust valves/ports (the displacement phase). During this phase, the exhaust gas does not contain any fresh air and, hence, this phase is also called the perfect scavenging phase. In the second phase, a part of the mixture (fresh air and combusted gas), which formed during the first stage and which continues to form due to the presence of both fresh air and combusted gas in the cylinder, leaves the cylinder as exhaust gas. This is termed the perfect mixing phase. The third phase is the short-circuiting phase, which occurs when some of the incoming fresh air passes straight through to the exhaust ports/valves.

The combustion model was based on nonuniform mixtures within the cylinder due to fuel/air stratification. This was modeled by using multiple zones and the details of this model are given elsewhere [8, 9]. Each zone (not to be confused with the regions of the scavenging model) is formed by dividing the total fuel requirement into a number of packets as the fuel is injected. The mass of fuel in each packet is then divided into a number of fixed diameter droplets and particles. For most of this work, the slurry fuel was assumed to be atomized into droplets and coal particles with 30 and 10-μ diameters, respectively. Each packet is identified by a time of entry into the cylinder and by a classification scheme to permit different characteristics. Once injected, air from the "unburned zone" is entrained into each of the packets based on an entrainment function.

Fuel/air stratification is achieved by using an entrainment function which mixes different amounts of air into each of the packets. The entrainment function was formulated to include the major features of air entrainment while still remaining relatively simple. It was based on the fact that the entrained mass should be related to the mass of the unburned mixture and that during injection the entrained mass should increase as the jet develops. The entrained mass was also assumed to be a function of a packet's time of entry and classification. Such features were included in a simple exponential function [8, 9]. The entrained mass m_{ea} is given by

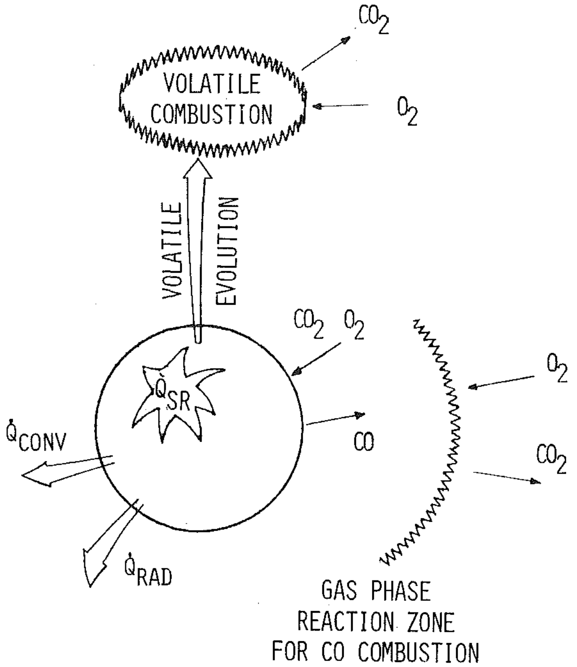

Fig. 3 A schematic of the components and processes for the combustion and devolatilization of a coal particle

$$m_{ea}(I, J)=\frac{m_{ub}}{I_t J_t}\left(\frac{\Delta\theta_{calc}}{\theta_b}\right)\exp\left[-\frac{I}{I_t}\frac{J}{J_t}\right] \qquad (4)$$

where I = index of packet entry into cylinder; J = index of packet classification; θ_b = entrainment constant (°CA); m_{ub} = instantaneous mass of unburned zone; I_t = total number of packet entry times; J_t = total number of packet classifications; $\Delta\theta_{calc}$ = calculation time step (°CA). Each packet is described by an entry index I and a packet classification index J. The first packets injected into the cylinder have an index of 1; the second have an index of 2; and so forth. At each entry time the packets are also identified with a classification index (e.g., 1, 2 . . .).

The thermodynamic state of the gas in each of the zones is given by equation (3), where

$$\sum_i \dot{Q}_i=\dot{Q}_{comb}-\dot{Q}_{conv} \qquad (5)$$

$$\sum_j \dot{m}_j h_j=\dot{m}_{ea}h_{ea}-\dot{m}_p h_p-\dot{m}_v h_v-\dot{m}_l h_l \qquad (6)$$

The combustion term $\dot{Q}_{comb}$ is composed of three constituents which represent the energy release from the coal, volatiles, and liquid fuel vapor combustion. During injection, a charge of fuel mixture which is composed of specified amounts of liquid carrier and coal enters the cylinder. The coal consists of a specified mass fraction of char and volatiles. The particle combustion model is similar to the one developed by Caton and Rosegay [12] and modified to include devolatilization by Bell and Caton [13]. This model assumes spherical particles with uniform but time-varying temperatures. Also, this model includes variable particle heating values and variable particle densities due to devolatilization. Figure 3 shows schematically the coal particle combustion process which includes solid phase reactions, gas phase reactions, and devolatilization. The particles are assumed to burn via two mechanisms yielding carbon monoxide

$$C_{(s)} + \frac{1}{2} O_{2(g)} \rightarrow CO_{(g)} \tag{7}$$

and

$$C_{(s)} + CO_{2(g)} \rightarrow 2CO_{(g)} \tag{8}$$

The carbon monoxide is then assumed to mix immediately with available oxygen in the packet and burn in the gas phase away from the particle. The standard surface kinetics was obtained from the literature as reported in [12, 14]. By simultaneously satisfying the mass conservation equations and surface kinetics of the particle, the reaction rates are calculated [12, 14].

A second constituent to the combustion term in the energy equation is from volatile combustion. A detailed description of the devolatilization model may be found elsewhere [13, 15] and, therefore, is only summarized here. Based on the assumption that the volatiles are locally released and jet away from the particle, a simple model was formulated for the devolatilization process. Once evolved, the volatiles are assumed to react with available oxygen in the packet (after an ignition delay) far from the particle. The assumption that the volatiles are locally released from the particle has been supported by several experimental observations [16–18]. If thermochemical conditions are sufficient, simultaneous solid particle reaction and devolatilization may occur. Since fundamental, mechanistic rate expressions for devolatilization are not available due to the complexities of the process, empirical data were used which have been approximated with first-order reactions such as

$$\frac{dV}{dt} = (\alpha_1 k_1 + \alpha_2 k_2) F (V_{max} - V) \tag{9}$$

where the rate constants k_i are given by Arrhenius expressions. For the current study, the rate constants recommended by Kobayashi et al. [19] were used and 50 percent of the coal mass was assumed to be the maximum volatile yield.

A final constituent of the combustion term is the liquid fuel combustion. For simplicity, the steady-state, isolated, single drop approach of Spalding [20] was used. Vaporized fuel then mixes with available oxygen in the packet and reacts after an ignition delay.

The ignition delay correlation is used to determine the time between when the fuel is injected and the vaporized mixture ignites. (The correlation used here for the fuel vapor and volatiles should not be confused with the overall engine ignition delay times, which are based on the net effect of all the fuel on pressure recovery in the cylinder after injection.) The ignition delay correlation used in this study was that of Spadacinni and TeVelde [21] and is of the form

$$\tau = \frac{A}{P^n} \exp\left(\frac{E}{RT}\right) \tag{10}$$

where $A = 2.43 \times 10^{-9}$, $E = 41.56$ kcal/mole, and $n = 2$. This correlation has been used successfully in other cycle simulations [22].

Table 1 Engine specifications

	Engine A*	Engine B†
Bore (*mm*)	760	230.2
Stroke (*mm*)	1550	279.4
Compression Ratio	10.63	16
Speed (rpm)	120	900
Normal Injection Timing (bTDC)	6°	15°
Inlet Air Temperature (K)	350	310
Air Receiver Pressure (kPa)	240	260
Exhaust Pressure (kPa)	200	220
Scavenging	Loop	Uniflow
Exhaust valve/port	Port	Valve
Number per Cylinder	5	4
Valve/Port open (bBDC)	67°	71°
Valve/Port close (aBDC)	67°	67°
Port Height (*mm*)	217	-
Port Breadth (*mm*)	110	-
Valve Diameter (*mm*)	-	63.5
Valve Max. Lift (*mm*)	-	17.42
Intake Ports		
Number per Cylinder	8 big/4 small	18
Height (*mm*) x Breadth (*mm*)	big : 180 x 55 small: 103 x 93	30 x 22
Ports open (bBDC)	45°	43.5°
Ports close (aBDC)	45°	43.5°

* Similar to the Sulzer Brothers' research engine 1 RSA 76.

† Similar to the General Motors' EMD710 engine.

Table 2 Coal/water slurry fuel specification

% Liquid Carrier (by mass)	50.0
Maximum Volatile Yield (V_{max})	0.50
% Volatile Matter (by mass)	50.0
Coal Heat of Combustion (kJ/kg)	34,337
Volatile Heat of Combustion (kJ/kg)	35,000
Char Heat of Combustion (kJ/kg)	32,790

Other terms in equation (3) such as piston work were calculated with a knowledge of the instantaneous cylinder conditions. The convective heat transfer includes convection from the particle and heat losses to the droplet and cylinder walls. The heat losses to the walls were calculated using an empirical correlation from Woschni [23] based on the average cylinder gas temperature. Heat transfer between the packets and the unburned zone was based on the volume (surface area) and temperature of the specific packet. Depending on the temperature of the packet this heat transfer may be to or from the packet. In addition to heat transfer across packet boundaries, packet work due to expansion or contraction is also transferred between packets. Droplet and particle convection rates were based on coefficients corresponding to droplets and particles in a quiescent atmosphere. Radiation losses from the particle to the cylinder wall were also included in the model.

Results

The purpose of this study was to use a cycle simulation for medium-speed locomotive engines to investigate engine operation using coal fuels. Further, the purpose of this work was also to conduct a sensitivity and parametric analysis of model variables, engine design parameters, and fuel properties. The only available experimental data for coal/water slurry fueled engines are for a slow-speed, large engine [3] (designated as engine A). The cycle simulation results were first compared to these experimental data. The model variables were varied to find the sensitivity of the computed results to their selection. These variables included the amount of pilot fuel, the coal particle size, the diesel droplet size, the surface and volatile reaction rates, the air receiver pressure, the entrainment constant, and the scavenging parameters. A detailed description

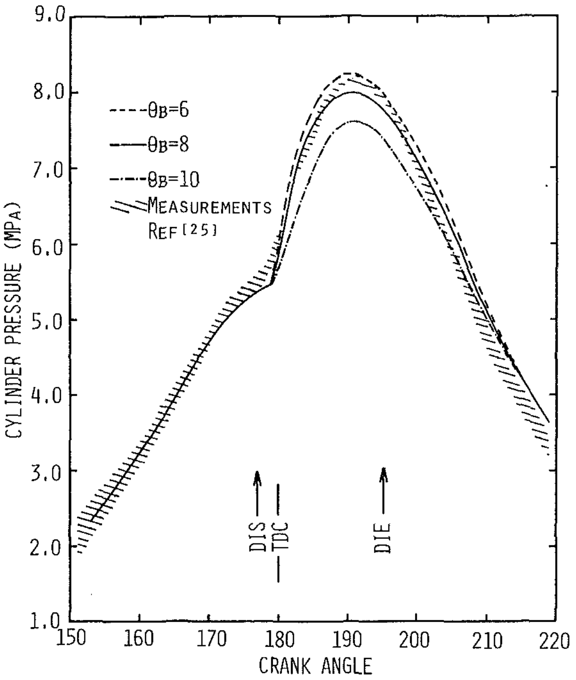

Fig. 4 Cylinder gas pressure as a function of crank-angle for engine A using diesel fuel at 90 percent load for three entrainment constants

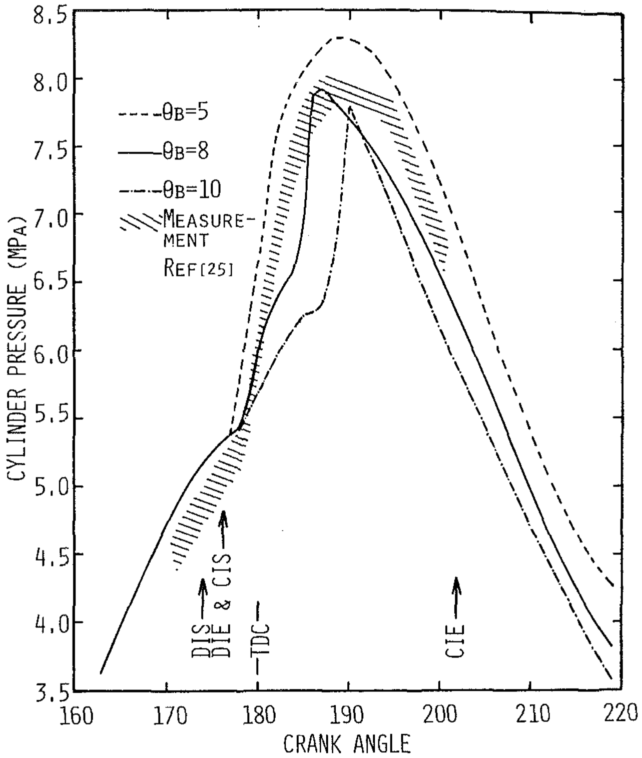

Fig. 5 Cylinder gas pressure as a function of crank angle for engine A using coal/water slurry fuel at 90 percent load for three entrainment constants

Table 3 Engine A performance using diesel fuel (90 percent load)

Parameter	Computed	Measured
Indicated Power (kW/cyl)	1390	1400*
Indicated MEP (kPa)	989	995*
Indicated SFC (g/kW-hr)	195	198*
$\eta_{indicated}$(%)	42.8	43.3*
Air Flow Rate (kg/hr/cyl)	13,172	13,760
Fuel Flow Rate (kg/hr/cyl)	272	272
Maximum Pressure (MPa), at (aTDC)	8.0, 10.1°	8.2, 10°

---

* Based on brake performance and 94.5% mechanical efficiency [3,25,26]

of the effect of all these variables on the results is given elsewhere [24]. In this paper, the effect of only a few of the significant variables on the computed results will be described.

Table 1 lists the specifications for the slow-speed engine, as well as for the medium-speed engine (designated as engine B). Table 2 lists the specifications of the coal slurry fuel. The results are for monosize particles and droplets with 10 and 30-μ diameters, respectively. The particles and droplets were assumed to be independently present in each of the packets and the liquid component was assumed not to cover the particles. Results for other particle/droplet arrangements have been presented by Bell and Caton [9]. For the cases they examined, they concluded that the specific arrangement did not significantly affect the results. The results section of this work is divided into two main sections, one for each engine.

Engine A. As very limited experimental data are available for coal slurry combustion in reciprocating engines, complete validation of coal-fueled engine simulations is not yet possible. The comparisons are limited to cylinder pressure as a function of crank angle. For engine A, the resutls that follow are first for the diesel fuel case and then for coal/water slurry fuel case. These results for engine A are for 90 percent load since the available experimental data [25] were for 90 percent load. Figures 4 and 5 (for diesel and coal/water slurry fuel, respectively) show the comparison of computed and measured cylinder pressures as a function of crank angle for engine A for three entrainment constants. The hatched regions on these figures represent estimates of the measured cylinder pressure from [25]. The cylinder pressure data presented in [25] did not include an absolute pressure scale. The actual cylinder pressures were scaled from the curves presented in [25] by knowing the peak firing pressure and the peak motoring pressure [26]. This procedure resulted in some uncertainties which are reflected by the hatched region.

Table 3 lists the comparison of the indicated performance parameters for engine A using diesel fuel. The indicated perforemance figures were compiled from [3, 25, 26] based on brake performance and an assumed 94.5 percent mechanical efficiency. The results in Fig. 4 and Table 3 indicate that the cycle simulation yields results which are in good agreement with the measurements. The specific set of model parameters selected for these calculations, however, is not unique. The sensitivity of the results to the model parameters was examined [24] and the effects of major model variables on the results are described in the following paragraphs. As illustrated in Fig. 4, the selection of the entrainment constant θ_b affects the computed cylinder pressures in a modest manner. A lower entrainment constant θ_b causes a higher rate of air entrainment resulting in better combustion. As shown, an entrainment constant of 8 (the units of the entrainment constant are °CA, but these units will be omitted in the subsequent discussion for simplicity) resulted in cylinder pressures which agreed the best with the available data.

Figure 5 shows the comparison of computed and measured cylinder pressure for engine A using coal/water slurry fuel with a diesel fuel pilot. The pilot used was 17 percent of the total energy input [3] and was injected for 3°CA before the coal/water slurry was injected. The computed results for the coal slurry fuel case were based on the same power output as for diesel fuel (90 percent load). Data from [3, 25] were then used to compute the fuel input. Table 4 lists the computed performance parameters. The indicated performance figures were

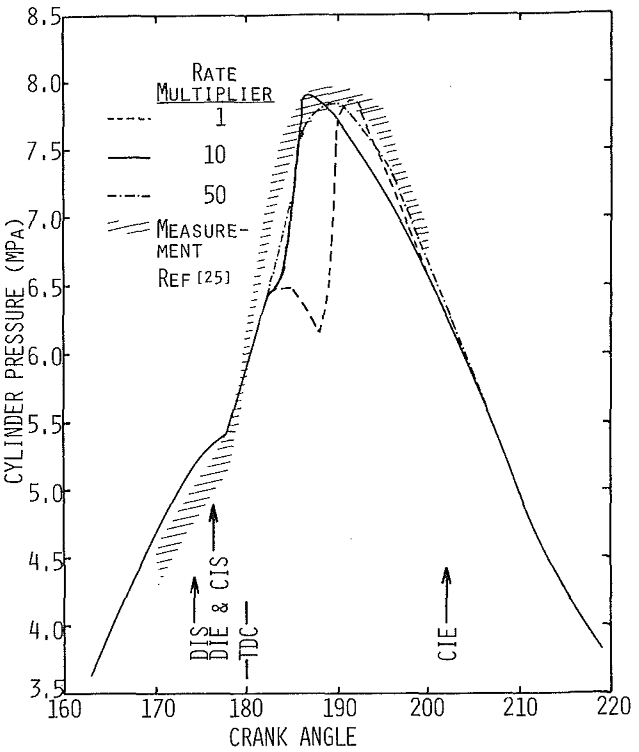

Fig. 6 Cylinder gas pressure as a function of crank angle for engine A using coal/water slurry fuel at 90 percent load for three pre-exponential reaction rate multipliers

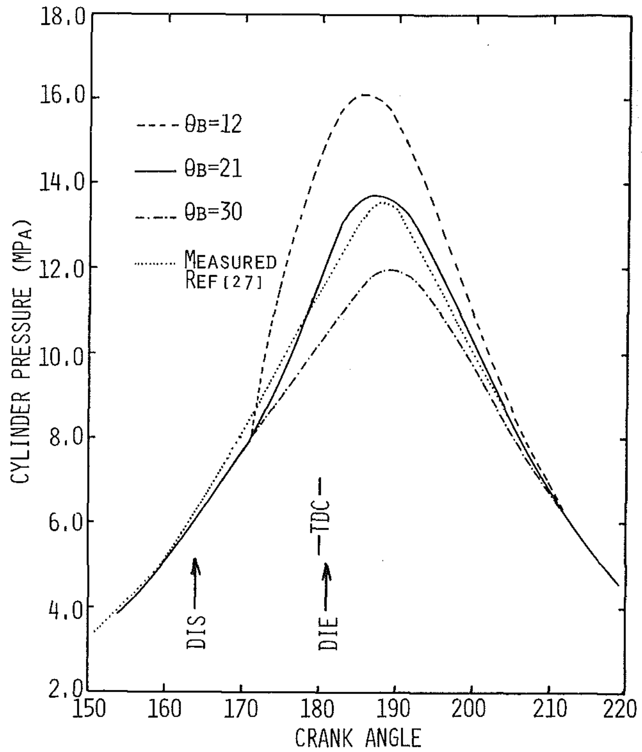

Fig. 7 Cylinder gas pressure as a function of crank angle for engine B using diesel fuel at 100 percent load for three entrainment constants

not available and, since the measured cylinder pressures [25] were only available for 80°CA near top dead center (TDC), no estimate of measured indicated engine performance could be inferred from the pressure measurements.

The computed performance was dependent on the selected model parameters and coal properties [24]. Figure 5 shows the variation of computed cylinder pressure for three values of the entrainment constant θ_b. The pilot diesel fuel injected evaporates (due to the high gas temperatures) and is available to form combustible mixtures within the first few crank angles. The quantity of air in each of the packets, however, is limited by the entrainment process. Lower values of θ_b result in faster entrainment and better combustion for the diffusion limited reactions. As shown in Fig. 5, an entrainment constant of 8, as for the diesel case, yielded cylinder pressures which agreed with the measurements. The figure also shows that for engine A, a θ_b of 10 is very close to the critical value required for successful ignition. A comparison between the results of Figs. 4 and 5 indicates that for the operating conditions studied the combustion process was more sensitive to the amount of entrainment for the coal fuel than for the diesel fuel.

Figure 6 shows the sensitivity of the combustion process to the surface reaction rates and the devolatilization rates. These results provide information regarding the use of coals with higher reactivities. The figure shows the variation of the cylinder pressure for engine A using coal/water slurry fuel (Table 2) for three different kinds of coal. This was achieved by multiplying both the surface reaction and devolatilization rates by factors of 50, 10, and 1. For the lowest reactive coal (a multiplying factor of 1), the cylinder pressure trace has two peaks. The first peak results as the diesel pilot burns completely but, due to the low-reactivity coal, the particle surface temperatures are not high enough to promote active devolatilization or surface reactions, which results in a decrease in cylinder pressure. As the fuel particle continues to heat up, the coal particles finally ignite and this results in the second pressure peak. Increasing the reactivities by a factor of 10 improved the combustion characteristics but further increases in reaction rates did not have a significant effect on the ignition and combustion characteristics. All the base-case computations for engine A have used surface reaction and devolatilization rates increased by a factor of 10.

Table 4 Computed performance using coal slurry fuel (90 percent load, engine A)

Indicated Power (kW)	1425
Indicated MEP (kPa)	10.1
Indicated SFC (g/kW-hr)	607
$\eta_{indicated}$(%)	35.3
Air Flow Rate (kg/hr)	13,200
Fuel Flow Rate (kg/hr)	866
Maximum Pressure (MPa), at (aTDC)	7.9, 8°

Engine B. No experimental data are available for coal/water slurry combustion in locomotive engines. For the purposes of this study, the engine simulation was first validated with experimental data for engine B using diesel fuel. Table 5 shows the comparison of the computed and measured performance parameters derived from [27]. Figure 7 shows the computed and measured cylinder pressures as a function of crank angle. The entrainment constant θ_b was varied from 12 to 30 to find the best match between the computed and experimental data. As mentioned earlier, a higher value of θ_b results in lower entrainment rates which yields richer packet equivalence ratios, lower burning rates and lower cylinder pressures. Figure 7 and Table 5 show that good agreement between computed and measured data was obtained for an entrainment constant of 21. The diesel fuel case was, therefore, used for verification purposes.

The next set of results are for coal/water slurry fuel (Table 2) in engine B. No pilot was used as in the engine A case. Instead, good ignition characteristics were obtained with preheated (450 K) inlet air. The effects of the degree of preheat

Table 5 Engine B performance using diesel fuel

Parameter	Computed	Measured
Indicated Power (kW/cyl)	209	-
Indicated MEP (MPa)	1.2	-
Indicated SFC (g/kW-hr)	178.6	-
Air Flow Rate (kg/hr/cyl)	1455	1449
Fuel Flow Rate (kg/hr/cyl)	37.3	36.1
Maximum Pressure (MPa), at (aTDC)	13.7, 7.3°	13.3, 7.4°

Table 6 Engine B computed performance using coal-water slurry fuel

Indicated Power (kW)	137.21
Indicated MEP (kPa)	786
Indicated SFC (g/kW-hr)	223.3
$\eta_{indicated}$(%)	47.6
Maximum Pressure (MPa), at (aTDC)	12.1, 9.7°

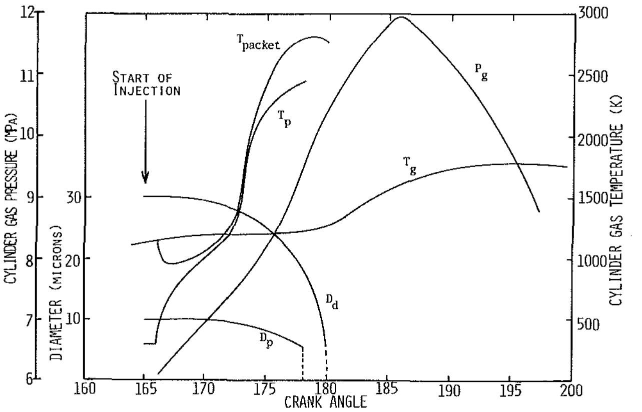

Fig. 8 Results as a function of crank angle for a packet injected at the first crank angle of injection for engine B using coal/water slurry fuel

on the ignition and combustion processes were also investigated [24]. Table 6 lists the performance results for this base case.

Figure 8 shows typical combustion results for engine B for the base case engine B as a function of crank angle. These results show the variation of packet, gas, and particle temperatures, particle and droplet diameters, and cylinder gas pressure and temperature for a packet injected at the first crank angle of injection and with a mid-classification. All packets behave in a similar fashion but have their own individual characteristics based on the crank angle of injection and their classification. The variation of cylinder gas pressure and temperature indicated the overall effect of all the individual packet burning on the cylinder gas. After injection, the liquid component of the slurry (water) immediately begins evaporating due to the high cylinder gas pressures and temperatures. The liquid evaporation causes a reduction in the local packet temperature, but this is only a short-term phenomenon. The coal particles start devolatilizing and, as the volatiles start burning (when the local equivalence ratios are lean enough), both the packet gas and particle temperatures increase. The increases in local gas temperatures further increase the particle temperature until significant devolatilization and coal combustion starts.

For all the parametric study results that follow, the injection timing was adjusted to obtain the best performance. The performance of the base case engine B was examined as a function of load (equivalence ratio) and particle sizes.

Figure 9 shows the indicated thermal efficiency as a function of equivalence ratio for engine B at a constant engine speed of 900 rpm. As the equivalence ratio is reduced from 1.0 to 0.3, the expected trend of increasing thermal efficiencies was obtained due to the presence of excess air, improved burn times, and reduced absolute heat losses. As the equivalence ratio is reduced further, the indicated performance decreases for the case when injection duration is kept constant at 15° CA (solid line). These lower efficiencies are due to a small quantity of fuel injected over a relatively long injection duration leading to the heat release being spread over a longer crank angle duration. As the injection duration for the lower equivalence ratios is reduced (dashed line), in accordance with a lower rack setting at low loads, the small quantity of fuel is concentrated over a smaller injection duration and the heat release is closer to TDC leading to better performance as indicated by the dashed line in Fig. 9.

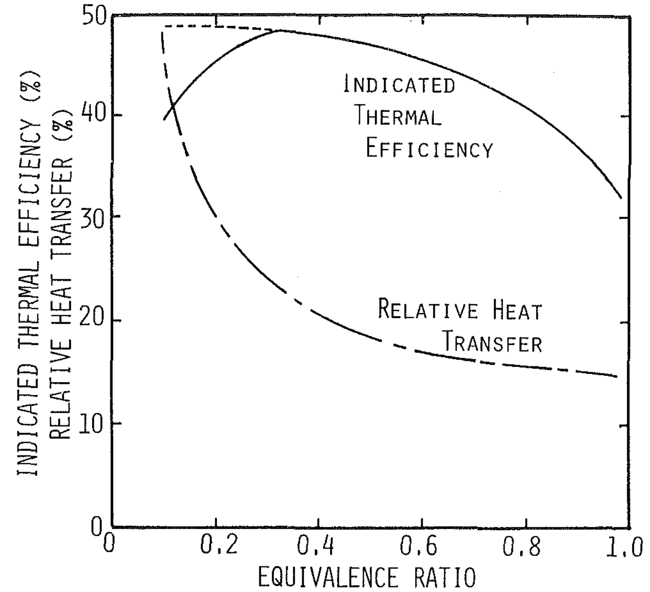

Fig. 9 Indicated thermal efficiency and relative heat transfer as a function of equivalence ratio for engine B using coal/water slurry fuel

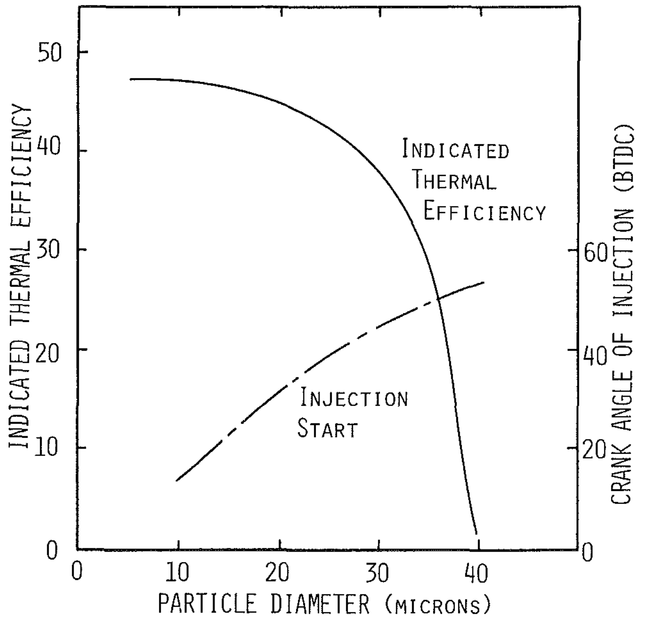

Fig. 10 Indicated thermal efficiency and start of injection (for maximum efficiency) as a function of particle diameter of engine B using coal/water slurry

The lower curve in Fig. 9 shows the variation of relative heat transfer with equivalence ratio. Relative heat transfer is defined as the total heat transfer to the walls as a percentage of the total heat input. The curve is seen to increase sharply at lower equivalence ratios mainly due to decreasing values of heat input. At lower equivalence ratios, the cylinder gas temperatures do not decrease much; therefore, the total wall heat transfer does not change substantially. The heat input decreases significantly, however, causing relative heat transfer to increase sharply.

Figure 10 shows the indicated thermal efficiency as a function of particle size for engine B. At a constant equivalence ratio, increasing the particle diameter resulted in fewer number of particles per packet. The larger particles had a smaller overall surface area available for surface reactions. This resulted in lower reaction rates, since energy is released over a greater crank angle duration, and lower indicated efficiencies. The lower plot in the figure shows the injection timing in crank angle degrees bTDC for best performance. Advanced injection timings are required for the large particles to compensate for the longer burn times.

Summary and Conclusions

An engine cycle simulation was used which was based on a thermodynamic analysis with detailed combustion submodels to investigate the behavior of coal/water slurry combustion in large, two-stroke cycle engines. In brief, conclusions of this study include:

1 The combustion model developed in this work included a parameter, the entrainment constant, to model the process of air entrainment. An evaluation of this entrainment constant, as well as other model parameters and fuel properties was completed to establish the sensitivity of the cycle simulation to these parameters. For a specific set of model parameters and coal properties, computed engine characteristics indicated good agreement with limited available measurements.

2 Higher air entrainment rates resulted in better performance characteristics, which indicates that the combustion process is largely a diffusion or mixing-controlled process.

3 Coal fuels with higher reactivities exhibited better ignition characteristics, and yielded higher indicated efficiencies for the specific injection timings due to faster burning rates.

4 The engine inlet air temperature was an important parameter which controlled the ignition characteristics of coal/water slurry. Increasing the inlet air temperature resulted in better ignition characteristics.

5 Coal/water slurry fuel with smaller particle sizes exhibited higher indicated thermal efficiencies. At the same inlet air temperature, 40-μ particles did not ignite but 10-μ particles resulted in a 48 percent indicated thermal efficiency.

Acknowledgments

This work was supported by the U.S. Department of Energy, Morgantown Energy Technology Center, Contract No. DE-AC21-84MC21175, and by the Center for Energy and Mineral Resources, Texas A&M University.

References

1 Caton, J. A., and Rosegay, K. H., "A Review and Comparison of Reciprocating Engine Operation Using Solid Fuels," SAE Paper No. 831362, 1983.

2 Carpenter, L. K., and Crouse, F. W., Jr., "Coal-Fueled Diesels, Fossil Energy Activities," ASME Paper No. 85-DGP-18, 1985.

3 Nydick, S. S., "Coal/Water Slurry Fueled Slow-Speed Diesel Engine Program: Past, Present and Future," Thermo Electron Corporation, MA, presented at "Coal-Fueled Diesel for Cogeneration Seminar," Rosemont, IL, July 25, 1985, Report No. TE4319-123-85.

4 Robben, F., Brehob, D. D., Namazian, M., Sawyer, R. F., and Sherman, P., "Coal Fueled Diesel Engines," *Proceedings of the Sixth International Symposium on Coal Slurry Combustion and Technology*, Orlando, FL, June 25–27, 1984.

5 Siebers, D. L., and Dyer, T. M., "The Autoignition and Combustion of Coal-Water Slurry Under Simulated Diesel Engine Conditions," ASME Paper No. 85-DGP-15, 1985.

6 Kishan, S., "Simulation Study of Two-Stroke Cycle Compression Ignition Engines," M.S. Thesis, Texas A&M University, May 1985.

7 Kishan, S., and Caton, J. A., "Simulation of a Two-Stroke Cycle, Locomotive Engine Using Diesel or Coal Fuels," presented at the Spring Central States Meeting of the Combustion Institute, San Antonio, TX, Apr. 22–23, 1985, Paper No. 1-1A.

8 Bell, S. R., and Caton, J. A., "Ignition and Combustion Characteristics of Coal Fuels in Diesel Engines," Report No. CF-85-01, Texas A&M University, Sept. 1985.

9 Bell, S. R., and Caton, J. A., "Analytical Evaluations of Ignition Options for a Coal/Water Slurry Fueled Engine," presented at the Fall Meeting of the American Flame Research Committee, Livermore, California, Oct. 17–18, 1985.

10 Dedeoglu, N., "Scavenging Solves Problems in Gas Burning Engines," SAE Paper No. 710579, 1971.

11 Benson, R. S., "A New Gas Dynamic Model for the Gas Exchange Process in a Two-Stroke Loop and Cross Scavenged Engines," *Inst. J. Mech. Sci.*, Vol. 19, 1977, pp. 693–710.

12 Caton, J. A., and Rosegay, K. H., "An Analysis of Solid Particle Combustion in an I.C. Engine Environment," presented at the Central States Section Meeting of the Combustion Institute, Lexington, KY, Mar. 21–22, 1983, Paper No. CSS/CI 83-02.

13 Bell, S. R., and Caton J. A., "Cycle Simulations for a Reciprocating, Internal Combustion Engine Using a Coal Slurry Fuel: the Role of Volatiles," presented at the American Flame Research Committee International Symposium on Alternate Fuels and Hazardous Wastes, Tulsa, OK, Oct. 9–11, 1984, Paper No. 4.1.

14 Rosegay, K. H., and Caton, J. A., "Cycle Simulation of Coal Particle Fueled Reciprocating Internal Combustion Engine," SAE Paper No. 831299, 1983.

15 Bell, S. R., and Caton, J. A., "Cycle Simulations for a Reciprocating, Internal Combustion Engine Using a Coal Slurry Fuels," presented at the Spring Central States Meeting of the Combustion Institute, San Antonio, TX, Apr. 22–23, 1985, Paper No. 2-1A.

16 Mathews, K. J., and Street, P. J., "Combustion Histories of Various Coal-Water Fuels," presented at the Sixth International Symposium on Coal Slurry Combustion and Technology, Orlando, FL, June 25–27, 1984.

17 Seeker, W. R., Samuelson, G. S., Heap, M. P., and Trolinger, J. D., "The Thermal Decomposition of Pulverized Coal Particles," *Eighteenth Symposium (International) on Combustion*, 1981, p. 1213.

18 McLean, W. J., Hardestey, D. R., and Pohl, J. H., "Direct Observations of Pulverized Coal in a Combustion Environment," presented at the Central States Section Meeting of the Combustion Institute, Baton Rouge, LA, Mar. 24–25, 1980, Paper No. CSS/CI 80-11.

19 Kobayashi, H., Howard, J. B., and Sarofin, A. F., "Coal Devolatilization at High Temperatures," *Sixteenth Symposium (International) on Combustion*, 1977, p. 411.

20 Spalding, D. B., *Some Fundamentals of Combustion*, Academic Press, London, 1955.

21 Spadacinni, L. J., and TeVelde, J. A., "Autoignition Characteristics of Aircraft-Type Fuels," *Combustion and Flame*, 1982, p. 46.

22 Mansouri, S. H., Heywood, J. B., and Radhakrishnan, K., "Divided Chamber Diesel Engine, Part I: A Cycle Simulation Which Predicts Performance and Emissions," SAE Paper No. 820273, 1982.

23 Woschni, G., "A Universally Applicable Equation for the Instantaneous Heat Transfer Coefficient in Internal Combustion Engines," SAE Paper No. 670937, 1967.

24 Kishan, S., Bell, S. R., and Caton, J. A., "Two-Stroke Cycle Engine Simulations: a Sensitivity Study," Report No. CF-85-04, Texas A&M University, Dec. 1985.

25 Steiger, H. A., "Sulzer Single Cylinder Test Results With Various Coal Water Slurries," presented at "Coal-Fueled Diesel for Cogeneration Seminar," Rosemont, IL, July 25, 1985.

26 Dunlay, J. B., Davis, J. P., Maslen, P. L., Stieger, H. A., and Eberie, M. K., "Economic and Technological Assessment of Diesel Engines Using Coal-Based Fuels for Electric Power Generation," Report No. TE4234-37-80, Thermo Electron Corporation, MA, Sept. 1979.

27 Kotlin, J. J., Dunteman, N. R., Chen, J., and Heilenbach, J. W., "The General Motors EMD Model 710G Series Turbocharged Two-Stroke Cycle Diesel Engine," ASME Paper No. 85-DGP-24-1985.

Performance of a Stirling Engine Regenerator Having Finite Mass

J. D. Jones[1]
University of Reading,
Reading, Berks, United Kingdom

The performance of a Stirling engine regenerator subjected to sinusoidal mass flow rate and pressure variation is analyzed. It is shown that cyclic variations in the temperature of the matrix due to its finite mass lead to an increase in the apparent regenerator effectiveness, but a decrease in engine power. Approximate closed-form expressions for both of these effects are deduced. The results of this analysis are compared with the predictions of a finite-element system model, and good agreement is found.

Introduction

Two approaches to Stirling engine design are current [1-3]. The first divides the engine spaces and their contents into a number of control volumes and solves the resulting system of equations by standard computing techniques [4]. The second treats the engine as an ideal isothermal [1] or adiabatic [5] cycle, and adds correction terms to account for the real behavior of engine components. In this paper, an analysis is developed which provides correction terms for the effect on engine performance of temperature fluctuations in the regenerator matrix. Analyses of regenerator behavior have been published by Qvale and Smith [6] and by Rios [5] which include the effect of flow and pressure cycling but omit the effect of finite matrix mass. The engine analysis of Martini [1] adds a correction term for matrix temperature swing, but does not consider the interaction of the swing with pressure and mass flow variation.

It will be shown that this interaction determines the net enthalpy flow through the regenerator, affecting the efficiency of the engine, and that it has a previously unreported effect on the power output by the engine.

Power and Efficiency

The mass of the regenerator matrix affects performance in two ways: It affects the engine power output and the engine efficiency. The engine efficiency is reduced by the net leakage of energy through the regenerator from heater to cooler.

In classical regenerator theory, the loss of heat through the regenerator is measured by a parameter known as the effectiveness E. E is defined as the ratio of the heat gained by the gas passing through the regenerator from the cold side to the hot side to the heat given up by an equal mass of gas in being cooled from the heater temperature to the cooler temperature. The classical assumption of distinct hot and cold blows through a regenerator of negligible volume on which this definition is based does not apply to the Stirling engine regenerator, and we must therefore modify the definition. The definition used in the present work gives the ineffectiveness, $1-E$, as the ratio of the net enthalpy flux H through the regenerator to an average reference enthalpy flow

$$1-E=\frac{H}{c_{pg}\Delta T(m_{ahr}+m_{acr})} \tag{1}$$

where m_{ahr} and m_{acr} are the amplitudes of the quasi-sinusoidal variation in mass flow through the hot and cold ends of the matrix respectively.

A Simple Model

The two effects of reducing matrix mass can be well understood by considering an extreme case. Consider the following design for a regenerator: Take an empty regenerator capsule and imagine it to be divided by a perfectly elastic insulating membrane. Suppose the volume of the capsule to be greater than either of the engine's swept volumes. Now, as gas leaves the expansion space, the regenerator will fill with hot gas, though none will pass through to the cold side. Then, as gas leaves the compression space, the regenerator will fill with cold gas from the other side, and the hot gas will be displaced to whence it came. This device will have an effectiveness as conventionally defined of ≥ 100 percent and has zero frictional losses. Its only failing is that the associated engine will produce zero power. (A detailed analysis of an engine with such a "diaphragm" regenerator shows that it will actually consume power in pumping heat from cooler to heater, thus giving an apparent effectiveness of more than 100 percent.)

Closed-Form Solutions

We now seek to derive reasonably accurate closed-form expressions for the enthalpy flow through the regenerator and the effect of the regenerator upon engine power.

Expressions for the time-varying mean regenerator temperature and the temperature gradient used in this derivation are deduced in the Appendix.

Engine Power. We obtain an expression for the effect of temperature variation in the regenerator on engine power by performing a modified Schmidt analysis [8], in which the mean temperature of the regenerator is allowed to vary.

---

[1] This work was completed at the University of Reading as part of my PhD thesis. Since completion of the work, but prior to submission for publication of this portion of the work, I have joined the Engine Research Department at General Motors Research Laboratories, Warren, Michigan, as a Senior Research Engineer.

Contributed by the Advanced Energy Systems Division for publication in the JOURNAL OF ENGINEERING FOR GAS TURBINES AND POWER. Manuscript received by the Advanced Energy Systems Division July 1985.

Consider the regenerator to have free-flow area A_f. For a slice of the regenerator of thickness dx, taking the matrix and gas temperatures within that slice as being uniform and identical, the mass of gas contained in the slice is given by

$$dm = \frac{pA_f dx}{RT(x)} \tag{2}$$

Integrating this along the length of the matrix gives

$$m_R = \frac{pA_f}{R} \int_0^L \frac{dx}{T(x)} \tag{3}$$

Summing the mass of gas for the engine gives

$$m_T = \frac{p}{R} \left(\frac{V_e}{T_e} + \frac{V_c}{T_c} + \Sigma \frac{V_d}{T_d} + A_f \int_0^L \frac{dx}{T(x)} \right) \tag{4}$$

where Σ denotes summation over dead space other than that in the regenerator and V_e and V_c are the cyclically varying volumes of the expansion and compression spaces.

Now, making p the subject and substituting for $A_f \int dx/T(x)$, using equations (A3) and (A4) from the Appendix,

$$p = \frac{m_T R}{\left(\frac{V_e}{T_e} + \frac{V_c}{T_c} + \Sigma \frac{V_d}{T_d} + \frac{V_R \Delta T \cos(\omega t + \phi_T)}{2\Gamma T_E T_C} + V_R \frac{\ln(T_E/T_C)}{\Delta T} \right)} \tag{5}$$

Using equation (5), work per cycle may be evaluated following standard procedures for obtaining a Schmidt equation. It may be shown that matrix temperature swing reduces predicted power by a factor of

$$\text{Power loss factor} = 1 - \frac{V_R}{\Gamma V_E V_C} \sin\phi_c (V_E \sin\phi_T + V_C \sin(\phi_C - \phi_T)) \tag{6}$$

from that predicted by an unmodified Schmidt equation.

In equation (6), V_E and V_C are the maximum volumes of the expansion and compression space, respectively, and ϕ_c is the phase angle between volume variations in the two variable volume spaces. In many common engine designs $V_E = V_C$ and $\phi_c = 90$ deg. Equation (6) then becomes

$$\text{Power loss factor} = 1 - \frac{V_R}{\Gamma V_E} (\sin\phi_T - \cos\phi_T) \tag{7}$$

ϕ_T can be found from a simple adiabatic analysis [5]; for the example of Fig. 1, $\phi_T = 120$ deg. The predictions of formula (7) are graphed against the predictions of a finite-difference computer model [7] for the U.K. 20 kW Consortium engine in Fig. 1. It will be noted that there is surprisingly good agreement, and that the power loss is already 5 percent when the thermal mass of the matrix is thirty times that of the tidal gas—a ratio not unusual in Stirling engines; the GPU-3, the Mod-1, and the P-40 all have Γ in this region [1].

Net Enthalpy Flux. This section modifies the analysis of Qvale and Smith [6] to take account of the temperature variation of the matrix.

Consider a cross section of the regenerator of distance x from the hot end. The mass flow through this cross section will be assumed to vary sinusoidally according to the equation

$$\dot{m}_x = m_{ax}\omega \sin(\alpha + \phi_x) \tag{8}$$

where m_{ax} is the amplitude of the mass flow variation and ϕ_x is the phase angle of this variation with respect to the variation through some reference cross section. The amplitude of mass variation through this reference cross section we define as m_{axr}. The pressure variation is given by

$$p = p_m - p_a \cos(\alpha - \phi_p) \tag{9}$$

where ϕ_p is a phase angle referred to the mass variation through the reference cross section. The matrix temperature, assumed to be uniform across the cross section, is given by

$$T_{mx} = T_{mxr} + \delta T_{mx} \tag{10}$$

where T_{mxr} is a reference temperature and δT_{mx} a small cyclically varying departure from it. The gas temperature at the cross section is

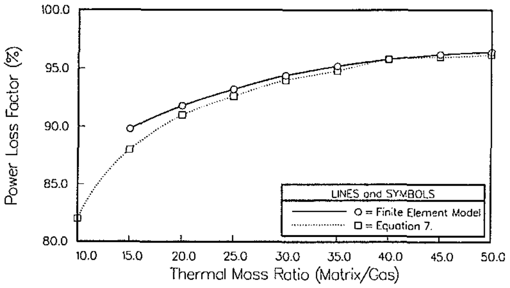

Fig. 1 Regenerator mass and power loss

Nomenclature

A_f = free-flow area of matrix, m^2
A_h = heat transfer area of matrix, m^2
c_m = specific heat of matrix material, J/kg•K
c_{pg} = specific heat of gas at constant pressure, J/kg•K
c_{vg} = specific heat of gas at constant volume, J/kg•K
h = coefficient of convective heat transfer, W/m^2•K
k = reference heat transfer coefficient: $h = k \mid \dot{m}_x \mid^n$
L = length of matrix, m
m_{acr} = amplitude of mass flow variation at cold end of matrix
m_{ahr} = amplitude of mass flow variation at hot end of matrix
m_{ax} = amplitude of mass flow variation at x
m_{axr} = amplitude of mass flow variation at a reference plane
M_{ax} = dimensionless ratio of the mass flow variation amplitude at x to its amplitude at the reference plane
M_m = mass of the regenerator matrix, kg
m_R = mass of gas stored in regenerator matrix, kg
m_T = total mass of gas in engine, kg
$\dot{m}_x$ = rate of increase of mass of gas stored to the hot side of the cross section at x, kg/s
p = pressure, Pa
p_a = amplitude of cyclic pressure variation, Pa
p_m = mean pressure over the cycle, Pa
P = dimensionless pressure ratio $= p/p_a$
R = gas constant, J/kg•K
T_C = compression space temperature, K
T_D = temperature of an engine dead space
T_E = expansion space temperature
T_H = mean temperature of gas in heater
T_K = mean temperature of gas in cooler
T_R = mean temperature of gas in regenerator
T_{mx} = matrix temperature at x (cyclically varying)
T_{mxr} = matrix temperature at x at start of cycle
T_x = gas temperature at x (cyclically varying)

$$T_x = T_{mx} + \delta T_x \tag{11}$$

The net enthalpy passing through this cross section of the regenerator during a cycle will therefore be

$$H = -c_{pg}\int_0^{2\pi/\omega} \dot{m}_x(\delta T_x + \delta T_{mx})dt \tag{12}$$

To evaluate this, we write the governing equations:

For gas continuity

$$\frac{\partial \rho}{\partial t} + \frac{1}{A_f}\frac{\partial \dot{m}_x}{\partial x} = 0 \tag{13}$$

We introduce the dimensionless variables

$P = p/p_a \qquad \chi = x/L \qquad M_{ax} = m_{ax}/m_{axr} \qquad \theta_x = T_x/\Delta T$

and rearrange equation (13) to obtain

$$\frac{p_aA_fL}{m_{axr}R\Delta T}\frac{\partial(P/\theta_x)}{\partial\alpha} + \frac{\partial}{\partial\chi}(M_{ax}\sin(\alpha+\phi_x)) = 0 \tag{14}$$

which we will write as

$$A_1\frac{\partial(P/\theta_x)}{\partial\alpha} + \frac{\partial}{\partial\chi}(M_{ax}\sin(\alpha+\phi_x)) = 0 \tag{15}$$

For gas energy

$$\frac{c_{vg}A_f}{R}\frac{\partial p}{\partial t} + c_{pg}\dot{m}_x\frac{\partial T_x}{\partial x} + c_{pg}T_x\frac{\partial \dot{m}_x}{\partial x} = \frac{-hA_h\delta T_x}{L}$$

whence

$$\frac{V_Rp_a}{\gamma m_{axr}\Delta TR}\frac{\partial P}{\partial\alpha} + M_{ax}\sin(\alpha+\phi_x)\frac{\partial\theta_x}{\partial\chi} + \theta_x\frac{\partial M_{ax}\sin(\alpha+\theta_x)}{\partial\chi}$$
$$= \frac{-kA_h|M_{ax}\sin(\alpha+\phi_x)|^n\delta\theta_x}{\omega^{1-n}m_{axr}^{1-n}c_{pg}} \tag{16}$$

which we write as

$$C_1\frac{\partial P}{\partial\alpha} + M_{ax}\sin(\alpha+\phi_x)\frac{\partial\theta_x}{\partial\chi} + \theta_x\frac{\partial M_{ax}\sin(\alpha+\theta_x)}{\partial\chi}$$
$$= -C_2|M_{ax}\sin(\alpha+\phi_x)|^n\delta\theta_x \tag{17}$$

For matrix energy

$$c_mM_m\frac{\partial T_{mx}}{\partial t} = hA_h\delta T_x$$

$$\Rightarrow \frac{\partial\theta_{mx}}{\partial\alpha} = \frac{km_{axr}^n\omega^{n-1}}{c_mM_m}|M_{ax}\sin(\alpha+\phi_x)|^n\delta\theta_x \tag{18}$$

which we write as

$$\frac{\partial\theta_{mx}}{\partial\alpha} = E_1|M_{ax}\sin(\alpha+\phi_x)|^n\delta\theta_x \tag{19}$$

Now, from equation (14) we may obtain

$$\frac{A_1}{\theta_x}\frac{\partial P}{\partial\alpha} - \frac{A_1P}{\theta_x^2}\frac{\partial\theta_x}{\partial\alpha} = \frac{-\partial}{\partial\chi}(M_{ax}\sin(\alpha+\phi_x)) \tag{20}$$

$\partial\theta_x/\partial\alpha$ is negligible, so we may suppress the second term on the left-hand side. Substituting equation (20) into equation (17) and rearranging, we get

$$\delta\theta_x = \frac{(A_1-C_1)\sin(\alpha-\phi_p) - M_{ax}\sin(\alpha+\phi_x)\dfrac{\partial\theta_x}{\partial\chi}}{C_2|M_{ax}\sin(\alpha+\phi_x)|^n} \tag{21}$$

Now combining equation (19) and equation (21) we get

$$\frac{\partial\theta_{mx}}{\partial\alpha} = \frac{E_1}{C_2}\left((A_1-C_1)\sin(\alpha-\phi_p) - M_{ax}\sin(\alpha+\phi_x)\frac{\partial\theta_x}{\partial\chi}\right)$$

$$\Rightarrow \theta_{mx} = \theta_{mxr} + \frac{E_1}{C_2}\int_0^\alpha\Big((A_1-C_1)\sin(\psi-\phi_p)$$
$$- M_{ax}\sin(\psi+\phi_x)\frac{\partial\theta_x}{\partial\chi}\Big)d\psi \tag{22}$$

By comparison with equation (10) we may write

$$\delta\theta_{mx} = \frac{E_1}{C_2}\int_0^\alpha\Big((A_1-C_1)\sin(\psi-\phi_p)$$
$$- M_{ax}\sin(\psi+\phi_x)\frac{\partial\theta_x}{\partial\chi}\Big)d\psi \tag{23}$$

Now, rewriting equation (12) in dimensionless variables,

$$H = -c_{pg}m_{axr}\Delta T\int_0^{2\pi}M_{ax}\sin(\alpha+\phi_x)(\delta\theta_x+\delta\theta_{mx})d\alpha \tag{24}$$

We may evaluate H from equations (11) and (23). Given a choice of mass flow reference plane at any cross section of the regenerator and evaluating the integrals of equations (23) and (24) at this plane, $\phi_x = 0$ and $M_{ax} = 1$. Thus

$$\delta\theta_{mx} = \frac{E_1}{C_1}\big((A_1-C_1)(\cos\phi_p - \cos(\alpha-\phi_p))$$
$$+ \frac{\partial\theta_x}{\partial\chi}(\cos\alpha - 1)\big) \tag{25}$$

Nomenclature (cont.)

δT_x = $T_x - T_{mx}$
δT_{mx} = $T_{mx} - T_{mxr}$
v = fraction of the total matrix length with a time-varying temperature
v_C = fraction of the total matrix length at cooler temperature
v_H = fraction of the total matrix length at heater temperature
V_C = maximum volume of compression space, m^3
V_c = time-varying volume of compression space
V_D = volume of engine dead space
V_E = maximum volume of expansion space
V_e = time-varying volume of expansion space
V_R = void volume of regenerator
x = distance from hot end of the regenerator
α = crank angle in radians, referred to variation in V_e
β = beta function
γ = ratio of gaseous specific heats
χ = dimensionless distance along regenerator
ρ = density of working fluid
ϕ_c = phase angle between volume variation in compression space and volume variation in expansion space
ϕ_p = phase angle between pressure variation and reference mass flow variation
ϕ_T = phase angle between matrix temperature variation and volume variation in expansion space
ϕ_x = phase angle between mass flow variation at x and reference mass flow variation
θ = dimensionless temperature
ψ = temporary variable used for integration
ω = angular velocity of crank, rad/s

Dimensionless Groups

A_1 = $p_aV_R/(m_{axr}R\Delta T)$
C_1 = A_1/γ
C_2 = $kA_h/(c_{pg}\omega^{1-n}m_{axr}^{1-n})$
E_1 = $kA_h\omega^{1-n}m_{ax}^n/c_mM_m$
Γ_x = ratio of matrix mass to tidal mass of gas at x = $c_mM_m/(2c_{pg}m_{axr})$
Φ_x = ratio of tidal mass of gas at x to mass resident in matrix = $2m_{axr}RT_R/(p_mV_R)$

and

$$H=\frac{c_{pg}m_{axr}\Delta T}{C_2}\left(2\left((A_1-C_1)\cos\phi_p-\frac{\partial\theta_x}{\partial\chi}\right)\beta(m'',n'')\right.$$

$$\left.-\pi E_1(A_1-C_1)\sin\phi_p\right) \tag{26}$$

where β is the beta function, $m''=(3-n)/2$ and $n''=0.5$.

We have obtained an expression for H, the net enthalpy flow through a particular cross section. Since at equilibrium there is no net cyclic heat transfer from gas to matrix, this also gives the net enthalpy flow through the matrix as a whole. If the cross section chosen is sufficiently far from the ends, $\partial\theta_x/\partial\chi$ can be obtained from equation (A6) in the Appendix.

We can now use equation (1) to obtain a measure of ineffectiveness. If we choose our reference section in the middle of the regenerator, the amplitude of mass flow through this cross section will be approximately equal to the arithmetic mean of the mass flows through the hot and cold ends

$$m_{axr}=\frac{m_{ahr}+m_{acr}}{2} \tag{27}$$

Combining equations (1), (26), and (27) gives

$$1-E=\frac{1}{2C_2}\left(2\left((A_1-C_1)\cos\phi_p-\frac{\partial\theta_x}{\partial\chi}\right)\beta(m'',n'')\right.$$

$$\left.-\pi E_1(A_1-C_1)\sin\phi_p\right) \tag{28}$$

The effect of finite matrix mass appears chiefly in the second term. If we neglect its effect upon $\partial\theta_x/\partial\chi$ we may approximate equation (28) by

$$1-E=(1-E_\infty)+\frac{\pi}{2}(1-\gamma^{-1})\ \frac{p_a}{p_m}\ \frac{T_R}{\Delta T}\ \frac{1}{\Gamma_x\Phi_x}\sin\phi_p \tag{29}$$

where E_∞ is the effectiveness the regenerator would have were its mass infinite, and Φ_x is the ratio of the mass of tidal gas passing x to the mass of gas resident in the matrix. ϕ_p may be evaluated by elementary cycle analysis; its value will vary slightly with position in the matrix.

Equation (29) is evaluated for a range of values of Γ_x, taking $\phi_p=-90$ deg. The results of this comparison are compared with the results of a finite-difference computer model in Fig. 2. Equations (28) and (29) show the effect of finite matrix mass in two ways: a relatively minor effect due to the term $\partial\theta_x/\partial\chi$ and a larger effect due to the second term in each equation. This larger effect is wholly due to the pressure oscillation, as may be seen from the influence of the term p_a, and represents what we have called the "heat-pumping" effect.

It may be noted that the second term in equation (29), representing the "heat pumping" effect, may be either positive or negative, depending on the sign of ϕ_p, the phasing of the pressure variation with respect to the flow through a reference cross section of the regenerator. In many Stirling engines, the swept volumes of the expansion space and the compression space are approximately equal, and it would hence be expected that the pressure would reach a minimum during that part of the cycle when most of the gas had flowed through the regenerator to the cooler and compression space. ϕ_p would therefore be negative and close to 90 deg, as is the case for the example depicted in Fig. 2. Given an engine which departed sufficiently widely from this design, however—in which, for example, the hot swept volume was much greater than the cold—it is possible that ϕ_p might take a positive value; in this case heat would be pumped from heater to cooler, reducing regenerator effectiveness.

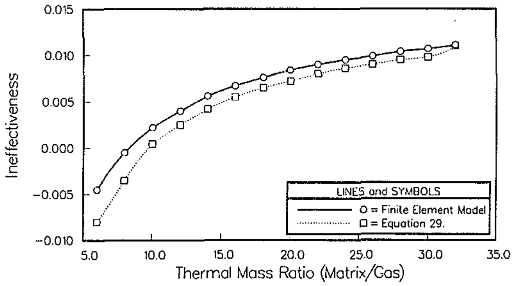

Fig. 2 Regenerator mass and ineffectiveness

Conclusion

For many Stirling engine designs, the ratio of matrix thermal mass to the thermal mass of the tidal gas in the regenerator is between twenty and forty. It has been shown, firstly, that the effects of this ratio on engine power and efficiency are important for engines in this region; secondly, that equations (6) and (28) are in good agreement with a sophisticated computer model in this region. It is recommended that these equations be used in design of the Stirling engine regenerator.

Acknowledgments

I gratefully acknowledge the help of my colleagues at the University of Reading Engineering Department, in particular Mr. John Bayes, and of my thesis supervisor Dr. Graham Rice.

References

1 Martini, W. R., *Stirling Engine Design Manual*, NASA-Lewis N78-23999, 1978.

2 Martini, W. R., *Thermodynamic Design of Stirling Engines by Computer*, Martini Engineering, 1980.

3 Urieli, I., "A Review of Stirling Cycle Machine Analysis," *Proc. 14th IECEC*, Paper No. 799236, Aug. 1979, p. 1086.

4 Urieli, I., "A Computer Simulation of Stirling Cycle Machines," PhD Thesis, Witwatersand University, South Africa, 1977.

5 Rios, P. A., "An Analytical and Experimental Investigation of the Stirling Cycle," PhD Thesis, MIT, 1969.

6 Qvale, E. B., and Smith, J. L., Jr., "An Approximate Solution for the Thermal Performance of a Stirling Engine Regenerator," ASME JOURNAL OF ENGINEERING FOR POWER, Vol. 91, Apr. 1969, pp. 109–112.

7 Jones, J. D., "Thermodynamic Design of the Stirling Engine," PhD Thesis, University of Reading, U.K., 1982.

8 Schmidt, G., "The Theory of Lehman's Heat Machine," *Journal of German Engineers' Union*, Vol. 15, No. 1, 1871.

APPENDIX

In this Appendix, it is assumed that the mass flow variation through any cross section of the regenerator has the same amplitude and is at the same phase angle ϕ_T to the volume variation in the expansion space. While these assumptions would be exactly true were the expansion and compression volume variations 180 deg out of phase, in a real engine these variations are usually about 90 deg out of phase. There is consequently a difference between the amplitudes of the flow variations at the two ends of the regenerator, m_{acr} and m_{ahr}, and in their phasing. For the engines mentioned in this paper, and for most other conventional engine designs, m_{acr} may be 30 percent greater than m_{ahr}, and the difference in phase between the two ends will be about 30 deg. These differences will be disregarded in the following treatment.

It is further assumed that the temperature profile along the length of the matrix is as represented in Fig. A1. This will be approximately true if thermal contact between the gas and matrix is good, and if the heat capacities of gas and matrix are contstant; both these conditions will be satisfied for a typical Stirling regenerator. It is shown in [7] that the results obtained below do not depend critically on the exact shape of the temperature profile.

Referring to Fig. A1, we may consider the regenerator to be divided into three volumes. For the first fraction v_h/L of its

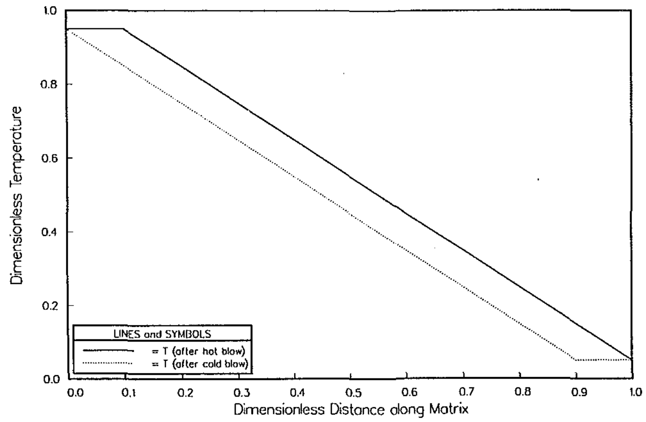

Fig. A1 Variation in matrix temperature profile over cycle

length, the matrix and the gas in contact with it are at T_E, where v_H/L varies with crank angle according to

$$v_H = \frac{v}{2}(1 - \cos(\omega t + \phi_T)) \quad \text{(A1)}$$

where ϕ_t is a phase angle.

For the final fraction of its length v_C/L, the matrix and the gas in contact with it are at T_C, where

$$v_C = \frac{v}{2}(1 + \cos(\omega t + \phi_T)) \quad \text{(A2)}$$

In the intermediate portion of the matrix, a constant fraction $(L - v)/L$ of the total, the temperature profile is a linear ramp between T_E and T_C. Now, as the tidal gas moves through the matrix, a fraction v/L of the matrix shifts from T_C to T_E, thereby absorbing the heat energy carried in the tidal gas. We may, therefore, write

$$v/L = \frac{\text{thermal mass of tidal gas}}{\text{thermal mass of matrix}} = \frac{1}{\Gamma}$$

where Γ is the ratio of the thermal mass of the matrix to that of the tidal gas.

We may now write an expression for the matrix temperature as a function of x, the distance along the matrix

$$T(x) = \begin{cases} T_E & \text{for } 0 \le x \le 0.5v(1 - \cos(\omega t + \phi_T)) \\ T_E - \dfrac{\Delta T}{L - v}(x - 0.5v(1 - \cos(\omega t + \phi_T))) & \\ & \text{for } 0.5v(1 - \cos(\omega t + \phi_T)) \le x \le L \\ & -0.5v(1 + \cos(\omega t + \phi_T)) \\ T_C & \text{for } L - 0.5v(1 + \cos(\omega t + \phi_T)) \le x \le L \end{cases}$$

Using this expression, we can evaluate $A_f \int_0^L dx/T(x)$

$$A_f \int_0^L \frac{dx}{T(x)} = V_R\left(\frac{(\Gamma - 1)\ln(T_E/T_C)}{\Gamma \Delta T} + \frac{T_R}{\Gamma T_E T_C}\right) + \frac{V_R \Delta T \cos(\omega t + \phi_T)}{2\Gamma T_E T_C} \quad \text{(A3)}$$

where

$$T_A = \frac{T_E + T_C}{2} \quad \text{and} \quad \Delta T = T_E - T_C$$

We can approximate the first term in equation (A3) by

$$V_R\left(\frac{(\Gamma - 1)\ln(T_E/T_C)}{\Gamma \Delta T} + \frac{T_R}{\Gamma T_E T_C}\right) \approx \frac{V_R \ln(T_E/T_C)}{\Delta T} \quad \text{(A4)}$$

Equations (A3) and (A4) together allow us to perform the modified Schmidt analysis to obtain engine power. To obtain regenerator effectiveness, we need an expression for the temperature gradient in the middle of the regenerator. This can be obtained from equation (A3)

$$\frac{\partial T_x}{\partial x} = \frac{\Delta T}{L - v} = \frac{\Gamma}{\Gamma - 1}\frac{\Delta T}{L} \quad \text{(A5)}$$

In dimensionless coordinates

$$\frac{\partial \theta_x}{\partial \chi} = \frac{\Gamma}{\Gamma - 1} \quad \text{(A6)}$$

D. L. Rhode
Assistant Professor.

S. R. Sobolik[1]
Graduate Student.

Mechanical Engineering Department,
Texas A&M University,
College Station, TX 77843

Simulation of Subsonic Flow Through a Generic Labyrinth Seal

A new method for predicting the leakage through labyrinth seals has been developed and is shown to provide realistic results which agree with measurements. It utilizes a finite-difference computer code which was developed in order to compute the pressure drop across a single cavity of the seal. This quantity is obtained at several leakage flow Mach numbers to be used subsequently in predicting the leakage rate. The model is widely applicable and does not require an estimate of the kinetic energy carry-over coefficient, whose value is often uncertain for many untested configurations. Detailed cavity distributions of basic flowfield quantities are also presented and examined. Specifically, the predicted results of four seal leakage mass flow rates at given cavity inlet pressure and temperature are compared, and important variations are examined. Also, realistic approximations of flow variable distributions within a single cavity are made from the included figures to assist in the development of analytical methods.

Introduction

Labyrinth seals are commonly found in turbines and compressors as well as in some pumps. They are designed to provide a highly dissipative flow path between high and low-pressure regions. The primary objective is to control fluid leakage. For example, in high-capacity fuel pumps seals are used to minimize the leakage flow around the impellers, whereas for turbines they are used in some locations to maintain a minimal leakage flow for cooling high-temperature components. Figure 1 illustrates the expected streamline pattern for flow in a straight-through labyrinth seal. As shown, the leakage flow passes over a series of restrictor teeth and dissipation cavities. A portion of the available pressure head is converted to kinetic energy at each restriction, and some of that kinetic energy is dissipated by small turbulent eddies within the cavity immediately downstream.

One of the earliest analytical methods for predicting leakage in a labyrinth [1] remains as probably the most widely used today. In that study, Martin modeled the labyrinth as a series of discrete throttling processes such as flow through a series of orifices. He derived a leakage equation assuming a series of identical constrictions separated by identical cavities in which the kinetic energy was completely destroyed. Numerous investigators have extended the applicability of the Martin equation by relaxing some of his assumptions.

Existing methods have been classified into: (*a*) purely analytical, (*b*) analytical-experimental, and (*c*) friction coefficient categories. Analytical methods include: Martin [1], Dollin-Brown [2], Gercke [3], Stodola [4], and Scheel [5]. Examples of analytical-experimental methods are: Jerie [6], Egli [7], Vermes [8], and Hodkinson [9]. Friction coefficient methods utilize a rough wall duct friction factor as a function of seal geometry, and examples include: Trutnovsky [10], Idel'cik [11], and Zabriskie and Sternlicht [12]. An overall assessment and comparison with measurements for incompressible flows is found in Morrison et al. [13]. The performance of particularly sophisticated seal geometries is discussed by Stocker [14].

By carefully employing a judicious combination of theory and empirical data, one can reasonably accurately predict the leakage of an ideal labyrinth if the shaft speed is not too high. However, many designs exhibit significant kinetic energy carry-over, which renders their prediction uncertain in the absence of experimental data for determining the extent of this effect. This results from the fact that the cavity flowfield which dissipates the mean mechanical energy is quite complex, as observed in the flow visualization of Keller [15], Jerie [6], and Groddeck [16].

It is clear that the effect of carry-over is quite substantial. Various assumptions have been made to account for it, although none have proven entirely satisfactory for widespread application. No papers giving detailed distributions of such basic flowfield quantities within a single cavity were found for compressible labyrinth flows. However, two

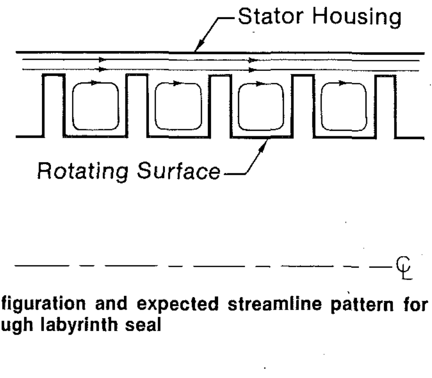

Fig. 1 Configuration and expected streamline pattern for a generic, straight-through labyrinth seal

---

[1] Presently at Sandia National Laboratories, Albuquerque, NM

Contributed by the Gas Turbines Division for publication in the JOURNAL OF ENGINEERING FOR GAS TURBINE AND POWER. Manuscript received at ASME Headquarters November 4, 1985.

papers concerning incompressible flows were found. Stoff [17] compared his numerical predictions of mean swirl velocity at a single axial location with his LDA measurements of a large-scale water test facility. Rhode et al. [18] presented numerous cavity distributions from numerical simulations of liquid hydrogen flowing through two seal designs.

Objective

There is a need for a more widely applicable leakage model which is free of the inherent uncertainty associated with assuming a kinetic energy carry-over coefficient for a new seal configuration. The primary objective of this paper is to assess the current feasibility of a new method which employs an experimentally verified finite difference code as the first stage in predicting the compressible flow leakage through a multicavity labyrinth seal. A second objective is to present and examine the detailed cavity distribution of basic flowfield quantities. This serves to enhance physical insight as well as the development of refined leakage and rotordynamic stability models for labyrinth seals.

Single-Cavity Computation

Numerical Approach. The flow through a multicavity labyrinth is clearly elliptic, with one or more large recirculation zones within each cavity. If possible, one should obviously include all of the cavities in the computational domain since downstream as well as upstream conditions may affect the flow. However, numerical tests for a single-cavity domain confirmed the fact that approximately a 33×33 grid density is required for a grid-independent solution using essentially uniform grid spacing and the QUICK differencing scheme. Thus, the prospects for including multiple cavities in a single accurate solution domain are impractical due to current computing resource limitations.

Therefore a more approximate approach was adopted in developing the leakage model. A two-step procedure is utilized in which the numerical solution of a single cavity, shown in Fig. 2, is obtained for several cavity inlet Mach numbers. The resulting cavity inlet-to-outlet pressure drop values are subsequently employed in a separate leakage model computer code (see Leakage Model section).

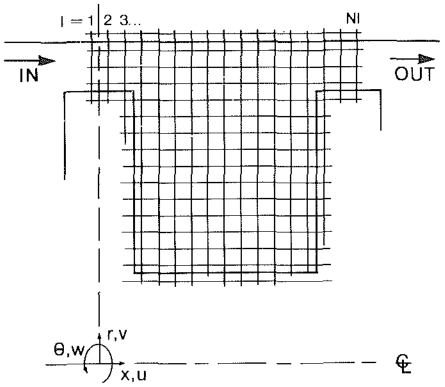

Fig. 2 Computational domain for a labyrinth seal cavity showing a coarse grid

Naturally the cavity inlet boundary conditions are important, but no such detailed measurements for compressible flow in a labyrinth seal cavity are available. In a previous incompressible flow study [18], the inlet boundary values were calculated along with the solution by setting the inlet value of each variable except pressure equal to the corresponding outlet value at each numerical iteration. This was based on the assumption that the incompressible flow along the cavities is streamwise periodic. This assumption is not strictly valid for variable density flow situations. However, leakage model predictions indicate that the cavity inlet Mach number remains relatively low for the great majority of the cavities, increasing abruptly near the seal exit. Therefore the shape of the dimensionless inlet profiles from the incompressible flow solution was adopted as an approximation for the corresponding profiles of the compressible flow through the identical seal cavity.

In achieving the present objective, a previously developed computer program [18] for incompressible flow predictions in a labyrinth seal was extended to allow variable density flowfields. The following paragraph summarizes the computational methodology of the incompressible flow version; subsequent paragraphs discuss the current work of developing the compressible flow extension.

The computer program for incompressible flow in labyrinth seals is a descendant of the TEACH program [19]. Six simultaneous, partial differential equations are solved. These

Nomenclature

A = tooth-clearance flow area
c = tooth clearance
C_p = specific heat
d = radial distance from cavity base to stator wall
H = stagnation enthalpy
K = effective thermal conductivity
k = turbulence kinetic energy
L = axial length of seal cavity
M = Mach number
$\dot{m}$ = leakage mass flow rate
P = absolute static pressure
P_{ow} = inlet stator (outer) wall static pressure
Pe = Peclet number
Pr = effective Prandtl number
R_s = radius of seal stator wall
r_{sh} = shaft radius to the base of a cavity
Re = Reynolds number
S = source term of equation
T = air temperature
Ta = Taylor number
U = Bulk axial velocity
V = (u, v, w) = time-mean velocity (in x, r, θ direction)
W = bulk swirl velocity
x, r, θ = axial, radial, azimuthal cylindrical polar coordinates
Γ = turbulent exchange coefficient, or ratio of specific heats
Δ = internodal mesh spacing
ϵ = turbulence dissipation rate
μ = laminar viscosity
ν = kinematic viscosity
ρ = time-mean density
τ = shear stress
Ω = shaft speed

Subscripts

d = downstream of the seal
e = spatially averaged cavity exit value
eff = effective
H = stagnation enthalpy
i = spatially averaged cavity inlet value
u = upstream of the seal

Superscripts

$*$ = sonic value

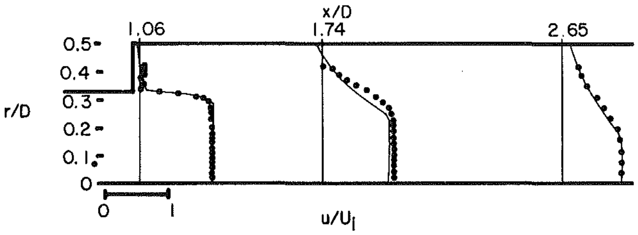

Fig. 3 Predicted (———) and measured [22] (• • •) mean axial velocity within a pipe expansion at $M_i = 0.67$

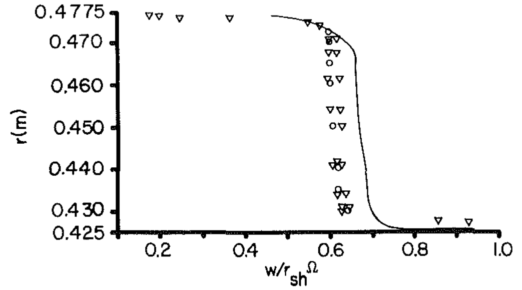

Fig. 4 Predicted (———) and measured [17] (○ ○ ○, ▽ ▽ ▽) mean swirl velocity at $x/L = 0.5$ for a generic seal

are: (*a*) the incompressible, axisymmetric form of the Reynolds-averaged equations for conservation of momentum (with x, r, and θ time-mean velocity components u, v, w), (*b*) two turbulence transport equations constituting the k-ϵ turbulence model, and (*c*) a pressure correction equation which calculates the pressure field and enforces continuity. An assumed isotropic effective viscosity defined as

$$\mu_{\rm eff} = C_\mu \rho k^2/\epsilon + \mu$$

is employed in accordance with the k-ϵ turbulence model of Launder and Spalding [20].

Development of the compressible flow version of the computer code entailed four basic modifications. These consist of: evaluating density from the ideal gas law, inserting compressible stress terms into the governing equations, incorporating the conservation of energy equation, and deriving a new variable-density version of the pressure correction equation. The implementation of the ideal gas law and the compressible stress terms was straightforward. These stress terms are the velocity divergence terms which had been neglected for incompressible flow cases.

The compressible formulation for stress is given by

$$\tau_{ij} = \mu_{\rm eff}(\partial_i v_j + \partial_j v_i) - \delta_{ij}\,\frac{2}{3}\,(\rho k + [\underline{\mu_{\rm eff}\partial_i v_i}])$$

where the underlined quantity is the new contribution.

The stagnation enthalpy form of the conservation of energy equation was employed. It is given as

$$\partial_j(\rho v_j H) - \partial_j(\Gamma_H \partial_j H) = S_H$$

where

$$\Gamma_H = K/C_p = \mu_{\rm eff}/\mathrm{Pr}$$

and

$$S_H = \partial_j\left[v_m \tau_{mj} - \Gamma_H \partial_j\left(\frac{V^2}{2}\right)\right]$$

Temperature is calculated from stagnation enthalpy as

$$T = \left(H - \frac{1}{2}\,V^2\right)\Big/C_p$$

with constant specific heat assumed. The enthalpy boundary conditions include the assumption of adiabatic walls, and the log-law wall function was employed to calculate the appropriate stress terms. The wall functions utilized along the rotating surfaces were appropriately modified to account for the surface velocity.

False Diffusion. Until recently, the use of upwind differencing for convection terms has been the most effective approach for obtaining stable numerical solutions of convection-dominated flows. However, this scheme is only first-order accurate and may introduce serious truncation error known as false diffusion. This is especially true for flows where convection dominates, i.e., where the grid Peclet number $|\mathrm{Pe}| \equiv |V|\Delta/\Gamma_\phi$ exceeds 2.0, with substantial streamline-to-grid skewness and diffusive transport normal to the flow direction.

False diffusion can result in an excessively diffusive solution. A turbulent recirculating flow, such as that within some labyrinth seals, is particularly susceptible to the effects of false diffusion because of its regions of considerable velocity gradient and streamline-to-grid skewness. To remedy this problem, the recent QUICK (Quadratic Upstream Interpolation for Convective Kinematics) finite differencing scheme of Leonard [21] was employed. It has been shown by Rhode et al. [18] that predictions using the QUICK scheme provide a realistic, grid-independent solution using considerably fewer grid points than that using the Hybrid upwind/central differencing scheme, i.e., 33 × 31 versus 53 × 53 grid point density.

Comparison With Experiment. Since distributions of compressible flow quantities within a rotating cavity were unavailable, other internal flows were selected for experimental verification of the computer code. One case consists of the subsonic flow through the sudden pipe expansion test facility of Drewry [22]. After passing through a 63.5-mm-dia inlet pipe, the flow enters the test section through the abrupt pipe expansion as shown in Fig. 3. The test section diameter $D = 97.5$ mm and length $L = 381$ mm. Based on inlet pipe conditions, the Reynolds number and Mach number are 1.42×10^6 and 0.67, respectively. Figure 3 shows the predicted and measured time-mean axial velocity profiles, nondimensionalized by the spatially averaged inlet duct velocity $U = 212.3$ m/s. Observe the excellent agreement at the first and third axial stations in the presence of significantly less agreement at the second station. This is somewhat surprising as the large $\partial u/\partial r$ gradient at the first station appears to represent the most substantial prediction challenge. The discrepancy at the second station is primarily attributed to local measurement inaccuracy resulting from the use of a simple stagnation pressure probe rather than a five-hole pressure probe, for example. This measurement error occurs at $x/D = 1.74$ for $r/D > 0.3$, a location where the streamlines exhibit nonzero slope. It apparently stems from the fact that the probe orientation did not account for the slope of the local incident flow.

The incompressible flow measurements of Stoff [17] constitute another convincing test case. That study concerned water flowing through a large scale test section model of a generic seal such as that shown in Fig. 1. A laser Doppler anemometer was employed. The flow was characterized by the leakage Reynolds number $\mathrm{Re} \equiv 2Uc/\nu \sim 3.4 \times 10^2$ and the Taylor number $\mathrm{Ta} \equiv (Wd/\nu)(d/r_{sh})^{1/2} \sim 1.1 \times 10^4$. Mean velocity measurements were presented only for the circumferential velocity component at a single axial station located midway between adjacent teeth. Figure 4 shows the corresponding predictions to be within 7.0 percent. Further, Stoff's computations utilized the same numerical approach and are essentially identical to those shown here.

Leakage Model

A new approach for leakage modeling has been developed. The new model may be employed to determine the overall pressure drop-leakage characteristic for a wide variety of

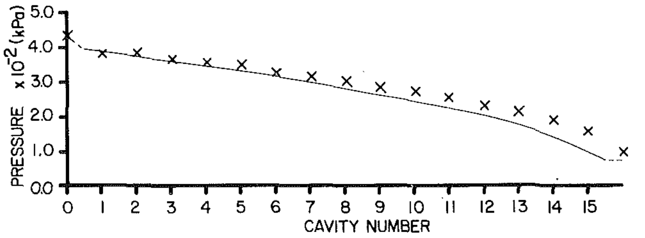

Fig. 5 Predicted (———) and measured [23] (× × ×) pressure distribution in a fifteen-cavity generic seal at 8000 cpm

designs without any assumption concerning kinetic energy carry-over. It does, however, require results from single-cavity computations. Hence, the prediction of leakage for a new design involves a two-step procedure. First, the single-cavity procedure is used to determine the all-important inlet-to-outlet cavity pressure drop for the given seal configuration. This is done at several cavity inlet Mach numbers and at a fixed approximate value of leakage Reynolds number. This Reynolds number may be evaluated from an initial leakage estimate using any existing technique, since it was determined that dimensionless cavity pressure drop is only slightly sensitive to Reynolds number over the Reynolds number range commonly encountered.

Second, the resulting inlet-to-outlet cavity pressure drop predictions are inserted into the leakage model using a second-order polynomial representation of log $[(P_i - P_e)/\frac{1}{2}\rho_i U_i^2]$ versus M_i. The leakage model was developed as a simple computer program to which the user specifies the desired mass leakage rate and the upstream pressure and temperature. The corresponding throttling pressure centered above each tooth is then calculated sequentially, marching downstream from tooth to tooth.

For each cavity, the procedure for calculating the cavity outlet bulk values from known cavity inlet bulk values is as follows: (*a*) The inlet-to-outlet cavity pressure drop, and subsequently the cavity-outlet pressure, is evaluated from the polynomial expression at the known cavity inlet Mach number M_i, (*b*) the cavity outlet density is evaluated from the ideal gas law, and (*c*) the cavity outlet velocity, and subsequently the corresponding Mach number, is calculated from the mass conservation equation using an assumed value of 0.675 for the contraction coefficient of the vena contracta. Since the outlet conditions for a given cavity are the inlet conditions for the next cavity downstream, the above sequence is repeated for each cavity.

For situations in which the last tooth is choked, a modified procedure was found to be slightly more accurate. In that procedure the first step involves the calculation of the cavity inlet Mach number M_i for each cavity assuming each throttling lies along the Fanno line. Using the single-cavity predictions of inlet and exit cavity bulk pressure P_i and P_e, a second-order polynomial representation of P_i/P_e versus M_e is employed to evaluate P_i/P_e for the appropriate M_e of any given cavity. Beginning with the far downstream cavity where both M_e and P_e/P^* are known to be 1.0, the following pair of equations are used to calculate the cavity inlet Mach number M_i

$$P_i/P^* = (P_e/P^*)(P_i/P_e)$$

$$P_i/P^* = M_i^{-1}\left\{\frac{\Gamma+1}{2+(\Gamma-1)M_i^2}\right\}^{1/2}$$

The second equation is simply the well-known pressure-Mach number relation for a Fanno flow. By marching upstream with this calculation, all throttling Mach numbers are easily evaluated, whereupon the downstream-marching calculation procedure itemized above is initiated. With either the choked or nonchoked procedure, the throttle pressure at the first tooth must be evaluated before the downstream-marching calculation procedure can begin. This pressure is estimated from the upstream pressure and temperature using a Bernoulli-type approximation.

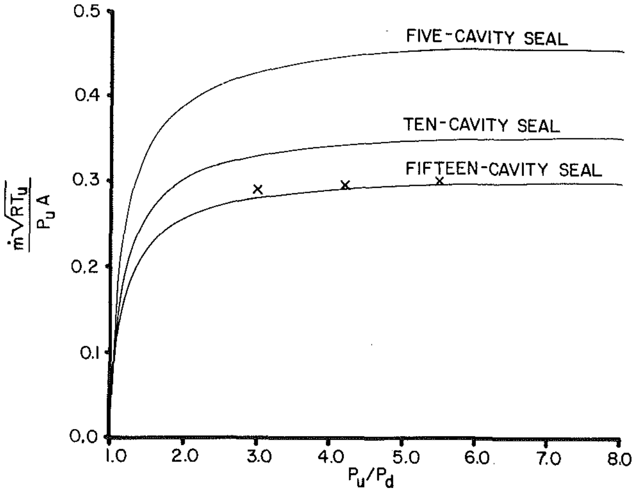

Fig. 6 Predicted (———) and measured [23] (× × ×) leakage flow parameter for generic seals at 8000 cpm

Results

Leakage. The generic seal configuration selected for leakage analysis is one which was recently tested with air at the Turbomachinery Laboratories of Texas A&M University. The pitch $L = 3.10$ mm, stator wall radius $R_s = 76.09$ mm, tooth clearance $c = 0.406$ mm, and radial distance from cavity base to stator wall $d = 3.581$ mm. The sixteen teeth were slightly tapered with a thickness $t = 0.1524$ mm at the periphery. The shaft speed $\Omega = 8000$ cpm and the seal inlet air temperature was 293 K. Leakage Reynolds numbers typically ranged from approximately 1.5×10^4 to 3.0×10^4, and the Taylor number was approximately 1.81×10^3.

A comparison of the predicted pressure distribution with the measurements of Childs et al. [23] is shown in Fig. 5. The dashed line at the seal inlet illustrates that an approximation was employed to estimate the pressure at the first tooth from the upstream value. The dashed line at the seal exit shows that the pressure is assumed constant downstream of the last tooth. The Mach number at the first tooth is near 0.35 and the flow is choked at the last tooth. This increase in Mach number in the streamwise direction yields the larger inlet-to-outlet cavity pressure drop near the exit as exhibited in Fig. 13.

By specifying different leakage rates and tabulating the resulting overall upstream-to-downstream pressure ratio P_u/P_d, a predicted leakage performance curve may be plotted. Such curves for the current generic seal are given in Fig. 6 in terms of conventional leakage flow parameter $\dot{m}\sqrt{RT_u}/P_u A$. Close agreement with the measurements available for the fifteen-cavity case is obtained. For comparison, the predictions for a five-cavity and a ten-cavity seal are included.

Details Within a Single Cavity. The following distributions of flowfield quantities had previously been obtained for a similar cavity of slightly different dimensions in order to allow direct comparisons with earlier seal computations involving liquid hydrogen. The present cavity configuration is of pitch $L = 1.113$ mm, stator wall radius $R_s = 42.89$ mm, tooth radial clearance $c = 0.216$ mm, and radial distance from cavity base to stator wall $d = 1.105$ mm. The shaft speed $\Omega = 3.5 \times 10^4$ cpm, the mean cavity inlet air temperature $T_i = 294.4$ K, and the cavity inlet absolute pressure on the stator wall $P_{ow} = 306$ kPa. Most of the results presented are for the leakage rate case in which the cavity inlet Mach number $M_i = 0.65$ based on bulk axial velocity. Other dimensionless parameters for this case are $Re = 2.07 \times 10^4$ and $Ta = 4.16 \times$

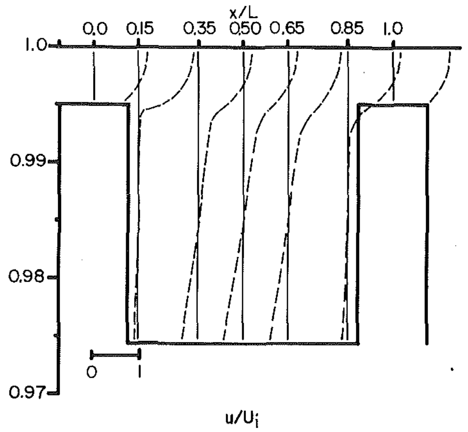

Fig. 7 Predicted mean axial velocity for $M_i = 0.65$

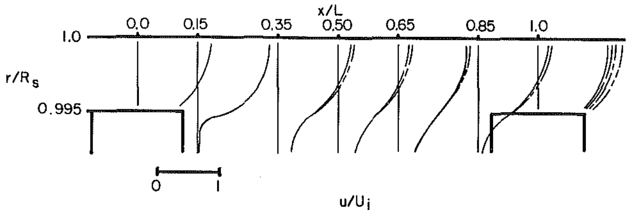

Fig. 8 Magnified view of predicted mean axial velocity showing four mass leakage rates: (*a*) $M_i = 0.2$ (——), (*b*) $M_i = 0.5$ (—— ——), (*c*) $M_i = 0.65$ (—— — ——), and (*d*) $M_i = 0.72$ (—— — — ——).

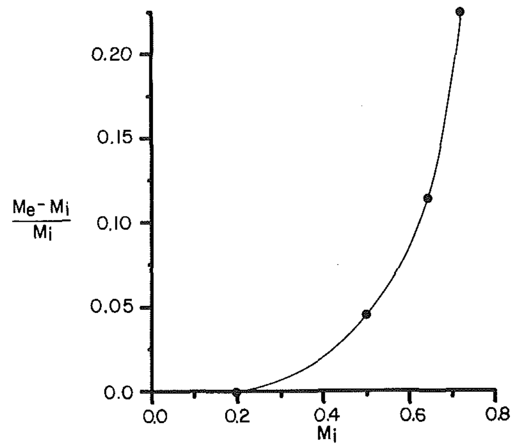

Fig. 9 Predicted variation of cavity inlet-to-outlet Mach number increase with inlet Mach number

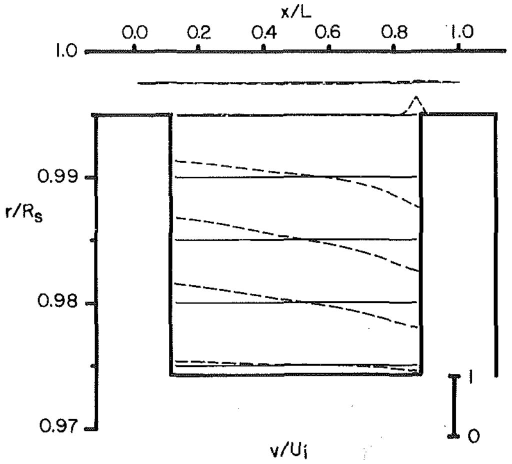

Fig. 10 Predicted mean radial velocity for $M_i = 0.65$

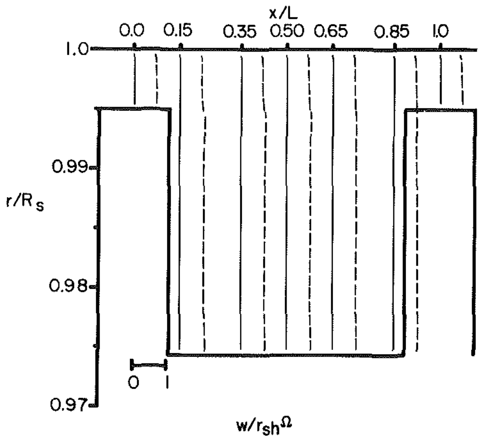

Fig. 11 Predicted mean swirl velocity for $M_i = 0.65$

10^3. Solutions were also obtained for other leakage mass flow rates with inlet Mach number values of 0.2, 0.5, and 0.72 using the same inlet pressure and temperature. These additional leakage flow cases have essentially the above Taylor number with Reynolds numbers of 6.36×10^3, 1.59×10^4, and 2.29×10^4, respectively.

The present predictions were obtained using a 33×31 grid employing the QUICK scheme. The convergence criterion was 0.1 percent for the normalized sum of residual mass source magnitudes, for example. Since the dimensionless predictions for the various leakage cases are generally similar, most plots presented here pertain to the $M_i = 0.65$ case. As the cavity distribution of each variable is discussed, important variations among the solutions of the four cases are examined in detail.

The free shear layer emanating from the separation corner gives rise to the expected recirculation zone in the cavity. There is no indication from these predictions that an additional small recirculation zone exists in the lower corners of the cavity near the base of each tooth. By comparing the results for the various values of M_i, it is seen that the recirculation mass flow rate as a percentage of leakage mass flow rate decreases slightly for increasing M_i. This percentage for the $M_i = 0.2$ case is 40.2 and it decreases steadily to 35.4 for $M_i = 0.72$. This result for the incompressible case of $M_i = 0.2$ agrees with that for the flow of liquid hydrogen through this identical cavity at $Re_x = 1.0 \times 10^6$ and $Ta = 1.3 \times 10^5$ [18], which produces a reciruclation strength of 39.0 percent.

Figure 7 shows the axial velocity component nondimensionalized by the cavity inlet bulk value $U_i = 223.6$ m/s. The solution indicates the expected large value of $\partial u / \partial r$ near the separation corner. This reveals a high level of turbulence energy generation in this thin shear layer region. For such high leakage rate cases, the large bulk pressure drop from inlet to outlet of the cavity results in a density decrease and hence a convective acceleration of the leakage flow in accordance with mass conservation, i.e., the Fanno effect. The magnitude of this phenomenon is found in Fig. 8 by comparing the inlet with the outlet axial velocity values for each leakage case. These values have been normalized by the bulk cavity inlet value corresponding to each situation. This acceleration is more easily observed, however, by comparing the cavity exit values. This variation among the four cases is plotted in Fig. 9; it increases very sharply for $M_i \gtrsim 0.5$. Also note from Fig. 8 that this phenomenon is confined to the tooth clearance region above the downstream tooth.

The dimensionless mean radial velocity component is presented in Fig. 10. This quantity is negligible throughout the leakage flow region as expected, except near the outer periphery of the downstream tooth. The swirl velocity values are given in Fig. 11; the distribution is essentially uniform at a

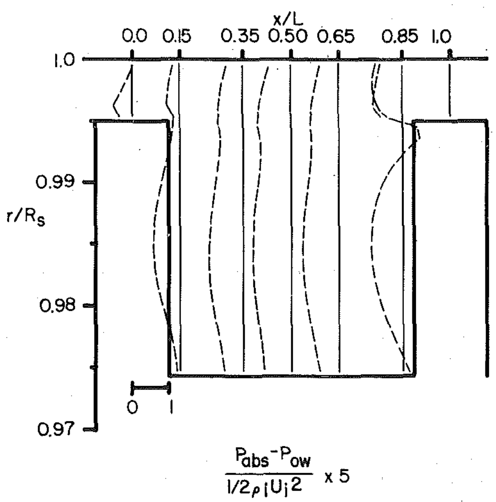

Fig. 12 Predicted mean relative pressure for $M_i = 0.65$

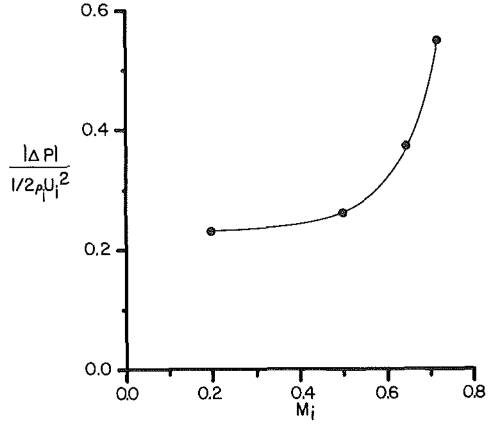

Fig. 13 Predicted variation of cavity inlet-to-outlet bulk pressure drop with inlet Mach number

value of 0.70 when normalized by the shaft tangential velocity. The liquid hydrogen flowfield investigated earlier [18] exhibited a uniform distribution of 0.65 at the same shaft speed.

Figure 12 shows the pressure distribution relative to the inlet stator wall absolute pressure P_{ow}, which is 3.06×10^5 Pa. This relative pressure is normalized by the cavity inlet dynamic pressure. The pressure decreases slowly until $x/L=0.5$ and then increases slightly until approximately $x/L=0.75$. Finally, it decreases sharply as the flow accelerates over the downstream tooth. The sharp pressure peak observed at $x/L=0.85$ results from flow stagnation on the downstream tooth. For the $M_i=0.65$ case shown in Fig. 12, the overall bulk pressure drop across the cavity $(P_i-P_e)/\frac{1}{2}\rho_i U_i^2=0.384$. This quantity is shown in Fig. 13 for each leakage flow rate considered. As implied earlier in reference to Fig. 9, the pressure drop increases dramatically for $M_i \gtrsim 0.5$.

Figure 14 shows density, normalized by the bulk cavity inlet value. It is seen that density in the free stream is very slightly higher than in the recirculation zone. This is a combined effect of the slight variation in the pressure and temperature fields. The decrease in density from cavity inlet to exit is approximately 14 percent for this case.

Dimensionless turbulence kinetic energy contours are plotted in Fig. 15. As mentioned previously, it is the large value of $\partial u/\partial r$ in the free shear layer which produces intense turbulence energy in that region. This promotes the desired high values for bulk pressure drop. As expected, the greatest value occurs near the stagnation point on the downstream tooth. The recirculation region effectively acts as a turbulence energy sink as the figure indicates a lack of turbulence intensity there.

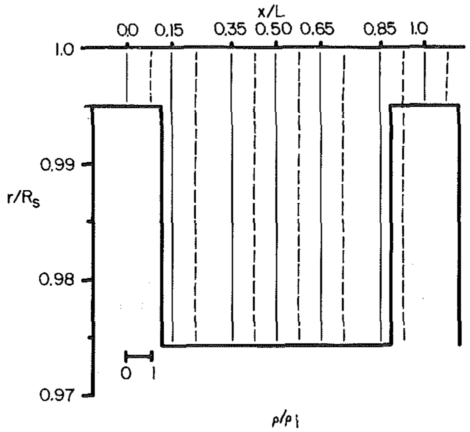

Fig. 14 Predicted mean density for $M_i = 0.65$

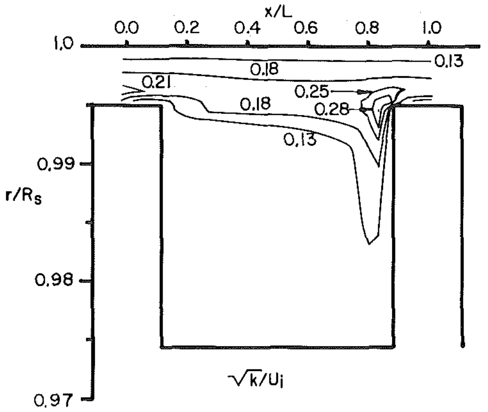

Fig. 15 Predicted turbulence kinetic energy contours for $M_i = 0.65$

Conclusions

A new approach for modeling the leakage through labyrinth seals has been developed and compared with measurements. Also, a family of experimentally verified performance curves for seals containing five, ten, and fifteen cavities is presented. The model is seen to provide realistic results and is highly applicable for untested cavity configurations without the commonly worrisome uncertainty associated with assuming a mean flow kinetic energy carry-over coefficient.

Further, the cavity distributions presented can facilitate the refinement of analytical seal rotordynamic stability models as well as leakage models. One particular finding is the degree of variation of inlet-to-outlet cavity bulk pressure drop and the corresponding convective acceleration of the leakage fluid. This behavior arises from the compressibility effect, and is observed to be largely confined to the tooth clearance region above the downstream tooth. Also of interest are the realistic approximations of flowfield variable distributions which are now possible from the included figures. For example, the cavity distribution of dimensionless swirl velocity may be realistically represented with a cavity-averaged value ranging from 0.73 to 0.70, respectively, for Mach numbers ranging from $M_i=0.2$ to 0.72. Cavity-averaged dimensionless density values range from 0.98 to 0.86 over this M_i range.

Acknowledgments

These results were obtained in an early phase of a fundamental study for which the financial support of AFOSR is gratefully acknowledged. The authors are also indebted to Professor D. Childs and Mr. J. Scharrer for supplying the seal measurements and for numerous helpful discussions. In addition, the expertise of Mr. G. Nail and Ms. Bich-N. Ho is greatly appreciated.

References

1 Martin, H. M., "Labyrinth Packings," *Engineering*, Jan. 10, 1908, pp. 35-36.

2 Dollin, F., and Brown, W. S., "Flow of Fluids Through Openings in Series," *Engineering*, Aug. 27, 1937, pp. 223-224.

3 Gercke, M. J., "Berechnung der Ausflusmengen von Labyrinth-dichtungen," *Die Warme*, No. 32, Aug. 11, 1934, pp. 513-517.

4 Stodola, A., *Steam and Gas Turbines*, McGraw-Hill, New York, 1927.

5 Scheel, L. F., *Gas Machinery*, Gulf Publishing Company, Houston, Texas, 1972.

6 Jerie, J., "Flow Through Straight-Through Labyrinth Seals," *Proc. of the 7th Int. Cong. for Appl. Mech.*, Vol. 2, 1948, pp. 70-82.

7 Egli, A., "The Leakage of Steam Through Labyrinth Seals," *Trans. ASME*, Vol. 57, 1935, pp. 115-122.

8 Vermes, G., "A Fluid Mechanics Approach to the Labyrinth Seal Leakage Problem," ASME JOURNAL OF ENGINEERING FOR POWER, Apr. 1961, pp. 161-169.

9 Hodkinson, B., "Estimation of the Leakage Through a Labyrinth Gland," *Proc. of Inst. Mech. Eng.*, Vol. 141, 1939, pp. 283-286.

10 Trutnovsky, K., *Beruhrungsfreie Dichtungen*, VDI-Verlag GmbH, Dusseldorf, 1973.

11 Idel'cik, *Memento des pertes de charge*, Eyrolles Editeur, Paris.

12 Zabriskie, W., and Sternlicht, B., "Labyrinth Seal Leakage Analysis," *Journal of Basic Engineering*, Series D, Vol. 81, 1959, pp. 332-340.

13 Morrison, G. L., Rhode, D. L., Cogan, K. C., Chi, D., and Demko, J., "Labyrinth Seals for Incompressible Flow," Final Report for Contract NAS8-34536, Nov. 30, 1983.

14 Stocker, H. L., "Advanced Labyrinth Seal Design Performance for High Pressure Ratio Gas Turbines," ASME Paper No. 75-WA/GT-22.

15 Keller, C., "Labyrinthstromungen bei Turbomaschinen," *Escher Wyss Mitt.*, 1935, p. 160.

16 Groddeck, K. H., "Probleme der Beruhrungsfreien Hochdruck-Stopbuchsen," *Forschung auf dem gebieie des Ingenieurwesens*, 1957, No. 5, pp. 183-185.

17 Stoff, H., "Incompressible Flow in a Labyrinth Seal," *J. Fluid Mech.*, Vol. 100, 1980, pp. 817-829.

18 Rhode, D. L., Demko, J. A., Traegner, U. K., Morrison, G. L., and Sobolik, S. R., "On the Prediction of Incompressible Flow in Labyrinth Seals," presented at the 7th Annual Energy-Sources Technology Conference, New Orleans, LA, Feb. 12-16, 1984.

19 Gosman, A. D., and Pun, W. M., "Calculations of Recirculating Flows," Rept. No. HTS/74/2, Department of Mechanical Engineering, Imperial College, London, England, 1974.

20 Launder, B. E., and Spalding, D. B., "The Numerical Computation of Turbulent Flows," *Comp. Methods in Appl. Mech. and Engr.*, Vol. 3, 1974, pp. 269-289.

21 Leonard, B. P., "A Stable and Accurate Convective-Modelling Procedure Based on Quadratic Upstream Interpolation," *Comp. Meths. Appl. Mech. Eng.*, Vol. 19, 1979, pp. 59-98.

22 Drewry, J. E., "Characterization of Sudden-Expansion Dump Combustor Geometries," AFAPL-TR-76-52, July 1976.

23 Childs, D. W., and Scharrer, J. K., Personal Communication, 1985.